

REPORT DOCUMENTATION PAGE

AFRL-SR-BL-TR-00-

0607

Public reporting burden for this collection of information is estimated to average 1 hour per response, including the time for reviewing instructions, searching existing data sources, gathering and maintaining the data needed, and completing and reviewing the collection of information. Send comments regarding this burden estimate or any other aspect of this collection of information, including suggestions for reducing this burden, to Washington Headquarters Service, Directorate for Information Operations and Reports, 1215 Jefferson Davis Highway, Suite 1204, Arlington, VA 22202-4302, and to the Office of Management and Budget, Paperwork Project, Washington, DC 20503.

ating and reviewing
ate for Information

1. AGENCY USE ONLY (Leave blank)		2. REPORT DATE 31 OCT 00		3. Final Tech Report 01 May 97 to 31 Dec 99	
4. TITLE AND SUBTITLE Coherent Structures and Chaos in Beam Plasmas				5. FUNDING NUMBERS F49620-97-1-0325	
6. AUTHOR(S) Chiping Chen					
7. PERFORMING ORGANIZATION NAME(S) AND ADDRESS(ES) Massachusetts Institute of Technology Plasma Science & Fusion Center 77 Massachusetts Avenue, NW16 Cambridge, MA 02139-4307				8. PERFORMING ORGANIZATION REPORT NUMBER	
9. SPONSORING/MONITORING AGENCY NAME(S) AND ADDRESS(ES) Air Force Office of Scientific Research AFOSR/NM 801 N. Randolph Street, Rm 732 Arlington, VA 22203-1977				10. SPONSORING/MONITORING AGENCY REPORT NUMBER F49620-97-1-0325	
11. SUPPLEMENTARY NOTES					
12a. DISTRIBUTION AVAILABILITY STATEMENT Approved for public release; distribution unlimited.				12b. DISTRIBUTION CODE	
13. ABSTRACT (Maximum 200 words) This report summarizes our research carried out under the auspices of the above referenced grants from May 1, 1997 to December 31, 1999. The goal of this research is to investigate coherent structures and chaos in beam plasmas in regimes relevant to the development of advanced microwave/millimeter wave sources. Preprints and reprints describing detailed findings in recent investigations are provided in a compendium of 1997-2000 reprints in refereed journals at the end of the report.					
20001120 200					
14. SUBJECT TERMS				15. NUMBER OF PAGES	
				16. PRICE CODE	
17. SECURITY CLASSIFICATION OF REPORT UNCLASSIFIED	18. SECURITY CLASSIFICATION OF THIS PAGE UNCLASSIFIED	19. SECURITY CLASSIFICATION OF ABSTRACT UNCLASSIFIED	20. LIMITATION OF ABSTRACT UL		

Final Report
Coherent Structures and Chaos in Beam Plasmas
AFOSR Grant No. F49620-97-1-325

October 5, 2000

Submitted to:
Dr. Arje Nachman
Program Manager
Air Force Office of Scientific Research
801 North Randolph Street, Room 732
Arlington, VA 22203-1977

Submitted by
Dr. Chiping Chen
Principal Investigator

Final Report
Coherent Structures and Chaos in Beam Plasmas
AFOSR Grant No. F49620-97-1-325

This report summarizes our research carried out under the auspices of the above referenced grant from May 1, 1997 to December 31, 1999. The goal of this research is to investigate coherent structures and chaos in beam plasmas in regimes relevant to the development of advanced microwave/millimeter wave sources. Preprints and reprints describing detailed findings in recent investigations are provided in a compendium of 1997-2000 reprints in refereed journals at the end of this report. The following is a brief summary of our research accomplishments in selected areas.

1. Mechanisms of Chaotic Electron Motion and Beam Halo Formation [1-3]

An important issue in the design of HPM tubes is how to prevent high-intensity relativistic electron beams from forming halos because they cause electron beam losses and subsequent plasma formation, rf pulse shortening and rf breakdown [4]. Under the auspices of this grant, investigations were conducted of mechanisms by which chaotic particle motion and halo formation occurs [1-3].

In particular, it was found [5,6] that there are two important mechanisms for chaotic particle motion and halo formation in high-intensity electron beams in such systems as high power klystrons. One mechanism is due to a root-mean-square (rms) mismatch between the beam and externally applied focusing field [5]. The rms mismatch is induced by the bunching of the electron beam by intense rf (radiation plus electrostatic wave) fields inside the device. Above a certain threshold, rms mismatched electron beams produce pronounced (sizable) halos asymptotically. For high-intensity electron beams, the threshold occurs at the relative envelope mismatch of 42%, as predicated analytically and confirmed by self-consistent simulations in earlier work [7]. The other mechanism is due to the subtle effect of a mismatch in the particle phase-space distribution (e.g., a nonuniform charge density distribution) under the rms matching condition [6]. In HPM tubes, the former is primarily responsible for halo formation in highly bunched electron beams caused by intense rf fields, whereas the latter is primarily responsible for halo formation in the transport of electron beams in the absence of any significant rf field.

Detailed comparisons were made between the 2-D Green's function-based simulations [1-3,5] and the experimental observations of electron beam halo formation and beam loss in the 50 MW, 11.4 GHz periodic permanent magnet (PPM) focusing klystron experiment [8] at the Stanford Linear Accelerator Center (SLAC). Because of the availability of more precise experimental data, considerable improvements [1-3] were made in the comparisons after we reported initial results of our investigation [5]. The results were presented at a number of technical meetings, including an *invited paper* [1] at the 1999 APS Division of Plasma Physics Annual Meeting in Seattle, Washington.

2. Discovery of Intense Electron Beam Equilibria in Periodic Focusing Fields [1,9,10]

The fundamental reason for the two important mechanisms [5,6] for chaotic particle motion and halo formation is that the electron beam is far from equilibrium (or quasi-equilibrium) in the field configuration consisting of external applied (static and/or rf) fields and the self-fields generated by the beam. Therefore, in order to invent techniques for prevent intense electron beams from developing halos, a better understanding of the equilibrium properties of high-intensity electron beams must be gained. Under the auspices of this grant, we investigated intense electron beam equilibria in periodic solenoidal focusing fields and studied the influence of the equilibrium profile on the phase-space structure of the beam.

2.1. Determination of the Phase Space Structure for an Intense Beam in the Rigid-Rotor Vlasov Equilibrium [10]

An analysis [10] was made of the phase space structure for test particle motion in the field configuration consisting of an applied periodic solenoidal magnetic field and the self-fields of an intense beam in the rigid-rotor Vlasov equilibrium [11] to address the fundamental question: How does the phase space structure vary with beam intensity, focusing field strength, and beam rotation under the 'best' conditions corresponding a matched equilibrium beam. By examining the intrinsic properties of the phase space of the test particle motion as a function of these parameters, valuable insights were gained as to which operating regimes are more or less robust against the ejection of halo electrons from the beam interior (core) under small beam mismatch and/or collective excitations in the beam core. Detailed findings of this investigation are reported in [10], two important results are:

- a) Increasing the beam intensity induces more pronounced nonlinear resonances and chaotic structures in the phase space of the particle motion; and
- b) Increasing the average canonical angular momentum of the beam reduces the chaotic behavior in the phase space of the particle motion.

These results may be used in future design of HPM tubes to prevent beam losses.

2.2. Cold-Fluid Corkscrewing Elliptic Beam Equilibrium [1,9]

It was shown [1,9] that there exist a new class of cold-fluid corkscrewing elliptic beam equilibria for intense electron or ion beam propagation through a linear focusing channel consisting of uniform solenoidal, periodic solenoidal and alternating-gradient quadrupole focusing magnets in an arbitrary arrangement including field tapering. The equilibrium density and flow velocity profiles were determined, and generalized beam envelope equations were derived. The equilibrium beam theory was verified [1,9] with self-consistent simulations using the Green's function based code [12].

The stability properties of the corkscrewing elliptic beam equilibrium are being studied. It is anticipated that the new corkscrewing elliptic beam equilibrium may be used to improve beam transport and beam confinement in high-power microwave sources.

3. Discovery of Ultrahigh-Frequency Stimulated Radiation from Spatiotemporally Gyating Relativistic Electron Beams [13-15]

Under the auspices of this grant, a theoretical investigation was made of stimulated electromagnetic interactions in relativistic gyrating beam with strong spatial, temporal, or spatiotemporal correlations [13-15]. In this investigation, the equilibrium distribution function for a spatiotemporally gyrating beam is assumed to be of the form $f_0(p_\perp, p_z, \chi)$, where the magnitude of the perpendicular momentum p_\perp , axial momentum p_z , and variable $\chi = \phi - \omega_c(z - v_p t) / (v_z - v_p)$ are the single-particle constants of motion for the electrons, and ϕ and ω_c are the electron gyrophase and electron cyclotron frequency, respectively. An axial-dependent distribution corresponds to the $v_p = 0$ limit of the spatiotemporal distribution, whereas a time-dependent distribution corresponds to the $v_p = \infty$ limit of the spatiotemporal distribution. Beams with axial dependent distributions have been used in gyroamplifier and cyclotron autoresonance maser (CARM) experiments [16], and those with time-dependent distributions have been used in gyroklystrons [17]. More recently, spatiotemporally gyrating beams are used in harmonic converter experiments [18].

While results of our investigation are detailed in [13-15], the important findings are as follows.

- a) The growth rate of the cyclotron maser instability is sensitive to the detailed distribution in the variable χ , including the enhancement of the instability growth rate [13];
- b) The gain bandwidth depends critically on the phase velocity v_p [14,15]; and
- c) Spatiotemporally gyrating relativistic electron beams with $v_p \approx v_z$ exhibit a new effect, namely, stimulated interactions at ultrahigh frequencies with $\omega \gg 2\gamma^2 \omega_c$ [14,15].

Item c) listed above can be used to develop high-frequency gyroamplifiers that can operate with low-voltage electron beams and low magnetic fields to satisfy key requirements in airborne radar applications.

4. Discovery of Omnidirectional Reflectivity and Omniguide [19,20]

As a spin-off of the research and excellent education funded under the auspices of this grant, a novel dielectric omnidirectional reflector [19] has been invented recently and

demonstrated experimentally by a team of Massachusetts Institute of Technology's researchers. Such an omnidirectional reflector, which consists of multiple alternating layers of dielectric materials with sharp contrast in the index of refraction, can reflect light in arbitrary direction with arbitrary polarization over a wide range of wavelength. Since the publication of this invention [19], it has generated considerable interests from government (especially DOD) laboratories, private industries, and news media [21,22]. An omniguide was also invented based on the principles of omnidirectional reflectivity [20]. We are currently developing a Photonic Bandgap Structure Simulator (PBGSS) for the modeling of metallic photonic bandgap structures for use in HPM sources.

5. Interactions with Air Force Research Laboratory and Industries

We made numerous contacts with researchers (e.g., Dr. Tom Spencer and Dr. J. A. Gaudet) at Air Force Research Laboratory, and communicated our research results with them, through 1999 seminar presentation at AFRL as well as technical meetings such as the 1997, 1998 and 1999 APS DPP Meetings and 1998, 1999 and 2000 SPIE AeroSense. We will continue our strong ties with AFRL.

In an effort to transfer technology to private industry, we completed a conceptual design for a high-power X-band relativistic two-stream amplifier. The design was done in collaboration with Microwave Technologies, Inc. in Fairfax, Virginia, which is interested in the experimental demonstration of the relativistic two-stream amplifier. Results of the design were presented in the Intense Microwave Pulses Session at the SPIE Meeting held in San Diego from July 31 to August 1, 1997, and were published [23]. In addition, we are also establishing collaboration with Mission Research Corporation (MRC, contact persons: Dr. Las Ludeking and Dr. Richard Smith) on relativistic magnetron research.

In the area of photonic bandgap research, we are establishing collaborations with both Raytheon Systems Company (Contact person: Dr. Delmar Barker) and Omniguide, Inc., a start-up company co-founded by our graduate student (Dr. Yoel Fink).

6. References

1. C. Chen and Pakter, "Mechanisms and control of beam halo formation in intense microwave sources and accelerators," (Invited Paper), *Phys. Plasmas* **7**, 2203 (2000).
2. R. Pakter and C. Chen, "Electron beam halo formation in periodic permanent focusing klystron amplifiers," *IEEE Trans. Plasma Sci.*, Vol. 28, No. 3, June, in press (2000).
3. C. Chen, M. Hess, and R. Pakter, "Electron beam halo formation in periodic permanent focusing klystron amplifiers," in *Intense Microwave Pulses VII*, edited by H. E. Brandt, SPIE Proc., in press (2000).
4. See, for example, *Special Issue on High-Power Microwave Generation*, edited by E. Schamiloglu and Y. Y. Lau, *IEEE Trans. Plasma Sci.* **PS-26**, No. 3 (1998).
5. R. Pakter and C. Chen, "Halo formation in intense electron beams in high-power klystron amplifiers," in *Intense Microwave Pulses VI*, edited by H. E. Brandt, SPIE Proc. **3702**, 21 (1999).
6. C. Chen and R. A. Jameson, "Self-consistent studies of periodically focused intense charged-particle beams," *Phys. Rev.* **E52**, 3074 (1995).
7. Y. Fink, C. Chen, and W. P. Marable, "Halo formation and chaos in rms matched beam propagation through a periodic solenoidal focusing channel," *Phys. Rev.* **E55**, 7557 (1997).
8. D. Sprehn, G. Caryotakis, E. Jongewaard, and R. M. Phillips, "Periodic permanent magnetic development for linear collider X-band klystrons," *Proc. XIX International Linac Conf.* (Argonne National Laboratory Report ANL-98/28, 1998), p. 689.
9. R. Pakter and C. Chen, "Cold-fluid equilibrium for a corkscrewing elliptic beam in a variable focusing channel," *Phys. Rev.* **E62**, 2789 (2000).
10. C. Chen, R. Pakter, and R. C. Davidson, "Phase space structure for matched intense charged-particle beams in periodic focusing transport systems," *Phys. Plasmas* **6**, 3647 (1999).
11. C. Chen, R. Pakter, and R. C. Davidson, "Rigid-rotor Vlasov equilibrium for an intense charged-particle beam propagating through a periodic solenoidal magnetic field," *Phys. Rev. Lett.* **79**, 225 (1997).
12. M. Hess, C. Chen, and R. Pakter, "Three dimensional Green's function description of space charge in intense charged-particle beams," *Proc. 1999 Part. Conf.* (1999), p. 2752.
13. J. A. Davies and C. Chen, "Stability properties of coherently gyrating relativistic electron beams," *Phys. Plasmas* **5**, 3416 (1998).
14. J. A. Davies and C. Chen, "Stimulated radiation from spatiotemporally gyrating relativistic electron beams," *Phys. Plasmas* **7**, in press (2000).
15. J. A. Davies and C. Chen, "New method for ultrahigh frequency cyclotron maser at low magnet field," in *Intense Microwave Pulses VII*, edited by H. E. Brandt, SPIE Proc. **4031**, in press (2000).
16. J. L. Rullier, et al., *Nucl. Instruments and Methods Phys. Res.* **A241**, 93 (1994).
17. W. Lawson, et al., *J. Appl. Phys.* **78**, 550 (1995).
18. J. L. Hirshfield, *Phys. Rev.* **A46**, 1561 (1992).
19. Y. Fink, J. N. Winn, S. Fan, C. Chen, J. Michel, J. D. Joannopoulos, and E. L. Thomas, "A Dielectric Omnidirectional Reflector," *Science* **282**, 1679(1998).

20. Y. Fink, D. J. Ripin, S. Fan, C. Chen, J. D. Joannopoulos, and E. L. Thomas, "Guiding Optical Light in Air Using an All Dielectric Structure," *IEEE Journal of Lightwave Technology* **17**, 2039 (1999).
21. B. Schechter, "MIT scientists turn a simple idea into perfect mirror," *The New York Times*, Science Section, December 15 (1998).
22. C. Lee, "Perfect mirror design technology," Air Force Office of Scientific Research, Research Highlights (January-February, 1999).
23. C. Chen and J. E. Velazco, "Development of a high-power X-band relativistic two-stream amplifier," *Proc. SPIE* **3158**, 171 (1998).

**List of Researchers Supported under
AFOSR Grant No. F49620-97-1-325**

Dr. Chiping Chen	Principal Research Scientist MIT Plasma Science and Fusion Center
Mr. Yoel Fink	Graduate Student MIT Material Science and Engineering Department
	Degree Received: Ph.D Date: May, 2000 Current Position: Assistant Professor Department of Material Science and Engineering MIT
Mr. Mark Hess	Graduate Student MIT Physics Department
Prof. John A. Davies	Physics Department Clark University Visiting Scientist MIT Plasma Science and Fusion Center
Dr. Renato Pakter	Postdoctoral Research Associate MIT Plasma Science and Fusion Center

Compendium of 1997-2000 Reprints in Refereed Journals
Coherent Structures and Chaos in Beam Plasmas
AFOSR Grant No. F49620-97-1-325

1. C. Chen and Pakter, "Mechanisms and control of beam halo formation in intense microwave sources and accelerators," (**Invited Paper**), Phys. Plasmas **7**, 2203 (2000).
2. R. Pakter and C. Chen, "Cold-fluid equilibrium for a corkscrewing elliptic beam in a variable focusing channel," Phys. Rev. E **62**, 2789 (2000).
3. R. Pakter and C. Chen, "Electron beam halo formation in periodic permanent focusing klystron amplifiers," IEEE Trans. Plasma Sci., Vol. 28, No. 3, June, in press (2000).
4. J. A. Davies and C. Chen, "Stimulated radiation from spatiotemporally gyrating relativistic electron beams," Phys. Plasmas **7**, in press (2000).
5. C. Chen, R. Pakter, and R. C. Davidson, "Phase space structure for matched intense charged-particle beams in periodic focusing transport systems," Phys. Plasmas **6**, 3647 (1999).
6. Y. Fink, D. J. Ripin, S. Fan, C. Chen, J. D. Johnnopolous, and E. L. Thomas, "Guiding Optical Light in Air Using an All Dielectric Structure," IEEE Journal of Lightwave Technology **17**, 2039 (1999).
7. J. A. Davies and C. Chen, "Stability properties of coherently gyrating relativistic electron beams," Phys. Plasmas **5**, 3416 (1998).
8. Y. Fink, J. N. Winn, S. Fan, C. Chen, J. Michel, J. D. Joannopoulos, and E. L. Thomas, "A Dielectric Omnidirectional Reflector," Science **282**, 1679(1998).

Mechanisms and control of beam halo formation in intense microwave sources and accelerators*

C. Chen[†] and R. Pakter

Plasma Science and Fusion Center, Massachusetts Institute of Technology, Cambridge, Massachusetts 02139

(Received 3 November 1999; accepted 7 February 2000)

Halo formation and control in space-charge-dominated electron and ion beams are investigated in parameter regimes relevant to the development of high-power microwave (HPM) sources and high-intensity electron and ion linear accelerators. In particular, a mechanism for electron beam halo formation is identified in high-power periodic permanent magnet (PPM) focusing klystron amplifiers. It is found in self-consistent simulations that large-amplitude current oscillations induce mismatched beam envelope oscillations and electron beam halo formation. Qualitative agreement is found between simulations and the 50 MW 11.4 GHz PPM focusing klystron experiment at Stanford Linear Accelerator Center (SLAC) (D. Sprehn, G. Caryotakis, E. Jongewaard, and R. M. Phillips, "Periodic permanent magnetic development for linear collider X-band klystrons," *Proceedings of the XIXth International Linac Conference*, Argonne National Laboratory Report ANL-98/28, 1998, p. 689). Moreover, a new class of cold-fluid corkscrewing elliptic beam equilibria is discovered for ultrahigh-brightness, space-charge dominated electron or ion beam propagation through a linear focusing channel consisting of uniform solenoidal magnetic focusing fields, periodic solenoidal magnetic focusing fields, and/or alternating-gradient quadrupole magnetic focusing fields in an arbitrary arrangement including field tapering. As an important application of such new cold-fluid corkscrewing elliptic beam equilibria, a technique is developed and demonstrated for controlling of halo formation and beam hollowing in a rms-matched ultrahigh-brightness ion beam as it is injected from an axisymmetric Pierce diode into an alternating-gradient magnetic quadrupole focusing channel. © 2000 American Institute of Physics. [S1070-664X(00)96105-6]

I. INTRODUCTION

One of the most challenging tasks in the development of high-intensity microwave sources and high-intensity particle accelerators is to prevent intense electron or ion beams from beam losses.^{1,2} In high-intensity microwave sources, such as those considered for directed energy applications and for powering the next linear collider (NLC), a small fractional loss of electrons into the radio-frequency (rf) structure will inevitably induce secondary emission of electrons which, in the presence of intense rf fields, may cause an avalanche of secondary electron emission and subsequent plasma formation and alteration in the frequency response or dispersion characteristics of the rf structure. It is likely that a sequence of such events ultimately leads to rf pulse shortening in high-power microwave (HPM) sources.^{1,3-7} In high-intensity electron or ion accelerators, such as high-gradient electron linacs, rf proton linacs for spallation neutron source, and induction linacs for heavy ion fusion applications, losses of electrons or ions in the accelerating structure may also result in intolerable radioactivity in the structure,⁸ in addition to the secondary emission of electrons and/or ions.

While disruptive beam loss is caused by violent instabilities such as the beam-breakup (BBU) instability⁹⁻¹¹ in the beam, mild beam loss is often associated with the formation of a tenuous halo¹²⁻²¹ around a dense core of a beam, mak-

ing physical contact with the inner wall of a microwave tube or accelerator. From the point of view of beam transport, there are two main processes for halo formation in high-intensity particle (electron or ion) beams. One process is caused by a mismatch in the root-mean-square (rms) beam envelope,¹²⁻¹⁵ and the other is due to a mismatch in the particle phase-space distribution relative to an equilibrium distribution.¹⁶⁻²¹ Both processes can occur when the beam intensity is sufficiently high, so that the particle beam becomes space-charge-dominated.

For a periodic focusing channel with periodicity length S and vacuum phase advance σ_0 , a *space-charge-dominated beam* satisfies the condition²⁰

$$\frac{SK}{4\sigma_0\epsilon} > 1,$$

whereas an *emittance dominated beam* satisfies the condition

$$\frac{SK}{4\sigma_0\epsilon} \ll 1.$$

Here, $K = 2q^2 N_b / \gamma_b^3 \beta_b^2 m c^2$ is the normalized self-field perveance, ϵ is the unnormalized transverse rms emittance of the beam, N_b is the number of particles per unit axial length, q and m are the particle charge and rest mass, respectively, $\beta_b c$ and γ_b are the average axial velocity and relativistic mass factor of the particles in the beam, respectively, and c is the speed of light *in vacuo*. The emittance, which is essentially the beam radius times a measure of randomness in the

*Paper JI2 5 Bull. Am. Phys. Soc. 44, 163 (1999).

[†]Invited speaker.

transverse particle motion, is often measured experimentally or calculated in terms of the normalized transverse rms emittance $\epsilon_n = \gamma_b \beta_b \epsilon$. For a uniform density beam with radius a and temperature T_b , the normalized transverse rms emittance is given by

$$\epsilon_n = \gamma_b \beta_b \epsilon = \frac{a}{2} \left(\frac{\gamma_b \beta_b T_b}{m c^2} \right)^{1/2},$$

where k_B is the Boltzmann constant. For an electron beam, the dimensionless parameter $SK/4\sigma_0\epsilon$ can be expressed as

$$\frac{SK}{4\sigma_0\epsilon} = 2.9 \times 10^{-5} \frac{1}{\sigma_0} \left(\frac{S}{\epsilon_n} \right) \frac{I_b}{\gamma_b^2 \beta_b^2},$$

where I_b is the electron beam current in amperes, ϵ_n is the normalized rms emittance in meter-radians, and S is in meters. For an ion beam,

$$\frac{SK}{4\sigma_0\epsilon} = 1.6 \times 10^{-8} \frac{1}{\sigma_0 A} \left(\frac{q}{e} \right) \left(\frac{S}{\epsilon_n} \right) \frac{I_b}{\gamma_b^2 \beta_b^2},$$

where A and q/e are the atomic mass and magnitude of the charge state of the ion, respectively, I_b is the ion beam current in amperes, $\epsilon_n = \gamma_b \beta_b \epsilon$ is the normalized rms emittance in meter-radians, and S is in meters.

In this paper, halo formation and control in space-charge-dominated electron and ion beams are investigated in parameter regimes relevant to the development of HPM sources and high-intensity electron and ion linacs. A mechanism for electron beam halo formation is identified in high-power periodic permanent magnet (PPM) focusing klystron amplifiers. A new class of cold-fluid corkscrewing elliptic beam equilibria is discovered for ultrahigh-brightness, space-charge-dominated electron or ion beam propagation through a linear focusing channel consisting of uniform solenoidal magnetic focusing fields, periodic solenoidal magnetic focusing fields, and/or alternating-gradient quadrupole magnetic focusing fields in an arbitrary arrangement including field tapering. As an important application of such new cold-fluid corkscrewing elliptic beam equilibria, a technique is developed and demonstrated for controlling of halo formation and beam hollowing in a rms-matched ultrahigh-brightness ion beam as it is injected from an axisymmetric Pierce diode into an alternating-gradient magnetic quadrupole focusing channel. In these studies, two-dimensional cold-fluid and self-consistent electrostatic and magnetostatic models are used whenever appropriate. The self-consistent model is based on a Green's function technique rather than a particle-in-cell (PIC) technique.

In the study of electron beam halo formation in high-power PPM focusing klystron amplifiers, the two-dimensional self-consistent electrostatic and magnetostatic model¹⁵ for the transverse beam dynamics is used to analyze equilibrium beam transport in a periodic magnetic focusing field in the absence of a radio-frequency signal, and the behavior of a high-intensity electron beam under a current-oscillation-induced mismatch between the beam and the periodic magnetic focusing field during high-power operation of the device. Detailed simulation results are presented for choices of system parameters corresponding to the 50 MW,

11.4 GHz periodic permanent magnet (PPM) focusing klystron experiment²² performed at the Stanford Linear Accelerator Center (SLAC). It is found that sizable halos appear once the beam envelope undergoes several oscillations.

In the analysis and applications of cold-fluid corkscrewing elliptic beam equilibria, the steady-state cold-fluid equations are solved with a general magnetic focusing field profile. Generalized beam envelope equations for equilibrium flow are obtained. It is shown that limiting cases of cold-fluid elliptic beam equilibria include the familiar cold-fluid round rigid-rotor beam equilibrium in a uniform magnetic focusing field²³⁻²⁵ and both the familiar round rigid-rotor Vlasov beam equilibrium²⁶⁻²⁸ in a periodic solenoidal focusing field and the familiar Kapchinskij-Vladimirskij beam equilibrium²⁹ in alternating-gradient quadrupole magnetic focusing field in the zero-emittance limit. As a simple example, a cold-fluid corkscrewing elliptic beam equilibrium in a uniform magnetic focusing field is discussed. As an application of the present equilibrium beam theory, a general technique is developed, and demonstrated with an example for the controlling of beam halo formation and beam hollowing in ultrahigh-brightness beams. This technique is effective before any collective instability may develop to reach considerably large amplitudes.

The paper is organized as follows. In Sec. II, steady-state cold-fluid equations and two-dimensional self-consistent model are presented for transverse electrostatic and magnetostatic interactions in a highintensity charged-particle beam propagating through a linear focusing channel with a general magnetic focusing field profile. In Sec. III, both equilibrium beam transport and halo formation in high-power PPM focusing klystron amplifiers are studied. The equilibrium (well-matched) beam envelope is determined for intense electron beam propagation through a PPM focusing field, and self-consistent simulations of equilibrium beam transport are performed. The effects of large-amplitude charge-density and current oscillations on inducing mismatched beam envelope oscillations are discussed, and use is made of the self-consistent model to study the process of halo formation in a high-intensity electron beam during high-power operation of such a device. The results are compared with the SLAC PPM focusing klystron amplifier experiment.²² In Sec. IV, a solution to the steady-state cold-fluid equations presented in Sec. II is obtained, and generalized beam envelope equations for equilibrium flow are derived. Examples of corkscrewing elliptic beam equilibria in a uniform magnetic field are presented. In Sec. V, a technique for controlling of the beam halo and beam hollowing is developed and demonstrated as an important application of the cold-fluid equilibrium beam theory. Finally, conclusions are given in Sec. VI.

II. MODELS AND ASSUMPTIONS

We consider a thin, continuous, space-charge-dominated charged particle beam propagating with axial velocity $\beta_b c \hat{e}_z$ through a linear focusing channel consisting of uniform solenoidal magnetic focusing fields, periodic solenoidal magnetic focusing fields, and/or alternating-gradient quadrupole magnetic focusing fields in an arbitrary arrangement. The

fields can be tapered, and the quadrupole magnets are allowed to be at various angles in the transverse direction. In the thin-beam approximation, the focusing magnetic field is expressed approximately as

$$\mathbf{B}^{\text{ext}}(x, y, s) = B_z(s)\hat{\mathbf{e}}_z - \frac{1}{2}B_z'(s)(x\hat{\mathbf{e}}_x + y\hat{\mathbf{e}}_y) + (\partial B_z^q/\partial \bar{y})_0(\bar{y}\hat{\mathbf{e}}_x + \bar{x}\hat{\mathbf{e}}_y). \quad (1)$$

In Eq. (1), $s=z$ is the axial coordinate, $\mathbf{x}_\perp = x\hat{\mathbf{e}}_x + y\hat{\mathbf{e}}_y$ is the transverse displacement from the z -axis in the laboratory frame, the prime denotes a derivative with respect to s , $\bar{\mathbf{x}}_\perp = \bar{x}\hat{\mathbf{e}}_x + \bar{y}\hat{\mathbf{e}}_y$ is the transverse displacement from the z -axis in a frame of reference that is rotated transversely by an angle of φ_q with respect to the laboratory frame, and $(\partial B_z^q/\partial \bar{y})_0 = (\partial B_z^q/\partial \bar{x})_0$ with subscript "zero" denoting $(\bar{x}, \bar{y}) = 0$.

In the present analysis, we consider the transverse electrostatic and magnetostatic interactions in the beam. We make the usual paraxial approximation, assuming that (a) the Budker parameter is small compared with γ_b , i.e., $q^2 N_b / \gamma_b m c^2 \ll 1$, (b) the beam is thin compared with the characteristic length scale over which the beam envelope varies, and (c) the kinetic energy associated with the transverse particle motion is small compared with that associated with the axial particle motion. In the following, we present steady-state cold-fluid equations describing equilibrium beam propagation in the magnetic focusing field defined in Eq. (1), and a two-dimensional self-consistent model describing the transverse dynamics of the beam.

A. Steady-state cold-fluid equations

For an ultrahigh-brightness beam, such as a high-intensity heavy ion beam, kinetic (emittance) effects are negligibly small, and the beam can be adequately described by cold-fluid equations. In the paraxial approximation, the steady-state cold-fluid equations for time-stationary flow ($\partial/\partial t = 0$) in cgs units are

$$\beta_b c \frac{\partial}{\partial s} n_b + \nabla_\perp \cdot (n_b \mathbf{V}_\perp) = 0, \quad (2)$$

$$\nabla_\perp^2 \phi^s = \beta_b^{-1} \nabla_\perp^2 A_z^s = -4\pi q n_b, \quad (3)$$

$$n_b \left(\beta_b c \frac{\partial}{\partial s} + \mathbf{V}_\perp \cdot \frac{\partial}{\partial \mathbf{x}_\perp} \right) \mathbf{V}_\perp = \frac{q n_b}{\gamma_b m} \left[-\frac{1}{\gamma_b^2} \nabla_\perp \phi^s + \beta_b \hat{\mathbf{e}}_z \times \mathbf{B}_{0\perp} + \frac{\mathbf{V}_\perp}{c} \times B_z(s) \hat{\mathbf{e}}_z \right], \quad (4)$$

where $\gamma_b = (1 - \beta_b^2)^{-1/2}$, use has been made of $\beta_z \equiv \beta_b = \text{const}$, and the self-electric and self-magnetic fields \mathbf{E}^s and \mathbf{B}^s are determined from the scalar and vector potentials ϕ^s and $A_z^s \hat{\mathbf{e}}_z$, i.e., $\mathbf{E}^s = -\nabla_\perp \phi^s$ and $\mathbf{B}^s = \nabla \times A_z^s \hat{\mathbf{e}}_z$. It will be shown in Sec. IV that the steady-state cold-fluid equations (2)–(4) support a class of solutions that, in general, describe corkscrewing elliptic beam equilibria in the magnetic focusing field defined in Eq. (1).

B. Two-dimensional self-consistent model

For moderately high-brightness beams, such as electron beams in high-power PPM focusing klystron amplifiers, kinetic (emittance) effects play an important role in the beam dynamics, and the evolution of the phase space of such beams must be studied. In the paraxial approximation, the self-consistent electrostatic and magnetostatic interactions in such a charged-particle beam can be described by a two-dimensional model involving N_p macroparticles (i.e., charged rods). In the laboratory frame, the transverse dynamics of the macroparticles is governed by^{15,30,31}

$$\frac{d^2 x_i}{ds^2} + \kappa_q(s)(x_i \cos 2\varphi_q + y_i \sin 2\varphi_q) - 2\sqrt{\kappa_z(s)} \frac{dy_i}{ds} - y_i \frac{d}{ds} \sqrt{\kappa_z(s)} + \frac{q}{\gamma_b^3 \beta_b^2 m c^2} \frac{\partial \phi^s}{\partial x_i} = 0, \quad (5)$$

$$\frac{d^2 y_i}{ds^2} - \kappa_q(s)(-x_i \sin 2\varphi_q + y_i \cos 2\varphi_q) + 2\sqrt{\kappa_z(s)} \frac{dx_i}{ds} + x_i \frac{d}{ds} \sqrt{\kappa_z(s)} + \frac{q}{\gamma_b^3 \beta_b^2 m c^2} \frac{\partial \phi^s}{\partial y_i} = 0, \quad (6)$$

where $i=1, 2, \dots, N_p$, and the focusing parameters $\kappa_z(s)$ and $\kappa_q(s)$ and self-field potential $\phi^s(x_i, y_i, s)$ are defined by

$$\sqrt{\kappa_z(s)} = \frac{q B_z(s)}{2 \gamma_b \beta_b m c^2} = \frac{\Omega_c(s)}{2 \beta_b c}, \quad (7)$$

$$\kappa_q(s) = \frac{q}{\gamma_b \beta_b m c^2} \left(\frac{\partial B_z^q}{\partial \bar{y}} \right)_0, \quad (8)$$

$$\phi^s(x_i, y_i, s)$$

$$= \frac{q N_b}{N_p} \sum_{j=1(N \neq i)}^{N_p} \ln \frac{(x_i - x_j)^2 + (y_i - y_j)^2}{(x_i - x_j r_w^2/r_j^2)^2 + (y_i - y_j r_w^2/r_j^2)^2} - \frac{q N_b}{N_p} \ln[(x_i - x_i r_w^2/r_i^2)^2 + (y_i - y_i r_w^2/r_i^2)^2], \quad (9)$$

respectively. Here, $\Omega_c(s)$ is the (local) relativistic cyclotron frequency associated with the axial magnetic field $B_z(s)$, and $r_i \equiv (x_i^2 + y_i^2)^{1/2}$. The beam is assumed to propagate inside a perfectly conducting cylindrical tube of radius r_w , such that the self-field potential satisfies the boundary condition $\phi^s(r_i = r_w, s) = 0$. Note that the parameter $\sqrt{\kappa_z(s)}$ can be positive, negative, or zero at any given axial position.

The two-dimensional self-consistent model described by Eqs. (5) and (6) will be used to simulate equilibrium beam transport in a PPM focusing field in the absence of a rf signal and electron beam halo formation in the transverse direction induced by large-amplitude longitudinal current oscillations in a PPM focusing klystron amplifier (Sec. III). It will also be used to verify cold-fluid corkscrewing elliptic beam equilibria in a linear focusing channel consisting of uniform solenoidal magnetic focusing fields, periodic solenoidal magnetic focusing fields, and/or alternating-gradient quadrupole magnetic focusing fields in an arbitrary arrangement, and to demonstrate control of halo formation and beam hollowing

TABLE I. SLAC 50 MW, 11.4 GHz, PPM focusing klystron experiment.

Beam current I_b	190 A
Beam voltage	464 kV
Cathode radius	2.86 cm
Cathode temperature T_b	800°C ^a
Beam radius	2.38 mm ^a
Pipe radius	4.7625 mm
Total tube length	90.0 cm
Focusing field period length	2.1 cm
PPM focusing section length	42.0 cm
RMS axial magnetic field	1.95 kG

^aEstimated.

in a rms-matched ultrahigh-brightness ion beam as it is injected from an axisymmetric Pierce diode into an alternating gradient focusing channel (Sec. V).

III. ELECTRON BEAM HALO FORMATION IN PPM FOCUSING KLYSTRONS

In this section, we study the dynamics of relativistic electron beams in high-power PPM focusing klystron amplifiers. Of particular interest are the properties of equilibrium beam transport in the absence of a rf signal and the mechanism for electron beam halo formation during high-power operation of such a device. To make comparisons with experiment, the following analysis is carried out with system parameters corresponding to those in the SLAC 50 MW, 11.4 GHz PPM focusing klystron experiment.²²

A. Equilibrium beam transport

In the absence of a rf signal, the relativistic electron beam propagates through the PPM focusing field in an equilibrium state. It has been shown previously^{26,27} that one of the equilibrium states for the system described by Eqs. (5) and (6) is the rigid-rotor Vlasov equilibrium in which the beam density is uniform transverse to the direction of beam propagation. The outermost beam radius $r_b(s) = r_b(s+S)$ obeys the envelope equation,²⁶

$$\frac{d^2 r_b}{ds^2} + \kappa_z(s) r_b - \frac{K}{r_b} - \frac{\langle \hat{P}_\theta \rangle^2}{r_b^3} - \frac{(4\epsilon)^2}{r_b^3} = 0, \quad (10)$$

where $\gamma_b \beta_b m_e c \langle \hat{P}_\theta \rangle = \text{constant}$ is the macroscopic canonical angular momentum of the beam at $r = r_b(s)$, and ϵ is the unnormalized transverse rms emittance associated with the random motion of the electrons. If there is no magnetic field at the cathode, then $\langle \hat{P}_\theta \rangle = 0$. Any residual magnetic field at the cathode will lead to $\langle \hat{P}_\theta \rangle \neq 0$.

We analyze the beam envelope for equilibrium beam transport in the SLAC 50 MW, 11.4 GHz PPM focusing klystron experiment.²² The system parameters of the experiment are shown in Table I. To examine the influence of a small residual magnetic field on the beam transport, we analyze two different cases shown in Table II. In Case I, we assume no residual magnetic field at the cathode, such that $\langle \hat{P}_\theta \rangle = 0$. In Case II, however, a residual field of 6.86 G is assumed, corresponding to a beam with a finite canonical angular momentum given by $\gamma_b \beta_b m_e c \langle \hat{P}_\theta \rangle = 4.5$

TABLE II. System parameters used in the simulation.

Basic parameter	Case I	Case II
Beam current I_b	190 A	190 A
Beam voltage	464 kV	464 kV
Cathode radius	2.86 cm	2.86 cm
Residual magnetic field at cathode	0.0 G	6.86 G
Cathode temperature T_b	800°C	800°C
Beam radius	2.05 mm	2.38 mm
Pipe radius	9.0 mm	9.0 mm
Total tube length	90.0 cm	90.0 cm
Focusing field period length	2.1 cm	2.1 cm
PPM focusing section length	42.0 cm	42.0 cm
RMS axial magnetic field	1.95 kG	1.95 kG

$\times 10^{-26} \text{ Kg m}^2/\text{s}$. The following dimensionless parameters are derived from Table II: $S^2 \kappa_z(s) = [1.04 \times \sin(2\pi s/S)]^2$ (with $S = 2.1 \text{ cm}$), $\sigma_0 = 42.3^\circ = 0.738$, $SK/4\sigma_0\epsilon = 10.1$, and $\langle \hat{P}_\theta \rangle/4\epsilon = 0.0$ in Case I and $\langle \hat{P}_\theta \rangle/4\epsilon = 6.93$ in Case II.

Figure 1 shows plots of the axial magnetic field $B_z(s)$ and outermost beam radius $r_b(s)$ versus the propagation distance s for Cases I and II. In both cases, the amplitude of well-matched (equilibrium) envelope oscillations about the average beam radius is only about 0.005 mm, as seen in Figs. 1(b) and 1(c).

Self-consistent simulations based on the model described in Sec. II B are performed to further investigate the equilibrium beam transport. In the simulations, 4096 macroparticles are used. The macroparticles are loaded according to the rigid-rotor Vlasov distribution²⁶ with an initial beam radius equal to the equilibrium (matched) beam radius at $s=0$ [see Figs. 1(b) and 1(c) for Cases I and II, respectively].

Figure 2 shows, respectively, the initial and final phase-space distributions at $s=0.0 \text{ cm}$ and $s=42.0 \text{ cm}$ for Case I. The final distribution in the configuration space shown in Fig. 2(d) agrees very well with the initial distribution shown in Fig. 2(a), and the effective beam radius obtained from the simulation agrees with that obtained from Eq. (10) within 0.2%. In the simulation, no beam loss is detected. A comparison between the final phase-space plots in Figs. 2(e) and 2(f) and the initial phase-space plots in Figs. 2(b) and 2(c) shows a slight emittance growth. This is because of numerical noise in the simulation. Nevertheless, the emittance growth has little effect on the beam transport properties because the beam transport is dominated by space charge. Similar results are also obtained for Case II,³² showing preservation of the initial distribution and no beam loss. In both cases, we find that the equilibrium beam transport in the PPM focusing klystron is robust, and that there is no beam loss in the absence of a rf signal. Within the experimental error, these results are in good agreement with the experimental observation²² of 99.9% beam transmission in the absence of a rf signal.

B. Halos induced by large-amplitude current oscillations

Microwave generation in a klystron is due to the coupling of large-amplitude charge-density and current oscillations.

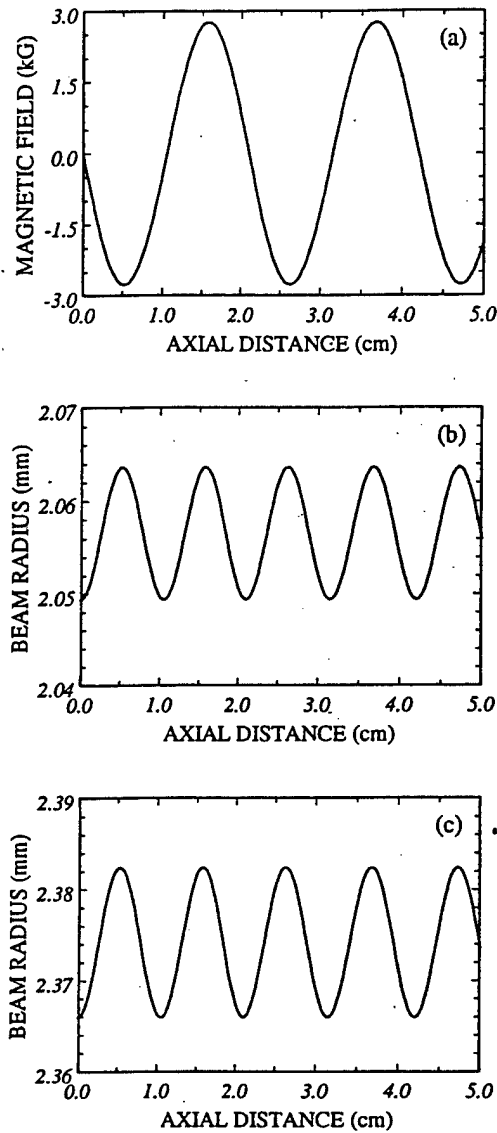


FIG. 1. Plots of the axial magnetic field in (a) and outermost beam radius $r_b(s)$ versus the propagation distance s for equilibrium beam propagation corresponding to Case I in (b) and Case II in (c). The dimensionless parameters are $S^2\kappa_z(s) = [1.04 \times \sin(2\pi s/S)]^2$, $\sigma_0 = 42.3^\circ = 0.738$, $SK/4\sigma_0\epsilon = 10.1$, and $\langle \dot{P}_\theta \rangle / 4\epsilon = 0.0$ in (b) and $\langle \dot{P}_\theta \rangle / 4\epsilon = 6.93$ in (c).

tions in the electron beam with the output rf cavity or structure. The charge-density and current oscillations result from the beating of the fast- and slow-space-charge waves on the electron beam, and are primarily longitudinal. From the point of view of beam transport, the charge-density and current oscillations perturb the equilibrium beam envelope. Although a quantitative understanding of the effects of such large-amplitude charge-density and current oscillations on the transverse dynamics of the electron beam requires three-dimensional modeling which is not available at present, a qualitative two-dimensional study of such effects is presented in the remainder of this section.

The amplitude of the envelope mismatch induced by longitudinal current oscillations can be estimated using the standard one-dimensional fluid model based on the continuity, Lorentz force, and full Maxwell's equations. It follows from the linearized continuity equation that the current perturba-

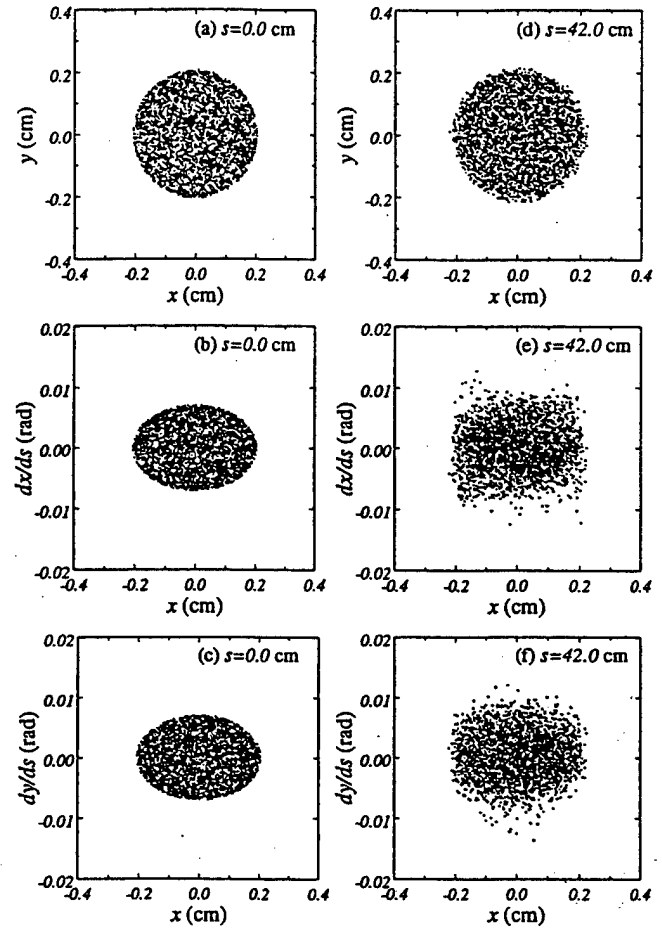


FIG. 2. Plots of the initial and final particle distributions at $s=0.0$ and 42.0 cm for the equilibrium beam corresponding to the parameters in Case I.

tion $(\delta I_b)_{f,s}$ is related to the axial velocity perturbation $c(\delta\beta_b)_{f,s}$ by^{33,34}

$$\frac{(\delta I_b)_{f,s}}{I_b} \equiv -\frac{\omega}{\omega - \beta_b c k_{f,s}} \frac{(\delta\beta_b)_{f,s}}{\beta_b}, \quad (11)$$

where subscripts f and s denote the fast- and slow-space-charge waves, respectively, and ω and $k_{f,s}$ are the frequency and wave numbers of the perturbations, respectively. Making the long-wavelength approximation for a thin beam, it can be shown that the dispersion relations for the fast- and slow-space-charge waves can be expressed as³³

$$\omega - \beta_b c k_{f,s} = \pm \frac{\sqrt{\epsilon_{sc}}}{\gamma_b \beta_b^2} \omega, \quad (12)$$

where k_f assumes a plus sign, and k_s assumes a minus sign. In Eq. (12), ϵ_{sc} is the longitudinal space-charge coupling parameter. The effective value of ϵ_{sc} is estimated to be $\epsilon_{sc} = 0.012$ for the SLAC PPM focusing klystron.²² In the klystron, the total current oscillations are the sum of fast- and slow-space-charge waves with a phase difference of $\sim 180^\circ$. As a result, the total current oscillations and the total velocity oscillations are out of phase by $\sim 180^\circ$. Therefore, the amplitude of the total current oscillations is given by

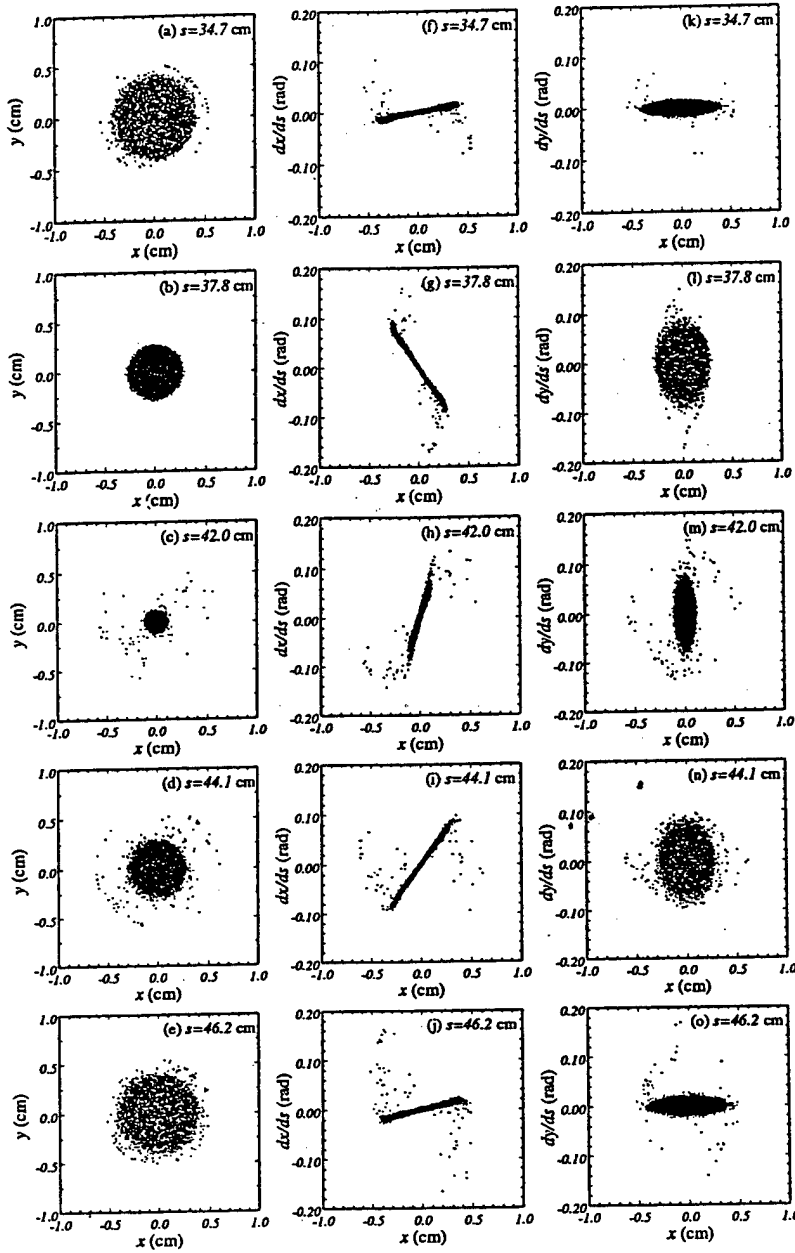


FIG. 3. Plots of particle distributions in phase space at $s = 34.7, 37.8, 42.0, 44.1$, and 46.2 cm for Case I.

$$\frac{(\delta I_b)_{\text{total}}}{I_n} \cong -\frac{2\gamma_b\beta_b^2}{\sqrt{\epsilon_{sc}}} \frac{(\delta\beta_b)_{\text{total}}}{\beta_b} \quad (13)$$

This has the important consequence that the perveance of the electron beam varies dramatically along the beam during high-power operation. From the definition of the perveance, i.e., $K = 2e^2 N_b / \gamma_b^3 \beta_b^2 m_e c^2$, it is readily shown that the amplitude of perveance variation is given by

$$\frac{\delta K}{K} \cong \left(1 + \frac{3\gamma_b\sqrt{\epsilon_{sc}}}{2\beta_b^2}\right) \frac{(\delta I_b)_{\text{total}}}{I_b} \quad (14)$$

For the SLAC PPM focusing klystron, Eq. (14) yields $\delta K/K = 1.45 \times (\delta I_b)_{\text{total}}/I_b$. At the rf output section, $\delta K/K$ exceeds unity considerably because $\delta I_b/I_b \approx 1$. (Note that the current oscillations are highly nonlinear in the rf output section and the maximum current exceeds $2I_b$ during high-power operation.) From the beam envelope equation (10),

the relative amplitude of beam envelope mismatch is estimated to be $\delta r_b/r_b = 0.56$, where r_b is the equilibrium beam radius and $\delta I_b/I_b = 1$ is assumed. In the self-consistent simulations presented below, we use $\delta r_b/r_b = 1.0$ in order to take into account the fact that the instantaneous current exceeds $2I_b$ during high-power operation of the klystron.

The process of halo formation in intense electron beams is studied using the two-dimensional self-consistent model described in Sec. II B. In the simulations, 4096 macroparticles are used, and the macroparticles are loaded according to the rigid-rotor Vlasov distribution²⁶ with an initial beam radius of $2r_b(0)$, where $r_b(0)$ is the equilibrium beam radius at $s=0$ [see Figs. 1(b) and 1(c) for Cases I and II, respectively]. The effect of current oscillation build up in the PPM focusing klystron, which requires three-dimensional modeling, is not included in the present two-dimensional simulation. In the limited space of this paper, we discuss

only the results of the self-consistent simulation for Case I, although the effect of a small residual magnetic field at the cathode in the halo formation process is also studied for Case II and is reported elsewhere.³²

Figure 3 shows the phase-space distributions of the electrons at several axial distances during the fourth period of the beam core radius oscillation for Case I. In contrast to the equilibrium phase-space distribution (Fig. 2), significant halos appear at $s=34.7, 37.8, 42.0, 44.1$, and 46.2 cm. In the configuration space plots shown in Figs. 3(a)–3(e), we observe a large variation in the beam core radius during the mismatched envelope oscillation period. The halo particles reach a maximum radius of $r_h=6.4$ mm at $s=42.0$ cm, where the beam core radius is a minimum and the traveling-wave rf output section is located. Around 1.5% of the electrons are found in the halo at that axial position. Because the maximum halo radius of $r_h=6.4$ mm is greater than the actual beam tunnel radius $r_T=4.7625$ mm, these halo electrons are lost to the waveguide wall. Therefore, the simulation results show that there will be 1.5% beam electron loss. In terms of beam power loss, 1.5% beam electron loss in the simulation corresponds to 0.2% beam power loss because the lost electrons have given up 88% of their kinetic energies (or have slowed down by about a factor of 2 in their axial velocities). The simulation results agree qualitatively with 0.8% beam power loss observed in the experiment.²² The discrepancy between the simulation and experimental measurements may be caused by nonlinearities in the applied magnetic fields which are not included in the present simulation.

As the beam propagates in the focusing field, its distribution rotates clockwise in the $(x, dx/ds)$ phase space, as shown in Figs. 3(f) to 3(j). The particles are initially dragged into the halo at the edges of the phase-space distribution, where a chaotic region is formed around an unstable periodic orbit that is located just outside the beam distribution.¹³ The unstable periodic orbit is a result of a resonance between the mismatched core envelope oscillations and the particle dynamics. As the halo particles move away from the beam core, the influence of space-charge forces decreases and these halo particles start rotating faster than the core particles, creating the S-shaped distributions observed in Figs. 3(f) to 3(j).

The halo formation is also observed in the $(x, dy/ds)$ phase-space distributions shown in Figs. 3(k) to 3(o). Although the macroscopic (average) canonical angular momentum $\langle \hat{P}_\theta \rangle$ is constant in the simulation, the distributions presented in Figs. 3(k) to 3(o) indicate that the distribution of single particle canonical angular momenta induces spread in the $(x, dy/ds)$ phase space.

Figure 4 shows the halo radius and effective beam core radius as a function of the propagation distance for Case I. The halo radius is the maximum radius achieved by all of the macroparticles in the self-consistent simulation. It is apparent in Fig. 4 that the halo formation process takes place essentially during the first 4 periods of the envelope oscillations. After reaching $r_h=6.4$ mm at $s=42.0$ cm, the halo radius saturates. It is interesting to note that once the halo is

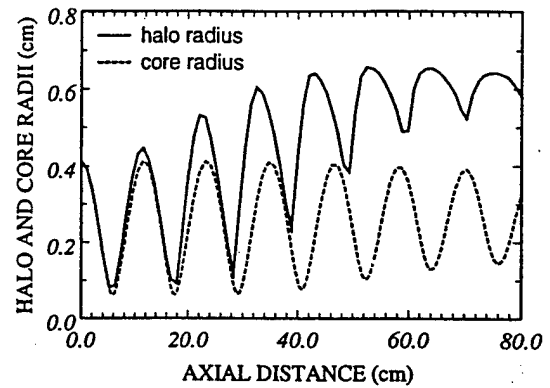


FIG. 4. Plots of the halo radius (solid curve) and core radius (dashed curve) as a function of the propagation distance s for Case I.

developed, the halo radius and core envelope radius oscillate in an opposite phase, with the former being maximum when the latter is minimum [as seen in Fig. 3(c)] and vice versa.

To summarize briefly, we studied equilibrium beam transport in a periodic magnetic focusing field in the absence of a rf signal and the behavior of a high-intensity electron beam under a current-oscillation-induced mismatch between the beam and the magnetic focusing field. Detailed simulation results were presented for choices of system parameters corresponding to the SLAC 50 MW, 11.4 GHz periodic permanent magnetic (PPM) focusing klystron experiment.²² We found that in the absence of the rf signal, the equilibrium beam transport is robust, and that there is no beam loss in agreement with experimental measurements. During the high-power operation of the klystron, however, we found that the current-oscillation-induced mismatch between the beam and the magnetic focusing field produces large-amplitude envelope oscillations whose amplitude is estimated using a one-dimensional cold-fluid model. From self-consistent simulations, we found that for a mismatch amplitude equal to the beam equilibrium radius, the halo reaches 0.64 cm in size and contains about 1.5% of total beam electrons at the rf output section for a beam generated with a zero magnetic field at the cathode. In terms of beam power loss, 1.5% beam electron loss in the simulation corresponds to 0.2% beam power loss because the lost electrons have given up 88% of their kinetic energies, which agrees qualitatively with 0.8% beam power loss observed in the experiment.²²

IV. CORKSCREWING ELLIPTIC BEAM EQUILIBRIA

In this section, we show that there exists a class of solutions to the steady-state cold-fluid equations (2)–(4) which, in general, describe corkscrewing elliptic beam equilibria³⁵ for ultrahigh-brightness, space-charge-dominated beam propagation in the linear focusing channel defined in Eq. (1).

We seek solutions to Eqs. (2)–(4) of the form³⁵

$$n_b(\mathbf{x}_\perp, s) = \frac{N_b}{\pi a(s)b(s)} \Theta \left[1 - \frac{\bar{x}^2}{a^2(s)} - \frac{\bar{y}^2}{b^2(s)} \right], \quad (15)$$

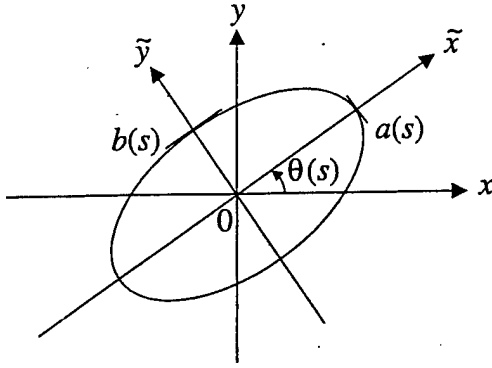


FIG. 5. Laboratory and rotating coordinate systems.

$$\mathbf{V}_\perp(\mathbf{x}_\perp, s) = [\mu_x(s)\tilde{x} - \alpha_x(s)\tilde{y}]\beta_b c \hat{\mathbf{e}}_{\tilde{x}} + [\mu_y(s)\tilde{y} + \alpha_y(s)\tilde{x}]\beta_b c \hat{\mathbf{e}}_{\tilde{y}}. \quad (16)$$

In Eqs. (15) and (16), $\mathbf{x}_\perp = \tilde{x}\hat{\mathbf{e}}_{\tilde{x}} + \tilde{y}\hat{\mathbf{e}}_{\tilde{y}}$ is a transverse displacement in a rotating frame illustrated in Fig. 5; $\theta(s)$ is the angle of rotation of the ellipse with respect to the laboratory frame; $\Theta(x) = 1$ if $x > 0$ and $\Theta(x) = 0$ if $x < 0$; and the functions $a(s)$, $b(s)$, $\mu_x(s)$, $\mu_y(s)$, $\alpha_x(s)$, $\alpha_y(s)$, and $\theta(s)$ are to be determined self-consistently.

Substituting Eqs. (15) and (16) into Eq. (2) and expressing the result in terms of the tilde variables, we find

$$\left(\mu_x + \mu_y - \frac{a'}{a} - \frac{b'}{b} \right) \Theta \left[1 - \frac{\tilde{x}^2}{a^2} - \frac{\tilde{y}^2}{b^2} \right] + 2 \left[\left(\frac{a'}{a} - \mu_x \right) \frac{\tilde{x}^2}{a^2} + \left(\frac{b'}{b} - \mu_y \right) \frac{\tilde{y}^2}{b^2} + \left(-\frac{b\theta'}{a} + \frac{a\theta'}{b} + \frac{b\alpha_x}{a} - \frac{a\alpha_y}{b} \right) \frac{\tilde{x}\tilde{y}}{ab} \right] \times \delta \left[1 - \frac{\tilde{x}^2}{a^2} - \frac{\tilde{y}^2}{b^2} \right] = 0, \quad (17)$$

where the 'prime' denotes a derivative with respect to s , $\delta(x) \equiv d\Theta(x)/dx$, and use has been made of the identities $\partial\tilde{x}/\partial s = \theta'\tilde{y}$, $\partial\tilde{y}/\partial s = -\theta'\tilde{x}$, and $\nabla \cdot \mathbf{F} = \partial F_{\tilde{x}}/\partial\tilde{x} + \partial F_{\tilde{y}}/\partial\tilde{y}$ for any vector field \mathbf{F} . Since Eq. (17) must be satisfied for all \tilde{x} and \tilde{y} , the coefficients of the terms proportional to Θ , $\tilde{x}^2\delta$, $\tilde{y}^2\delta$, and $\tilde{x}\tilde{y}\delta$ must vanish independently. This leads to the following equations:

$$\mu_x = \frac{1}{a} \frac{da}{ds}, \quad \mu_y = \frac{1}{b} \frac{db}{ds}, \quad (18)$$

$$\frac{d\theta}{ds} = \frac{a^2\alpha_y - b^2\alpha_x}{a^2 - b^2}, \quad (19)$$

where the functions $a(s)$, $b(s)$, $\alpha_x(s)$, and $\alpha_y(s)$ still remain to be determined.

Solving for the scalar and vector potentials from Eq. (3), we obtain

$$\phi^s = \beta_b^{-1} A_z^s = -\frac{2qN_b}{a+b} \left(\frac{\tilde{x}^2}{a} + \frac{\tilde{y}^2}{b} \right) \quad (20)$$

in the beam interior with $\tilde{x}^2/a^2 + \tilde{y}^2/b^2 < 1$. In deriving Eq. (20), use has been made of $\nabla_\perp^2 = \partial^2/\partial\tilde{x}^2 + \partial^2/\partial\tilde{y}^2$.

To solve the force equation (4) we substitute Eqs. (15), (16), (18)–(20) into Eq. (4), express the results in terms of

the tilde variables, and use the relations $\partial\tilde{x}/\partial s = \theta'\tilde{y}$, $\partial\tilde{y}/\partial s = -\theta'\tilde{x}$, $\partial\hat{\mathbf{e}}_{\tilde{x}}/\partial s = \theta'\hat{\mathbf{e}}_{\tilde{y}}$, and $\partial\hat{\mathbf{e}}_{\tilde{y}}/\partial s = -\theta'\hat{\mathbf{e}}_{\tilde{x}}$. We obtain

$$\{f_x + \kappa_q \cos[2(\theta - \varphi_q)]\}\tilde{x} - \{g_y + \kappa_q \sin[2(\theta - \varphi_q)]\}\tilde{y} = 0, \quad (21a)$$

$$\{g_x - \kappa_q \sin[2(\theta - \varphi_q)]\}\tilde{x} + \{f_y - \kappa_q \cos[2(\theta - \varphi_q)]\}\tilde{y} = 0, \quad (21b)$$

in the \tilde{x} and \tilde{y} directions, respectively. In Eq. (21),

$$f_x = \frac{1}{a} \frac{d^2a}{ds^2} - \frac{b^2(\alpha_x^2 - 2\alpha_x\alpha_y) + a^2\alpha_y^2}{a^2 - b^2} - 2\alpha_y\sqrt{\kappa_z} - \frac{2K}{a(a+b)}, \quad (22a)$$

$$f_y = \frac{1}{b} \frac{d^2b}{ds^2} + \frac{a^2(\alpha_y^2 - 2\alpha_x\alpha_y) + b^2\alpha_x^2}{a^2 - b^2} - 2\alpha_x\sqrt{\kappa_z} - \frac{2K}{b(a+b)}, \quad (22b)$$

$$g_y = \frac{1}{b^2} \left\{ \frac{d}{ds} [b^2(\alpha_x + \sqrt{\kappa_z})] - \frac{a^3b(\alpha_x - \alpha_y)}{a^2 - b^2} \frac{d}{ds} \left(\frac{b}{a} \right) \right\}, \quad (22c)$$

$$g_x = \frac{1}{a^2} \left\{ \frac{d}{ds} [a^2(\alpha_y + \sqrt{\kappa_z})] - \frac{ab^3(\alpha_x - \alpha_y)}{a^2 - b^2} \frac{d}{ds} \left(\frac{a}{b} \right) \right\}. \quad (22d)$$

Since Eqs. (21a) and (21b) must be satisfied for all \tilde{x} and \tilde{y} , we obtain the generalized beam envelope equations,

$$f_x + \kappa_q \cos[2(\theta - \varphi_q)] = 0, \quad (23a)$$

$$f_y - \kappa_q \cos[2(\theta - \varphi_q)] = 0, \quad (23b)$$

$$g_y + \kappa_q \sin[2(\theta - \varphi_q)] = 0, \quad (23c)$$

$$g_x - \kappa_q \sin[2(\theta - \varphi_q)] = 0. \quad (23d)$$

Making use of Eq. (22), we can express the generalized beam envelope equations as³⁵

$$\frac{d^2a}{ds^2} + \left\{ \kappa_q(s) \cos[2(\theta - \varphi_q)] - \frac{b^2(\alpha_x^2 - 2\alpha_x\alpha_y) + a^2\alpha_y^2}{a^2 - b^2} - 2\alpha_y\sqrt{\kappa_z} \right\} a - \frac{2K}{(a+b)} = 0, \quad (24a)$$

$$\frac{d^2b}{ds^2} + \left\{ -\kappa_q(s) \cos[2(\theta - \varphi_q)] + \frac{a^2(\alpha_y^2 - 2\alpha_x\alpha_y) + b^2\alpha_x^2}{a^2 - b^2} - 2\alpha_x\sqrt{\kappa_z} \right\} b - \frac{2K}{(a+b)} = 0, \quad (24b)$$

$$\frac{d}{ds} [b^2(\alpha_x + \sqrt{\kappa_z})] - \frac{a^3b(\alpha_x - \alpha_y)}{a^2 - b^2} \frac{d}{ds} \left(\frac{b}{a} \right) + \kappa_q(s)b^2 \sin[2(\theta - \varphi_q)] = 0, \quad (24c)$$

$$\frac{d}{ds} [a^2(\alpha_y + \sqrt{\kappa_z})] - \frac{ab^3(\alpha_x - \alpha_y)}{a^2 - b^2} \frac{d}{ds} \left(\frac{a}{b} \right) - \kappa_q(s)a^2 \sin[2(\theta - \varphi_q)] = 0, \quad (24d)$$

$$\frac{d\theta}{ds} - \frac{a^2\alpha_y - b^2\alpha_x}{a^2 - b^2} = 0, \quad (24e)$$

$$\mu_x = \frac{1}{a} \frac{da}{ds}, \quad (24f)$$

$$\mu_y = \frac{1}{b} \frac{db}{ds}. \quad (24g)$$

Equations (18) and (19) are added here as Eqs. (24e)–(24g) for completeness. Equations (24a)–(24g), together with the density and velocity profiles defined in Eqs. (15) and (16), describe cold-fluid equilibrium states for variably focused ultrahigh-brightness beams.

A wide variety of cold-fluid beam equilibria can be constructed with Eqs. (15), (16), and (24) for proper choices of magnetic focusing field profiles. While cold-fluid beam equilibria are elliptic and corkscrewing in general, they do recover familiar beam equilibria in proper limits. In particular, such limiting cases of cold-fluid elliptic beam equilibria include (a) the familiar cold-fluid round rigid-rotor beam equilibrium^{23–25} in a uniform magnetic focusing field with $\kappa_z(s) = \text{const} \neq 0$, $\kappa_q(s) = 0$, $\theta(s) = 0$, $a(s) = b(s) = \text{const}$, and $\alpha_x(s) = \alpha_y(s) = \text{const}$ as discussed in more detail below, (b) the familiar round rigid-rotor Vlasov beam equilibrium^{26–28} in a periodic solenoidal focusing field in the zero-emittance limit with $\kappa_z(s) = \kappa_z(s+S) \neq \text{const}$, $\kappa_q(s) = 0$, $\theta(s) = 0$, $a(s) = a(s+S) = b(s) \neq \text{const}$, and $\alpha_x(s) = \alpha_y(s) \neq \text{const}$ and (c) the familiar Kapchinskij–Vladimirskij beam equilibrium²⁹ in an alternating-gradient quadrupole magnetic focusing field in the zero-emittance limit with $\kappa_z(s) = 0$, $\kappa_q(s) = \kappa_q(s+S) \neq \text{const}$, $\theta(s) = 0$, $a(s) = a(s+S)$, $b(s) = b(s+S)$, and $\alpha_x(s) = \alpha_y(s) \neq 0$. Furthermore, for $\theta(s) = 0$ and $\alpha_x(s) = \alpha_y(s) = 0$, the present corkscrewing elliptic beam equilibria also recover geometrically nonrotating beam equilibria reported recently.³⁶

As a simple example, we consider corkscrewing elliptic beam equilibria in a uniform magnetic field with $\mathbf{B}^{\text{ext}} = B_{z0}\hat{e}_z$. Setting $\sqrt{\kappa_z(s)} = \sqrt{\kappa_{z0}} = qB_{z0}/2\gamma_b\beta_b mc^2 = \text{const}$ and $\kappa_q(s) = 0$, it can be shown that Eq. (24) has the following two branches of physically acceptable special solutions:

$$a = a_1 = \left(\frac{\alpha_x}{\alpha_y} \right)^{1/2} \left[\frac{K}{\kappa_{z0} - (\alpha_x + \sqrt{\kappa_{z0}})(\alpha_y + \sqrt{\kappa_{z0}})} \right]^{1/2}, \quad (25a)$$

$$b = b_1 = \left(\frac{\alpha_y}{\alpha_x} \right)^{1/2} \left[\frac{K}{\kappa_{z0} - (\alpha_x + \sqrt{\kappa_{z0}})(\alpha_y + \sqrt{\kappa_{z0}})} \right]^{1/2}, \quad (25b)$$

$$\theta(s) = \omega_1 s = \frac{\alpha_x \alpha_y}{\alpha_x + \alpha_y} s + \theta(0), \quad (25c)$$

for branch A, and

$$a = a_2 = \left(\frac{\alpha_x + 2\sqrt{\kappa_{z0}}}{\alpha_y + 2\sqrt{\kappa_{z0}}} \right)^{1/2} \left[\frac{K}{\kappa_{z0} - (\alpha_x + \sqrt{\kappa_{z0}})(\alpha_y + \sqrt{\kappa_{z0}})} \right]^{1/2}, \quad (26a)$$

$$b = b_2 = \left(\frac{\alpha_y + 2\sqrt{\kappa_{z0}}}{\alpha_x + 2\sqrt{\kappa_{z0}}} \right)^{1/2} \left[\frac{K}{\kappa_{z0} - (\alpha_x + \sqrt{\kappa_{z0}})(\alpha_y + \sqrt{\kappa_{z0}})} \right]^{1/2}, \quad (26b)$$

$$\theta(s) = \omega_2 s = \frac{\alpha_x \alpha_y - 4\kappa_{z0}}{\alpha_x + \alpha_y + 4\sqrt{\kappa_{z0}}} s + \theta(0), \quad (26c)$$

for branch B. In Eqs. (25) and (26), both α_x and α_y are constant.

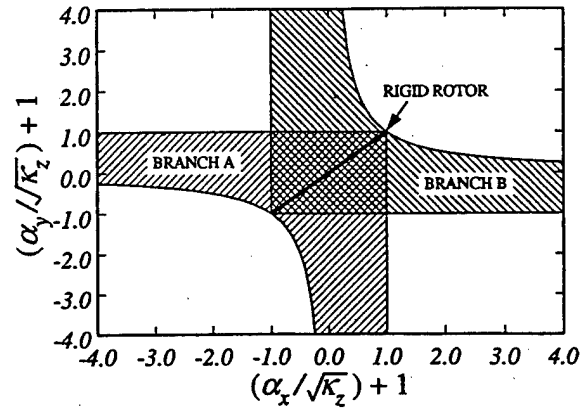


FIG. 6. Regions in the parameter space for the confinement of corkscrewing elliptic beam equilibria in a uniform magnetic field.

For branch A, the conditions for the confinement of corkscrewing elliptic beam equilibria are

$$\alpha_x < 0, \quad \alpha_y < 0, \quad \text{and} \quad (\alpha_x + \sqrt{\kappa_{z0}})(\alpha_y + \sqrt{\kappa_{z0}}) < \kappa_{z0}, \quad (27)$$

for positively charged particle beams with $\sqrt{\kappa_{z0}} = qB_{z0}/2\gamma_b\beta_b mc^2 > 0$, and

$$\alpha_x > 0, \quad \alpha_y > 0, \quad \text{and} \quad (\alpha_x + \sqrt{\kappa_{z0}})(\alpha_y + \sqrt{\kappa_{z0}}) < \kappa_{z0}, \quad (28)$$

for negatively charged particle beams with $\sqrt{\kappa_{z0}} = -|q|B_{z0}/2\gamma_b\beta_b mc^2 < 0$. Because α_x and α_y have the same sign, the internal flow for branch A is always rotation-like.

For branch B, the conditions for the confinement of corkscrewing elliptic beam equilibria are

$$\alpha_y > -2\sqrt{\kappa_{z0}}, \quad \alpha_x > -2\sqrt{\kappa_{z0}}, \quad (29)$$

and

$$(\alpha_x + \sqrt{\kappa_{z0}})(\alpha_y + \sqrt{\kappa_{z0}}) < \kappa_{z0},$$

for positively charged particle beams with $\sqrt{\kappa_{z0}} = qB_{z0}/2\gamma_b\beta_b mc^2 > 0$, and

$$\alpha_y < -2\sqrt{\kappa_{z0}}, \quad \alpha_x < -2\sqrt{\kappa_{z0}}, \quad (30)$$

and

$$(\alpha_x + \sqrt{\kappa_{z0}})(\alpha_y + \sqrt{\kappa_{z0}}) < \kappa_{z0},$$

for negatively charged particle beams with $\sqrt{\kappa_{z0}} = -|q|B_{z0}/2\gamma_b\beta_b mc^2 < 0$. In contrast to the internal flow for branch A, the internal flow for branch B can be either rotation-like with α_x and α_y in the same sign, or quadrupole-flow-like with α_x and α_y in the opposite signs.

Figure 6 shows the regions in parameter space for the confinement of corkscrewing elliptic beam equilibria in a uniform magnetic field applicable for both positively and negatively charged particle beams. It is important to point out that the familiar cold-fluid round rigid-rotor beam equilibria^{23–25} are recovered in the present analysis by setting $\alpha_x = \alpha_y$ in either Eq. (25) or Eq. (26), as indicated by the dark solid line shown in Fig. 6.

V. CONTROL OF HALO FORMATION AND BEAM HOLLOWING

As discussed in the Introduction, one of the key mechanisms for halo formation in high-intensity electron or ion

beams is due to a mismatch in the particle phase-space distribution relative to an equilibrium distribution. In general, distribution mismatch can lead to rather complex evolution in a beam, including not only halo formation but also beam hollowing. This mechanism for halo formation and beam hollowing occurs for rms matched beams because rms beam matching does not necessarily guarantee the beam in an equilibrium state.

For example, both halo formation and beam hollowing were observed in the heavy ion beam injector experiment at Lawrence Berkeley National Laboratory (LBNL),¹⁹ in which an ultrahigh-brightness, space-charge-dominated potassium ion beam was generated with an axisymmetric Pierce diode and then accelerated by a set of electrostatic quadrupoles. More recently, experimental evidence of beam hollowing was found in a high-brightness, space-charge-dominated electron beam experiment at the University of Maryland.^{37,38}

As an important application of the equilibrium beam theory presented in Sec. IV, we develop and demonstrate a technique for controlling of beam halo formation and beam hollowing in ultrahigh-brightness beams. This technique is widely applicable in the design of ultrahigh-brightness beams, and is effective before any collective instability develops to reach considerably large amplitudes.

To demonstrate the efficacy of this technique, we consider here a specific example, namely, the matching of a round particle beam generated by an axisymmetric particle source into an alternating-gradient magnetic quadrupole focusing channel. For comparison, we analyze two non-rotating rms matched beams with the same intensity; one beam will be in equilibrium and the other beam has an initial perturbation about the equilibrium transverse flow velocity. At the entrance of the alternating-gradient magnetic focusing channel ($s=0$), both beams have the same density profile defined in Eq. (15), but the transverse flow velocities of the beams are of the form³¹

$$\frac{d\mathbf{x}_\perp}{ds} = \frac{\mathbf{x}_\perp}{a} \left(\frac{da}{ds} \right) \left[1 + \nu \left(1 - \frac{2\mathbf{x}_\perp \cdot \mathbf{x}_\perp}{a^2} \right) \right], \quad (31)$$

where ν is a parameter that measures the nonlinearity in the velocity profile. For example, an initial velocity profile with $\nu > 0$ in Eq. (31) may model the effects of the concave shape of a Pierce-type ion diode.¹⁹ For equilibrium beam propagation, $\nu = 0$.

The rms matching is obtained by numerically solving the rms envelope equations,³⁹

$$\frac{d^2\bar{a}}{ds^2} + \kappa_q(s)\bar{a} - \frac{K}{2(\bar{a} + \bar{b})} = 0, \quad (32a)$$

$$\frac{d^2\bar{b}}{ds^2} - \kappa_q(s)\bar{b} - \frac{K}{2(\bar{a} + \bar{b})} = 0, \quad (32b)$$

where $\bar{a} \equiv \langle x^2 \rangle^{1/2}$ and $\bar{b} \equiv \langle y^2 \rangle^{1/2}$ are the rms envelopes, $\langle \dots \rangle$ denotes average over the particle distribution, and emittance terms are neglected. For given beam intensity K and focusing channel parameters C_3 and η shown in Fig. 7, we make use of Eq. (32) to determine the injection parameters for the

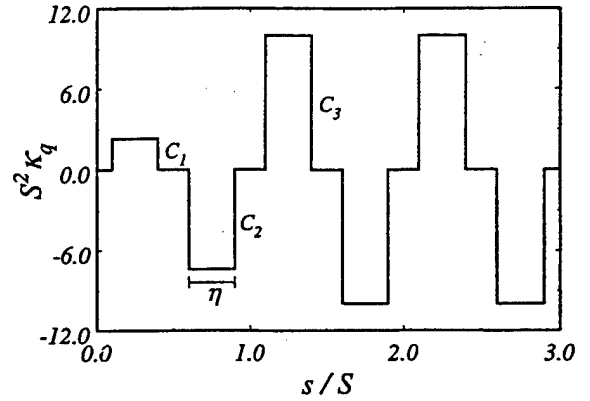


FIG. 7. Plot of the focusing parameter $S^2\kappa_q$ as a function of the propagation distance s .

axisymmetric beam, namely, $\bar{a}(0)$, $\bar{b}(0)$, $\bar{a}'(0)$, and $\bar{b}'(0)$, as well as the strengths of the two quadrupoles centered at $s=S/4$ and $s=3S/4$ in the first lattice, C_1 and C_2 , as shown in Fig. 7, assuming all quadrupoles having the same width η and equally spaced. Because Eq. (32) has a unique solution for a rms matched beam in the constant-parameter alternating-gradient focusing section with $s/S > 1$, integrating Eq. (32) from $s=S$ to $s=0$ yields four implicit functions: $\bar{a}(C_1, C_2)$, $\bar{b}(C_1, C_2)$, $\bar{a}'(C_1, C_2)$, and $\bar{b}'(C_1, C_2)$. The conditions for an initially converging round beam, i.e., $\bar{a}(0) = \bar{b}(0) = a(0)/2 = b(0)/2$ and $\bar{a}'(0) = \bar{b}'(0)$, uniquely determine the parameters C_1 and C_2 , which is done numerically with Newton's method. The results are presented in Figs. 7 and 8.

Figure 7 shows the focusing field parameter $S^2\kappa_q$ as a function of s , where $\eta=0.3$, $C_1=2.31$, $C_2=7.44$, and $C_3=10.0$. In Fig. 8, the solid and dashed curves show, respectively, the rms matched envelopes $\bar{a}(s)$ and $\bar{b}(s)$ for the focusing channel with vacuum phase advance $\sigma_0=70.8^\circ$ and beam perveance $SK/4\epsilon(0)=16.0$ (corresponding to a space-charge-depressed phase advance of $\sigma=5.4^\circ$), where a negligibly small unnormalized rms emittance of $\epsilon(0)=0.15 \times 10^{-6}$ m-rad has been assigned to the beam at $s=0$.

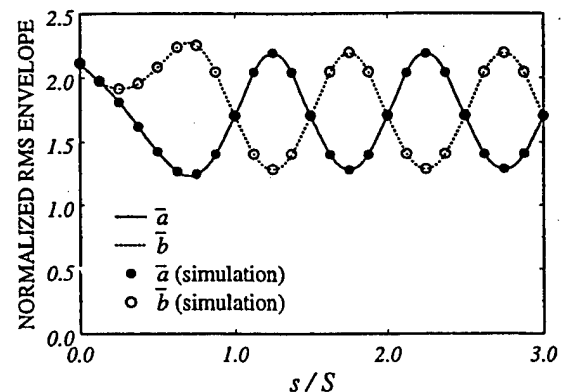


FIG. 8. Plots of rms beam envelopes versus propagation distances. Here, the solid and dashed curves are obtained from Eq. (32), whereas the solid dots and open circles are from the self-consistent simulation for a beam with $\nu=0.25$. Here, \bar{a} and \bar{b} are normalized to $\sqrt{\epsilon(0)S}$.

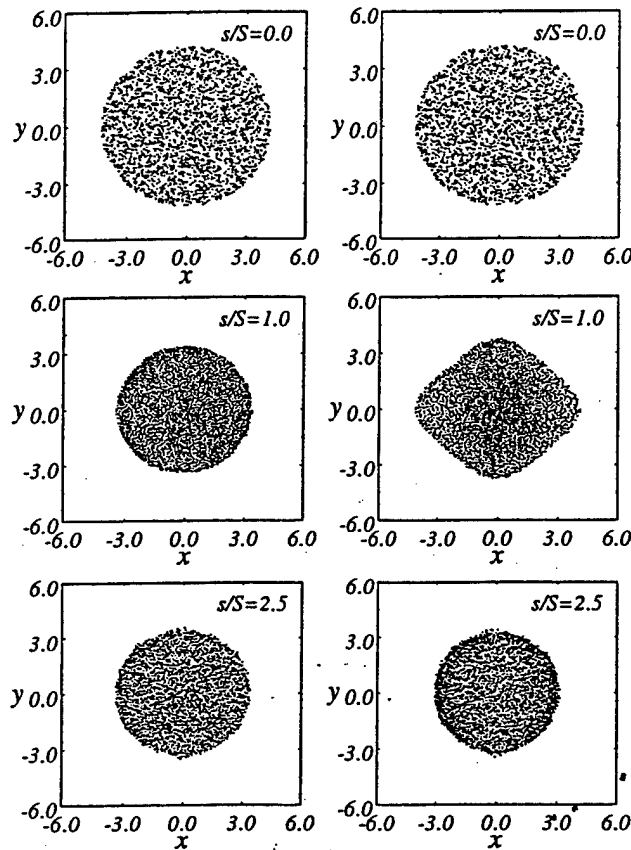


FIG. 9. Particle distributions in the configuration space for $\nu=0$ (left) and $\nu=0.25$ (right). Here, the coordinates x and y are normalized to $\sqrt{\epsilon(0)S}$.

Self-consistent simulations are performed with $N_p = 3072$ and free-space boundary conditions to study the phase-space evolution for the two beams in the focusing channel shown in Fig. 7. In Fig. 8, the solid dots and open circles correspond to the rms envelopes $\bar{a}(s)$ and $\bar{b}(s)$ obtained from a self-consistent simulation for a beam initially with a nonlinear velocity profile with $\nu=0.25$. It is evident in Fig. 8 that there is excellent agreement between the prediction of the rms envelope equations (32a) and (32b) and the results of the self-consistent simulation, despite that the transverse flow velocity is perturbed substantially.

We now examine the evolution of the particle distribution if the nonlinearity in the initial transverse flow velocity profile is introduced, and compare with equilibrium beam propagation. The results are summarized in Figs. 9 and 10. Figure 9 shows a comparison between particle distributions in the configuration space with and without nonlinearity in the initial transverse flow velocity at three axial positions: $s/S=0, 1.0$, and 2.5 . These axial positions are chosen such that $\bar{a}(s)=\bar{b}(s)$. In Fig. 9, the plots shown on the left correspond to $\nu=0$ and those on the right to $\nu=0.25$. For $\nu=0.25$, the initially round beam develops sharp edges after the first lattice, becoming partially hollow subsequently at $s/S=2.5$. In Fig. 10(b), the radial distribution of 3072 macroparticles at $s/S=2.5$ shows that the density at the edge is twice the density at the center of the beam, and that there is a small halo extending outward beyond the radius where the

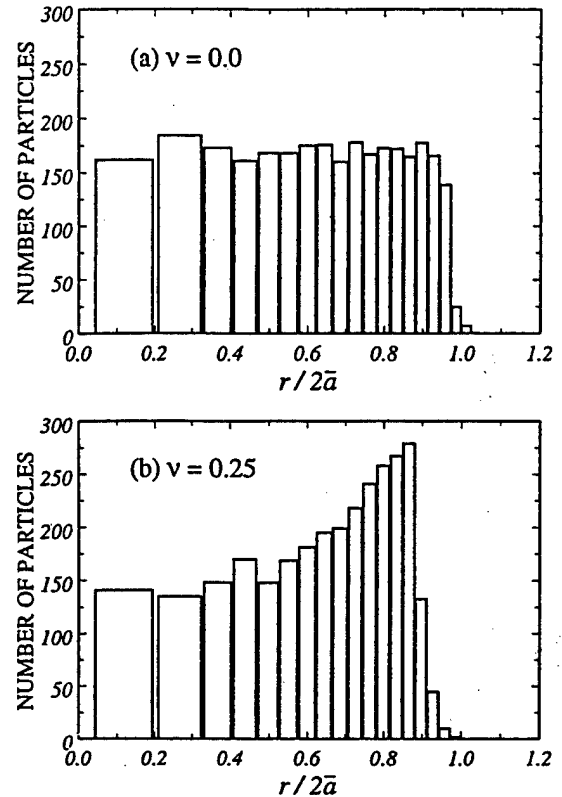


FIG. 10. Radial distribution of the macroparticles at $s/S=2.5$ for (a) $\nu=0$ and (b) $\nu=0.25$.

density reaches its maximum. The partially hollow density profile shown in Fig. 10(b) is similar to, but not as pronounced as, that observed in the heavy ion beam injector experiment at LBNL.¹⁹ In contrast to the case with $\nu=0.25$, the beam propagates in an equilibrium state for $\nu=0$ without beam hollowing and without any significant beam halo formation, as shown in Fig. 10(a).

VI. CONCLUSIONS

Halo formation and control in space-charge-dominated electron and ion beams have been investigated analytically and computationally in parameter regimes relevant to the development of high-power microwave (HPM) tubes and high-intensity electron or ion linear accelerators. In particular, a mechanism for electron beam halo formation was identified in high-power periodic permanent magnetic focusing klystron amplifiers, and a new class of cold-fluid corkscrewing elliptic beam equilibria was discovered for ultrahigh-brightness beam propagation in a linear focusing channel consisting of uniform and periodic solenoidal and alternating-gradient quadrupole magnetic fields in an arbitrary arrangement including field tapering.

In the exploration of electron beam halo formation in PPM focusing klystron amplifiers, equilibrium beam transport was analyzed in a periodic magnetic focusing field in the absence of a rf signal, and the behavior of a high-intensity electron beam was studied under a current-oscillation-induced mismatch between the beam and the magnetic focusing field. Detailed simulation results were

presented for choices of system parameters corresponding to the SLAC 50 MW, 11.4 GHz periodic permanent magnetic (PPM) focusing klystron experiment. It was found that in the absence of a rf signal, that the equilibrium beam transport is robust, and that there is no beam loss in agreement with experimental measurements. During high-power operation of the klystron, however, it was found that the current-oscillation-induced mismatch between the beam and the magnetic focusing field produces large-amplitude envelope oscillations whose amplitude was estimated using a one-dimensional cold-fluid model. Self-consistent simulations showed that for a mismatch amplitude equal to the beam equilibrium radius, the halo reaches 0.64 cm in size and contains about 1.5% of total beam electrons at the rf output section for a beam generated with a zero magnetic field at the cathode. Because the halo radius is greater than the actual beam tunnel radius, these halo electrons are lost to the waveguide wall, yielding 0.2% beam power loss. The simulation results agree qualitatively with 0.8% beam power loss observed in the experiment.²² The discrepancy between the simulation and experimental measurements may be caused by nonlinearities in the applied magnetic fields which are not included in the present simulation.

In the analysis and applications of cold-fluid corkscrewing elliptic beam equilibria, the steady-state cold-fluid equations were solved for an ultrahigh-brightness, space-charge-dominated beam in general magnetic focusing field profile including periodic and uniform solenoidal fields and alternating-gradient quadrupole magnetic fields. Generalized beam envelope equations for equilibrium flow were obtained. It was shown that limiting cases of cold-fluid corkscrewing elliptic beam equilibria include the familiar cold-fluid round rigid-rotor beam equilibrium in a uniform magnetic focusing field and both the familiar round rigid-rotor Vlasov beam equilibrium in a periodic solenoidal focusing field and the familiar Kapchinskij-Vladimirskij beam equilibrium in an alternating-gradient quadrupole magnetic focusing field in the zero-emittance limit. As a simple example, a cold-fluid corkscrewing elliptic beam equilibrium in a uniform magnetic focusing field was discussed. As an application of the present equilibrium beam theory, a general technique was developed, and demonstrated with an example, for the controlling of beam halo formation and beam hollowing in ultrahigh-brightness beams. This technique is effective before any collective instability may develop to reach considerably large amplitudes.

ACKNOWLEDGMENTS

This work was supported in part by the Air Force Office of Scientific Research Grant No. F49620-97-1-0325, in part by the Department of Energy, Office of High Energy and Nuclear Physics Grant No. DE-FG02-95ER-40919, and in part by the Department of Energy through a subcontract with Princeton Plasma Physics Laboratory.

Beams, edited by S. Y. Lee, AIP Conf. Proc. 377 (American Institute of Physics, New York, 1996).

- ³F. J. Agee, IEEE Trans. Plasma Sci. PS-26, 235 (1998).
- ⁴J. Benford and G. Benford, "Pulse shortening in high-power microwave sources," *Proceedings of the 11th International Conference on High-Power Particle Beams* (Institute of Plasma Physics, Academy of Science of the Czech Republic, 1996), p. 217.
- ⁵K. J. Hendricks, P. D. Coleman, R. W. Lemke, M. J. Arman, and L. Bowers, Phys. Rev. Lett. 76, 154 (1996), and references therein.
- ⁶M. D. Haworth, G. Baca, J. N. Benford *et al.*, IEEE Trans. Plasma Sci. PS-26, 312 (1998).
- ⁷F. Hegeler, C. Grabowski, and E. Schamiloglu, IEEE Trans. Plasma Sci. PS-26, 275 (1998).
- ⁸R. A. Jameson, in *Advanced Accelerator Concepts*, edited by J. S. Wurtele, AIP Conf. Proc. 279 (American Institute of Physics, New York, 1993), p. 969.
- ⁹R. B. Neal and W. K. H. Panofsky, Science 152, 1353 (1966).
- ¹⁰W. K. H. Panofsky and M. Bander, Rev. Sci. Instrum. 39, 206 (1968).
- ¹¹A. W. Chao, *Physics of Collective Beam Instabilities in High-Energy Accelerators* (Wiley, New York, 1993), p. 136.
- ¹²J. S. O'Connell, T. P. Wangler, R. S. Mills, and K. R. Crandall, *Proceedings of the 1993 Particle Accelerator Conference*, Washington DC, 1993 (IEEE, Piscataway, NJ, 1993), p. 3657.
- ¹³R. L. Gluckstern, Phys. Rev. Lett. 73, 1247 (1994).
- ¹⁴C. Chen and R. C. Davidson, Phys. Rev. Lett. 72, 2195 (1994); Phys. Rev. E 49, 5679 (1994).
- ¹⁵C. Chen and R. A. Jameson, Phys. Rev. E 52, 3074 (1995).
- ¹⁶Q. Qian, R. C. Davidson, and C. Chen, Phys. Rev. E 51, 5216 (1995).
- ¹⁷L. M. Lagniel, Nucl. Instrum. Methods Phys. Res. A 345, 1576 (1995).
- ¹⁸C. Chen, in *Space Charge Dominated Beams and Applications of High-Brightness Beams*, AIP Conf. Proc. 377, edited by S. Y. Lee (American Institute of Physics, New York, 1996).
- ¹⁹S. Yu, S. Eylon, E. Henestroza, and D. Grote, in Ref. 18.
- ²⁰Y. Fink, C. Chen, and W. P. Marable, Phys. Rev. E 55, 7557 (1997).
- ²¹C. Chen, "Halo formation in intense linacs," *Proceedings of the XIX International Linac Conference*, Argonne National Laboratory Report ANL-98/28, 1998, p. 729.
- ²²D. Sprehn, G. Caryotakis, E. Jongewaard, and R. M. Phillips, "Periodic permanent magnetic development for linear collider X-band klystrons," in Ref. 21, p. 689.
- ²³R. C. Davidson and N. A. Krall, Phys. Fluids 13, 1543 (1970).
- ²⁴A. J. Theiss, R. A. Mahaffey, and A. W. Trivelpiece, Phys. Rev. Lett. 35, 1436 (1975).
- ²⁵R. C. Davidson, *Physics of Non-neutral Plasmas* (Addison-Wesley, Reading, MA, 1990), p. 99.
- ²⁶C. Chen, R. Pakter, and R. C. Davidson, Phys. Rev. Lett. 79, 225 (1997).
- ²⁷R. C. Davidson and C. Chen, Part. Accel. 59, 175 (1998).
- ²⁸R. C. Davidson, P. Stoltz, and C. Chen, Phys. Plasmas 4, 3710 (1997).
- ²⁹I. M. Kapchinskij and V. V. Vladimirskij, *Proceedings of the International Conference on High Energy Accelerators* (CERN, Geneva, 1959), p. 274.
- ³⁰See, for example, Chap. 10 of Ref. 25.
- ³¹M. Hess, R. Pakter, and C. Chen, "Green's function description of space charge in intense charged particle beams," *Proceedings of the 1999 Particle Accelerator Conference* (Institute of Electrical and Electronics Engineers, Piscataway, NJ, 1999), p. 2752.
- ³²R. Pakter and C. Chen, "Electron beam halo formation in high-power klystron amplifiers," to appear in IEEE Trans. Plasma Sci.; "Halo formation in intense electron beams in high-power klystron amplifiers," in *Intense Microwave Pulses VI*, edited by H. E. Brandt, SPIE Proc. 3702, 1999, p. 21.
- ³³C. Chen, G. Bekefi, and P. Catravas, Appl. Phys. Lett. 62, 1579 (1993).
- ³⁴M. Friedman, J. Krall, Y. Y. Lau, and V. Serlin, Rev. Sci. Instrum. 61, 171 (1990).
- ³⁵R. Pakter and C. Chen, "Corkscrewing elliptic beam equilibria," submitted to Phys. Rev. Lett.
- ³⁶R. Pakter and C. Chen (unpublished).
- ³⁷S. Bernal, P. Chin, R. A. Kishek, Y. Li, M. Reiser, J. G. Wang, T. Godlove, and I. Haber, *Physical Review Special Topics—Accelerators and Beams*, 1, 1998, Vol. I, p. 44 202.
- ³⁸S. Bernal, R. A. Kishek, M. Reiser, and I. Haber, Phys. Rev. Lett. 78, 4002 (1999).
- ³⁹F. J. Sacherer, IEEE Trans. Nucl. Sci. NS-18, 1105 (1971).

¹Special issue on high-power microwave generation, edited by E. Schamiloglu and Y. Y. Lau, IEEE Trans. Plasma Sci. PS-26 (1998).

²Space Charge Dominated Beams and Applications of High-Brightness

Cold-fluid equilibrium for a corkscrewing elliptic beam in a variably focusing channel

Renato Pakter* and Chipping Chen

Plasma Science and Fusion Center, Massachusetts Institute of Technology, Cambridge, Massachusetts 02139

(Received 5 November 1999; revised manuscript received 5 April 2000)

It is shown that there exists a new class of cold-fluid corkscrewing elliptic beam equilibria for ultrahigh-brightness, space-charge-dominated beam propagation through a linear focusing channel consisting of uniform solenoidal, periodic solenoidal, and/or alternating-gradient quadrupole focusing magnets in an arbitrary arrangement including field tapering. The equilibrium beam density and flow velocity profiles and equilibrium self-electric and self-magnetic fields are determined by solving generalized beam envelope equations. In proper limits, such cold-fluid corkscrewing elliptic beam equilibria recover many familiar beam equilibria in beam physics, including the round rigid-rotor Vlasov beam equilibria in uniform and periodic solenoidal focusing fields and the Kapchinskij-Vladimirskij beam equilibrium in an alternating-gradient quadrupole focusing field. For beams with negligibly small emittance, the equilibrium solutions are validated with self-consistent simulations. Examples and applications of the present equilibrium beam theory are discussed. As an important application of the present equilibrium beam theory, a general technique is developed and demonstrated with an example to control large-amplitude density and flow velocity fluctuations (such as beam hollowing and halo formation) often observed in ultrahigh-brightness beams.

PACS number(s): 29.27.-a, 41.75.-i, 41.85.-p

I. INTRODUCTION

The equilibrium and stability properties of charged-particle beams have been an important subject of investigation in beam physics, plasma physics, and vacuum electronics. Indeed, the principles of vacuum electronics [1] are based on electron beam interactions with radio-frequency structures, and the discovery of strong focusing in the early 1950s [2] has provided the scientific basis for modern particle accelerators such as synchrotrons, linacs, and high-energy colliders.

Recently, there have been vigorous activities in the research and development of high-intensity vacuum electronic devices and high-intensity accelerators in order to meet the needs in communication, in high-energy and nuclear physics research, in the development of spallation neutron sources, in heavy ion fusion applications, and in advanced x-ray radiography, to mention a few examples.

In the design of high-intensity charged-particle beam systems, the most challenging task is to properly match high-intensity beams into focusing systems, so that the beams are in equilibrium or quasiequilibrium states in the combination of applied fields and self-fields [3]. A widely used tool for the determination of matching conditions of high-intensity charged-particle beam systems is based on the rms beam description [4-7]. However, rms beam matching is inadequate for ultrahigh-brightness beams, because detailed information about the beam dynamics, especially the evolution of the density and flow velocity profiles, is lost by performing phase-space averages in the rms analysis. In general, rms beam matching does not guarantee well-behaved beam transport if the beam becomes space-charge dominated. In fact, without detailed equilibrium flow matching of high-intensity

beams, many undesirable phenomena can occur, including chaotic particle motion [8] and chaotic beam envelope oscillations [9], beam halo formation [10], beam hollowing [11], emittance growth [12], and multimode excitations, as observed in recent high-intensity beam experiments.

In this paper, we present exact steady-state solutions to the cold-fluid equations governing the evolution of an ultrahigh-brightness, space-charge-dominated beam propagating through a linear focusing channel consisting of uniform solenoidal, periodic solenoidal, and alternating-gradient quadrupole focusing magnets in an arbitrary arrangement including field tapering. The equilibrium beam density and flow velocity profiles and equilibrium self-electric and self-magnetic fields are determined by solving generalized beam envelope equations. For beams with negligibly small emittance, these steady-state solutions are validated with self-consistent simulations using the Green's function method. In general, these steady-state solutions correspond to corkscrewing elliptic beam equilibria. They recover many familiar beam equilibria in beam physics, such as the cold-fluid round rigid-rotor equilibrium [13,14] and both the periodically focused rigid-rotor Vlasov equilibrium [15] and Kapchinskij-Vladimirskij equilibrium [16] in the zero-emittance limit.

Examples and applications of the present equilibrium beam theory are discussed. As a simple example, a corkscrewing elliptic beam equilibrium in a uniform solenoidal magnetic field is obtained. As an important application of the present equilibrium beam theory, a general technique is developed and demonstrated with an example to control large-amplitude density and flow velocity fluctuations (such as beam hollowing and halo formation) often observed in ultrahigh-brightness beams. For comparison, we investigate numerically the beam transport for distributions that substantially deviate from the equilibrium solutions. In this case, the occurrence of beam hollowing and halo formation is found. As a final example, we consider an ultrahigh-brightness beam equilibrium in a periodic focusing channel consisting

*Present address: Instituto de Física, Universidade Federal do Rio Grande do Sul, Caixa Postal 15051, 91501-970 Porto Alegre, RS, Brazil.

of overlapping solenoidal and quadrupole focusing fields to illustrate a wide range of applicability of the present equilibrium beam theory in manipulating ultrahigh-brightness beams.

The paper is organized as follows. In Sec. II, steady-state cold-fluid equations are presented for transverse electrostatic and magnetostatic interactions in a high-intensity charged-particle beam propagating through a linear focusing channel with general magnetic focusing field profile. In Sec. III, an equilibrium solution to the steady-state cold-fluid equations presented in Sec. II is obtained and generalized beam envelope equations for equilibrium flow are derived. In Sec. IV, it is shown that the steady-state cold-fluid solutions found in Sec. III recover familiar beam equilibria in proper limits. In Sec. V, examples and applications of the present equilibrium beam theory are discussed. Conclusions are given in Sec. VI.

II. THEORETICAL MODEL AND ASSUMPTIONS

We consider a thin, continuous, ultrahigh-brightness, space-charge-dominated beam propagating with constant axial velocity $\beta_b c \hat{e}_z$ through a linear focusing channel with multiple periodic solenoidal and alternating-gradient quadrupole focusing sections. The focusing fields can be tapered, and the quadrupoles are allowed to be at various angles in the transverse direction. The focusing magnetic field is approximated by

$$\mathbf{B}_0(\mathbf{x}) = B_z(s) \hat{e}_z - \frac{1}{2} B'_z(s) (x \hat{e}_x + y \hat{e}_y) + (\partial B_x^2 / \partial y)_0 (\bar{y} \hat{e}_x + \bar{x} \hat{e}_y), \quad (1)$$

where $B'_z(s) = (\partial B_z / \partial s)_0$, $s = z$ is the axial coordinate, \bar{x} , \bar{y} , \hat{e}_x , and \hat{e}_y are coordinates and unit vectors of a frame of reference that is rotated by an angle of φ_q with respect to the x axis in the laboratory frame, $(\partial B_x^2 / \partial y)_0 = (\partial B_y^2 / \partial x)_0$, and the subscript "zero" denotes $(x, y) = 0 = (\bar{x}, \bar{y})$.

In the present analysis, we consider the transverse electrostatic and magnetostatic interactions in the beam. We make the usual paraxial approximation, assuming that (a) the Budker parameter is small compared with γ_b , i.e., $q^2 N_b / \gamma_b m c^2 \ll 1$, (b) the beam is thin compared with the characteristic length scale over which the beam envelope varies, and (c) the kinetic energy associated with the transverse particle motion is small compared with that associated with the axial particle motion.

For an ultrahigh-brightness beam, kinetic (emittance) effects are negligibly small, and the beam can be adequately described by cold-fluid equations. In the paraxial approximation, the steady-state cold-fluid equations for time-stationary flow ($\partial / \partial t = 0$) are

$$\beta_b c \frac{\partial}{\partial s} n_b + \nabla_\perp \cdot (n_b \mathbf{V}_\perp) = 0, \quad (2)$$

$$\nabla_\perp^2 \phi^s = \beta_b^{-1} \nabla_\perp^2 A_z^s = -4 \pi q n_b, \quad (3)$$

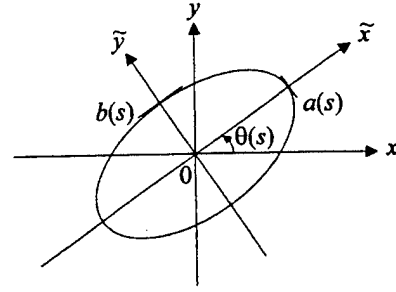


FIG. 1. Laboratory and rotating coordinate systems.

$$n_b \left(\beta_b c \frac{\partial}{\partial s} + \mathbf{V}_\perp \cdot \frac{\partial}{\partial \mathbf{x}_\perp} \right) \mathbf{V}_\perp = \frac{q n_b}{\gamma_b m} \left[-\frac{1}{\gamma_b^2} \nabla_\perp \phi^s + \beta_b \hat{e}_z \times \mathbf{B}_{0\perp} + \frac{\mathbf{V}_\perp}{c} \times B_z(s) \hat{e}_z \right], \quad (4)$$

where $\mathbf{x}_\perp = x \hat{e}_x + y \hat{e}_y$, $\gamma_b = (1 - \beta_b^2)^{-1/2}$, and the self-electric and self-magnetic fields \mathbf{E}^s and \mathbf{B}^s are determined from the scalar and vector potentials ϕ^s and $A_z^s \hat{e}_z$, i.e., $\mathbf{E}^s = -\nabla_\perp \phi^s$ and $\mathbf{B}^s = \nabla \times A_z^s \hat{e}_z$. In Sec. III, it will be shown that the steady-state cold-fluid equations (2)–(4) support a class of solutions that, in general, describe corkscrewing elliptic beam equilibria in the magnetic focusing field defined in Eq. (1).

III. CORKSCREWING BEAM EQUILIBRIUM

In this section, we show that there exists a class of solutions to the steady-state cold-fluid equations (2)–(4) which, in general, describe corkscrewing elliptic beam equilibria for ultrahigh-brightness, space-charge-dominated beam propagation in the linear focusing channel defined in Eq. (1).

We seek solutions to Eqs. (2)–(4) of the form

$$n_b(\mathbf{x}_\perp, s) = \frac{N_b}{\pi a(s) b(s)} \Theta \left[1 - \frac{\bar{x}^2}{a^2(s)} - \frac{\bar{y}^2}{b^2(s)} \right], \quad (5)$$

$$\mathbf{V}_\perp(\mathbf{x}_\perp, s) = [\mu_x(s) \bar{x} - \alpha_x(s) \bar{y}] \beta_b c \hat{e}_x + [\mu_y(s) \bar{y} + \alpha_y(s) \bar{x}] \beta_b c \hat{e}_y. \quad (6)$$

In Eqs. (5) and (6), $\mathbf{x}_\perp = \bar{x} \hat{e}_x + \bar{y} \hat{e}_y$ is a transverse displacement in a rotating frame illustrated in Fig. 1, $\theta(s)$ is the angle of rotation of the ellipse with respect to the laboratory frame, $\Theta(x) = 1$ if $x > 0$ and $\Theta(x) = 0$ if $x < 0$, and the functions $a(s)$, $b(s)$, $\mu_x(s)$, $\mu_y(s)$, $\alpha_x(s)$, $\alpha_y(s)$, and $\theta(s)$ are to be determined self-consistently.

Substituting Eqs. (5) and (6) into Eq. (2) and expressing the result in terms of the tilded variables, we find

$$\left(\mu_x + \mu_y - \frac{a'}{a} - \frac{b'}{b} \right) \Theta \left[1 - \frac{\bar{x}^2}{a^2} - \frac{\bar{y}^2}{b^2} \right] + 2 \left[\left(\frac{a'}{a} - \mu_x \right) \frac{\bar{x}^2}{a^2} + \left(\frac{b'}{b} - \mu_y \right) \frac{\bar{y}^2}{b^2} + \left(-\frac{b \theta'}{a} + \frac{a \theta'}{b} + \frac{b \alpha_x}{a} - \frac{a \alpha_y}{b} \right) \frac{\bar{x} \bar{y}}{ab} \right] \times \delta \left[1 - \frac{\bar{x}^2}{a^2} - \frac{\bar{y}^2}{b^2} \right] = 0, \quad (7)$$

where the prime denotes derivative with respect to s , $\delta(x) \equiv d\Theta(x)/dx$, and use has been made of the identities $\partial\bar{x}/\partial s = \theta'\bar{y}$, $\partial\bar{y}/\partial s = -\theta'\bar{x}$, and $\nabla \cdot \mathbf{F} = \partial F_{\bar{x}}/\partial\bar{x} + \partial F_{\bar{y}}/\partial\bar{y}$ for any vector field \mathbf{F} . Since Eq. (7) must be satisfied for all \bar{x} and \bar{y} , the coefficients of the terms proportional to Θ , $\bar{x}^2\delta$, $\bar{y}^2\delta$, and $\bar{x}\bar{y}\delta$, must vanish independently. This leads to the following equations:

$$\mu_x = \frac{1}{a} \frac{da}{ds}, \quad \mu_y = \frac{1}{b} \frac{db}{ds}, \quad (8)$$

$$\frac{d\theta}{ds} = \frac{a^2\alpha_y - b^2\alpha_x}{a^2 - b^2}, \quad (9)$$

where the functions $a(s)$, $b(s)$, $\alpha_x(s)$, and $\alpha_y(s)$ still remain to be determined.

Solving for the scalar and vector potentials from Eq. (3), we obtain

$$\phi^s = \beta_b^{-1} A_z^s = -\frac{2qN_b}{a+b} \left(\frac{\bar{x}^2}{a} + \frac{\bar{y}^2}{b} \right) \quad (10)$$

in the beam interior with $\bar{x}^2/a^2 + \bar{y}^2/b^2 < 1$. In deriving Eq. (10), use has been made of $\nabla_{\perp}^2 = \partial^2/\partial\bar{x}^2 + \partial^2/\partial\bar{y}^2$.

To solve the force equation (4), we substitute Eqs. (5), (6), and (8)–(10) into Eq. (4), express the results in terms of the tilded variables, and use the relations $\partial\bar{x}/\partial s = \theta'\bar{y}$, $\partial\bar{y}/\partial s = -\theta'\bar{x}$, $\partial\hat{e}_{\bar{x}}/\partial s = \theta'\hat{e}_{\bar{y}}$, and $\partial\hat{e}_{\bar{y}}/\partial s = -\theta'\hat{e}_{\bar{x}}$. We obtain

$$\{f_x + \kappa_q \cos[2(\theta - \varphi_q)]\}\bar{x} - \{g_y + \kappa_q \sin[2(\theta - \varphi_q)]\}\bar{y} = 0, \quad (11a)$$

$$\{g_x - \kappa_q \sin[2(\theta - \varphi_q)]\}\bar{x} + \{f_y - \kappa_q \cos[2(\theta - \varphi_q)]\}\bar{y} = 0 \quad (11b)$$

in the \bar{x} and \bar{y} directions, respectively. In Eq. (11),

$$f_x = \frac{1}{a} \frac{d^2 a}{ds^2} - \frac{b^2(\alpha_x^2 - 2\alpha_x\alpha_y) + a^2\alpha_y^2}{a^2 - b^2} - 2\alpha_y\sqrt{\kappa_z} - \frac{2K}{a(a+b)}, \quad (12a)$$

$$f_y = \frac{1}{b} \frac{d^2 b}{ds^2} + \frac{a^2(\alpha_y^2 - 2\alpha_x\alpha_y) + b^2\alpha_x^2}{a^2 - b^2} - 2\alpha_x\sqrt{\kappa_z} - \frac{2K}{b(a+b)}, \quad (12b)$$

$$g_y = \frac{1}{b^2} \left\{ \frac{d}{ds} [b^2(\alpha_x + \sqrt{\kappa_z})] - \frac{a^3b(\alpha_x - \alpha_y)}{a^2 - b^2} \frac{d}{ds} \left(\frac{b}{a} \right) \right\}, \quad (12c)$$

$$g_x = \frac{1}{a^2} \left\{ \frac{d}{ds} [a^2(\alpha_y + \sqrt{\kappa_z})] - \frac{ab^3(\alpha_x - \alpha_y)}{a^2 - b^2} \frac{d}{ds} \left(\frac{a}{b} \right) \right\}. \quad (12d)$$

Since Eqs. (11a) and (11b) must be satisfied for all \bar{x} and \bar{y} , we obtain the generalized beam envelope equations

$$f_x + \kappa_q \cos[2(\theta - \varphi_q)] = 0, \quad (13a)$$

$$f_y - \kappa_q \cos[2(\theta - \varphi_q)] = 0, \quad (13b)$$

$$g_y + \kappa_q \sin[2(\theta - \varphi_q)] = 0, \quad (13c)$$

$$g_x - \kappa_q \sin[2(\theta - \varphi_q)] = 0. \quad (13d)$$

Making use of Eq. (12), we can express the generalized beam envelope equations as [17]

$$\frac{d^2 a}{ds^2} + \left\{ \kappa_q(s) \cos[2(\theta - \varphi_q)] - \frac{b^2(\alpha_x^2 - 2\alpha_x\alpha_y) + a^2\alpha_y^2}{a^2 - b^2} - 2\alpha_y\sqrt{\kappa_z} \right\} a - \frac{2K}{(a+b)} = 0, \quad (14a)$$

$$\frac{d^2 b}{ds^2} + \left\{ -\kappa_q(s) \cos[2(\theta - \varphi_q)] + \frac{a^2(\alpha_y^2 - 2\alpha_x\alpha_y) + b^2\alpha_x^2}{a^2 - b^2} - 2\alpha_x\sqrt{\kappa_z} \right\} b - \frac{2K}{(a+b)} = 0, \quad (14b)$$

$$\frac{d}{ds} [b^2(\alpha_x + \sqrt{\kappa_z})] - \frac{a^3b(\alpha_x - \alpha_y)}{a^2 - b^2} \frac{d}{ds} \left(\frac{b}{a} \right) + \kappa_q(s)b^2 \sin[2(\theta - \varphi_q)] = 0, \quad (14c)$$

$$\frac{d}{ds} [a^2(\alpha_y + \sqrt{\kappa_z})] - \frac{ab^3(\alpha_x - \alpha_y)}{a^2 - b^2} \frac{d}{ds} \left(\frac{a}{b} \right) - \kappa_q(s)a^2 \sin[2(\theta - \varphi_q)] = 0, \quad (14d)$$

$$\frac{d\theta}{ds} - \frac{a^2\alpha_y - b^2\alpha_x}{a^2 - b^2} = 0, \quad (14e)$$

$$\mu_x = \frac{1}{a} \frac{da}{ds}, \quad (14f)$$

$$\mu_y = \frac{1}{b} \frac{db}{ds}. \quad (14g)$$

Equations (8) and (9) are added here as Eqs. (14e)–(14g) for completeness. Equations (14a)–(14g), together with the density and velocity profiles defined in Eqs. (5) and (6), describe cold-fluid equilibrium states for variably focused ultrahigh-brightness beams.

IV. LIMITING CASES

A wide variety of cold-fluid beam equilibria can be constructed with Eqs. (5), (6), and (14) for proper choices of magnetic focusing field profiles. While cold-fluid beam equilibria are elliptic and corkscrewing in general, they do recover familiar beam equilibria in proper limits. In this section, we discuss some of these limiting cases.

First, let us consider the case of an axisymmetric beam in a periodic solenoidal focusing field with $\kappa_z(s) = \kappa_z(s+S) \neq 0$, $\kappa_q(s) = 0$, and $a(s) = a(s+S) = b(s)$. In this limit, Eqs. (14c)–(14e) imply that

$$\frac{d\theta}{ds} = \alpha_x = \alpha_y = \frac{\varepsilon_d}{a^2(s)} - \sqrt{\kappa_z(s)}, \quad (15)$$

where $\varepsilon_d = \text{const}$ is an unnormalized emittance associated with beam rotation relative to the Larmor frequency $\sqrt{\kappa_z(s)}$. Equation (15) indicates that the beam rotates at a rate that is

a periodic function of the axial propagation distance s . Substituting Eq. (15) into Eqs. (14a) and (14b), setting $\alpha_x = \alpha_y$, and taking the limit $a = b$, it is readily shown that the beam envelope equations reduce to

$$\frac{d^2 a}{ds^2} + \kappa_z(s)a - \frac{K}{a} - \frac{\epsilon_d^2}{a^3} = 0. \quad (16)$$

The equilibrium described by Eqs. (5), (6), (15), and (16) is identical to the familiar round rigid-rotor Vlasov beam equilibrium [15] in the zero-emittance limit.

Second, in a uniform magnetic focusing field with $\kappa_z(s) = \kappa_{z0} = \text{const}$, $\kappa_q(s) = 0$, and $a(s) = b(s)$, a special solution to the beam envelope equation (16) is

$$a = \left[\frac{K + (K^2 + 4\kappa_{z0}\epsilon_d^2)^{1/2}}{2\kappa_{z0}} \right]^{1/2} = \text{const}, \quad (17)$$

and the equilibrium recovers the familiar cold-fluid round rigid-rotor beam equilibrium [13,14]. A general class of corkscrewing elliptical beam equilibria with constant radii $a \neq b$ in a uniform solenoidal focusing field is discussed in detail in Sec. IV A.

As a third limiting case, we consider a nonrotating elliptical beam in an alternating-gradient quadrupole focusing field with $\kappa_z(s) = 0$, $\kappa_q(s) = \kappa_q(s+S)$, $\theta(s) = 0$, $a(s) = a(s+S)$, $b(s) = b(s+S)$, and $\alpha_x(s) = \alpha_y(s) = 0$. In this case, Eqs. (14c)–(14e) are automatically satisfied and the envelope equations reduce to

$$\frac{d^2 a}{ds^2} + \kappa_q(s)a - \frac{2K}{a+b} = 0, \quad (18a)$$

$$\frac{d^2 b}{ds^2} + \kappa_q(s)b - \frac{2K}{a+b} = 0. \quad (18b)$$

Note that the internal flow must satisfy $\alpha_x(s) = \alpha_y(s) = 0$ in order to prevent the beam from rotating with a finite $d\theta/ds$. The equilibrium described by Eqs. (5), (6), and (18) correspond to the familiar Kapchinskij-Vladimirskij beam equilibrium [16] in alternating-gradient quadrupole magnetic focusing field in the zero-emittance limit.

V. EXAMPLES AND APPLICATIONS

In this section, we discuss three examples of cold-fluid corkscrewing elliptic beam equilibria predicted by the equilibrium beam theory presented in Sec. IV. These examples are (a) cold-fluid corkscrewing elliptic beam equilibria in a uniform magnetic field (Sec. V A), (b) matching and transport of an ultrahigh-brightness round beam generated by an axisymmetric particle source into an alternating-gradient magnetic quadrupole focusing channel (Sec. V B), and (c) matching and transport of an ultrahigh-brightness round beam into a periodic focusing channel consisting of overlapping solenoidal and quadrupole focusing fields (Sec. V C).

In addition to illustrating a large class of beam equilibria predicted by the present equilibrium beam theory, these examples are also intended to demonstrate a general technique for controlling of large-amplitude beam density and flow velocity fluctuations and associated emittance growth and beam

halo formation often observed in ultrahigh-brightness beam experiments. To demonstrate the efficacy of this beam control technique, the transport for an ultrahigh-brightness beam with an initial perturbation about the equilibrium transverse flow velocity is compared with the equilibrium beam transport (Sec. V B).

A. Corkscrewing elliptic beam equilibria in a uniform magnetic field

As a simple example, we consider corkscrewing elliptic beam equilibria in a uniform magnetic field with $\mathbf{B}^{\text{ext}} = B_{z0}\hat{e}_z$. Setting $\sqrt{\kappa_z(s)} = \sqrt{\kappa_{z0}} = qB_{z0}/2\gamma_b\beta_b mc^2 = \text{const}$ and $\kappa_q(s) = 0$, it can be shown that Eq. (14) has the following two branches of physically acceptable special solutions:

$$a = a_1 = \left(\frac{\alpha_x}{\alpha_y} \right)^{1/2} \left[\frac{K}{\kappa_{z0} - (\alpha_x + \sqrt{\kappa_{z0}})(\alpha_y + \sqrt{\kappa_{z0}})} \right]^{1/2},$$

$$b = b_1 = \left(\frac{\alpha_y}{\alpha_x} \right)^{1/2} \left[\frac{K}{\kappa_{z0} - (\alpha_x + \sqrt{\kappa_{z0}})(\alpha_y + \sqrt{\kappa_{z0}})} \right]^{1/2},$$

$$\theta(s) = \omega_1 s = \frac{\alpha_x \alpha_y}{\alpha_x + \alpha_y} s + \theta(0), \quad (19)$$

for branch A, and

$$a = a_2 = \left(\frac{\alpha_x + 2\sqrt{\kappa_{z0}}}{\alpha_y + 2\sqrt{\kappa_{z0}}} \right)^{1/2} \left[\frac{K}{\kappa_{z0} - (\alpha_x + \sqrt{\kappa_{z0}})(\alpha_y + \sqrt{\kappa_{z0}})} \right]^{1/2},$$

$$b = b_2 = \left(\frac{\alpha_y + 2\sqrt{\kappa_{z0}}}{\alpha_x + 2\sqrt{\kappa_{z0}}} \right)^{1/2} \left[\frac{K}{\kappa_{z0} - (\alpha_x + \sqrt{\kappa_{z0}})(\alpha_y + \sqrt{\kappa_{z0}})} \right]^{1/2},$$

$$\theta(s) = \omega_2 s = \frac{\alpha_x \alpha_y - 4\kappa_{z0}}{\alpha_x + \alpha_y + 4\sqrt{\kappa_{z0}}} s + \theta(0), \quad (20)$$

for branch B. In Eqs. (19) and (20), α_x and α_y are constant.

For branch A, the conditions for the confinement of corkscrewing elliptic beam equilibria are

$$\alpha_x / \sqrt{\kappa_{z0}} < 0, \quad \alpha_y / \sqrt{\kappa_{z0}} < 0,$$

$$(\alpha_x + \sqrt{\kappa_{z0}})(\alpha_y + \sqrt{\kappa_{z0}}) < \kappa_{z0} \quad (21)$$

for both positively and negatively charged particle beams. Because α_x and α_y have the same sign, the internal flow for branch A is always rotation like. For branch B, the conditions for the confinement of corkscrewing elliptic beam equilibria are

$$\alpha_y / \sqrt{\kappa_{z0}} > -2, \quad \alpha_x / \sqrt{\kappa_{z0}} > -2,$$

$$(\alpha_x + \sqrt{\kappa_{z0}})(\alpha_y + \sqrt{\kappa_{z0}}) < \kappa_{z0} \quad (22)$$

for both positively and negatively charged particle beams. In contrast to the internal flow for branch A, the internal flow

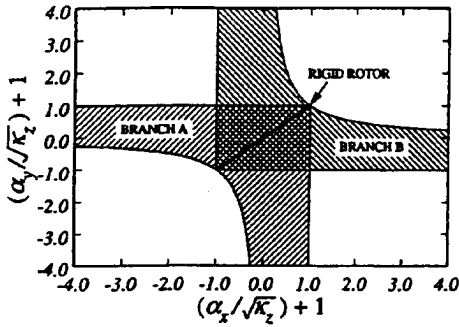


FIG. 2. Regions in parameter space for confinement of corkscrewing elliptic beam equilibria in a uniform magnetic field.

for branch B can be either rotation like with α_x and α_y in the same sign or quadrupole flow like with α_x and α_y in apposite signs. Figure 2 shows the regions of the confinement of corkscrewing elliptic beam equilibria in a uniform magnetic field applicable for both positively and negatively charged particle beams. It is important to point out that the familiar cold-fluid round rigid-rotor beam equilibria [13,14] are recovered in the present analysis by setting $\alpha_x = \alpha_y$ in either Eq. (19) or Eq. (20), as indicated by the dark solid line shown in Fig. 2.

B. Control of halo formation and beam hollowing in ultrahigh brightness beams

As discussed in the Introduction, one of the key mechanisms for halo formation in high-intensity electron or ion beams is due to a mismatch in the particle phase-space distribution relative to an equilibrium distribution. In general, a distribution mismatch can lead to rather complex evolution in a beam, including not only halo formation, but also beam hollowing. This mechanism for halo formation and beam hollowing occurs for rms matched beams because rms beam matching does not necessarily guarantee the beam in an equilibrium state.

For example, both halo formation and beam hollowing were observed in the heavy ion beam injector experiment at Lawrence Berkeley National Laboratory (LBNL) [11], in which an ultrahigh-brightness, space-charge-dominated potassium ion beam was generated with an axisymmetric Pierce diode and then accelerated by a set of electrostatic quadrupoles. More recently, experimental evidence of beam hollowing was found in a high-brightness, space-charge-dominated electron beam experiment at University of Maryland [18].

As an important application of the equilibrium beam theory presented in Sec. IV, we develop and demonstrate a technique for controlling of beam halo formation and beam hollowing in ultrahigh-brightness beams. This technique is widely applicable in the design of ultrahigh-brightness beams and is effective before any collective instability develops to reach considerably large amplitudes.

To demonstrate the efficacy of this technique, we consider here a specific example, namely, the matching of a round particle beam generated by an axisymmetric particle source into alternating-gradient magnetic quadrupole focusing channel. For comparison, we analyze two nonrotating rms matched beams with the same intensity; one beam will be in equilibrium, and the other beam has an initial perturbation about the equilibrium transverse flow velocity. At the en-

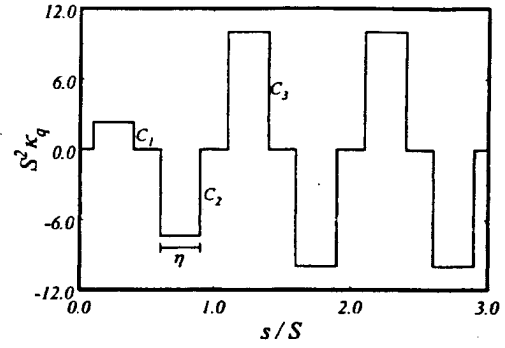


FIG. 3. Plot of the focusing parameter $S^2 \kappa_q$ as a function of the propagation distance s .

trance of the alternating-gradient magnetic focusing channel ($s=0$), both beams have the same density profile defined in Eq. (15), but the transverse flow velocities of the beams are of the form [19]

$$\frac{d\mathbf{x}_\perp}{ds} = \frac{\mathbf{x}_\perp}{a} \left(\frac{da}{ds} \right) \left[1 + \nu \left(1 - \frac{2\mathbf{x}_\perp \cdot \mathbf{x}_\perp}{a^2} \right) \right], \quad (23)$$

where ν is a parameter that measures the nonlinearity in the velocity profile. For example, an initial velocity profile with $\nu > 0$ in Eq. (23) may model the effects of the concave shape of a Pierce-type ion diode in the LBNL 2-MV Heavy Ion Beam Injector Experiment [11]. The value of ν in the LBNL experiment [11] is estimated to be $\nu = 0.25$. For equilibrium beam propagation, $\nu = 0$.

The rms matching for both beams with $\nu = 0$ and 0.25 is obtained by numerically solving the rms envelope equations [5]

$$\frac{d^2 \bar{a}}{ds^2} + \kappa_q(s) \bar{a} - \frac{K}{2(\bar{a} + \bar{b})} = 0, \quad (24a)$$

$$\frac{d^2 \bar{b}}{ds^2} - \kappa_q(s) \bar{b} - \frac{K}{2(\bar{a} + \bar{b})} = 0, \quad (24b)$$

where $\bar{a} \equiv \langle x^2 \rangle^{1/2}$ and $\bar{b} \equiv \langle y^2 \rangle^{1/2}$ are the rms envelopes, $\langle \dots \rangle$ denotes average over the particle distribution, and emittance terms are neglected. For given beam intensity K and focusing channel parameters C_3 and η shown in Fig. 3, we make use of Eq. (24) to determine the injection parameters for the axisymmetric beam, namely, $\bar{a}(0)$, $\bar{b}(0)$, $\bar{a}'(0)$, and $\bar{b}'(0)$, as well as the strengths of the two quadrupoles centered at $s=S/4$ and $s=3S/4$ in the first lattice, C_1 and C_2 , as shown in Fig. 3, assuming all quadrupoles having the same width η and equally spaced. Because Eq. (24) has a unique solution for an rms matched beam in the constant-parameter alternating-gradient focusing section with $s/S > 1$, integrating Eq. (24) from $s=S$ to $s=0$ yields four implicit functions $\bar{a}(C_1, C_2)$, $\bar{b}(C_1, C_2)$, $\bar{a}'(C_1, C_2)$, and $\bar{b}'(C_1, C_2)$. The conditions for an initially converging round beam, i.e., $\bar{a}(0) = \bar{b}(0) = a(0)/2 = b(0)/2$ and $\bar{a}'(0) = \bar{b}'(0)$, uniquely determine the parameters C_1 and C_2 , which is done numerically with Newton's method. The results are presented in Figs. 3 and 4.

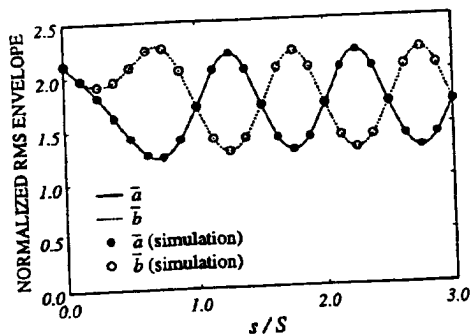


FIG. 4. Plots of rms beam envelopes versus propagation distances. Here the solid and dashed curves are obtained from Eq. (24), whereas the solid dots and open circles are from the self-consistent simulation for a beam with $\nu=0.25$. Here \bar{a} and \bar{b} are normalized to $\sqrt{\epsilon(0)S}$.

Figure 3 shows the focusing field parameter $S^2\kappa_q$ as a function of s , where $\eta=0.3$, $C_1=2.31$, $C_2=7.44$, and $C_3=10.0$. In Fig. 4, the solid and dashed curves show, respectively, the rms matched envelopes $\bar{a}(s)$ and $\bar{b}(s)$ for the focusing channel with vacuum phase advance $\sigma_0=70.8^\circ$ and beam perveance $SK/4\epsilon(0)=16.0$ (corresponding to a space-charge-depressed phase advance of $\sigma=5.4^\circ$), where a negligibly small unnormalized rms emittance of $\epsilon(0)=0.15 \times 10^{-6}$ m rad has been assigned to the beam at $s=0$.

Self-consistent simulations are performed with $N_p=3072$ and free-space boundary conditions to study the phase space evolution for the two beams in the focusing channel shown in Fig. 3. In Fig. 4, the solid dots and open circles correspond to the rms envelopes $\bar{a}(s)$ and $\bar{b}(s)$ obtained from a self-consistent simulation for a beam initially with a nonlinear velocity profile with $\nu=0.25$. It is evident in Fig. 4 that there is excellent agreement between the prediction of the rms envelope equations (24a) and (24b) and the results of the self-consistent simulation, despite that the transverse flow velocity is perturbed substantially.

We now examine the evolution of the particle distribution if the nonlinearity in the initial transverse flow velocity profile is introduced and compare with equilibrium beam propagation. The results are summarized in Figs. 5 and 6. Figure 5 shows a comparison between particle distributions in the configuration space with and without nonlinearity in the initial transverse flow velocity at three axial positions: $s/S=0, 1.0$, and 2.5 . These axial positions are chosen such that $\bar{a}(s)=\bar{b}(s)$. In Fig. 5, the plots shown on the left correspond to $\nu=0$ and those on the right to $\nu=0.25$. For $\nu=0.25$, the initially round beam develops sharp edges after the first lattice, becoming partially hollow subsequently at $s/S=2.5$. In Fig. 6(b), the radial distribution of 3072 macroparticles at $s/S=2.5$ shows that the density at the edge is twice the density at the center of the beam and that there is a small halo extending outward beyond the radius where the density reaches its maximum. The partially hollow density profile shown in Fig. 6(b) is similar to, but not as pronounced as, that observed in the heavy ion beam injector experiment at LBNL [11]. In contrast to the case with $\nu=0.25$, the beam propagates in an equilibrium state for $\nu=0$ without beam hollowing and without any significant beam halo formation, as shown in Fig. 6(a).

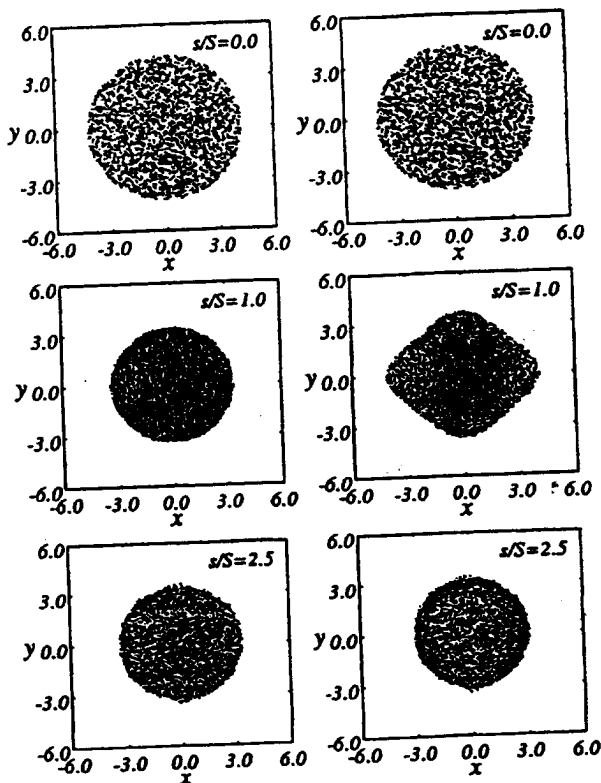


FIG. 5. Particle distributions in the configuration space for $\nu=0$ (left) and $\nu=0.25$ (right). Here the coordinates x and y are normalized to $\sqrt{\epsilon(0)S}$.

C. Matching and transport of a beam into a periodic focusing channel consisting of overlapping solenoidal and quadrupole focusing fields

As another example of corkscrewing elliptic beam equilibrium, we consider the matching and transport of an initially round beam into a periodic focusing channel consisting

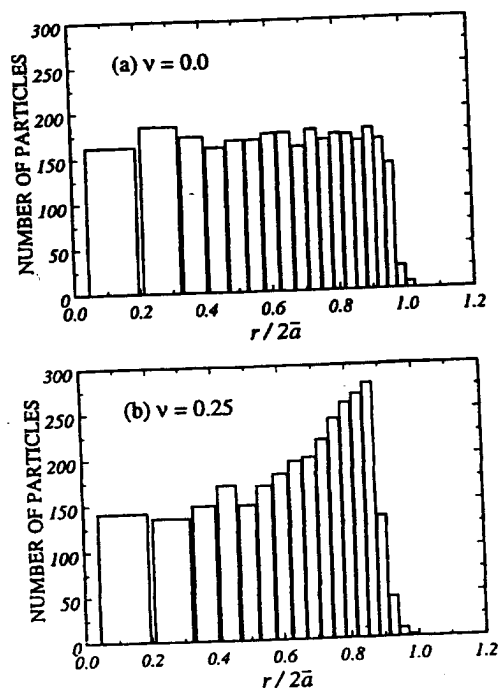


FIG. 6. Radial distribution of the macroparticles at $s/S=2.5$ for (a) $\nu=0$ and (b) $\nu=0.25$.

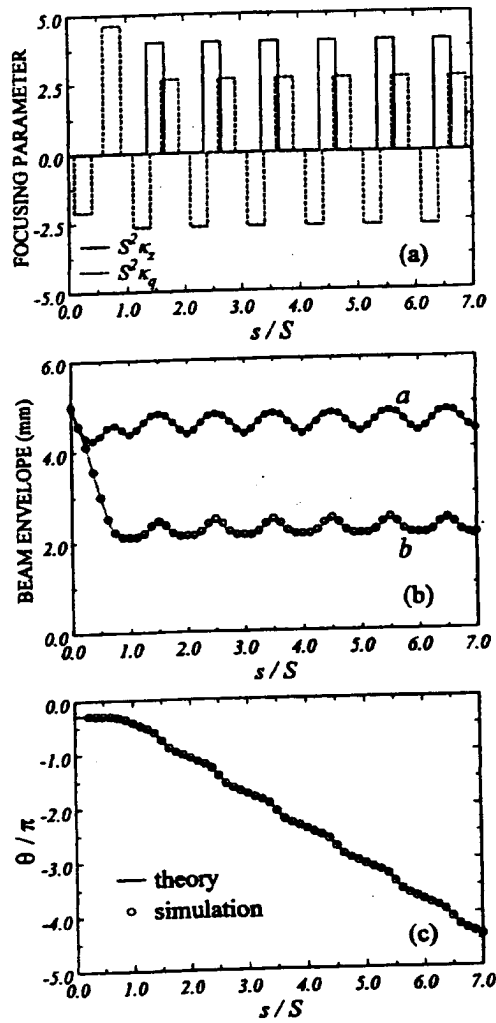


FIG. 7. Plots of focusing and beam parameters versus normalized propagation distance s/S for an equilibrium beam in a tapered linear focusing channel consisting of overlapping periodic solenoidal and alternating-gradient quadrupole magnetic fields. Here $K = 1.6 \times 10^{-5}$ and $S = 1.0$ m. In (a) the solid and dashed curves are dimensionless focusing parameters $S^2 \kappa_z(s)$ and $S^2 \kappa_q(s)$, respectively; in (b) the solid and dashed curves are the beam envelopes $a(s)$ and $b(s)$ predicted by Eq. (14), whereas the solid dots and open circles are obtained from the simulation; in (c) the solid curve and open circles are the angles of the beam ellipses obtained from Eq. (14) and the simulation, respectively.

of overlapping solenoidal and quadrupole focusing fields. Figure 7(a) shows plots of dimensionless focusing parameters $S^2 \kappa_z$ and $S^2 \kappa_q$ versus propagation distance s/S for the channel. In Fig. 7(a), the width of solenoidal and quadrupole magnets is $0.3S$. In the matching section ($0 < s < S$), two quadrupoles at $s/S = 0.25$ and $s/S = 0.75$ are placed at angles $\varphi_q = -50^\circ$ and $\varphi_q = -40^\circ$, respectively. In the periodic focusing section ($s > S$), the quadrupoles are placed at $\varphi_q = 0^\circ$ in the first cell ($1 < s/S \leq 2$) and are rotated by -120° in each of subsequent cells, yielding a periodicity of $3S$ for the channel. To determine the angles and the strengths of the matching quadrupoles, we first find from Eq. (14) periodic solutions with $a(s+S) = a(s)$, $b(s+S) = b(s)$, $\alpha_x(s+S) = \alpha_x(s)$, $\alpha_y(s+S) = \alpha_y(s)$, and $\theta(s+3S) = \theta(s)$ in the periodic focusing section and then match the initially round beam with $a(0) = b(0)$ and $\alpha_x(0) = \alpha_y(0)$ with the periodic

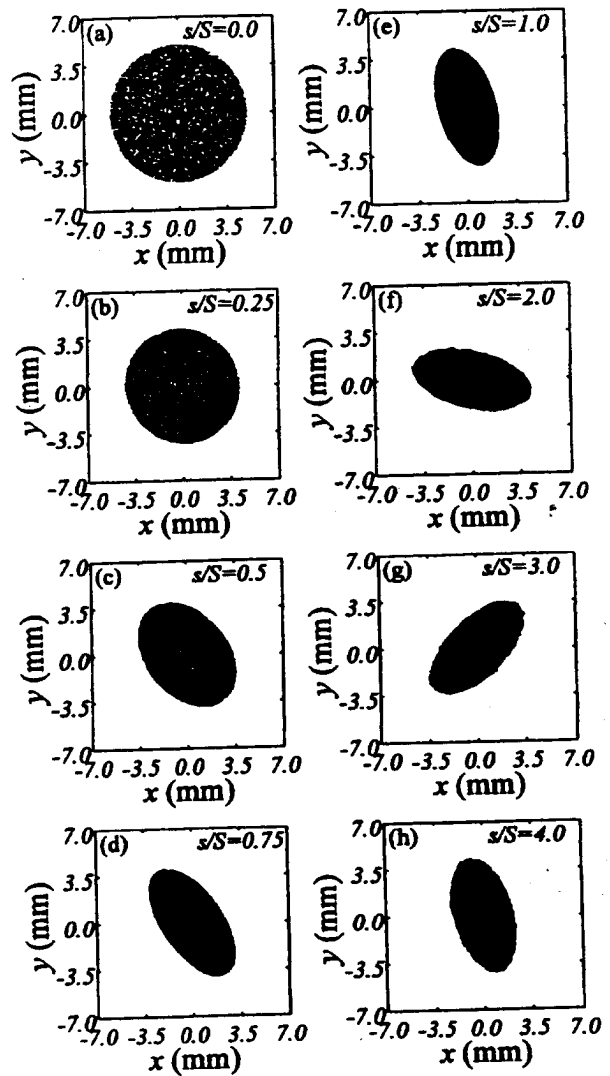


FIG. 8. Particle distributions in configuration space obtained from the simulation for the case shown in Fig. 7.

solution at $s/S = 1$ using a shooting method. The results are shown in Fig. 7 for $K = 1.6 \times 10^{-5}$ and $S = 1.0$ m. The solid and dashed curves in Fig. 7(b) are calculated envelopes $a(s)$ and $b(s)$, and the solid curve in Fig. 7(c) is the angle $\theta(s)$.

We have validated the exact steady-state solutions using self-consistent simulations. In the simulations, use is made of Green's function method to determine electrostatic fields generated by the charged particles in the beam and image charges due to a perfectly conducting cylindrical tube of radius r_w . A detailed description of the simulation code was presented earlier [19]. For the focusing parameters shown in Fig. 7(a), 10^4 macroparticles are loaded in the present simulation according to the initial distribution function

$$f(\mathbf{x}_\perp, \mathbf{x}'_\perp) = n_b(x_\perp, 0) \exp\{-[\mathbf{x}'_\perp \beta_b c - \mathbf{V}_\perp(\mathbf{x}_\perp, 0)]^2 / T(\mathbf{x}_\perp)\},$$

where $n_b(\mathbf{x}_\perp, 0)$ and $\mathbf{V}_\perp(\mathbf{x}_\perp, 0)$ are the initial density and velocity profiles defined in Eqs. (5) and (6), respectively, $T(\mathbf{x}_\perp) = T_0(x^2/a^2 + y^2/b^2 - 1)$ is an effective temperature profile, and T_0 is a constant chosen to give an initial total (4 times rms) emittance of 0.2×10^{-6} m rad. The conducting cylindrical tube radius is chosen to be $r_w = 10.0$ mm. Results of the simulation are summarized in Figs. 7(b), 7(c), and 8.

Shown in Figs. 7(b) and 7(c) is the excellent agreement between the beam envelopes $a(s)$ and $b(s)$ and angle $\theta(s)$ obtained from the self-consistent simulation and those predicted by the generalized beam envelope equations (14), as expected. In Fig. 8, particle distributions in the plane (x, y) are plotted at several axial locations of the matching section and the periodic focusing section, showing the transition from a round beam to a corkscrewing elliptic beam in the focusing channel. The elliptic beam completes a full clockwise turn from $s/S = 1$ to $s/S = 4$ [see Figs. 8(e)–8(h)]. Both image charge effects and emittance growth are negligibly small. The density profiles are computed at various axial locations in the simulation, and they are found in good agreement with the density profile defined in Eq. (5). It should be stressed that the beam propagates in a steady state without either beam hollowing or halo formation.

VI. CONCLUSIONS

We have shown that there exists a new class of cold-fluid corkscrewing elliptic beam equilibria for ultrahigh-brightness, space-charge-dominated beam propagation through a linear focusing channel consisting of uniform solenoidal, periodic solenoidal, and/or alternating-gradient quadrupole focusing magnets in an arbitrary arrangement including field tapering. Generalized beam envelope equations were derived. The equilibrium beam density and flow velocity profiles and equilibrium self-electric and self-magnetic fields were determined by solving generalized beam envelope equations. For beams with negligibly small emittance, these steady-state solutions were validated with self-consistent simulations using the Green's function method. While these steady-state solutions correspond to corkscrewing elliptic beam equilibria in general, they do recover many familiar beam equilibria in beam physics, such as the cold-

fluid round rigid-rotor equilibrium and both the periodically focused rigid-rotor Vlasov equilibrium and Kapchinskij-Vladimirskij equilibrium in the zero-emittance limit.

Examples and applications of the present equilibrium beam theory were discussed. In particular, a corkscrewing elliptic beam equilibrium in a uniform solenoidal magnetic field was obtained. As an important application of the present equilibrium beam theory, a general technique was developed and demonstrated with an example to control large-amplitude density and flow velocity fluctuations (such as beam hollowing and halo formation) often observed in ultrahigh-brightness beams. Furthermore, an ultrahigh-brightness beam equilibrium in a periodic focusing channel consisting of overlapping solenoidal and quadrupole focusing field was obtained to illustrate a wide range of applicability of the present equilibrium beam theory in manipulating ultrahigh-brightness beams.

It is anticipated that the equilibrium beam theory presented in this paper can be used to perfectly match ultrahigh-brightness beams in practical beam transport systems and to design electron beam equilibrium configurations in new vacuum electronic devices. Finally, the present cold-fluid equilibrium theory can be generalized to include the effect of finite beam emittance, which will be discussed in a future article.

ACKNOWLEDGMENTS

This work was supported by the Department of Energy, Office of High Energy and Nuclear Physics Grant No. DF-FG02-95ER-40919, the Air Force Office of Scientific Research Grant No. F49620-97-1-0325 and No. F49620-00-1-0007, and in part by the Department of Energy through a subcontract with Princeton Plasma Physics Laboratory. The research by R.P. was also supported by CNPq, Brazil.

-
- [1] J. Benford and J. A. Swegle, *High Power Microwaves* (Artech, Boston, 1992).
 - [2] E. D. Courant, M. S. Livingstone, and H. Snyder, *Phys. Rev.* **88**, 1190 (1952).
 - [3] *Space Charge Dominated Beams and Applications of High-Brightness Beams*, edited by S. Y. Lee, AIP Conf. Proc. No. 377 (AIP, New York, 1996).
 - [4] P. M. Lapostolle, *IEEE Trans. Nucl. Sci.* **NS-18**, 1101 (1971).
 - [5] F. J. Sacherer, *IEEE Trans. Nucl. Sci.* **NS-18**, 1105 (1971).
 - [6] D. Chernin, *Part. Accel.* **24**, 29 (1998).
 - [7] J. Barnard, in *Proceedings of the 1995 Particle Accelerators Conference* (Institute of Electrical and Electronics Engineering, Piscataway, NJ, 1995), p. 3241.
 - [8] Q. Qian, R. C. Davidson, and C. Chen, *Phys. Rev. E* **51**, 3704 (1995).
 - [9] C. Chen and R. C. Davidson, *Phys. Rev. Lett.* **72**, 2195 (1994).
 - [10] R. L. Gluckstern, *Phys. Rev. Lett.* **73**, 1247 (1994).
 - [11] S. Yu, S. Eylon, E. Henestroza, and D. Grote, in *Space Charge Dominated Beams and Applications of High-Brightness Beams* [3], p. 134.
 - [12] T. P. Wangler, K. R. Crandall, R. S. Mills, and M. Reiser, *IEEE Trans. Nucl. Sci.* **NS-32**, 2196 (1985).
 - [13] R. C. Davidson and N. A. Krall, *Phys. Fluids* **13**, 1543 (1970).
 - [14] A. J. Theiss, R. A. Mahaffey, and A. W. Trivelpiece, *Phys. Rev. Lett.* **35**, 1436 (1975).
 - [15] C. Chen, R. Pakter, and R. C. Davidson, *Phys. Rev. Lett.* **79**, 225 (1997).
 - [16] I. M. Kapchinskij, and V. V. Vladimirskij, in *Proceedings of the International Conference on High Energy Accelerators* (CERN, Geneva, 1959), p. 274.
 - [17] Equation (14) can be integrated numerically as a approaches b .
 - [18] S. Bernal, P. Chin, R. A. Kishek, Y. Li, M. Reiser, J. G. Wang, T. Godlove, and I. Haber, *Phys. Rev. ST Accel. Beams* **1**, 044202 (1998).
 - [19] M. Hess, R. Pakter, and C. Chen, in *Proceedings of the 1999 Particle Accelerator Conference*, edited by A. Luccio and W. Mackay (Institute of Electrical and Electronics Engineering, Piscataway, NJ, 1999), p. 2752.

Stimulated radiation from spatiotemporally gyrating relativistic electron beams

J. A. Davies^{a)} and C. Chen

Plasma Science and Fusion Center, Massachusetts Institute of Technology, Cambridge, Massachusetts 02139

(Received 24 March 2000; accepted 14 July 2000)

A stability analysis is made of an electron beam, propagating along and gyrating about a uniform magnetic field, for the case of a spatiotemporal equilibrium distribution in the phase angle of the transverse electron momentum component. The axial momentum component and the magnitude of the transverse momentum component are assumed to have definite values in the equilibrium distribution. The analysis is carried out by applying Lorentz transformations to previous results for nongyrotropic equilibrium distributions. The dispersion matrix, its eigenmodes (which relate field amplitudes), and the dispersion relation are obtained. Numerical results show that varying the spatiotemporal properties of a nongyrotropic equilibrium distribution has only a small effect on maximum growth rates of radiation, but has a strong effect on the frequencies and wavenumbers at which instability occurs. A novel mechanism is found by which electrons emit stimulated radiation at frequencies that, in principle, can be greater than the usual Doppler-shifted electron cyclotron frequency by orders of magnitude. © 2000 American Institute of Physics.

[S1070-664X(00)05010-2]

I. INTRODUCTION

Stimulated emission of radiation by electrons gyrating in magnetic fields has been an important subject of theoretical, computational, and experimental investigations in plasma physics, astrophysics, and vacuum electronics for several decades.¹⁻⁶ It is well known that the frequencies of such stimulated radiation correspond to the Doppler-shifted electron cyclotron frequency and its harmonics. For moderately and highly relativistic electrons, the fundamental frequency is approximately $2\gamma_z^2\omega_c$, where γ_z is the relativistic mass factor associated with the axial motion of the electrons and ω_c is the relativistic cyclotron frequency.

A number of papers have dealt with stability properties of a relativistic electron beam in the presence of a uniform magnetic field $\mathbf{B}_0 = B_0 \mathbf{e}_z$ for the case of a nonisotropic equilibrium distribution in the phase angle ϕ of the momentum component \mathbf{p}_\perp perpendicular to the field.⁷⁻¹⁴ In particular, it has been suggested that such distributions may be employed to enhance the growth rates of desired radiation modes in devices employing the cyclotron resonance maser instability. More recently, there has been some interest in harmonic conversion processes in spatiotemporal equilibrium distributions in ϕ .¹⁵⁻¹⁷

In order to gain a greater understanding of systems with spatiotemporal distributions in ϕ , we analyze the stability properties of such systems in this paper. Preliminary results are given in an earlier report.¹⁸ The analysis is limited to equilibrium distributions in which the axial momentum component p_z and the magnitude of the transverse momentum component \mathbf{p}_\perp have the definite values p_{z0} and $p_{\perp 0}$, respectively. Moreover, the systems are constrained to vary spa-

tially only in the direction of the applied magnetic field (z direction).

In Ref. 7, we analyzed the stability properties of such electron beam systems for two types of nonisotropic equilibrium distributions in the phase ϕ . These were the time-dependent distribution, which is a function of the equilibrium constant of the motion $\phi - \omega_c t$, and the axial-dependent distribution, which is a function of the equilibrium constant of the motion $\phi - \omega_c z/v_{z0}$.

It is shown in this paper that all relevant spatiotemporal distributions are obtained from the above distributions by Lorentz transformations. By making use of a Lorentz transformation of the results obtained in Ref. 7, we derive the amplitude equations and dispersion relations for small-amplitude wave perturbations on spatiotemporally gyrating relativistic electron beams. A detailed analysis is made of stability properties of such electron beams.

In the present stability analysis, we find a novel mechanism by which electrons emit stimulated radiation at frequencies that are greater than the usual Doppler-shifted electron cyclotron frequency by orders of magnitude. Two key requirements for this mechanism to occur are that the gyrophases of the electrons in the magnetic field have spatiotemporal correlations, and that the electrons have an inverted population in the transverse momentum space. In contrast to most previous studies of the stimulated radiation by gyrating electrons with a random or spatial-dependent gyrophase distribution and inverted population in the transverse momentum space, the present analysis assumes the gyrophase distribution to form a wave pattern in the direction of the magnetic field. When the phase velocity of the wave pattern is close to the average axial velocity of the electrons, the electrons emit right-hand, circularly polarized stimulated radiation at the relatively high frequency $\omega = 2|\beta_p$

^{a)}Permanent address: Department of Physics, Clark University, Worcester, Massachusetts 01610. Electronic mail: jdavies@clarku.edu

$-\beta_{x0}|\omega_c|^{-1}\omega_c$, where β_{pc} and $\beta_{x0}c$ are the phase and electron axial velocities, respectively, and c is the speed of light in vacuum.

It should be pointed out that the wave pattern in a spatiotemporally gyrating relativistic electron beam depends on how the beam is formed. One of the schemes to form a spatiotemporally gyrating electron beam is through the cyclotron laser (microwave) acceleration.¹⁹⁻²¹ In this case, the phase velocity of the wave pattern in the beam is given by $\beta_{pc} = \omega_0(\omega_0 - \omega_c)^{-1}\beta_{x0}c$, where ω_0 is the laser (microwave) frequency. In the limit $\omega_0 \gg \omega_c$ and $\beta_{x0} \rightarrow 1$, the stimulated radiation occurs at $\omega = 2\omega_0$.

The organization of this paper is as follows. In Sec. II, the spatiotemporal distribution is described, and the equilibrium distribution is defined in (4). The phase velocity β_p of a surface of constant distribution in phase is defined and evaluated in (9). The primary result of this paper is the dispersion relation for spatiotemporal equilibria with definite values of p_z and p_\perp . This result is stated in (13) of Sec. III. The derivation of our results from the results of Ref. 7 is given in the Appendix. Moreover, Eqs. (A19)-(A21) of the Appendix give the dispersion matrix for the electron beam systems considered in this paper. Another important result is the expression for the eigenmodes of the amplitude equation given in (19) of Sec. III. This result gives the wavenumbers and frequencies of coupled right-hand circularly polarized radiative waves, left-hand circularly polarized radiative waves, and longitudinal electrostatic waves. Numerical examples are presented in Sec. IV. In these examples, the choice of spatiotemporal distribution [namely, the choice of the phase velocity (β_p) of the phase pattern in the equilibrium distribution] is seen to have little effect on maximum growth rates of electromagnetic waves, but to have a strong effect on the range of unstable frequencies and wavenumbers and upon the wavenumbers and frequencies of coupled waves. These maximum growth rates of electromagnetic waves in the spatiotemporally gyrating relativistic electron beams are greater than those in the corresponding gyrotropic relativistic electron beams. We discuss and summarize our results in Sec. V.

II. SPATIOTEMPORALLY GYRATING EQUILIBRIUM

We consider a beam consisting of electrons moving along and gyrating about a uniform magnetic field $\mathbf{B}_0 = B_0 \hat{\mathbf{e}}_z$. Properties of the system are assumed to vary in the z direction only. All electrons in the equilibrium beam are assumed to have the same axial momentum ($p_z = p_{z0}$) and the same magnitude of transverse momentum ($p_\perp = p_{\perp 0}$). As shown in Fig. 1, the phase angle of \mathbf{p}_\perp is $\phi = \tan^{-1}(p_y/p_x)$, whereas $\alpha_0 = \tan^{-1}(p_\perp/p_z)$ is the pitch angle. The equilibrium distribution in phase is spatiotemporal; that is, at some $z = z_0$, we impose the condition

$$\phi(z_0, t) = \omega_0 t + \phi_0, \quad (1)$$

where ω_0 and ϕ_0 are constants and t is the time. This geometry is shown in Fig. 2(a). The value of ω_0 depends on how the electron beam is formed. For example, $\omega_0 = 0$ if the electron beam is formed by passing through a tapered static wig-

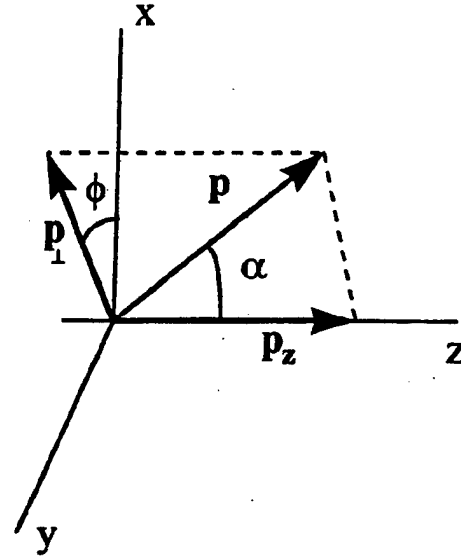


FIG. 1. The phase angle ϕ and pitch angle α_0 of a single-particle momentum \mathbf{p} .

glar magnetic field. If the electron beam is generated in a cyclotron resonance accelerator, then ω_0 corresponds to the rf frequency of the accelerator that is a shifted cyclotron frequency. The phase of an unperturbed electron at (z, t) is

$$\phi(z, t) = \omega_0 \left(t - \frac{z - z_0}{v_{z0}} \right) + \phi_0 + \omega_c \frac{z - z_0}{v_{z0}}. \quad (2)$$

In the above equation, the relativistic cyclotron frequency is denoted by $\omega_c = \Omega_c / \gamma_0$, where $\Omega_c = eB_0/mc$ is the nonrelativistic cyclotron frequency, $-e$ and m are, respectively, the electronic charge and mass, c is the speed of light, $\gamma_0 mc^2$ is the unperturbed relativistic electron energy, and $v_{z0} = p_{z0} / \gamma_0 m$. A spatiotemporally gyrating beam equilibrium is shown schematically in Fig. 2(b). In an experiment, z_0 would correspond to the point where the electron enters the region of interaction with \mathbf{B}_0 . However, boundary conditions are not dealt with in this paper, and the system is considered to extend over the full range (i.e., $-\infty < z < \infty$) of z .

A distribution of values of ϕ at each (z, t) will result in distributions of values of ϕ_0 and/or z_0 exist. From (2), such distributions will produce a distribution in the values of the equilibrium constant of the motion, χ , defined by

$$\chi = \phi(z, t) - \omega_0 t + (\omega_0 - \omega_c) \frac{z}{v_{z0}}. \quad (3)$$

Consequently, a suitable equilibrium distribution for the system is

$$f_0(p_\perp, p_z, \chi) = n_0 \frac{\delta(p_\perp - p_{\perp 0})}{p_\perp} \delta(p_z - p_{z0}) \Phi(\chi), \quad (4)$$

where $\Phi(\chi)$ is a periodic function of period 2π and n_0 is a constant particle density. We normalize the integral of $f_0(p_\perp, p_z, \chi)$ over momentum space to n_0 . Consequently,

$$\int_0^{2\pi} \Phi(\chi) d\phi = \int_0^{2\pi} \Phi(\chi) d\chi = 1. \quad (5)$$

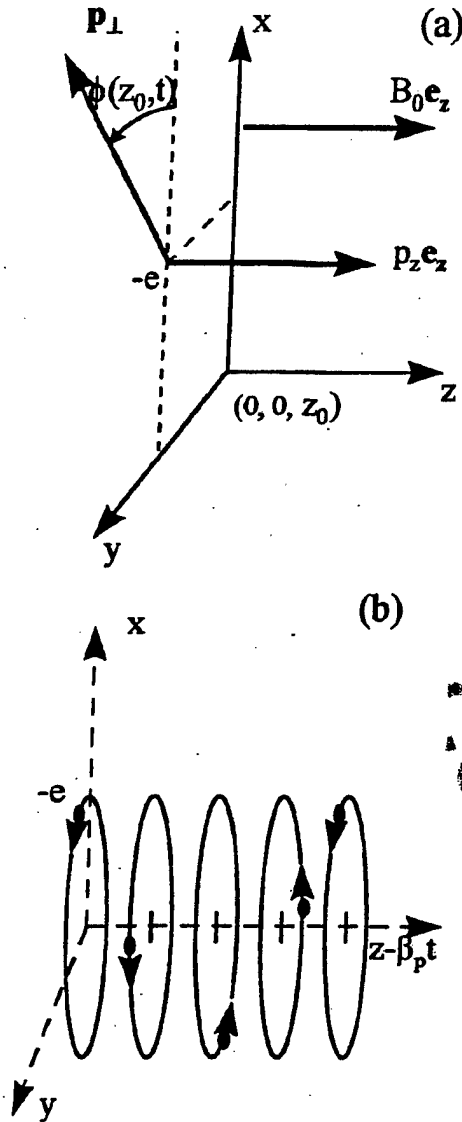


FIG. 2. (a) The generation of a spatiotemporally gyrating relativistic electron beam equilibrium with electrons arriving at $z=z_0$ with a gyrophase of $\phi(z_0, t) = \omega_0 t + \phi_0$. (b) A spatiotemporally gyrating relativistic electron beam equilibrium.

Two additional constants of the unperturbed motion are

$$\xi = \phi - \omega_c t = \phi - \frac{\Omega_c}{\gamma_0} t, \quad (6)$$

and

$$\zeta = \phi - \omega_c \frac{z}{\beta_{z0}} = \phi - \frac{m\Omega_c}{p_{z0}} z. \quad (7)$$

Using (3), we express χ as the following linear combination of ξ and ζ :

$$\chi = \frac{\omega_0}{\omega_c} \xi + \left(1 - \frac{\omega_0}{\omega_c}\right) \zeta. \quad (8)$$

If $\omega_0 = \omega_c$ in (8), then $\chi = \xi = \phi - \omega_c t$. In this case, the equilibrium distribution $[f_0(p_\perp, p_z, \chi) = f_0(p_\perp, p_z, \xi)]$ in (4)

does not depend on z , and we refer to it as the time-dependent equilibrium distribution. If $\omega_0 = 0$ in (8), then $\chi = \zeta = \phi - \omega_c z/v_{z0}$. In this case, the equilibrium distribution $[f_0(p_\perp, p_z, \chi) = f_0(p_\perp, p_z, \zeta)]$ in (4) does not depend on t , and we refer to it as the axial-dependent equilibrium distribution.

At each instant of time, there is a z -dependent distribution of phase angles given by (3) and (4). Each point on a surface of constant z will contain the same distribution of values of ϕ . As time progresses, a surface with a given distribution will move with a normalized phase velocity $\beta_p = dz/cdt$ obtained by differentiating (3) with respect to t at constant ϕ . This phase velocity is

$$\beta_p = \frac{\omega_0 \beta_{z0}}{\omega_0 - \omega_c}, \quad (9)$$

where $\beta_{z0} = v_{z0}/c$. Making use of (9), we can also express χ as $\chi = \phi - \omega_c (\beta_{z0} - \beta_p)^{-1} (z/c - \beta_p t)$, which is a single-particle constant of motion. We see that β_p is infinite for the time-dependent equilibrium distribution ($\omega_0 = \omega_c$), and that $\beta_p = 0$ for the axial-dependent equilibrium distribution ($\omega_0 = 0$).

III. DISPERSION RELATION

A stability analysis of systems with the time-dependent and axial-dependent equilibrium distribution functions has been carried out in Ref. 7. In that analysis, Fourier transforms are taken of the Vlasov and Maxwell equations in order to derive relations obeyed by the Fourier transforms of the perturbed electric field components. For the case of definite values of $p_z = p_{z0}$ and $p_\perp = p_{\perp 0}$, these are algebraic equations of the form

$$D(ck, \omega) E(ck, \omega) = 0, \quad (10)$$

where D is a three-by-three dispersion matrix and E is a three-component vector. The components of E are the Fourier transforms of the perturbed electric field components, $E_{1-} = E_{1x} - iE_{1y}$, $E_{1+} = E_{1x} + iE_{1y}$, and E_{1z} . Respectively, these represent the right-hand circularly polarized (RHP) radiative field, the left-hand circularly polarized (LHP) radiative field, and the longitudinal electric field. The dispersion relation for the system perturbations is given by

$$\det D(ck, \omega) = 0. \quad (11)$$

It is shown in Appendix A that any spatiotemporal equilibrium distribution with $|\beta_p| < 1$ can be obtained from a Lorentz transformation of the axial-dependent equilibrium distribution, and that any spatiotemporal equilibrium distribution with $|\beta_p| > 1$ can be obtained from a Lorentz transformation of the time-dependent equilibrium distribution. Consequently, a stability analysis of systems with spatiotemporal equilibrium distributions is obtained from Lorentz transformations of (10) and (11). Results for $|\beta_p| < 1$ and $|\beta_p| > 1$ have the same analytic form and are assumed to extend to the case of $|\beta_p| = 1$.

The primary result of this paper (derived in Appendix B) is the dispersion relation for systems having definite values of $p_{\perp}=p_{\perp 0}$ and $p_z=p_{z0}$. In terms of the dimensionless wavenumber k and the dimensionless frequency ω , defined by

$$\begin{aligned} k &= \frac{ck}{\omega_c}, \\ \omega &= \frac{\omega}{\omega_c}, \end{aligned} \quad (12)$$

the dispersion relation can be expressed as

$$\begin{aligned} M_{--}(k, \omega) M_{++}(k, \omega) M_{zz}(k, \omega) &= \frac{1}{2} \left(\frac{\omega_p^2}{\omega_c^2} \right)^2 \beta_{\perp 0}^2 |s_1|^2 \{ (\beta_{z0} \omega - k)^2 M_{++}(k, \omega) + [\beta_{z0} (\omega - 2\beta_p k_0) - (k - 2k_0)]^2 M_{--}(k, \omega) \} \\ &+ \frac{1}{4} \left(\frac{\omega_p^2}{\omega_c^2} \right)^2 \beta_{\perp 0}^4 |s_2|^2 [\omega (\omega - 2\beta_p k_0) - k(k - 2k_0)]^2 M_{zz}(k, \omega) - \frac{1}{4} \left(\frac{\omega_p^2}{\omega_c^2} \right)^3 \beta_{\perp 0}^4 (s_2 s_{-1}^2 + s_{-2} s_1^2) [\omega (\omega - 2\beta_p k_0) \\ &- k(k - 2k_0)] [\beta_{z0} (\omega - 2\beta_p k_0) - (k - 2k_0)] (\beta_{z0} \omega - k), \end{aligned} \quad (13)$$

which is a tenth-degree polynomial equation in either k or ω . In Eq. (13),

$$\begin{aligned} M_{--}(k, \omega) &= (\omega^2 - k^2)(\omega - k\beta_{z0} - 1)^2 \\ &- \frac{\omega_p^2}{\omega_c^2} (\omega - k\beta_{z0})(\omega - k\beta_{z0} - 1) \\ &+ \frac{1}{2} \frac{\omega_p^2}{\omega_c^2} \beta_{\perp 0}^2 (\omega^2 - k^2), \\ M_{++}(k, \omega) &= [(\omega - 2\beta_p k_0)^2 - (k - 2k_0)^2](\omega - k\beta_{z0} - 1)^2 \\ &- \frac{\omega_p^2}{\omega_c^2} (\omega - k\beta_{z0} - 2)(\omega - k\beta_{z0} - 1) \\ &+ \frac{1}{2} \frac{\omega_p^2}{\omega_c^2} \beta_{\perp 0}^2 [(\omega - 2\beta_p k_0)^2 - (k - 2k_0)^2], \\ M_{zz}(k, \omega) &= (\omega - k\beta_{z0} - 1)^2 - \frac{\omega_p^2}{\omega_c^2} (1 - \beta_{z0}^2). \end{aligned} \quad (14)$$

Moreover, $\omega_p^2 = 4\pi n_0 e^2 / \gamma_0 m$, $\beta_{\perp 0} = p_{\perp 0} / \gamma_0 m c$,

$$k_0 = ck_0 / \omega_c = (\beta_p - \beta_{z0})^{-1}, \quad (15)$$

and

$$s_n = \int_0^{2\pi} d\chi \Phi(\chi) \exp(-in\chi). \quad (16)$$

Notice that $\beta_p k_0 = \omega_0 / \omega_c - 1$, where ω_0 is defined in (1).

The dispersion relation in (13) is invariant under the transformation

$$\begin{aligned} k &\rightarrow -k^* + 2k_0, \\ \omega &\rightarrow -\omega^* + 2\beta_p k_0. \end{aligned} \quad (17)$$

Under the transformation in (17), the $\Re(k), \Re(\omega)$ plane is inverted through the point $(k_0, \beta_p k_0)$, and $\Im(k)$ and $\Im(\omega)$

are unchanged. Consequently, a plot of $\Im(\omega)$ as a function of real k is unchanged by reflection through the vertical line $k = k_0$.

It follows from (A15) of Appendix B that the eigenmodes of the dispersion matrix for the case of a spatiotemporal equilibrium distribution are given in terms of the electric field by

$$\begin{aligned} \mathbf{E}(z, t) &= e^{i(kz - \omega t)} [2^{-1/2} E_{1-}(k, \omega) \hat{\mathbf{e}}_+ \\ &+ 2^{-1/2} E_{1+}(k - 2k_0, \omega - 2\omega_0) \hat{\mathbf{e}}_- e^{-2i(k_0 z - \omega_0 t)} \\ &+ E_{1z}(k - k_0, \omega - \omega_0) \hat{\mathbf{e}}_z e^{-i(k_0 z - \omega_0 t)}], \end{aligned} \quad (18)$$

where $\hat{\mathbf{e}}_{\pm} = 2^{-1/2} (\hat{\mathbf{e}}_x \pm i\hat{\mathbf{e}}_y)$, and

$$\mathbf{E}(k, \omega) = \begin{pmatrix} E_{1-}(k, \omega) \\ E_{1+}(k - 2k_0, \omega - 2\beta_p k_0) \\ E_{1z}(k - k_0, \omega - \beta_p k_0) \end{pmatrix}. \quad (19)$$

For positive $\Re(k)$, $E_{1-}(k, \omega)$ and $E_{1+}(k, \omega)$ are Fourier transforms of the right-hand circularly polarized (RHP) and the left hand circularly polarized (LHP) radiation fields, respectively. [These polarization assignments are reversed for negative $\Re(k)$.] The transform $E_{1z}(k, \omega)$ is that of the longitudinal electric field.

IV. NUMERICAL EXAMPLES

In all of the following numerical examples, the value chosen for $\Phi(\chi)$ in (4) is

$$\Phi(\chi) = \lim_{\epsilon \rightarrow 0} \delta(\chi - \epsilon), \quad 0 \leq \chi \leq 2\pi. \quad (20)$$

Consequently, all equilibrium electrons with the same z and t have the same phase ϕ . For these distributions, a system is stable for sufficiently large magnitudes of real k . The corresponding Fourier components in (16) are $s_1 = s_2 = 1$. In all

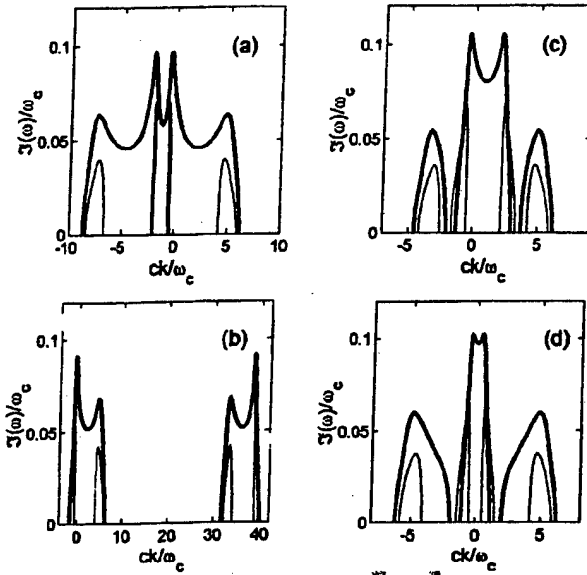


FIG. 3. Plots of $\mathcal{I}(\omega) = \mathcal{I}(\omega)/\omega_c$ vs $k = ck/\omega_c$ (real) for equilibrium parameters $\gamma_0 = 2$, $\omega_p^2/\omega_c^2 = 0.05$, $\alpha_0 = 0.4$, and $s_1 = s_2 = 1/2$. The corresponding value of $\beta_{x0} = 0.79766$. Values of the normalized phase velocity β_p and k_0 are (a) $\beta_p = 0$ ($\omega_0 = 0$) and $k_0 = -1.2537$, (b) $\beta_p = 0.85$ ($\omega_0 = 16.24\omega_c$) and $k_0 = 19.11$, (c) $\beta_p = 2$ ($\omega_0 = 1.663\omega_c$) and $k_0 = 0.8317$, and (d) $\beta_p = \infty$ ($\omega_0 = \omega_c$) and $k_0 = 0$. Wide lines indicate that instability is due to coupling of a cyclotron mode. Narrow lines indicate that instability is due to coupling of an electrostatic mode.

examples, $\omega_p^2/\omega_c^2 = 0.05$ and $\alpha_0 = 0.4$, where $\alpha_0 = \tan^{-1}(p_{10}/p_{x0})$ is the equilibrium pitch angle.

Figure 3 shows growth-rate curves $[\mathcal{I}(\omega) = \mathcal{I}(\omega)/\omega_c]$ vs $k = ck/\omega_c$ with k real for a system with $\gamma_0 = 2.0$ (and the corresponding real axial velocity $\beta_{x0} = 0.7977$). The resonance condition for the cyclotron maser instability is satisfied at $k = (1 - \beta_{x0})^{-1} = 4.94$. Plots are shown for several values of the normalized phase velocity β_p . Figures 3(a) and 3(d) refer, respectively, to the axial-dependent ($\beta_p = 0$ or $\omega_0 = 0$) and time-dependent ($\beta_p = \infty$ or $\omega_0 = \omega_c$) distributions. The corresponding values of $k_0 = (\beta_p - \beta_{x0})^{-1}$ in (15) are -1.254 and 0 , respectively. Figure 3(c) pertains to $\beta_p = 2.0$ (or $\omega_0 = 1.663\omega_c$) with $k_0 = 0.8317$, whereas Fig. 3(b) pertains to $\beta_p = 0.85$ (or $\omega_0 = 16.24\omega_c$) with $k_0 = 19.11$.

It is interesting to point out that the maximum growth rate for each of the nonisotropic phase distributions in Figs. 3(a)–3(d) is greater than the maximum growth rate for the corresponding gyrotropic relativistic electron beam, which is $\mathcal{I}(\omega) = 0.054$. (See Fig. 4 of Ref. 7.)

Reference to Fig. 3 shows that maximum growth rates and growth rates at the resonance value $k = 4.94$ are not very sensitive to the value of the phase velocity β_p . On the other hand, the range of values of k for which instability exists may be very sensitive to values of β_p . [A corresponding sensitivity of the range of unstable frequencies is present because, for unstable modes, $\Re(\omega) \approx \beta_{x0}k$ when $k \gg 1$.] In particular, instability of a RHP radiative component will occur at large values of k [and of $\Re(\omega)$] if $k_0 = (\beta_p - \beta_{x0})^{-1}$ is

large in magnitude. This effect is illustrated in Fig. 3(b), where $k_0 = 19.11$. The effect is explained by first noting that instability is expected for values of k near the resonance k and second recalling (from the discussion at the end of Sec. III) that plots of $\mathcal{I}(\omega)$ versus real k are symmetric under reflection through k_0 . It is also a consequence of the fact [evident from (19)] that frequencies and wavenumbers of coupled waves in an eigenmode become greatly divergent for large k_0 .

In Fig. 3 and in the following, Figs. 4–9, both wide and narrow solid curves are employed. Detailed numerical calculations of roots of the dispersion relation in (13) show that the wide curves refer to modes whose instability, in the low wavenumber region ($k < k_0$), is due to coupling of the cyclotron mode with the electromagnetic modes with $\omega \pm ck = 0$. In the high wavenumber region ($k > k_0$), the instability is due to coupling of the cyclotron mode with the electromagnetic modes with $\omega - 2\beta_{x0}ck_0 \pm c(k - 2k_0) = 0$. The wide curves are characterized by $\omega - 2\beta_{x0}ck - \omega_c \approx 0$ over the entire k interval of instability. The narrow solid curves refer to modes whose instability is due to coupling of the electrostatic modes. They are characterized by $\omega - \beta_{x0}ck - \omega_c + (\omega_p/\omega_c)(1 - \beta_{x0}^2)^{1/2} \approx 0$ over intervals of instability with $k < k_0$ and $\omega - \beta_{x0}ck - \omega_c - (\omega_p/\omega_c)(1 - \beta_{x0}^2)^{1/2} \approx 0$ over intervals of instability with $k > k_0$.

Figures 4(a) and 4(b) are, respectively, plots of $\Re(\omega)$ vs k and of $\mathcal{I}(\omega)$ vs k over the interval of the upper- k growth-rate peak in Fig. 3(b). Coupled radiative components of the field amplitude eigenvector in (19) are $E_{1-}(k, \omega)$ and $E_{1+}(k - 2k_0, \omega - 2\beta_{x0}ck_0) = E_{1+}(k - 38.21, \omega - 32.48)$. Consequently, $E_{1-}(k, \omega)$ represents high-frequency, forward-traveling, RHP radiation, whereas $E_{1+}(k - 38.21, \omega - 32.48)$ represents low-frequency radiation in the k interval in Fig. 4. It is evident from Fig. 4(a) that the high-frequency radiation is slow-wave radiation (i.e., its wave phase velocity $c\omega/k$ is less than the speed of light).

It is of interest to determine the relative contributions of the high- and low-frequency components to the total Poynting flux. As a measure of the relative contribution of the high-frequency component to the total Poynting flux, we employ the Poynting flux ratio \mathcal{S}_R , defined by

$$\mathcal{S}_R = \frac{\langle S_{-z}(ck, \omega) \rangle}{\langle S_{-z}(ck, \omega) + S_{+z}(ck - 2ck_0, \omega - 2\beta_{x0}ck_0) \rangle}. \quad (21)$$

In the above equation, $\langle S_{-z}(ck, \omega) \rangle$ and $\langle S_{+z}(ck - 2ck_0, \omega - 2\beta_{x0}ck_0) \rangle$ are the time-averaged z components of the Poynting fluxes produced by the high-frequency and low-frequency electromagnetic components, respectively. [Because the low-frequency flux may be backward traveling for some intervals of k , the ratio \mathcal{S}_R may exceed one and will approach infinity when high- and low-frequency fluxes cancel.] An expression for \mathcal{S}_R as a function of k and ω is presented in (A31).

A plot of $\log_{10} \mathcal{S}_R$ vs k for the system of Figs. 3(b) and

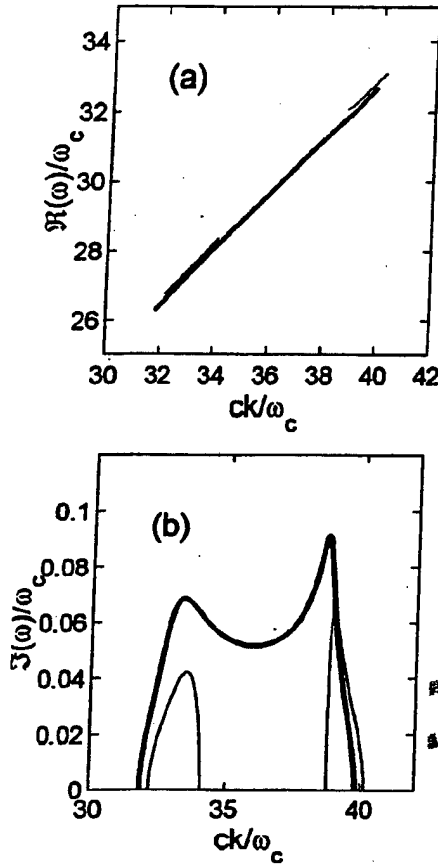


FIG. 4. Dispersion relations in the region of the higher- k growth peak for the system of Fig. 3(b), with equilibrium parameters $\gamma_0=2$, $\omega_p^2/\omega_c^2=0.05$, $\alpha_0=0.4$, $s_1=s_2=1$, and $\beta_p=0.85$ ($\omega_0=16.24\omega_c$). The corresponding values of β_{x0} and k_0 are 0.7977 and 19.11, respectively. Plots are (a) $\Re(\omega)/\omega_c$ vs $k=ck/\omega_c$ (real) for unstable modes, and (b) $\Im(\omega)/\omega_c$ vs k (real). Frequencies and wavenumbers refer to the component $E_-(ck, \omega)$. The second radiative component of the eigenvector is $E_+(ck-38.21\omega_c, \omega-32.48\omega_c)$. Wide lines indicate that instability is due to coupling of a cyclotron mode. Narrow lines indicate that instability is due to coupling of an electrostatic mode.

4 is presented in Fig. 5. We regard the high-frequency component as dominant if $S_R > \frac{1}{2}$ [i.e., if $\log_{10} S_R > -0.3010$]. Figure 5 shows that this condition is valid over the interval $37 < k < 40$, which corresponds to $30\omega_c < \Re(\omega) < 33\omega_c$ in Fig. 4(a). It is to be emphasized that these wavenumbers and frequencies greatly exceed the resonance frequency and wavenumber for the cyclotron maser instability ($\hat{\omega}=\hat{k}=4.94$). The frequency ω_0 (equal to $16.24\omega_c$ in this example) is exceeded by approximately a factor of 2.

The rapid variations in the value of S_R in the interval $37 < k < 40$ are explained as follows. Reference to (A29) shows that $S_{+z}(ck-2ck_0, \omega-2\beta_p ck_0)$ vanishes when $ck=2ck_0$ ($\hat{k}=38.21$) and when $\Re(\omega)=2\beta_p ck$ [$\Re(\hat{\omega})=32.48$ and $\hat{k}=39.6$ for the unstable branch associated with the highest maximum of the growth-rate peak in Fig. 4(b)]. At these values of \hat{k} , $\log_{10} S_R=0$. For values of \hat{k} between these zeros of the low-frequency flux, $S_{+z}(ck-2ck_0, \omega-2\beta_p ck_0)$ becomes negative, allowing $\log_{10} S_R$ to approach

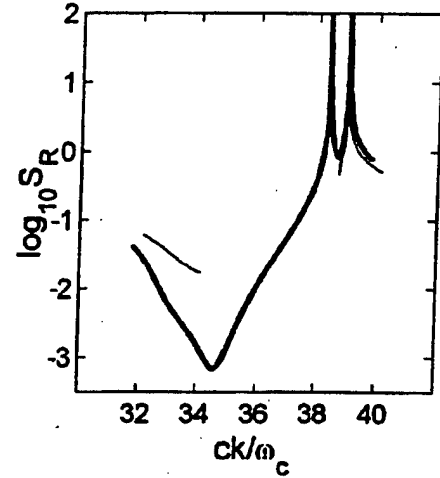


FIG. 5. Plots of the Poynting ratio S_R in (A31) vs $k=ck/\omega_c$ for unstable modes in the region of the higher- k growth peak for the system of Figs. 3(b), 4(a), and 4(b). Wide lines indicate that instability is due to coupling of a cyclotron mode. Narrow lines indicate that instability is due to coupling of an electrostatic mode.

infinity when the high-frequency and low-frequency fluxes cancel.

Next we consider mildly relativistic systems with $\gamma_0=1.2$ and the corresponding $\beta_{x0}=0.50914$. Resonance for the cyclotron maser instability occurs at $\hat{\omega}=\hat{k}=2.037$. Figures 6(a) and 6(b) show growth-rate [$\Im(\hat{\omega})$ vs \hat{k}] curves for the cases of $\beta_p=0$ ($k_0=-1.9644$ and $\omega_0=0$) and $\beta_p=0.67580$ ($k_0=6$ and $\omega_0/\omega_c=4.0548$). From (19), coupled radiative modes for the case of $\beta_p=0$ [Fig. 6(a)] are $E_{1-}(k, \hat{\omega})$ and $E_{1+}(k+3.9288, \hat{\omega})$. Figure 7 is a plot of $\Re(\omega)$ vs k for unstable modes in this case. It is evident from this plot that the highest frequency of unstable modes is approximately $2.1\omega_c$.

In Figs. 8(a) and 8(b), we present, respectively, plots of $\Re(\omega)$ vs k and $\Im(\omega)$ vs k of unstable modes when $\beta_p=0.67580$ for the k interval of the large- k growth peak in Fig. 6(b). Coupled radiative components, obtained from (19), in this case are $E_{1-}(k, \hat{\omega})$ and $E_{1+}(k-12, \hat{\omega}-8.1096)$. From Fig. 8(a), it is evident that growing electromagnetic waves with frequencies of approximately $7\omega_c$ are present in this system.

Figure 9 is a plot of the logarithm of the Poynting ratio in (21) as a function of \hat{k} over the interval of \hat{k} in Fig. 8. It is evident that the high-frequency RHP flux dominates the low-frequency flux (i.e., $\log_{10} S_R > -0.3010$) over a very narrow interval in this case. Numerical results show this interval to be $11.987 \leq \hat{k} \leq 12.036$ with $7.079 \leq \Re(\hat{\omega}) \leq 7.103$. These values are much greater than the resonance values of $\hat{\omega}=\hat{k}=2.037$ given above for the cyclotron resonance maser instability. Moreover, the values $7.079 \leq \Re(\hat{\omega}) \leq 7.103$ are slightly less than twice the value $\omega_0/\omega_c=4.0548$.

The above and other numerical examples indicate that the width of the interval of relatively large high-frequency

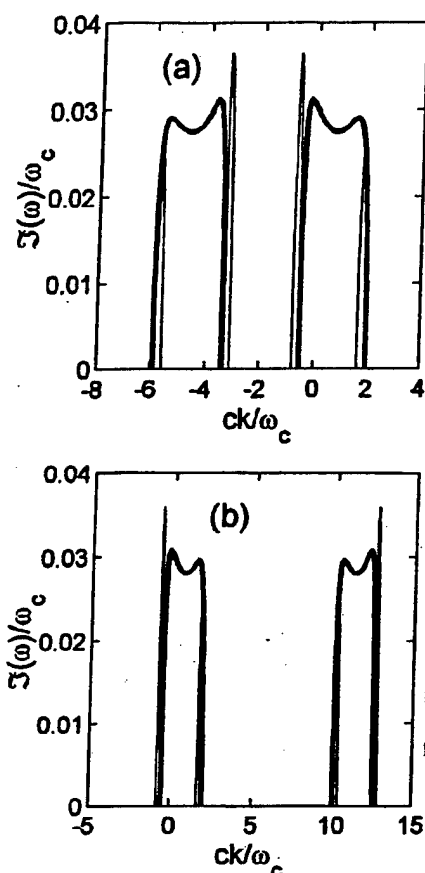


FIG. 6. Growth rate curves [$\Im(\omega)=\Im(\omega)/\omega_c$ vs $k=ck/\omega_c$ (real)] for the equilibrium parameters $\gamma_0=1.2$, $\omega_p^2/\omega_c^2=0.05$, $\alpha_0=0.4$, $s_1=s_2=1$, and the corresponding value $\beta_{x0}=0.5091$. In plot (a), $\beta_p=0$ ($\omega_0=0$) and $k_0=-1.964$; whereas in plot (b), $\beta_p=0.67580$ ($\omega_0=4.055\omega_c$) and $k_0=6$. Frequencies and wavenumbers refer to the component $E_-(ck, \omega)$. The second radiative component of the eigenvector in (19) is $E_+(ck - k_0\omega_c, \omega - \beta_p k_0\omega_c)$. Wide lines indicate that instability is due to coupling of a cyclotron mode. Narrow lines indicate that instability is due to coupling of an electrostatic mode.

flux decreases with increasing frequency (increasing k_0) and with decreasing γ_0 .

V. CONCLUSIONS

In Ref. 7, stability properties of an electron beam, propagating in a uniform magnetic field $\mathbf{B}_0=B_0\hat{\mathbf{e}}_z$, were analyzed under the constraint that all quantities depend spatially only on z . The equilibrium distribution in the phase angle ϕ of \mathbf{p}_\perp was assumed to be nonrandom, and two distributions were considered. These were the time-dependent distribution in which the distribution depends on ϕ through the constant of the unperturbed motion $\xi=\phi-\omega_c t$ and the axial-dependent distribution in which the distribution depends on ϕ through the constant of the unperturbed motion, $\zeta=\phi-\omega_c z/v_{z0}$. In this paper the analysis has been extended to spatiotemporal distributions, which depend on the constant of the unper-

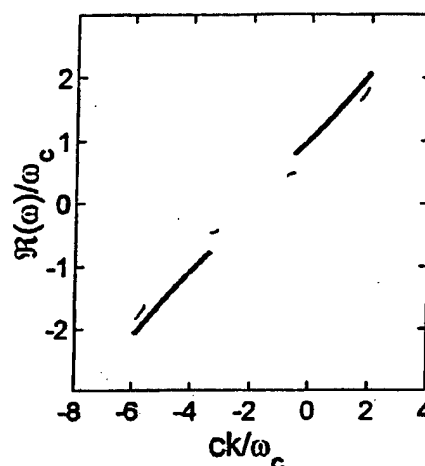


FIG. 7. Plot of $\Re(\omega)$ vs k (real) for unstable modes of the system of Fig. 6(a). Frequencies and wavenumbers refer to the component $E_-(ck, \omega)$. The second radiative component of the eigenvector in (19) is $E_+(ck + 3.929\omega_c, \omega)$. Wide lines indicate that instability is due to coupling of a cyclotron mode. Narrow lines indicate that instability is due to coupling of an electrostatic mode.

turbed motion $\chi=\phi-\omega_0 t+(\omega_0-\omega_c)z/v_{z0}$, defined in (3). This analysis is limited to equilibrium distributions [Eq. (4)] for which p_r and p_\perp have definite values.

By carrying out Lorentz transformations of the results of Ref. 7, we have obtained the dispersion relation in (13) for the spatiotemporal equilibrium distribution. The dispersion matrix is given in (A19)–(A21), and its eigenmodes (which describe the coupling of the RHP radiative, LHP radiative, and electrostatic waves) are given in (19). The parameters that define this spatiotemporal system are p_{r0} , $p_{\perp 0}$, ω_p^2/ω_c^2 , β_p , k_0 , and s_2 . The parameter β_p is the phase velocity of surfaces (normal to the z axis) upon which the equilibrium distribution $\rho(\chi)$ has a fixed form. The Fourier components s_1 and s_2 are given by (16). Once $\Phi(\chi)$ (and consequently s_1 and s_2) are fixed, the spatiotemporal distribution can still be changed by varying β_p , where $0 \leq |\beta_p| \leq \infty$.

Numerical computations indicate that the above variation in β_p has little effect on maximum growth rates or on the growth rate at the resonance frequency for the cyclotron-resonance maser instability. However, it has a strong effect on the range of real ω and real k of RHP radiation over which the system is unstable, and has a strong effect on the relative wavenumbers and frequencies of coupled RHP radiative, LHP radiative, and electrostatic waves. In particular, the distribution in (20) has been shown to result in unstable modes in which the RHP radiative component dominates over a relatively narrow frequency range at much higher frequencies than the resonance frequency for the cyclotron-maser instability. These high frequencies occur when the phase velocity β_p is close to the beam velocity β_{z0} . In such cases, these frequencies exceed ω_0 by approximately a factor of 2.

It is well known that the cyclotron maser instability in a gyrotropic beam is very sensitive to axial velocity spread if the instability occurs at a highly Doppler upshifted cyclotron frequency. The parameter regime of interest here is β_p

Belet 23, Sep. 22

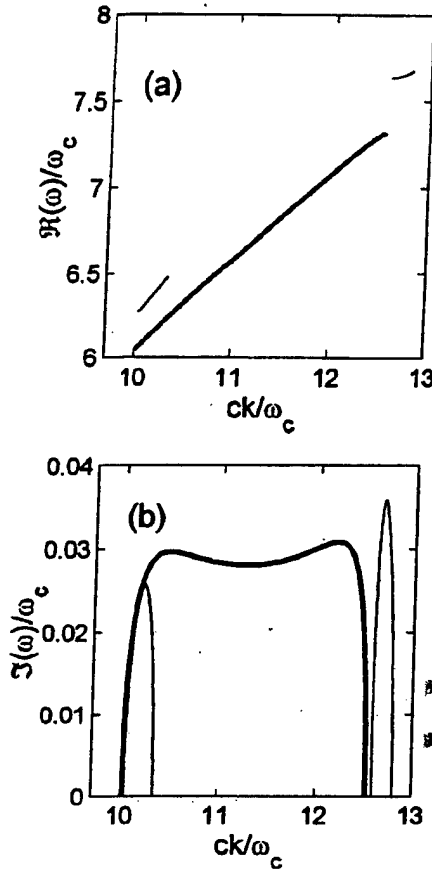


FIG. 8. Dispersion relations in the region of the higher- k growth peak for the system of Fig. 6(b), with equilibrium parameters $\gamma_0=1.2$, $\omega_p^2/\omega_c^2=0.05$, $\alpha_0=0.4$, $s_1=s_2=1$, and $\beta_p=0.6758$ ($\omega_0=4.055\omega_c$). The corresponding values of β_{z0} and k_z are 0.509 14 and 6, respectively. Plots are (a) $\Re(\omega)=\Re(\omega)/\omega_c$ vs $k=ck/\omega_c$ (real) for unstable modes, and (b) $\Im(\omega)$ vs k (real). Frequencies and wavenumbers refer to the component $E_-(ck, \omega)$. The second radiative component of the eigenvector in (19) is $E_+(ck-12\omega_c, \omega-8.110\omega_c)$. Wide lines indicate that instability is due to coupling of a cyclotron mode. Narrow lines indicate that instability is due to coupling of an electrostatic mode.

$=\beta_{z0}<1$. In this case, the dispersion relations for the system are a set of coupled integral equations if there is an axial momentum spread. [The integral equations are obtained by applying the Lorentz transformation to the integral equations in Eqs. (41)–(43) of Ref. 7.] We have begun an analysis of the properties of these integral equations in order to determine the degree to which thermal spread affects the instability reported in this paper.

ACKNOWLEDGMENTS

This work was supported in part by the Air Force Office of Scientific Research, Grants No. F49620-97-0325 and No. F49620-00-1-0007.

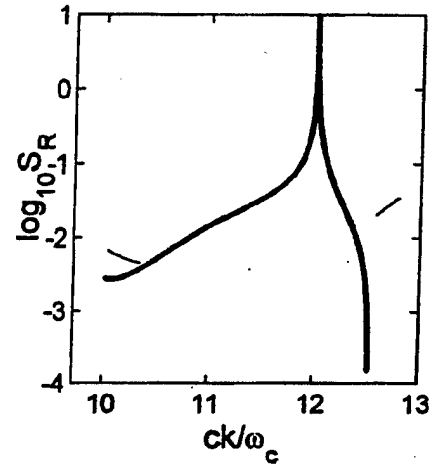


FIG. 9. Plots of the Poynting ratio S_R in (A31) versus $k=ck/\omega_c$ for unstable modes in the region of the higher- k growth peak for the system of Fig. 6(b). Wide lines indicate that instability is due to coupling of a cyclotron mode. Narrow lines indicate that instability is due to coupling of an electrostatic mode.

APPENDIX: DERIVATION OF DISPERSION RELATIONS AND THE POYNTING FLUX RATIO

1. Lorentz transformations of spatiotemporal equilibrium distributions

Consider a Lorentz transformation from an initial frame of reference S to a frame S' that moves with the normalized velocity β_u in the positive z direction relative to S . Under this transformation,

$$\begin{aligned} z' &= \gamma_u(z - \beta_u ct), & p'_{z0} &= \gamma_u(p_{z0} - \beta_u \gamma_0 mc), \\ ck' &= \gamma_u(ck - \beta_u \omega), \\ ct' &= \gamma_u(ct - \beta_u z), & \gamma_0 mc &= \gamma_u(\gamma_0 mc - \beta_u p_{z0}), \\ \omega' &= \gamma_u(\omega - \beta_u ck), \end{aligned} \quad (A1)$$

where $\gamma_u = (1 - \beta_u^2)^{-1/2}$. The quantities $\phi' = \phi$ and $p'_{\perp 0} = p_{\perp 0}$ are invariant under this transformation. The distribution function in (4) is also invariant. Expressed in terms of primed quantities, it is

$$\begin{aligned} f'_0(p'_\perp, p'_z, \chi) &= f_0(p_\perp, p_z, (p'_\perp, p'_z, \chi)) \\ &= n'_0 \frac{\delta(p'_\perp - p'_{\perp 0})}{p'_\perp} \delta(p'_z - p'_{z0}) \Phi(\chi), \end{aligned} \quad (A2)$$

where $n'_0 = n_0 \gamma'_0 / \gamma_0$.

Using (3) and the Lorentz transformations in (A1), we obtain the following expression for χ in terms of primed quantities:

$$\begin{aligned} \chi &= \frac{1}{\beta'_{z0} + \beta_u} \left(\frac{\omega'_0}{\omega'_c} \beta'_{z0} + \beta_u \right) \xi' + \frac{\beta'_{z0}}{\beta'_{z0} + \beta_u} \left(1 - \frac{\omega'_0}{\omega'_c} \right) \xi', \\ \xi' &= \phi - \omega'_c t', \end{aligned} \quad (A3)$$

$$\xi' = \phi - \omega'_c \frac{z'}{v'_{z0}}.$$

Quantities appearing in (A3) are $\omega'_c = eB_0/\gamma'_0 mc$ and $\omega'_0 = \omega_0/\gamma_u$. The phase velocity β'_p of surfaces of constant ϕ (or constant distribution in ϕ) relative to the reference frame S' is determined by differentiating (A3) with respect to t' at constant ϕ . The result, written in terms of both primed and unprimed quantities, is

$$\beta'_p = \frac{\omega'_0 \beta'_{x0} + \omega'_c \beta_u}{\omega'_0 - \omega'_c} = \frac{\omega_0(\beta_{x0} - \beta_u) + \omega_c \beta_u}{\omega_0(1 - \beta_u \beta_{x0}) - \omega_c}. \quad (\text{A4})$$

The transformation velocity β_u from a general reference frame S to a frame S' relative to which the distribution is time dependent is obtained by setting the coefficient of ξ' in (A3) equal to zero and solving for β_u . Expressing the result in terms of unprimed quantities and employing (9), we obtain

$$\beta_u = \frac{1}{\beta_p}. \quad (\text{A5})$$

Consequently, the transformation is possible if (relative to S) $|\beta_p| > 1$. Conversely, if a distribution is time dependent relative to S' , then $|\beta_p| > 1$ relative to any other reference frame S .

Similarly, the transformation velocity β_u from a general reference frame S to a frame S' relative to which the distribution is axial dependent is obtained by setting the coefficient of ξ' in (A3) equal to zero and solving for β_u . The result is

$$\beta_u = \beta_p. \quad (\text{A6})$$

Consequently, the transformation is possible if (relative to S) $|\beta_p| < 1$. Conversely, if a distribution is axial dependent relative to S' , then $|\beta_p| < 1$ relative to any other reference frame S .

2. Derivation of the dispersion matrix and eigenmodes

In the stability analysis of Ref. 7 for the time-dependent and axial-dependent equilibrium distributions, the Fourier transforms of the field components $E'(ck', \omega')$ were found to be related by matrix equations of the form

$$\mathbf{D}'(ck', \omega') \mathbf{E}'(ck', \omega') = 0, \quad (\text{A7})$$

where \mathbf{D}' is a three by three dispersion matrix and \mathbf{E}' is a three-component column matrix whose components are Fourier transforms of $E'_{1-} = E'_{1x} - iE'_{1y}$, $E'_{1+} = E'_{1x} + iE'_{1y}$, and E'_{1z} . The primes appear in these equations because the frame of reference in which the distribution is either time dependent or axial dependent is defined as the primed frame (S') in this treatment.

A. Derivation for the case of $|\beta_p| > 1$

The time-dependent equilibrium distribution function is given by (A2) with $\chi = \xi'$. From the discussion in Sec. 1 of this Appendix, it is clear that properties of a system with a spatiotemporal equilibrium distribution and $|\beta_p| > 1$ can be derived from Lorentz transformations of a system with a

time-dependent equilibrium distribution. It is shown in Ref. 7 that for the time-dependent equilibrium distribution the eigenmode $\mathbf{E}'(k', \omega')$ is of the form

$$\mathbf{E}'(ck', \omega') = \begin{pmatrix} E'_{1-}(ck', \omega') \\ E'_{1+}(ck', \omega' - 2\omega'_c) \\ E'_{1z}(ck', \omega' - \omega'_c) \end{pmatrix}, \quad (\text{A8})$$

where $\omega'_c = eB_0/\gamma'_0 mc$. The dispersion matrix for the time-dependent case is readily derived from (59) of Ref. 7. In order to determine stability properties of systems with spatiotemporal equilibrium distributions with phase velocities $|\beta_p| > 1$, it is necessary to apply the Lorentz transformation to the quantities appearing in (A7). Under the Lorentz transformation from S' to S (which travels with velocity $-\beta_u$ relative to S'), the electromagnetic fields (and their Fourier transforms) transform as

$$\begin{aligned} E_{1z} &= E'_{1z}, & B_{1z} &= B'_{1z}, \\ E_{1x} &= \gamma_u(E'_{1x} + \beta_u B'_{1y}), & B_{1x} &= \gamma_u(B'_{1x} - \beta_u E'_{1y}), \\ E_{1y} &= \gamma_u(E'_{1y} - \beta_u B'_{1x}), & B_{1y} &= \gamma_u(B'_{1y} + \beta_u E'_{1x}). \end{aligned} \quad (\text{A9})$$

From (19) and the Maxwell equation,

$$\frac{\partial}{\partial z'} E'_{1\pm}(z', t') = \pm \frac{\partial}{\partial t'} B'_{1\pm}(z', t'), \quad (\text{A10})$$

where $B'_{1\pm}(z', t') = B'_{1x}(z', t') \pm iB'_{1y}(z', t')$, we find that under the Lorentz transformation,

$$E_{1\pm}(ck, \omega) = \gamma_u \left(1 + \frac{\beta_u ck'}{\omega'} \right) E'_{1\pm}(ck', \omega'). \quad (\text{A11})$$

It follows from (A9) and (A11) that the transformation rule for the eigenvector $\mathbf{E}(ck', \omega')$ in (A7) and (A8) is

$$\mathbf{E}(ck, \omega) = \mathbf{L}(ck', \omega') \mathbf{E}'(ck', \omega'), \quad (\text{A12})$$

where

$$\mathbf{L}(ck', \omega') = \begin{pmatrix} \gamma_u \left(1 + \frac{\beta_u ck'}{\omega'} \right) & 0 & 0 \\ 0 & \gamma_u \left(1 + \frac{\beta_u ck'}{\omega' - 2\omega'_c} \right) & 0 \\ 0 & 0 & 1 \end{pmatrix} \quad (\text{A13})$$

and

$$\mathbf{E}(ck, \omega) = \begin{pmatrix} E_{1-}(ck, \omega) \\ E_{1+}(ck - 2\beta_u \gamma_u \omega'_c, \omega - 2\gamma_u \omega'_c) \\ E_{1z}(ck - \beta_u \gamma_u \omega'_c, \omega - \gamma_u \omega'_c) \end{pmatrix}. \quad (\text{A14})$$

Using (A5) and the Lorentz transformations in (A1), we can rewrite the arguments in the above expression entirely in terms of quantities pertaining to S to obtain

$$\mathbf{E}(ck, \omega) = \begin{pmatrix} E_{1-}(ck, \omega) \\ E_{1+}(ck - 2ck_0, \omega - 2\beta_p ck_0) \\ E_{1z}(ck - ck_0, \omega - \beta_p ck_0) \end{pmatrix} \quad (\text{A15})$$

where

$$ck_0 = \frac{\omega_c}{\beta_p - \beta_{z0}}. \quad (\text{A16})$$

By comparing (A7) and (A12), it is seen that the dispersion matrix in the unprimed (spatiotemporal) is given by

$$\mathbf{D}(ck, \omega) = \mathbf{L}(ck', \omega') \mathbf{D}'(ck', \omega') \mathbf{L}^{-1}(ck', \omega'). \quad (\text{A17})$$

An expression, obtained from (A1) and (A13), which is useful in the evaluation of (A17) is

$$\mathbf{L}^{-1}(ck', \omega') = \begin{pmatrix} \gamma_u \left(1 - \frac{\beta_u ck'}{\omega'}\right) & 0 & 0 \\ 0 & \gamma_u \left[1 - \beta_u \frac{ck' - 2\beta_u \gamma_u \omega'_c}{\omega' - 2\gamma_u \omega'_c}\right] & 0 \\ 0 & 0 & 1 \end{pmatrix} \quad (\text{A18})$$

The dispersion matrix for spatiotemporal equilibrium distributions is determined using (59) from Ref. 7, (A13), (A17), and (A18). When β_u is eliminated from the result by using (A5), we obtain

$$\mathbf{D}(ck, \omega) = \begin{pmatrix} D_{--}(ck, \omega) & -\eta_{-+} & -\eta_{-z} \\ -\eta_{+-} & D_{++}(ck - 2ck_0, \omega - 2\beta_p ck_0) & -\eta_{+z} \\ -\eta_{z-} & -\eta_{z+} & D_{zz}(ck - ck_0, \omega - \beta_p ck_0) \end{pmatrix} \quad (\text{A19})$$

The diagonal terms in the above equation are

$$\begin{aligned} D_{--}(ck, \omega) &= \omega^2 - c^2 k^2 - \frac{\omega_p^2}{2} \left[2 \left(\omega - \frac{kp_{z0}}{\gamma_0 m} \right) \right. \\ &\quad \times \left(\omega - \frac{kp_{z0}}{\gamma_0 m} \omega_c \right)^{-1} - \frac{p_{\perp 0}^2}{\gamma_0^2 m^2 c^2} \\ &\quad \left. \times (\omega^2 - c^2 k^2) \left(\omega - \frac{kp_{z0}}{\gamma_0 m} \omega_c \right)^{-2} \right] \\ D_{++}(ck - 2ck_0, \omega - 2\beta_p ck_0) &= (\omega - 2\beta_p ck_0)^2 - (ck - 2ck_0)^2 - \frac{\omega_p^2}{2} \\ &\quad \times \left[2 \left(\omega - \frac{kp_{z0}}{\gamma_0 m} - 2\omega_c \right) \left(\omega - \frac{kp_{z0}}{\gamma_0 m} \omega_c \right)^{-1} \right. \\ &\quad \left. - \frac{p_{\perp 0}^2}{\gamma_0^2 m^2 c^2} [(\omega - 2\beta_p ck_0)^2 - (ck - 2ck_0)^2] \right. \\ &\quad \left. \times \left(\omega - \frac{kp_{z0}}{\gamma_0 m} \omega_c \right)^{-2} \right] \\ D_{zz}(ck - ck_0, \omega - \beta_p ck_0) &= 1 - \omega_p^2 \left(1 - \frac{p_{z0}^2}{\gamma_0^2 m^2 c^2} \right) \left(\omega - \frac{kp_{z0}}{\gamma_0 m} \omega_c \right)^{-2}. \end{aligned} \quad (\text{A20})$$

The terms $D_{--}(ck, \omega)$, $D_{++}(ck, \omega)$, and $D_{zz}(ck, \omega)$ are, respectively, the dispersion functions for the RHP radiative field, the LHP radiative field, and the longitudinal electric field.

The off-diagonal elements of the dispersion matrix in (A19) are

$$\begin{aligned} \eta_{-+} &= -\frac{\omega_p^2}{2} s_2 \frac{p_{\perp 0}^2}{\gamma_0^2 m^2 c^2} \frac{\omega}{\omega - 2\beta_p ck_0} \\ &\quad \times [\omega(\omega - 2\beta_p ck_0) - ck(ck - 2ck_0)] \\ &\quad \times \left(\omega - \frac{kp_{z0}}{\gamma_0 m} \omega_c \right)^{-2}, \\ \eta_{+-} &= -\frac{\omega_p^2}{2} s_2 \frac{p_{\perp 0}^2}{\gamma_0^2 m^2 c^2} \frac{\omega - 2\beta_p ck_0}{\omega} \\ &\quad \times [\omega(\omega - 2\beta_p ck_0) - ck(ck - 2ck_0)] \\ &\quad \times \left(\omega - \frac{kp_{z0}}{\gamma_0 m} \omega_c \right)^{-2}, \\ \eta_{+z} &= -\omega_p^2 (\omega - 2\beta_p ck_0) s_{-1} \frac{p_{\perp 0}}{\gamma_0 mc} \\ &\quad \times \left[\frac{p_{z0}}{\gamma_0 mc} (\omega - 2\beta_p ck_0) - (ck - 2ck_0) \right] \\ &\quad \times \left(\omega - \frac{kp_{z0}}{\gamma_0 m} \omega_c \right)^{-2}, \\ \eta_{z-} &= -\frac{\omega_p^2}{2} \omega^{-1} s_{-1} \frac{p_{\perp 0}}{\gamma_0 mc} \left(\frac{p_{z0}}{\gamma_0 mc} \omega - ck \right) \\ &\quad \times \left(\omega - \frac{kp_{z0}}{\gamma_0 m} \omega_c \right)^{-2}, \end{aligned}$$

commas
should be
moved
right

$$\eta_{z+} = -\frac{\omega_p^2}{2}(\omega - 2\beta_p ck_0)^{-1} s_1 \frac{p_{\perp 0}}{\gamma_0 mc} \times \left[\frac{p_{z0}}{\gamma_0 mc} (\omega - 2\beta_p ck_0) - (ck - 2ck_0) \right] \times \left(\omega - \frac{kp_{z0}}{\gamma_0 m} - \omega_c \right)^{-2}. \quad (\text{A21})$$

In the above equation, $\omega_p^2 = 4\pi n_0 e^2 / \gamma_0 m$ is the relativistic plasma frequency squared. This quantity is invariant under Lorentz transformations. The quantities s_n are the Fourier series coefficients of $\Phi(\chi)$, defined by

$$s_n = \int_0^{2\pi} d\chi \Phi(\chi) \exp(-in\chi). \quad (\text{A22})$$

B. Derivation for the case of $|\beta_p| < 1$

Properties of systems having a spatiotemporal equilibrium distribution with phase velocity $|\beta_p|$ less than one are

$$L(ck', \omega') = \begin{pmatrix} \gamma_u \left(1 + \frac{\beta_u ck'}{\omega'} \right) & 0 & 0 \\ 0 & \gamma_u \left(1 + \beta_u \frac{ck' - 2\omega' \beta'_{z0}}{2\omega' \beta'_{z0}} \right) & 0 \\ 0 & 0 & 1 \end{pmatrix}. \quad (\text{A24})$$

The transformed eigenvector is obtained from (A12). When written in terms of β_u , the expression for this eigenvector differs from that in (A14). However, once (A6) is employed to set $\beta_u = \beta_p$, the expression for $E(ck, \omega)$ is the same as (A15). Consequently, (A15) gives the eigenmodes $E(ck, \omega)$ for spatiotemporal equilibrium distributions both for $|\beta_p| > 1$ and for $|\beta_p| < 1$.

Equation (A17) together with (A24) is used to obtain $D(ck, \omega)$, the dispersion matrix for the case of the spatiotemporal equilibrium distribution with $|\beta_p| < 1$. After (A6) is used to eliminate reference to β_u and the unprimed quantities are eliminated, the result is the same as that given by (A19)–(A21) for the case of $|\beta_p| > 1$. Consequently, (A19)–(A21) gives the dispersion matrix for the spatiotemporal equilibrium distribution for both the cases of $|\beta_p| > 1$ and of $|\beta_p| < 1$.

C. The case of $\beta_p = 1$

Equations (A15) for the eigenmodes and (A19)–(A21) are well behaved in the limit of $|\beta_p| = 1$. Consequently, we consider them to be valid when $|\beta_p| = 1$. The fact that $|\beta_p| = 1$ corresponds to $|\beta_u| = 1$ causes no difficulty, because such quantities as γ_0 , $p_{\perp 0}$, and p_{z0} are held fixed while the limit is taken.

To summarize, for all $-\infty < \beta_p < \infty$, the dispersion matrix for the case of spatiotemporal equilibrium distributions is given by (A19)–(A21) and the eigenmodes are of the form

determined by carrying out Lorentz transformations of results for the axial-dependent equilibrium distribution. The axial-dependent equilibrium distribution (for definite values of $p'_{\perp 0}$ and p'_{z0}) is attained by setting $\chi = \zeta'$ in (A2). In this case, the dispersion matrix D' in (A7) is readily obtained from (90) of Ref. 7. The eigenmode E' in (A7), given by (91) of Ref. 7, is

$$E'(ck', \omega') = \begin{pmatrix} E'_{1-}(ck', \omega') \\ E'_{1+} \left(ck' + 2 \frac{\omega'_c}{\beta'_{z0}}, \omega' \right) \\ E'_{1z} \left(ck' + \frac{\omega'_c}{\beta'_{z0}}, \omega' \right) \end{pmatrix}. \quad (\text{A23})$$

Equation (A12) governs the Lorentz transformation of the eigenvector from S' (the frame of the axial-dependent equilibrium distribution) to S (the frame of the spatiotemporal equilibrium distribution). From (A1), (A9), and (A11), it is seen that now the transformation matrix L is given by

given by (A15). The dispersion relation in (13) is obtained by setting the determinant of the matrix in (A19) equal to zero. It can also be obtained by substituting Lorentz transformed quantities into the dispersion relations in (69) and (100) of Ref. 7 and replacing the transformation velocity with the appropriate function of β_p .

3. Derivation of the Poynting flux ratio

In the analysis of the numerical results in Sec. IV, we employed the Poynting flux ratio \mathcal{S}_R in (21), which is the magnitude of the ratio of the x component of the average Poynting flux of the RHP radiation field to the z component of the average total Poynting flux. For a single eigenmode (A15) of the dispersion matrix in (A19), the Poynting flux vector is

$$\mathbf{S} = \frac{c}{4\pi} \Re(\mathbf{E}) \times \Re(\mathbf{B}), \quad (\text{A25})$$

where

$$\begin{aligned} \mathbf{E}(z, t) = & \hat{\mathbf{e}}_+ 2^{-1/2} E_{1-}(ck, \omega) \exp(ikz - i\omega t) + \hat{\mathbf{e}}_- 2^{-1/2} \\ & \times E_{1+}(ck - 2ck_0, \omega - 2\beta_p ck_0) \exp[i(k - 2k_0)z \\ & - i(\omega - 2\beta_p ck_0)t] + \hat{\mathbf{e}}_z E_{1z}(ck - ck_0, \omega - \beta_p ck_0) \\ & \times \exp[i(k - k_0)z - i(\omega - \beta_p ck_0)t], \end{aligned} \quad (\text{A26})$$

with

$$\hat{e}_{\pm} = 2^{-1/2}(\hat{e}_x \pm i\hat{e}_y). \quad (A27)$$

The application of the Maxwell equation in (A10) yields

$$\begin{aligned} B(\mathbf{x}, t) = & \hat{e}_+ 2^{-1/2} B_{1-}(ck, \omega) \exp(ikz - i\omega t) \\ & + \hat{e}_- 2^{-1/2} B_{1+}(ck - 2ck_0, \omega - 2\beta_p ck_0) \\ & \times \exp[i(k - 2k_0)z - i(\omega - 2\beta_p ck_0)t], \end{aligned}$$

where

$$\begin{aligned} B_{1-}(ck, \omega) = & -i \frac{ck}{\omega} E_{1-}(ck, \omega), \\ B_{1+}(ck - 2ck_0, \omega - 2\beta_p ck_0) = & i \frac{(ck - 2ck_0)}{(\omega - 2\beta_p ck_0)} E_{1+}(ck - 2ck_0, \omega - 2\beta_p ck_0). \end{aligned} \quad (A28)$$

Substituting (A27) and (A28) into the z component of (A25), averaging the result over the time interval $T = \pi/(\Re(\omega) - \beta_p ck_0)$, and assuming that

$$|2\pi\Im(\omega)| \ll |\Re(\omega) - \beta_p ck_0|, \quad (A29)$$

we obtain the time-averaged z component of the Poynting vector $\langle S_z \rangle$. The result is

$$\begin{aligned} \langle S_z \rangle = & \frac{c}{8\pi} \exp[2\Im(\omega)t] \left[ck \frac{\Re(\omega)}{|\omega|^2} \frac{1}{2} E_{1-}(ck, \omega) \right. \\ & \times E_{1-}^*(ck, \omega) + (ck - 2ck_0) \frac{[\Re(\omega) - 2\beta_p ck_0]}{|\omega - 2\beta_p ck_0|^2} \\ & \times \frac{1}{2} E_{1+}(ck - 2ck_0, \omega - 2\beta_p ck_0) \\ & \left. \times E_{1+}^*(ck - 2ck_0, \omega - 2\beta_p ck_0) \right] \end{aligned} \quad (A30)$$

It follows from (A30) that the value of the Poynting flux ratio S_R in (21) is

$$\begin{aligned} S_R = & \left| \frac{\langle S_{-z}(ck, \omega) \rangle}{\langle S_{-z}(ck, \omega) + S_{+z}(ck - 2ck_0, \omega - 2\beta_p ck_0) \rangle} \right| \\ = & |ck \Re(\omega) | \omega - 2\beta_p ck_0 |^2 [|\omega|^2 (ck - 2ck_0) \\ & \times (\Re(\omega) - 2\beta_p ck_0) RR^* + ck \Re(\omega) | \omega - 2\beta_p ck_0 |^2]^{-1} \end{aligned} \quad (22)$$

$$\begin{aligned} = & |ck \Re(\omega) | \omega - 2\beta_p ck_0 |^2 [|\omega|^2 (ck - 2ck_0) \\ & \times (\Re(\omega) - 2\beta_p ck_0) RR^* + ck \Re(\omega) | \omega - 2\beta_p ck_0 |^2]^{-1}, \end{aligned} \quad (A31)$$

where

$$R = \frac{E_{1+}(ck - 2ck_0, \omega - 2\beta_p ck_0)}{E_{1-}(ck, \omega)}. \quad (A32)$$

The amplitude ratio in (A32) is obtained from the amplitude (eigenvector) equation in (12). The flux ratio in (A31) can exceed one and may approach infinity at particular values of k .

¹R. C. Davidson, *Physics of Nonneutral Plasmas* (Addison-Wesley, Reading, MA, 1990), Chap. 7.

²R. O. Twiss, *Aust. J. Phys.* **11**, 564 (1958).

³J. Schneider, *Phys. Rev. Lett.* **2**, 504 (1959).

⁴A. V. Gapunov, *Izv. Vyssh. Uchebn. Zaved., Radiofiz.* **2**, 837 (1959).

⁵J. L. Hirshfield and J. M. Wachtel, *Phys. Rev. Lett.* **2**, 533 (1964).

⁶K. E. Kreischer, T. Kimura, B. G. Danly, and R. J. Temkin, *Phys. Plasmas* **4**, 1907 (1997).

⁷J. A. Davies and C. Chen, *Phys. Plasmas* **5**, 3416 (1998).

⁸A. Fruchtman and L. Friedland, *J. Appl. Phys.* **53**, 4011 (1982).

⁹A. Fruchtman and L. Friedland, *IEEE J. Quantum Electron.* **19**, 327 (1983).

¹⁰A. Fruchtman, *Phys. Fluids B* **4**, 4101 (1992).

¹¹H. P. Freund, J. Q. Dong, C. S. Wu, and L. C. Lee, *Phys. Fluids* **30**, 3106 (1987).

¹²T. H. Kho, A. T. Lin, and L. Chen, *Phys. Fluids* **31**, 3120 (1988).

¹³C. Chen, J. A. Davies, G. Zhang, and J. Wurtele, *Phys. Rev. Lett.* **69**, 73 (1992).

¹⁴C. Chen, B. G. Danly, G. Shevets, and J. S. Wurtele, *IEEE Trans. Plasma Sci.* **20**, 149 (1992).

¹⁵S. S. Kuo, D. B. McDermott, N. C. Luhmann, and K. R. Chu, *IEEE Trans. Plasma Sci.* **18**, 343 (1990).

¹⁶J. L. Hirshfield, *Phys. Rev. A* **44**, 6845 (1991); **46**, 1561 (1992).

¹⁷A. K. Ganguly and J. L. Hirshfield, *Phys. Rev. Lett.* **70**, 291 (1993); *Phys. Rev. E* **47**, 4364 (1993).

¹⁸J. A. Davies and C. Chen, *Intense Microwave Pulses V*, Proceedings of the SPIE, edited by B. Brandt, 1999, Vol. 3702, p. 88.

¹⁹C. Chen, *Phys. Rev.* **46**, 6654 (1992).

²⁰M. A. LaPointe, R. B. Yoder, C. Wang, A. K. Ganguly, and J. L. Hirshfield, *Phys. Rev. Lett.* **76**, 2718 (1996).

²¹R. Pakter, R. Schneider, and B. Rizzato, *Phys. Rev. E* **49**, 1594 (1994).

²²S. R. de Groot, W. A. van Leeuwen, and Ch. G. van Weert, *Relativistic Kinetic Theory* (North-Holland, Amsterdam, New York, 1980), p. 4.

²³R. C. Davidson and P. H. Yoon, *Phys. Rev. A* **39**, 2534 (1989).

ELECTRON BEAM HALO FORMATION IN HIGH-POWER PERIODIC PERMANENT MAGNET FOCUSING KLYSTRON AMPLIFIERS

R. Pakter and C. Chen

**Plasma Science and Fusion Center
Massachusetts Institute of Technology
Cambridge, Massachusetts 02139**

ABSTRACT

Electron beam halo formation is studied as a potential mechanism for electron beam losses in high-power periodic permanent magnet focusing klystron amplifiers. In particular, a two-dimensional self-consistent electrostatic model is used to analyze equilibrium beam transport in a periodic magnetic focusing field in the absence of radio-frequency signal, and the behavior of a high-intensity electron beam under a current-oscillation-induced mismatch between the beam and the periodic magnetic focusing field. Detailed simulation results are presented for choices of system parameters corresponding to the 50 MW, 11.4 GHz periodic permanent magnet (PPM) focusing klystron experiment performed at the Stanford Linear Accelerator Center (SLAC). It is found from the self-consistent simulations that sizable halos appear after the beam envelope undergoes several oscillations, and that the residual magnetic field at the cathode plays an important role in delaying the halo formation process.

Keywords: halo formation, klystron, periodic permanent magnet focusing, and microwave source.

I. INTRODUCTION

One of the main thrusts in high-power microwave (HPM) research is to overcome the problem of radio-frequency (RF) pulse shortening [1,2]. Several mechanisms of RF pulse shortening have been proposed [3], ranging from plasma formation at various locations in the device to nonlinear effects at the RF output section [4-7]. However, few of them have been fully verified in terms of theory, simulation and experiment. In this paper, we discuss halos around high-intensity electron beams as a mechanism by which electron beam loss and subsequent plasma formation may occur in high-power klystron amplifiers.

From the point of view of beam transport in a periodic or uniform solenoidal focusing field, there are two main processes for halo formation in high-intensity electron beams. One process is caused by a mismatch in the root-mean-square (rms) beam envelope [8], and the other is due to a mismatch in the electron phase-space distribution [9]. Both processes can occur when the beam intensity is sufficiently high so that the electron beam becomes space-charge-dominated. The purpose of this paper is to show that the former is responsible for electron beam halos in high-power klystron amplifiers.

For a periodic solenoidal focusing channel with periodicity length S and vacuum phase advance σ_0 , a *space-charge-dominated electron beam* satisfies the condition [8]

$$\frac{SK}{4\sigma_0\epsilon} = 2.9 \times 10^{-5} \frac{1}{\sigma_0} \left(\frac{S}{\epsilon_n} \right) \frac{I_b}{\gamma_b^2 \beta_b^2} > 1, \quad (1)$$

where $K = 2e^2 N_b / \gamma_b^3 \beta_b^2 m c^2$ is the normalized self-field perveance, I_b is the electron beam current in amperes, $\epsilon_n = \gamma_b \beta_b \epsilon$ is the normalized rms emittance in meter-radians, and S is in meters. In the expressions for the self-field perveance K and the normalized rms emittance ϵ_n , N_b is the number of electrons per unit axial length, m and $-e$ are the electron rest mass and charge, respectively, c is the speed of light in *vacuo*, and $\gamma_b = (1 - \beta_b^2)^{-1/2}$ is the characteristic relativistic mass factor for the electrons. The emittance is essentially the beam radius times a measure of randomness in the transverse electron motion. For a uniform density beam with radius a and temperature T_b , the normalized rms emittance ϵ_n is given by

$$\epsilon_n = \gamma_b \beta_b \epsilon = \frac{a}{2} \left(\frac{\gamma_b k_B T_b}{m c^2} \right)^{1/2}, \quad (2)$$

where k_B is the Boltzmann constant.

In particular, we study equilibrium beam transport in a periodic magnetic focusing field in the absence of RF signal and the behavior of a high-intensity electron beam under a current-oscillation-induced mismatch between the beam and the periodic magnetic focusing field, using a two-dimensional self-consistent electrostatic model. Detailed simulation results are presented for choices of system parameters corresponding to the 50 MW, 11.4 GHz periodic permanent magnet (PPM) focusing klystron experiment [10] performed at the Stanford Linear Accelerator Center (SLAC). It is found from the self-consistent simulations that sizable halos appear after the beam envelope undergoes several oscillations, and that the residual magnetic field at the cathode plays an important role in delaying the halo formation process.

The paper is organized as follows. In Section II, a two-dimensional self-consistent model is presented for transverse electrostatic interactions in a high-intensity relativistic electron beam propagating in a periodic focusing magnetic field. In Section III, the equilibrium state for intense electron beam propagation through a PPM focusing field is discussed, the equilibrium (well-matched) beam envelope is determined, and self-consistent simulations of equilibrium beam transport are performed. In Section IV, the effects of large-amplitude charge-density and current oscillations on inducing mismatched beam envelope oscillations are discussed, and use is made of the model presented in Section II to study the process of halo formation in a high-intensity electron beam. The results are compared with the SLAC PPM focusing klystron amplifier experiment. In Section V, conclusions are given.

II. MODEL AND ASSUMPTIONS

We consider a high-intensity relativistic electron beam propagating with axial velocity $\beta_b c \hat{e}_z$ through the periodic focusing magnetic field

$$\vec{B}^{\text{ext}}(x, y, s) = B_z(s) \hat{e}_z - \frac{1}{2} B_z'(s) (x \hat{e}_x + y \hat{e}_y), \quad (3)$$

where $s = z$ is the axial coordinate, $x \hat{e}_x + y \hat{e}_y$ is the transverse displacement from the z -axis, $B_z(s + S) = B_z(s)$, S is the fundamental periodicity length of the focusing field, and the prime denotes derivative with respect to s .

In the present two-dimensional analysis, we treat only the transverse electrostatic interactions in the electron beam. The effects of longitudinal charge-density and current oscillations in the electron beam, which are treated using the relativistic Lorentz equation and full Maxwell equations, will be considered in Section IV. For present purposes, we make the usual thin-beam approximation, assuming that (a) the Budker parameter is small, i.e., $e^2 N_b / \gamma_b mc^2 \ll 1$, (b) the beam is thin compared with the lattice period S , and (c) the electron motion in the transverse direction is nonrelativistic.

Under the thin beam approximation, the self-consistent electrostatic interactions in the electron beam can be described by a two-dimensional model involving N_p macroparticles (i.e., charged rods). In the Larmor frame, the transverse dynamics of the macroparticles is governed by [8,11]

$$\frac{d^2 x_i}{ds^2} + \kappa_z(s) x_i - \frac{e}{\gamma_b^3 \beta_b^2 mc^2} \frac{\partial}{\partial x_i} \phi^s(x_i, y_i, s) = 0, \quad (4)$$

$$\frac{d^2 y_i}{ds^2} + \kappa_z(s) y_i - \frac{e}{\gamma_b^3 \beta_b^2 mc^2} \frac{\partial}{\partial y_i} \phi^s(x_i, y_i, s) = 0, \quad (5)$$

where $i = 1, 2, \dots, N_p$, and the focusing parameter $\kappa_z(s)$ and self-field potential $\phi^s(x_i, y_i, s)$ are defined by

$$\kappa_z(s) = \left[\frac{e B_z(s)}{2 \gamma_b \beta_b mc^2} \right]^2 = \left[\frac{\Omega_c(s)}{2 \beta_b c} \right]^2, \quad (6)$$

$$\phi^s(x_i, y_i, s) = - \frac{e N_b}{N_p} \sum_{j=1(j \neq i)}^{N_p} \ln \left\{ \frac{[x_i - x_j]^2 + [y_i - y_j]^2}{[x_i - x_j r_w^2 / r_j^2]^2 + [y_i - y_j r_w^2 / r_j^2]^2} \right\}, \quad (7)$$

respectively. Here, $\Omega_c(s)$ is the (local) relativistic cyclotron frequency associated with the axial magnetic field $B_z(s)$, and $r_i \equiv (x_i^2 + y_i^2)^{1/2}$. The beam is assumed to propagate inside a perfectly conducting cylindrical tube of radius r_w , such that the self-field potential satisfies the boundary condition $\phi^s(r_i = r_w, s) = 0$. Detailed derivations of Eqs. (4)-(7) can be found in [8] for $r_w \rightarrow \infty$.

The two-dimensional self-consistent model described by Eqs. (4) and (5) will be used to simulate equilibrium beam transport in a PPM focusing field in the absence of RF signal (Section

III) and electron beam halo formation in the transverse direction induced by large-amplitude longitudinal current oscillations (Section IV).

III. EQUILIBRIUM BEAM TRANSPORT

In the absence of RF signal, the relativistic electron beam propagates through the focusing field in an equilibrium state. In this section, we discuss important properties of the equilibrium beam transport, and present results of our analysis and self-consistent simulations of periodically focused intense electron beam equilibria for choices of system parameters corresponding to those used in the SLAC 50 MW, 11.4 GHz PPM focusing klystron experiment [10].

A. Beam Envelope Equation for a Rigid-Rotor Vlasov Equilibrium

It has been shown previously [12,13] that one of the equilibrium states for the system described by Eqs. (4) and (5) is a rigid rotor Vlasov equilibrium in which the beam density is uniform transverse to the direction of beam propagation. The outermost beam radius $r_b(s) = r_b(s + S)$ obeys the envelope equation [12]

$$\frac{d^2 r_b}{ds^2} + \kappa_z(s) r_b - \frac{K}{r_b} - \frac{\langle \hat{P}_\theta \rangle^2}{r_b^3} - \frac{(4\varepsilon)^2}{r_b^3} = 0, \quad (8)$$

where $\gamma_b \beta_b m c \langle \hat{P}_\theta \rangle = \text{constant}$ is the macroscopic canonical angular momentum of the beam at $r = r_b(s)$, and ε is the unnormalized rms emittance associated with the random motion of the electrons. If there is no magnetic field at the cathode, then $\langle \hat{P}_\theta \rangle = 0$. Any residual magnetic field at the cathode will lead to $\langle \hat{P}_\theta \rangle \neq 0$.

We analyze the beam envelope for equilibrium beam transport in the SLAC 50 MW, 11.4 GHz PPM focusing klystron experiment [10]. The system parameters of the experiment are shown in Table 1. To examine the influence of small residual magnetic field on the beam transport, we analyze two different cases shown in Table 2. In Case I, we assume no residual magnetic field at the cathode, such that $\gamma_b \beta_b m c \langle \hat{P}_\theta \rangle = 0$. In Case II, however, a residual field of 6.86 G is assumed, corresponding to a beam with a finite canonical angular momentum given by $\gamma_b \beta_b m c \langle \hat{P}_\theta \rangle = 4.5 \times 10^{-26} \text{ Kgm}^2/\text{s}$. The following dimensionless parameters are derived from

Table 2: $S^2\kappa_z(s) = [1.04 \times \sin(2\pi s/S)]^2$ (with $S = 2.1$ cm), $\sigma_0 = 42.3^\circ = 0.738$, $SK/4\sigma_0\epsilon = 10.1$, and $\langle \hat{p}_\theta \rangle / 4\epsilon = 0.0$ in Case I and $\langle \hat{p}_\theta \rangle / 4\epsilon = 6.93$ in Case II.

Figure 1 shows plots of the axial magnetic field $B_z(s)$ and outermost beam radius $r_b(s)$ versus the propagation distance s for Cases I and II. In both cases, the amplitude of well-matched (equilibrium) envelope oscillations about the average beam radius is only about 0.005 mm, as seen in Figs. 1(b) and 1(c).

B. Self-Consistent Simulation of Equilibrium Beam Transport

Self-consistent simulations based on the model described in Sec. II are performed to further investigate the equilibrium beam transport. In the simulations, 4096 macroparticles are used. The macroparticles are loaded according to the rigid-rotor Vlasov distribution [12] with an initial beam radius equal to the equilibrium (matched) beam radius at $s = 0$ [see Figs. 1(b) and 1(c) for Cases I and II, respectively].

Figure 2 shows, respectively, the initial and final phase-space distributions at $s = 0.0$ cm and $s = 42.0$ cm for Case I. Comparing the phase-space plots shown in Figs. 2(e) and 2(f) with the initial phase-space plots in Figs. 2(b) and 2(c), we find an increase in the emittance (randomness) in the transverse electron momentum. The emittance growth is a result of numerical noise in the simulation. However, since the beam dynamics is mostly dictated by space-charge forces for the parameter regime considered here, the emittance growth has little effect on the beam transport properties. In fact, the distribution in the configuration space shown in Fig. 2(d) agrees very well with the initial distribution shown in Fig. 2(a). Moreover, the effective beam radius obtained from the simulation agrees with that obtained from Eq. (8) within 0.2%. In the simulation, no beam loss is detected.

Figure 3 shows, respectively, the initial and final phase-space distributions at $s = 0.0$ cm and $s = 42.0$ cm for Case II. The final distributions shown in Figs. 3(d), 3(e), and 3(f) agree very well with the initial distributions shown in Figs. 3(a), 3(b), and 3(c). In this case, the effects of numerical-noise-induced emittance growth are less pronounced than in Case I (Fig. 2) because the momentum distribution is primarily determined by the finite angular momentum but not by thermal

effects. The effective beam radius agrees with Eq. (8) within 0.5%, and no beam loss is detected in the simulation.

C. Phase Space Structure

It is known that the phase space structure for a matched intense beam in a periodic focusing system exhibits nonlinear resonances and chaotic behavior [14]. To determine how sensitive the equilibrium beam transport is against small perturbations for the parameter region of interest, we examine test-particle dynamics subject to the field configuration consisting of the applied focusing field and the equilibrium self-electric and self-magnetic fields. We make use of the Poincaré surface-of-section method to analyze the phase-space structure of test particles. The results are shown in Fig. 4(a) for Case I with $\hat{P}_0 / 4\epsilon = 0$, and in Fig. 4(b) for Case II with $\hat{P}_0 / 4\epsilon = -0.99$. In Fig. 4, the successive intersections of 15 test-particle trajectories with the phase space (r, P_r) are plotted every period of the focusing field for 1000 periods. One test particle is initialized at the phase-space boundary of the equilibrium distribution, and the corresponding test-particle orbit is represented by the inner curved arc in Fig. 4(a) and by the innermost contour in Fig. 4(b). The remaining test particles are initialized outside the beam. For both cases shown in Fig. 4, the values of \hat{P}_0 are chosen such that the boundary of the equilibrium distribution extends to $r = r_b$. Although the space-charge force outside the beam is nonlinear, the phase space is almost entirely regular. The same results showing regularity in phase space structure are obtained for different values of \hat{P}_0 for Cases I and II.

To summarize the results of this section briefly, we find from self-consistent simulations and detailed phase space analysis that in the absence of RF signal, the equilibrium beam transport in the PPM focusing klystron is robust and no beam loss is expected. These results are in good agreement with the experimental observation [10] of 99.9% beam transmission in the absence of RF signal.

IV. HALOS INDUCED BY MISMATCHED ENVELOPE OSCILLATIONS

Microwave generation in a klystron is due to the coupling of large-amplitude charge-density and current oscillations in the electron beam with the output RF cavity. The charge-density and

current oscillations result from the beating of the fast- and slow-space-charge waves on the electron beam, and are primarily longitudinal. From the point of view of beam transport, the charge-density and current oscillations perturb the equilibrium beam envelope discussed in Sec. III. Although a quantitative understanding of the effects of such large-amplitude charge-density and current oscillations on the dynamics of the electron beam is not available at present, especially in the transverse direction, a qualitative study of such effects is presented in this section. In the present analysis, use is made of the standard one-dimensional cold-fluid model to estimate the amplitude of the envelope mismatch induced by longitudinal current oscillations, and the two-dimensional electrostatic model described in Sec. II is used to explore the process of electron beam halo formation in the transverse phase space of the electron beam.

A. Estimation of the Mismatch Amplitude

It follows from the linearized continuity equation that the current perturbation $(\delta I_b)_{f,s}$ is related to the axial velocity perturbation $c(\delta\beta_b)_{f,s}$ by [15,16]

$$\frac{(\delta I_b)_{f,s}}{I_b} \equiv -\frac{\omega}{\omega - \beta_b c k_{f,s}} \frac{(\delta\beta_b)_{f,s}}{\beta_b}, \quad (9)$$

where subscripts f and s denotes the fast- and slow-space-charge waves, respectively, and ω and $k_{f,s}$ are the frequency and wave numbers of the perturbations, respectively. Making the long-wavelength approximation for a thin beam, it can be shown that the dispersion relations for the fast- and slow-space-charge waves can be expressed as [15]

$$\omega - \beta_b c k_{f,s} = \pm \frac{\sqrt{\epsilon_{sc}}}{\gamma_b \beta_b^2} \omega, \quad (10)$$

where k_f assumes plus sign, and k_s assumes minus sign. In Eq. (10), ϵ_{sc} is the longitudinal space-charge coupling parameter. The effective value of ϵ_{sc} is estimated to be $\epsilon_{sc} = 0.012$ for the SLAC PPM focusing klystron [10]. In the klystron, the total current oscillations are the sum of fast- and slow-space-charge waves with a phase difference of $\sim 180^\circ$. As a result, the total current oscillations and the total velocity oscillations are out of phase by $\sim 180^\circ$. Therefore, the amplitude of the total current oscillations is given by

$$\frac{(\delta I_b)_{total}}{I_n} \equiv -\frac{2\gamma_b \beta_b^2 (\delta \beta_b)_{total}}{\sqrt{\epsilon_{sc}} \beta_b}. \quad (11)$$

This has the important consequence that the perveance of the electron beam varies dramatically along the beam. From the definition of the perveance in Eq. (1), it is readily shown that the amplitude of perveance variation is given by

$$\frac{\delta K}{K} \equiv \left(1 + \frac{3\gamma_b \sqrt{\epsilon_{sc}}}{2\beta_b^2}\right) \frac{(\delta I_b)_{total}}{I_b}. \quad (12)$$

For the SLAC PPM focusing klystron [10], Eq. (12) yields $\delta K / K = 1.45 \times (\delta I_b)_{total} / I_b$. At the RF output section, $\delta K / K$ exceeds unity considerably because $\delta I_b / I_b \approx 1$. (Note that the current oscillations in the RF output section are highly nonlinear and the maximum current exceeds $2I_b$.) From the beam envelope equation (8), the relative amplitude of beam envelope mismatch is estimated to be $\delta r_b / r_b = 0.56$, where r_b is the equilibrium beam radius and $\delta I_b / I_b = 1$ is assumed. In the self-consistent simulations presented below, we use $\delta r_b / r_b = 1.0$ in order to take into account the fact that the instantaneous current exceeds $2I_b$ during high-power operation of the klystron.

B. Self-Consistent Simulation of Electron Beam Halo Formation

The process of halo formation in intense electron beams is studied using the two-dimensional self-consistent model described in Sec. II. Results of the simulations are summarized in Figs. 5-10 for Cases I and II. In the simulations, 4096 macroparticles are used, and the macroparticles are loaded according to the rigid-rotor Vlasov distribution [5] with an initial beam radius of $2r_b(0)$, where $r_b(0)$ is the equilibrium beam radius at $s = 0$ [see Figs. 1(b) and 1(c) for Cases I and II, respectively]. The effect of current oscillation build up in the PPM focusing klystron, which requires three-dimensional modeling, is not included in the present two-dimensional simulation.

We first discuss the results of the self-consistent simulation for Case I. In Fig. 5, the effective beam core radius is plotted as a function of the propagation distance s . The solid curve is obtained from the self-consistent simulation, and the dotted curve is obtained by numerically solving the envelope equation (8) with the emittance calculated in the self-consistent simulation.

As expected, results from the self-consistent simulation and envelope equation are in excellent agreement. Although the core radius oscillations are not exactly periodic due to emittance growth, the core radius oscillates with an approximate period of 11.5 cm, such that the envelope typically executes four periods of oscillations in the entire PPM focusing section of the SLAC PPM focusing klystron which is 42 cm long.

Figure 6 shows the phase-space distributions of the electrons at several axial distances during the fourth period of the beam core radius oscillation for Case I. In contrast to the equilibrium phase-space distribution (Fig. 3), significant halos appear at $s = 34.7, 37.8, 42.0, 44.1,$ and 46.2 cm. In the configuration space plots shown in Figs. 6(a) to 6(e) we observe a large variation in the beam core radius during the mismatched envelope oscillation period. The halo particles reach a maximum radius of $r_h = 6.4$ mm at $s = 42.0$ cm, where the beam core radius is a minimum and the traveling-wave RF output section is located. Around 1.5% of the electrons are found in the halo at that axial position. Because the maximum halo radius of $r_h = 6.4$ mm is greater than the actual beam tunnel radius $r_T = 4.7625$ mm, these halo electrons are lost to the waveguide wall. Therefore, the simulation results show that there will be 1.5% beam electron loss. In terms of beam power loss, 1.5% beam electron loss in the simulation corresponds to 0.2% beam power loss because the lost electrons have given up 88% of their kinetic energies (or have slowed down by about a factor of 2 in their axial velocities). The simulation results agree qualitatively with 0.8% beam power loss observed in the experiment [10]. The discrepancy between the simulation and experimental measurements may be caused by nonlinearities in the applied magnetic fields which are not included in the present simulation.

As the beam propagates in the focusing field, its distribution rotates clockwise in the $(x, dx/ds)$ phase space, as shown in Figs. 6(f) to 6(j). The particles are initially dragged into the halo at the edges of the phase space distribution, where a chaotic region is formed around an unstable periodic orbit that is located just outside the beam distribution [17]. The unstable periodic orbit is a result of a resonance between the mismatched core envelope oscillations and the particles dynamics. As the halo particles move away from the beam core, the influence of space charge forces decreases and these halo particles start rotating faster than the core particles, creating the S-shaped distributions observed in Figs. 6(f) to 6(j).

The halo formation is also observed in the $(x, dy/ds)$ phase space distributions shown in Figs. 6(k) to 6(o). Although the macroscopic (average) canonical angular momentum $\langle \hat{P}_\theta \rangle$ is constant in the simulation, the distributions presented in Figs. 6(k) to 6(o) indicate that the distribution of single particle canonical angular momenta induces spread in the $(x, dy/ds)$ phase space.

Shown in Fig. 7 are the halo radius, i.e., the maximum radius achieved by all of the macroparticles in the self-consistent simulation, and the effective beam core radius as a function of the propagation distance for Case I. It is apparent in Fig. 7 that the halo formation process takes place essentially during the first 4 periods of the envelope oscillations. After reaching $r_h = 6.4$ mm at $s = 42.0$ cm, the halo radius saturates. It is interesting to note that once the halo is developed, the halo radius and core envelope radius oscillate in opposite phase, with the former being maximum when the latter is minimum [as seen in Fig. 6(c)] and vice versa.

Second, we discuss the self-consistent simulation results for Case II and the role of small residual magnetic field at the cathode in the halo formation process. Figure 8 shows a plot of the effective beam core radius as a function of the propagation distance s . In Fig. 8, an excellent agreement is found between the envelope obtained from the self-consistent simulation (solid curve) and the envelope obtained by numerically solving the envelope equation (8) with the emittance calculated in the self-consistent simulation (dotted curve). One of the effects of the residual magnetic field at the cathode is to decrease the period of the envelope oscillations. The period for case II is 10.5 cm, slightly shorter than the period found in Case I (Fig. 5). The envelope executes four periods of oscillations in the entire PPM focusing section of the SLAC klystron.

Figure 9 shows the phase-space distributions of the electrons at several axial distances during the fourth period of the beam core radius oscillations for Case II. The configuration space distributions shown in Figs. 9(a) to 9(e) do not exhibit sizable halos. In particular, comparing Figs. 9(a)-9(e) with the configuration space distributions for Case I, shown in Figs. 6(a)-6(e), it is clear that the halos are much more pronounced in Case I. Analyzing Figs. 9(d) and 9(e) in more detail we observe hollow regions in the interior of the beam and that the existing halos appear in the form of vortices. Because the beam rotation period is calculated to be approximately 3 times the envelope oscillation period, the hollow regions and associated vortex structure might be a

result of a diocotron instability process driven by a resonance between the envelope oscillations and the beam rotation.

The properties of the phase space distributions shown in Figs. 9(f) to 9(o) resemble the properties discussed in Case I with regard to the rotation in the $(x, dx/ds)$ phase space and the spread in the $(x, dy/ds)$ phase space. In comparison with Case I, the main difference is that the phase space distributions in Case II exhibit vortex structures.

Figure 10 shows the halo radius and effective beam core radius as a function of the propagation distance for Case II. Although sizable halos arise in the simulation after many periods of envelope oscillations, it is evident that the halo formation process is slower in Case II than in Case I (see Fig. 7). In particular, despite that the initial beam radius in Case II is larger than in Case I, the halo radius in Case I is greater than that in Case II at the output section ($s = 42$ cm) of the PPM focusing klystron. Because the halo radius at $s = 40$ cm is 5.3 mm and is still greater than the beam tunnel radius, the electrons in the halo are lost to the waveguide wall. Nevertheless, these results indicate that a small residual magnetic field at the cathode plays an important role in delaying the halo formation process and might be used to prevent electron beam loss in future experiments.

V. CONCLUSIONS

We have studied equilibrium beam transport in a periodic magnetic focusing field in the absence of RF signal, and the behavior of a high-intensity electron beam under a current-oscillation-induced mismatch between the beam and the magnetic focusing field. Detailed simulation results were presented for choices of system parameters corresponding to the 50 MW, 11.4 GHz periodic permanent magnetic (PPM) focusing klystron experiment performed at the Stanford Linear Accelerator Center (SLAC).

From self-consistent simulations and detailed phase space analysis, we found that in the absence of RF signal, the equilibrium beam transport is robust, and that there is no beam loss, which is in agreement with experimental measurements. During the high-power operation of the klystron, however, we found that the current-oscillation-induced mismatch between the beam and the magnetic focusing field produces large amplitude envelope oscillations. We estimated the amplitude of envelope oscillations using a one-dimensional cold-fluid model. From self-consistent

simulations we found that for a mismatch amplitude equal to the beam equilibrium radius, the halo reaches 0.64 cm in size and contains about 1.5% of total beam electrons at the RF output section for a beam generated with a zero magnetic field at the cathode. Because the halo radius is greater than the actual beam tunnel radius, these halo electrons are lost to the waveguide wall, yielding 0.2% beam power loss. The simulation results agree qualitatively with 0.8% beam power loss observed in the experiment [10]. The discrepancy between the simulation and experimental measurements may be caused by nonlinearities in the applied magnetic fields which are not included in the present simulation.

We also studied the influence of a small residual magnetic field at the cathode on the equilibrium beam transport and electron beam halo formation during high-power operation of the klystron. We found that the equilibrium beam radius increases with the residual magnetic field. Although the halo grows in size to reach the waveguide wall the RF output section and a nonlinear vortex structure develops in the electron beam, we found that the onset of halo formation is delayed, which might be used to prevent electron beam loss in future experiments.

Although the results presented in this paper are based on a two-dimensional electrostatic model, they give a good qualitative description of the process of halo formation in high-power PPM focusing klystron amplifiers and suggest that halo formation is a potential mechanism for electron beam losses in such devices.

ACKNOWLEDGMENTS

This work was supported by the Air Force Office of Scientific Research, Grant No. F49620-97-1-0325, and in part by the Department of Energy, Office of High Energy and Nuclear Physics, Grant No. DE-FG02-95ER-40919.

REFERENCES

1. See, for example, *Special Issue on High-Power Microwave Generation*, edited by E. Schamiloglu and Y. Y. Lau, IEEE Trans. Plasma Sci., vol. 26, No. 3, June, 1998.
2. F. J. Agee, "Evolution of pulse shortening research in narrow band, high-power microwave sources," IEEE Trans. Plasma Sci., vol. 26, No. 3, pp. 235-245, 1998.
3. J. Benford and G. Benford, "Pulse shortening in high-power microwave sources," Proceedings of the 11th International Conference on High-Power Particle Beams, Institute of Plasma Physics, Academy of Science of the Czech Republic, 1996, p. 217.
4. K. J. Hendricks, P. D. Coleman, R. W. Lemke, M. J. Arman, and L. Bowers, "Extraction of 1 GW of rf power from an injection locked relativistic klystron oscillator," Phys. Rev. Lett., vol. 76, No. 1, pp. 154-157, Jan., 1996; and references therein.
5. M. D. Haworth, G. Baca, J. N. Benford, T. Englert, K. Hackett, K. J. Hendricks, D. Henley, M. LaCour, R. W. Lemke, D. Price, D. Ralph, M. Sena, D. Shiffler, and T. A. Spencer, "Significant pulse-lengthening in a multigigawatt magnetically insulated transmission line oscillator," IEEE Trans. Plasma Sci., vol. 26, No. 3, pp. 312-319, 1998.
6. F. Hegeler, C. Grabowski, and E. Schamiloglu, "Electron density measurements during microwave generation in a high-power backward-wave oscillator," IEEE Trans. Plasma Sci., vol. 26, No. 3, pp. 275-281, June, 1998.
7. D. Price, J. S. Levine, and J. N. Benford, "Diode plasma effects on the microwave pulse length from relativistic magnetrons," in *Intense Microwave Pulses V*, edited by H. E. Brandt, Proc. SPIE, vol. 3158, 1997, p. 13.
8. C. Chen and R. A. Jameson, "Self-consistent simulation studies of periodically focused intense charged-particle beams," Phys. Rev. E, vol. 52, No. 3, pp. 3074-3080, Sept., 1995.
9. Y. Fink, C. Chen, and W. P. Marable, "Halo formation and chaos in root-mean-square matched beams propagating through a periodic solenoidal focusing channel," Phys. Rev. E, vol. 55, No. 6, pp. 7557-7564, June, 1997.
10. D. Sprehn, G. Caryotakis, E. Jongewaard, and R. M. Phillips, "Periodic permanent magnetic development for linear collider X-band klystrons," Proc. XIX International Linac Conf., Argonne National Laboratory Report ANL-98/28, 1998, p. 689.

11. M. Hess, R. Pakter, and C. Chen, "Green's function description of space charge in intense charged-particle beams," Proceedings of 1999 Particle Accelerator Conference, 1999, p. 2752.
12. C. Chen, R. Pakter, and R. C. Davidson, "Rigid-rotor Vlasov Equilibrium for an intense charged-particle beam propagating through a periodic solenoidal magnetic field," Phys. Rev. Lett., vol. 79, No. 2, pp. 225-228, July, 1997.
13. R. C. Davidson and C. Chen, "Kinetic description of high-intensity beam propagation through a periodic focusing field based on the nonlinear Vlasov-Maxwell equations," Part. Accel., vol. 59, pp. 175-250, 1998.
14. C. Chen, R. Pakter, and R. C. Davidson, "Phase space structure for matched intense charged-particle beams in periodic focusing transport systems," Phys. Plasmas, vol. 6, No. 9, pp. 3674-3657, 1999.
15. C. Chen, G. Bekefi, and P. Catravas, "Growth and saturation of simulated beam modulation in a two-stream relativistic klystron amplifier," Appl. Phys. Lett., vol. 62, No. 14, pp. 1579-1581, April, 1993.
16. M. Friedman, J. Krall, Y. Y. Lau, and V. Serlin, "Efficient generation of multigigawatt rf power by a klystronlike amplifier," Rev. Sci. Instrum., vol. 61, No. 1, pp. 171-181, Jan., 1990.
17. R. L. Gluckstern, "Analytic model for halo formation in high-current ion linacs," Phys. Rev. Lett., vol. 72, No. 9, pp. 1247-1250, August, 1994.

Table 1. SLAC 50 MW, 11.4 GHz, PPM Focusing Klystron Experiment

Beam Current I_b	190 A
Beam Voltage	464 kV
Cathode Radius	2.86 cm
Cathode Temperature T_b	800° C [†]
Beam Radius	2.38 mm [†]
Pipe Radius	4.7625 mm
Total Tube Length	90.0 cm
Focusing Field Period Length	2.1 cm
PPM Focusing Section Length	42.0 cm
RMS Axial Magnetic Field	1.95 kG

[†] estimated

Table 2. System Parameters Used in the Simulation

BASIC PARAMETER	CASE I	CASE II
Beam Current I_b	190 A	190 A
Beam Voltage	464 kV	464 kV
Cathode Radius	2.86 cm	2.86 cm
Residual Magnetic Field at Cathode	0.0 G	6.86 G
Cathode Temperature T_b	800° C	800° C
Beam Radius	2.05 mm	2.38 mm
Pipe Radius	9.0 mm	9.0 mm
Total Tube Length	90.0 cm	90.0 cm
Focusing Field Period Length	2.1 cm	2.1 cm
PPM Focusing Section Length	42.0 cm	42.0 cm
RMS Axial Magnetic Field	1.95 kG	1.95 kG

FIGURE CAPTIONS

Figure 1. Plots of the axial magnetic field in (a) and outermost beam radius $r_b(s)$ versus the propagation distance s for equilibrium beam propagation corresponding to Case I in (b) and Case II in (c). The dimensionless parameters are: $S^2 \kappa_z(s) = [1.04 \times \sin(2\pi s/S)]^2$, $\sigma_0 = 42.3^\circ = 0.738$, $SK/4\sigma_0\epsilon = 10.1$, and $\langle \hat{P}_\theta \rangle / 4\epsilon = 0.0$ in (b) and $\langle \hat{P}_\theta \rangle / 4\epsilon = 6.93$ in (c).

Figure 2. Plots of the initial and final particle distributions at $s=0.0$ and 42.0 cm for the equilibrium beam corresponding to the parameters in Case I.

Figure 3. Plots of the initial and final particle distributions at $s=0.0$ and 42.0 cm for the equilibrium beam corresponding to the parameters in Case II.

Figure 4. Poincaré surface-of-section plots for 15 test particle trajectories under the influence of the PPM focusing field shown in Fig 1(a) and the self-electric and self-magnetic forces of the equilibrium beams. Shown in (a) is for Case I with single particle canonical angular momentum $\hat{P}_\theta = 0$, and in (b) for Case II with single particle canonical angular momentum $\hat{P}_\theta / 4\epsilon = -0.99$.

Figure 5. Plot of the effective beam core radius $r_b(s)$ versus the propagation distance s for mismatched beam propagation corresponding to Case I. The solid curve is obtained from the self-consistent simulation, whereas the dotted curve is obtained by numerically solving the envelope equation (8) with the emittance calculated in the self-consistent simulation.

Figure 6. Plots of particle distributions in phase space at $s = 34.7, 37.8, 42.0, 44.1$, and 46.2 cm for Case I.

Figure 7. Plots of the halo radius (solid curve) and core radius (dashed curve) as a function of the propagation distance s for Case I.

Figure 8. Plot of the effective beam core radius $r_b(s)$ versus the propagation distance s for mismatched beam propagation corresponding to Case II. The solid curve is obtained from the self-consistent simulation, whereas the dotted curve is obtained by numerically solving the envelope equation (8) with the emittance calculated in the self-consistent simulation.

Figure 9. Plots of particle distributions in phase space at $s = 31.5, 33.6, 36.8, 39.9$, and 42.0 cm for Case II.

Figure 10. Plots of the halo radius (solid curve) and core radius (dashed curve) as a function of the propagation distance s for Case II.

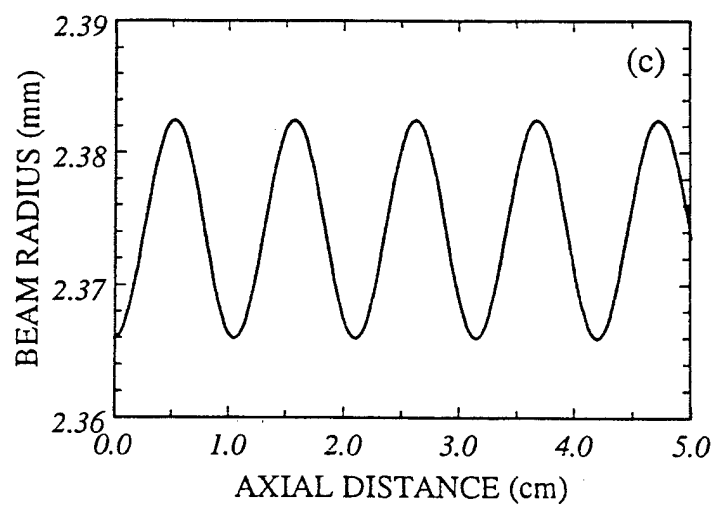
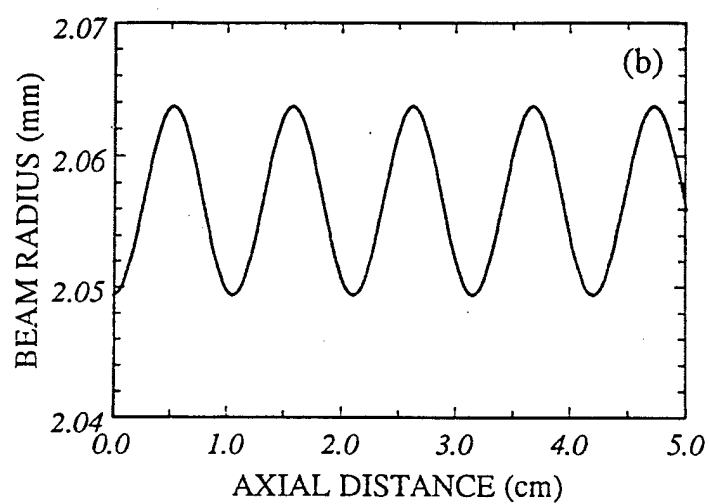
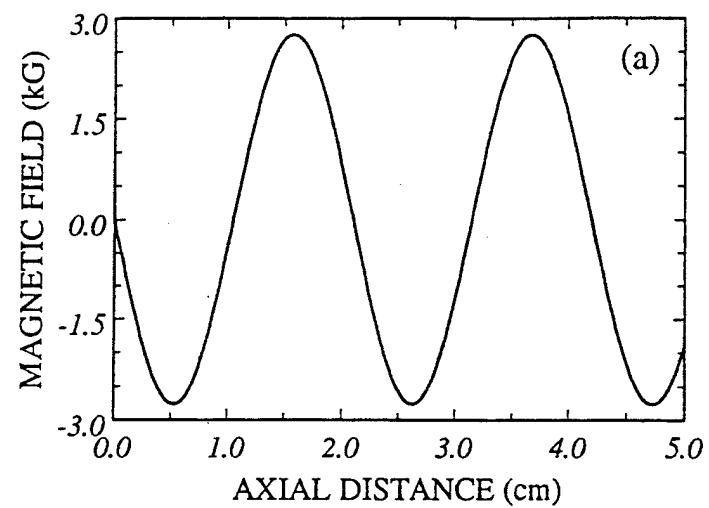


Fig. 1

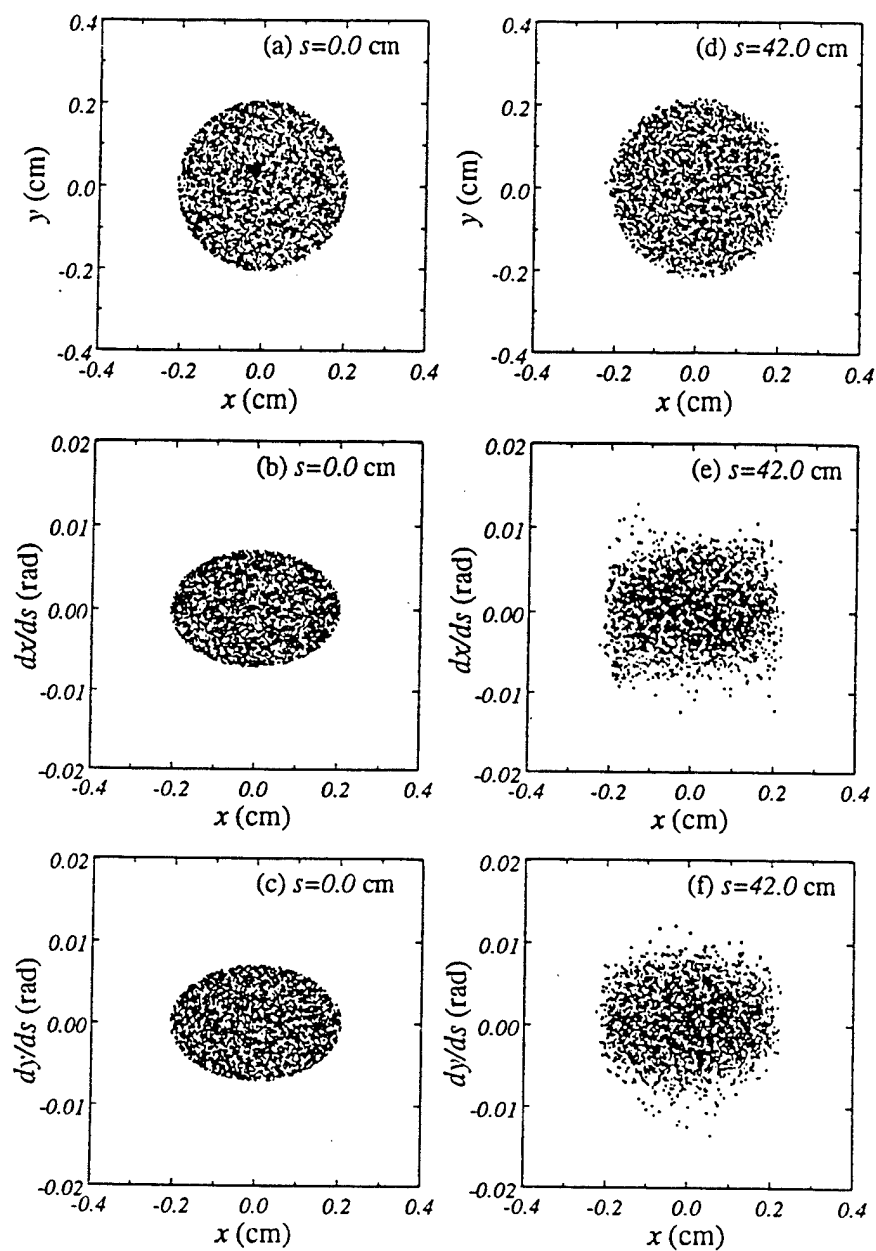


Fig. 2

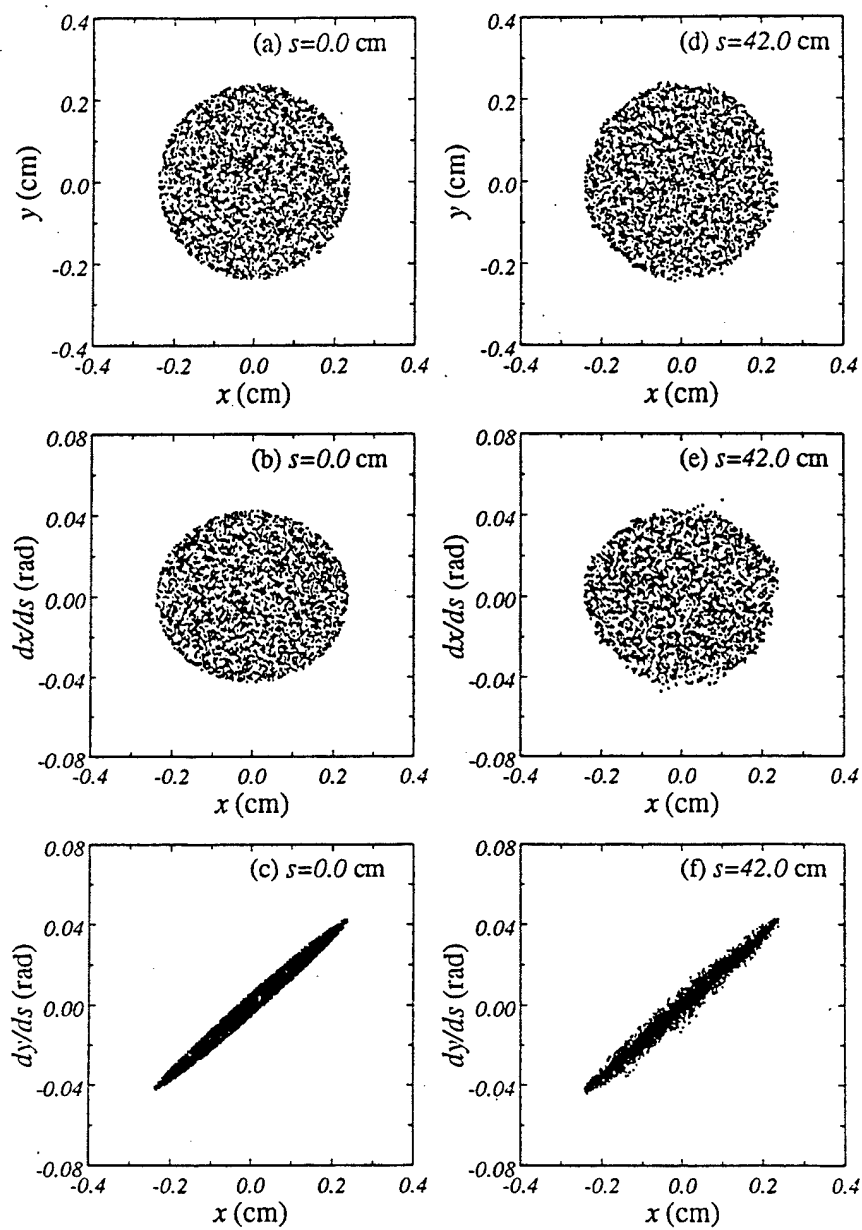


Fig. 3

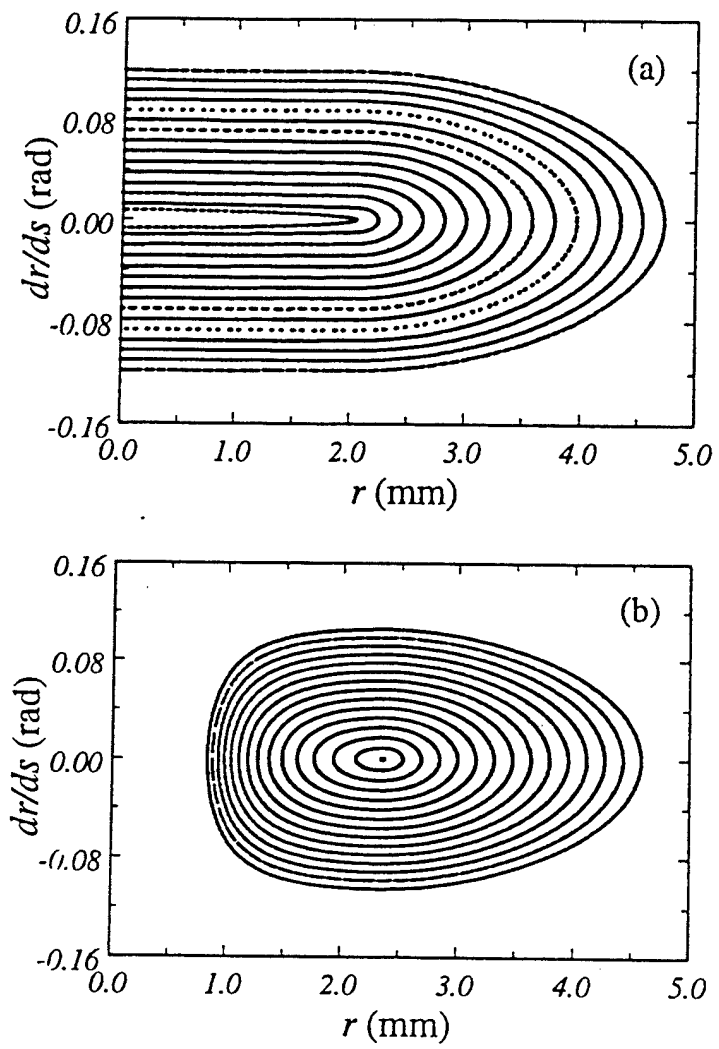


Fig. 4

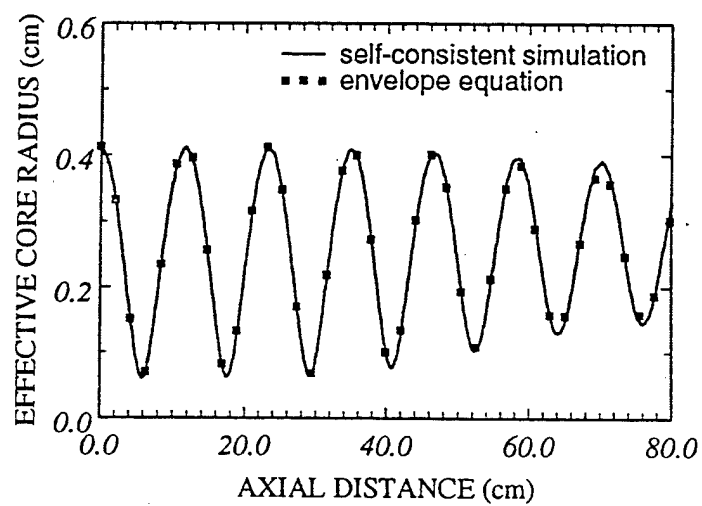


Fig. 5

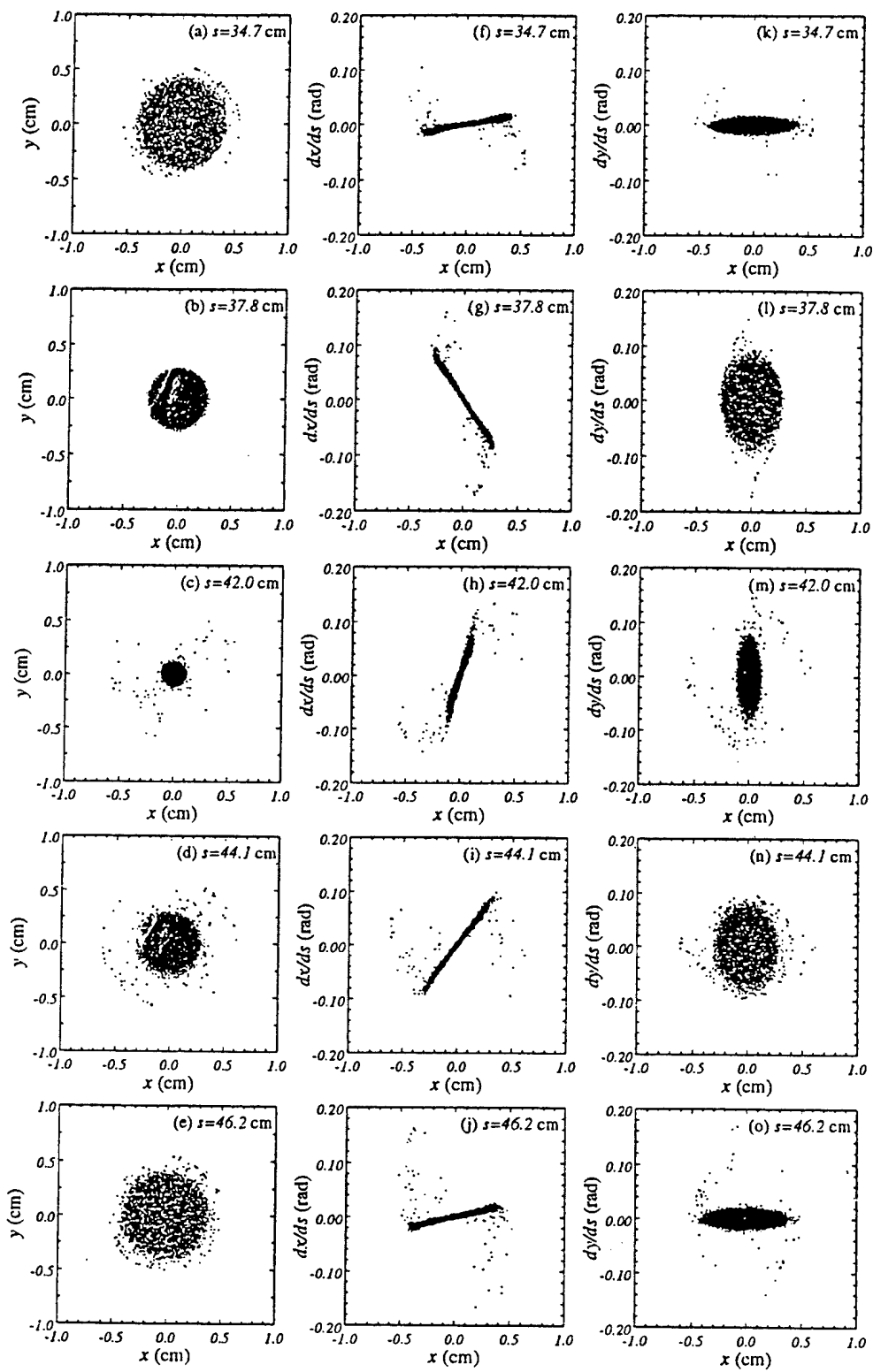


Fig. 6

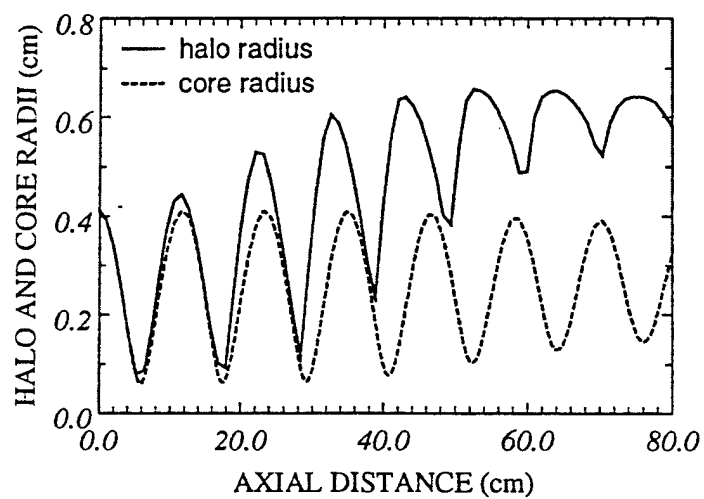


Fig. 7

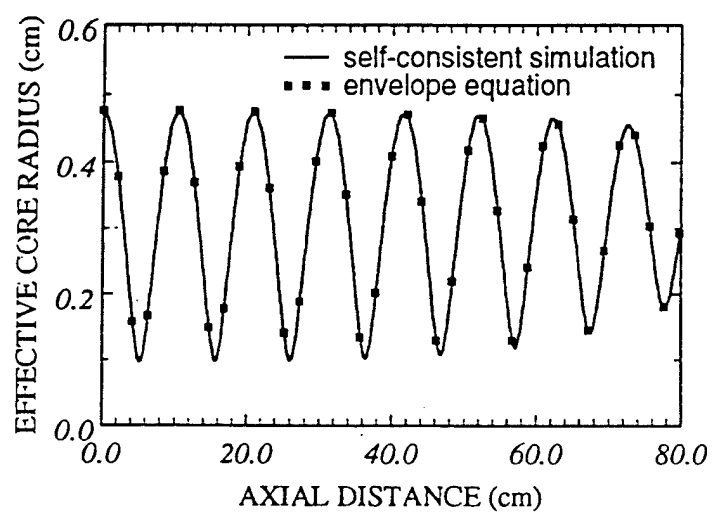


Fig. 8

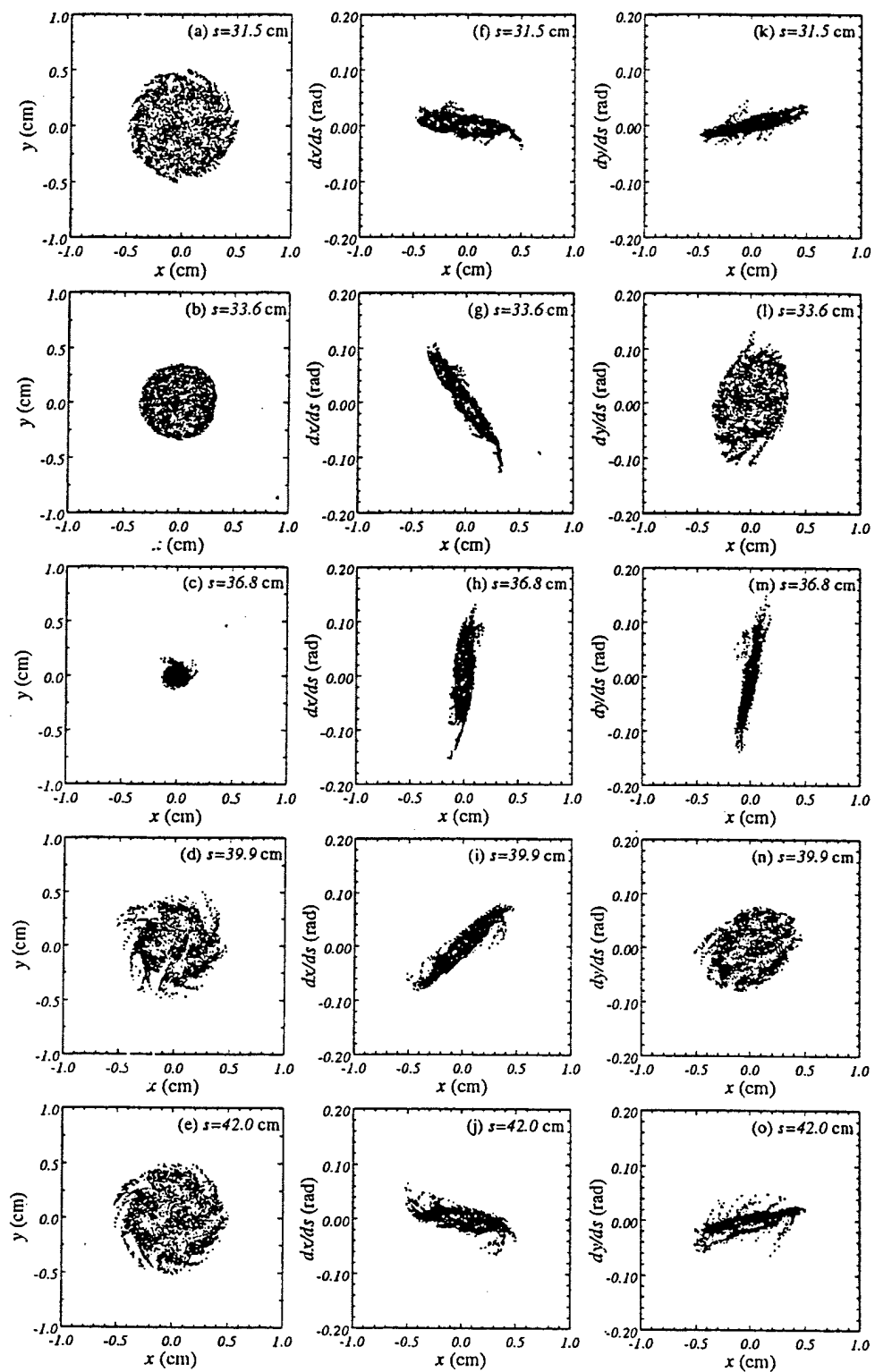


Fig. 9

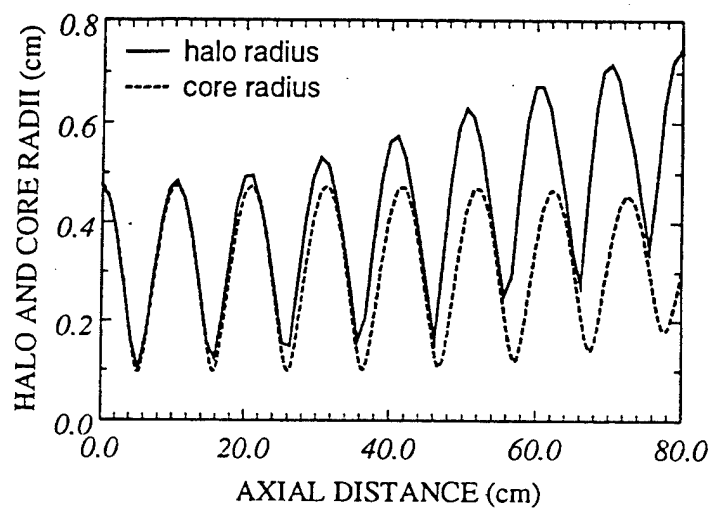


Fig. 10

Phase space structure for matched intense charged-particle beams in periodic focusing transport systems

Chiping Chen^{a)} and Renato Pakter

Plasma Science and Fusion Center, Massachusetts Institute of Technology, Cambridge, Massachusetts 02139

Ronald C. Davidson

Plasma Physics Laboratory, Princeton University, Princeton, New Jersey 08543

(Received 11 May 1999; accepted 15 June 1999)

Test particle motion is analyzed analytically and numerically in the field configuration consisting of the equilibrium self-electric and self-magnetic fields of a well-matched, thin, continuous, intense charged-particle beam and an applied periodic focusing solenoidal magnetic field. The self fields are determined self-consistently, assuming the beam to have a uniform-density, rigid-rotor Vlasov equilibrium distribution. Using the Hamilton–Jacobi method, the betatron oscillations of test particles in the average self fields and applied focusing field are analyzed, and the nonlinear resonances induced by periodic modulations in the self fields and applied field are determined. The Poincaré surface-of-section method is used to analyze numerically the phase-space structure for test particle motion outside the outermost envelope of the beam over a wide range of system parameters. For vacuum phase advance $\sigma_v = 80^\circ$, it is found that the phase-space structure is almost entirely regular at low beam intensity (phase advance $\sigma \geq 70^\circ$, say), whereas at moderate beam intensity ($30^\circ \leq \sigma \leq 70^\circ$), nonlinear resonances appear, the most pronounced of which is the third-order primary nonlinear resonance. As the beam intensity is further increased ($\sigma \lesssim 30^\circ$), the widths of the higher-order nonlinear resonances increase, and the chaotic region of phase space increases in size. Furthermore, the many chaotic layers associated with the separatrices of the primary and secondary nonlinear resonances are still divided by the remaining invariant Kolmogorov–Arnold–Moser surfaces, even at very high beam intensities. The implications of the rich nonlinear resonance structure and chaotic particle motion found in the present test-particle studies are discussed in the context of halo formation. © 1999 American Institute of Physics. [S1070-664X(99)03409-6]

I. INTRODUCTION

Halo formation and control in intense charged-particle beams has been the subject of recent vigorous theoretical, computational, and experimental investigations.^{1–20} It is of fundamental importance in the development of next-generation high-intensity accelerators for basic scientific research in high-energy and nuclear physics, as well as for a wide variety of applications ranging from heavy ion fusion, accelerator production of tritium, accelerator transmutation of nuclear waste, spallation neutron sources, and high-power free-electron lasers. In these high-intensity accelerators, beam halos must be controlled in order to minimize beam losses and activation of the accelerator structure.

It is well known that a space-charge-dominated beam can develop a sizable halo if there is a root-mean-square (rms) mismatch between the beam and the transport system.^{2–4,6,10–12} The mechanism for halo formation in rms-mismatched beams has been well developed in the particle-core model.^{3,6} When there is a sizable mismatch, the halo can contain a substantial fraction (up to 15%) of the entire beam.

Recently, it has been shown theoretically^{5,9,15,16} that in periodic focusing transport systems, radial nonuniformities in charge density in rms-matched space-charged-dominated

beams can also cause halo formation. The mechanism of halo formation in rms-matched beams has been identified with chaotic particle motion²¹ and nonlinear resonances occurring in the vicinity of the boundary of phase space occupied by the particles in the beam core. Invariant Kolmogorov–Arnold–Moser (KAM) surfaces²¹ play an important role in confining halo particles transverse to the direction of beam propagation.

The purpose of this paper is to analyze the dynamics of test particles in the field configuration consisting of the equilibrium self-electric and self-magnetic fields of a well-matched, thin, continuous, intense charged-particle beam and an applied periodic focusing solenoidal magnetic field. Unlike previous studies of halo formation in rms-mismatched beams and rms-matched beams with nonuniformities in charge density,^{1–20} this paper addresses the fundamental question of how the phase-space structure varies with beam intensity, focusing field strength and beam rotation under the best conditions corresponding to a matched equilibrium beam. Therefore, in the present analysis, the self fields²² are determined self-consistently, assuming the beam to have a uniform-density rigid-rotor Vlasov equilibrium distribution^{23,24} which includes the well-known Kapchinskij–Vladimirskij (KV) beam equilibrium distribution²⁵ as a special case. Using the Hamilton–Jacobi method, the betatron oscillations of test particles in the aver-

^{a)}Electronic mail: chenc@psfc.mit.edu

age self fields and applied field are analyzed, and the nonlinear resonances induced by periodic modulations in the self fields and applied field are determined. The Poincaré surface-of-section method²¹ is used to analyze the phase-space structure for test particle motion outside the outermost envelope of the beam over a wide range of system parameters. It is found that the phase-space structure changes significantly as the canonical angular momentum (P_θ), beam intensity (as measured by SK/ε_T or σ/σ_v), vacuum phase advance σ_v , or beam rotation (ω_b) is varied. The implications of the rich nonlinear resonance structure and chaotic particle motion found in the present test-particle studies are discussed in the context of halo formation. By examining the intrinsic properties of phase space of test particle motion outside of a perfectly matched beam as a function of beam intensity, focusing field strength and beam rotation, we gain valuable insights as to which operating regimes are more or less robust against the ejection of halo particles from the beam under small beam mismatch and/or collective excitations in the beam core.

To briefly summarize, based on a comprehensive study of the phase-space structure for test-particle motion for vacuum phase advance $\sigma_v = 80^\circ$, we find that the phase-space structure is almost entirely regular at low beam intensity (phase advance $\sigma \geq 70^\circ$, say), whereas at moderate beam intensity ($30^\circ \leq \sigma \leq 70^\circ$), nonlinear resonances appear, the most pronounced of which is the third-order primary nonlinear resonance. As the beam intensity is further increased ($\sigma \lesssim 30^\circ$), the widths of the higher-order nonlinear resonances increase, and the chaotic region of phase space increases in size. Furthermore, the many chaotic layers associated with the separatrices of the primary and secondary nonlinear resonances are still divided by the remaining invariant KAM surfaces, even at very high beam intensities. Therefore, in the context of the present test-particle analysis, chaotic layers do *not* form an extended chaotic region in phase space. In actual beam propagation experiments, however, it is expected that sufficient beam mismatch or perturbations about the periodically focused beam equilibrium can cause the particles to cross the invariant surfaces and form a halo.

The organization of this paper is as follows. After a discussion of the theoretical model and assumptions in Sec. II, the betatron oscillations and nonlinear resonances are analyzed using the Hamilton-Jacobi method in Sec. III. The phase-space structure of test particle motion over hundreds of lattice periods is examined numerically in Sec. IV. Conclusions are given in Sec. V.

II. THEORETICAL MODEL AND ASSUMPTIONS

In the present analysis, we consider a thin, continuous, intense charged-particle beam propagating in the z direction with characteristic axial velocity $\beta_b c$ and kinematic energy $\gamma_b mc^2$ through the periodic focusing solenoidal magnetic field

$$\mathbf{B}^{\text{sol}}(\mathbf{x}) = B_z(s)\mathbf{e}_z - \frac{1}{2}B'_z(s)(x\mathbf{e}_x + y\mathbf{e}_y). \quad (1)$$

Here, \mathbf{e}_x and \mathbf{e}_y are unit Cartesian vectors perpendicular to the beam propagation direction, $s = z$ is the axial coordinate, $x\mathbf{e}_x + y\mathbf{e}_y$ is the transverse displacement from the beam axis at $(x, y) = (0, 0)$, the superscript "prime" denotes d/ds with $B'_z(s) = dB_z(s)/ds$, and the axial component of magnetic field satisfies

$$B_z(s+S) = B_z(s), \quad (2)$$

where S is the axial period of the focusing field.

To determine the self-electric and self-magnetic fields²² consistently, we make the following assumptions: (a) the Budker parameter $\nu = N_b q^2 / mc^2$ for the beam is small compared with γ_b ; (b) the axial momentum spread of the beam particles is small in comparison with $\gamma_b m \beta_b c$; (c) the beam is axisymmetric ($\partial/\partial\theta = 0$); and (d) the beam is perfectly matched into the focusing field with uniform density profile over the beam cross section,

$$n_b(r, s) = \begin{cases} N_b / \pi r_b^2(s), & 0 \leq r < r_b(s) \\ 0, & r > r_b(s). \end{cases} \quad (3)$$

In Eq. (3), $r = (x^2 + y^2)^{1/2}$ is the radial coordinate, $r_b(s) = r_b(s+S)$ is the outer envelope of the beam, and $N_b = 2\pi \int_0^\infty n_b r dr = \text{const.}$ is the number of particles per unit axial length. The periodic outer beam envelope $r_b(s) = r_b(s+S)$ corresponds to a special solution of the beam envelope equation^{23,24}

$$\frac{d^2 r_b}{ds^2} + \kappa_z(s)r_b - \frac{K}{r_b} - \frac{\varepsilon_T^2}{r_b^3} = 0, \quad (4)$$

where $K = 2q^2 N_b / \gamma_b^3 \beta_b^2 mc^2$ is the normalized perveance, $\kappa_z(s) = [qB_z(s)/2\gamma_b \beta_b mc^2]^2 = [\Omega_c(s)/2\beta_b c]^2$ is the focusing parameter, $\varepsilon_T = \text{const.}$ is the total unnormalized emittance, q and m are the particle charge and rest mass, respectively, and c is the speed of light in *vacuo*. The transverse phase-space distribution that self-consistently generates the density profile in Eq. (3) is discussed in the Appendix.

Consistent with the thin-beam assumption ($r_b \ll S$), the scalar potential for the self-electric field $\mathbf{E}^s = -\nabla\phi^s$ is determined from

$$\frac{1}{r} \frac{\partial}{\partial r} r \frac{\partial \phi^s}{\partial r} = -4\pi q n_b(r, s), \quad (5)$$

where use has been made of the approximation $\nabla^2 \approx \nabla_\perp^2$. Integrating Eq. (5) for the density profile in Eq. (3), and applying the boundary condition $\phi^s(r=r_w, s) = 0$ at the wall of a perfectly conducting cylindrical tube with constant radius r_w yields

$$\phi^s(r, s) = \begin{cases} qN_b(1 - r^2/r_b^2) + 2qN_b \ln(r_w/r_b), & 0 \leq r < r_b(s) \\ 2qN_b \ln(r_w/r), & r_b(s) < r \leq r_w. \end{cases} \quad (6)$$

Because the axial momentum spread is assumed to be negligibly small, the vector potential for the self-magnetic field $\mathbf{B}^s = \nabla \times (A_z^s \mathbf{e}_z)$ is given approximately by

$$A_z^s(r, s) = \beta_b \phi^s(r, s), \quad (7)$$

where $\beta_b c$ is the characteristic axial velocity of the beam.

In the analysis of the particle motion, it is convenient to transform to the Larmor frame²⁶ which rotates with angular velocity $d\theta_L/ds = -\sqrt{\kappa_z(s)} = -qB_z(s)/2\gamma_b\beta_b mc^2$ relative to the laboratory frame, i.e.,

$$\bar{x}(s) = x(s)\cos[\theta_L(s)] + y(s)\sin[\theta_L(s)], \quad (8)$$

$$\bar{y}(s) = -x(s)\sin[\theta_L(s)] + y(s)\cos[\theta_L(s)]. \quad (9)$$

In cylindrical coordinates $(\bar{r}, \bar{\theta})$ in the Larmor frame, the equations of motion transverse to the direction of beam propagation can be derived from the normalized Hamiltonian

$$\bar{H}_\perp(\bar{r}, \bar{P}_r, \bar{P}_\theta, s) = \frac{1}{2} \left(\bar{P}_r^2 + \frac{\bar{P}_\theta^2}{\bar{r}^2} \right) + \frac{1}{2} \kappa_z(s) \bar{r}^2 + \psi(\bar{r}, s), \quad (10)$$

where the normalized self-field potential $\psi(\bar{r}, s)$ is defined by

$$\psi(\bar{r}, s) = \frac{q}{\gamma_b^3 m \beta_b^2 c^2} \phi^s(\bar{r}, s) = \begin{cases} (K/2)[1 - \bar{r}^2/r_b^2(s)] + K \ln[r_w/r_b(s)], & 0 \leq \bar{r} < r_b(s) \\ K \ln[r_w/\bar{r}], & r_b(s) < \bar{r} \leq r_w. \end{cases} \quad (11)$$

From Eq. (10), the equations of motion can be expressed as

$$\frac{d\bar{r}}{ds} = \frac{\partial}{\partial \bar{P}_r} \bar{H}_\perp = \bar{P}_r, \quad (12)$$

$$\frac{d\bar{\theta}}{ds} = \frac{\partial}{\partial \bar{P}_\theta} \bar{H}_\perp = \frac{\bar{P}_\theta}{\bar{r}^2}, \quad (13)$$

$$\frac{d\bar{P}_r}{ds} = -\frac{\partial}{\partial \bar{r}} \bar{H}_\perp = \frac{\bar{P}_\theta^2}{\bar{r}^3} - \kappa_z(s) \bar{r} - \frac{\partial}{\partial \bar{r}} \psi(\bar{r}, s), \quad (14)$$

$$\frac{d\bar{P}_\theta}{ds} = -\frac{\partial}{\partial \bar{\theta}} \bar{H}_\perp = 0. \quad (15)$$

It follows from Eq. (15) that the canonical angular momentum is conserved, i.e.,

$$\bar{P}_\theta = \bar{x}\bar{P}_y - \bar{y}\bar{P}_x = \text{const.}, \quad (16)$$

which is expected for axisymmetric beam propagation. Combining Eqs. (12) and (14) yields

$$\frac{d^2 \bar{r}}{ds^2} + \kappa_z(s) \bar{r} - \frac{\bar{P}_\theta^2}{\bar{r}^3} + \frac{\partial}{\partial \bar{r}} \psi(\bar{r}, s) = 0. \quad (17)$$

For a particle in the beam interior ($\bar{r} < r_b$), the equation of motion (17) is integrable. For a particle outside the beam ($\bar{r} > r_b$), the equation of motion is generally *nonintegrable*²¹ because of the nonlinear dependence of $\partial\psi/\partial\bar{r}$ on the radial coordinate \bar{r} .

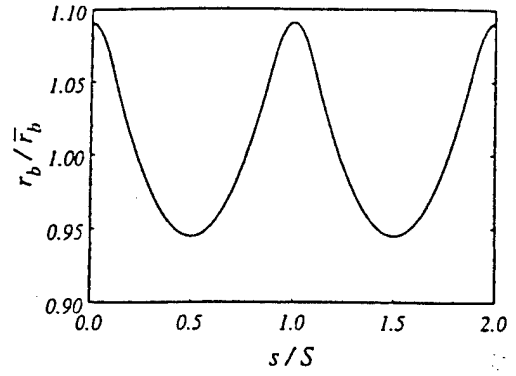


FIG. 1. Plot of the normalized beam radius $r_b(s)/\bar{r}_b$ vs normalized propagation distance s/S for intense beam propagation through a periodic step-function lattice. Here, $r_w/\bar{r}_b = 5$ is assumed, and the choice of system parameters corresponds to: $\eta = 0.2$, $S^2 \hat{\kappa}_z = 6.5$, and $SK/\epsilon_T = 4.0$.

III. ANALYSIS OF NONLINEAR RESONANCES

In this section, we analyze the nonlinear resonances in the particle motion in the Larmor frame described by Eq. (17). To simplify the notation, we omit the "tilde" in Larmor frame variables in the remainder of this paper. For present purposes, the Hamiltonian in Eq. (10) is expressed as

$$H_\perp(r, P_r, P_\theta, s) = H_0(r, P_r, P_\theta) + H_1(r, P_r, P_\theta, s), \quad (18)$$

where

$$H_0(r, P_r, P_\theta) = \frac{1}{2} P_r^2 + V_0(r, P_\theta) = \frac{1}{2} P_r^2 + \frac{1}{2} \bar{\kappa}_z r^2 + \frac{P_\theta^2}{2r^2} + \psi(r, s)|_{r_b(s)=\bar{r}_b}, \quad (19)$$

$$H_1(r, P_r, P_\theta, s) = \frac{1}{2} [\kappa_z(s) - \bar{\kappa}_z] r^2 + \psi(r, s) - \psi(r, s)|_{r_b(s)=\bar{r}_b}. \quad (20)$$

In Eqs. (18)–(20), $\psi(r, s)$ is defined in Eq. (11), and the effective mean beam radius \bar{r}_b is defined by

$$\bar{r}_b = \left(\frac{\epsilon_T S}{\sigma} \right)^{1/2}, \quad (21)$$

where $\sigma = \epsilon_T \int_s^{s+S} ds/r_b^2(s)$ is the space-charge-depressed phase advance for the rigid-rotor Vlasov equilibrium. The effective mean focusing parameter $\bar{\kappa}_z$ occurring in Eqs. (19) and (20) is defined by

$$\bar{\kappa}_z = \frac{K}{\bar{r}_b^2} + \frac{\epsilon_T^2}{\bar{r}_b^4}. \quad (22)$$

Physically, the Hamiltonian H_0 provides a good approximate description of the (slow) betatron oscillations, whereas the perturbation H_1 describes nonlinear resonances induced by the (fast) oscillations in $\kappa_z(s)$ and $r_b(s)$.

For future references, Fig. 1 shows a plot of the normalized beam radius $r_b(s)/\bar{r}_b$ versus normalized propagation distance s/S , obtained numerically by integrating the beam envelope equation (4) for intense beam propagation through a periodic step-function lattice with

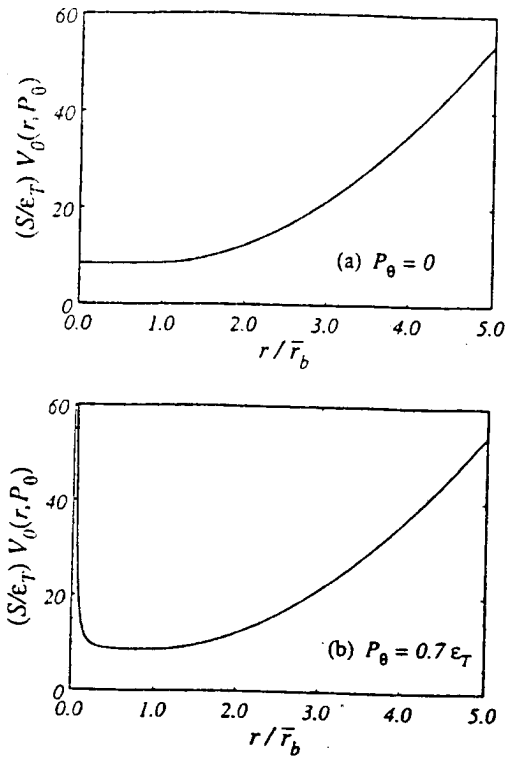


FIG. 2. Plots of the normalized effective potential $(S/\epsilon_T)V_0(r, P_\theta)$ [Eq. (19)] vs normalized radial coordinate r/\bar{r}_b for intense beam propagation through a periodic step-function lattice. Here, $r_w/\bar{r}_b = 5$ is assumed, and the two cases correspond to the choices of system parameters: (a) $\eta = 0.2$, $S^2\hat{\kappa}_z = 6.5$, $SK/\epsilon_T = 4.0$, and $P_\theta/\epsilon_T = 0$, and (b) $\eta = 0.2$, $S^2\hat{\kappa}_z = 6.5$, $SK/\epsilon_T = 4.0$, and $P_\theta/\epsilon_T = 0.7$. For both cases, the vacuum and space-charge-depressed phase advances are $\sigma_v = 68^\circ$ and $\sigma = 18.6^\circ$, respectively.

$$\kappa_z(s) = \begin{cases} \hat{\kappa}_z, & 0 \leq s < \eta S/2 \\ 0, & \eta S/2 \leq s < S - \eta S/2 \\ \hat{\kappa}_z, & S - \eta S/2 \leq s < S. \end{cases} \quad (23)$$

Here, $\hat{\kappa}_z = \text{const.}$, $\kappa_z(s+S) = \kappa_z(s)$, and η is the so-called filling factor for the lattice. In Fig. 1, $r_w/\bar{r}_b = 5$ is assumed, and the choice of system parameters corresponds to: $\eta = 0.2$, $S^2\hat{\kappa}_z = 6.5$, $SK/\epsilon_T = 4.0$. The vacuum and space-charge-depressed phase advances are found to be $\sigma_v = \epsilon_T \int_s^{s+S} ds/r_b^2(s)|_{K=0} = 68^\circ$ and $\sigma = \epsilon_T \int_s^{s+S} ds/r_b^2(s) = 18.6^\circ$, respectively.

A. Betatron oscillation frequency

Because P_θ is a constant of the motion and H_0 is independent of s , the unperturbed motion described by the Hamiltonian H_0 is integrable. Figure 2 shows a plot of the normalized effective potential $(S/\epsilon_T)V_0(r, P_\theta)$ versus normalized radial coordinate r/\bar{r}_b for intense beam propagation through the periodic step-function lattice defined in Eq. (23). In Fig. 2, $r_w/\bar{r}_b = 5$ is assumed, and the two cases correspond to the following choices of system parameters: (a) $\eta = 0.2$, $S^2\hat{\kappa}_z = 6.5$, $SK/\epsilon_T = 4.0$, and $P_\theta/\epsilon_T = 0$; and (b) $\eta = 0.2$, $S^2\hat{\kappa}_z = 6.5$, $SK/\epsilon_T = 4.0$, and $P_\theta/\epsilon_T = 0.7$. For both cases shown in Fig. 2, the vacuum and space-charge-depressed phase advances are given by σ_v

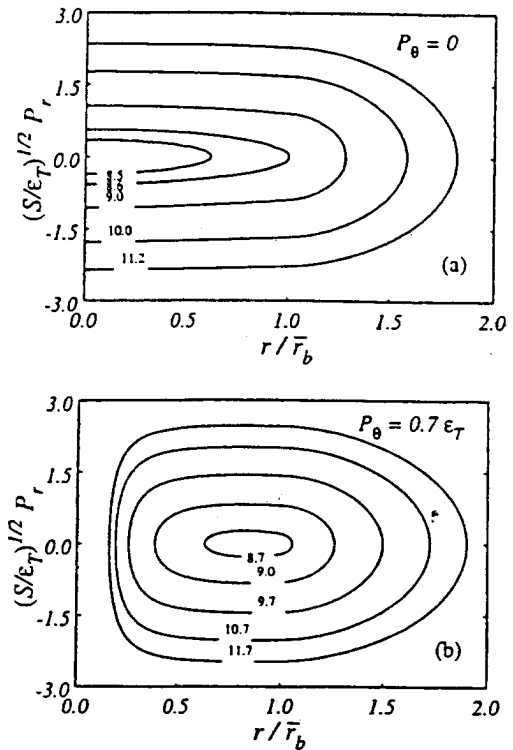


FIG. 3. Plots of constant- H_0 contours for several values of $(S/\epsilon_T)H_0$ as labeled in the phase space (r, P_r) for the same choices of system parameters as in Figs. 2(a) and 2(b), respectively.

$= \epsilon_T \int_s^{s+S} ds/r_b^2(s)|_{K=0} = 68^\circ$ and $\sigma = \epsilon_T \int_s^{s+S} ds/r_b^2(s) = 18.6^\circ$, respectively. As illustrated in Fig. 2, the effective potential $V_0(r, P_\theta)$ has a minimum at $r = r_0$, where r_0 is defined by

$$\frac{r_0^2}{\bar{r}_b^2} = \begin{cases} |P_\theta|/\epsilon_T, & |P_\theta| < \epsilon_T \\ [K + (K^2 + 4\bar{\kappa}_z P_\theta^2)^{1/2}] / [K + (K^2 + 4\bar{\kappa}_z \epsilon_T^2)^{1/2}], & |P_\theta| > \epsilon_T. \end{cases} \quad (24)$$

In Fig. 3, constant- H_0 contours are plotted in the phase space (r, P_r) for several values of $(S/\epsilon_T)H_0$, and the same choices of system parameters as in Fig. 2. For $P_\theta/\epsilon_T = 0.7$ and specified value of H_0 , the particle undergoes betatron oscillations about $r = r_0$, corresponding to motion on constant- H_0 contours in the phase space (r, P_r) as shown in Fig. 3(b). In general, the betatron oscillation frequency depends on the amplitude of the oscillations.

To determine the betatron oscillation frequency, we employ the Hamilton-Jacobi method²⁷ and perform a canonical transformation from (r, P_r) to the action-angle variables (ϕ, J) . Let $W(r, J)$ be the characteristic function satisfying the partial differential equation

$$\frac{1}{2} \left(\frac{\partial W}{\partial r} \right)^2 + V_0(r, P_\theta) = H_0 = \text{const.} \quad (25)$$

As discussed below, the dependence of W on J is uniquely determined because of the one-to-one correspondence between H_0 and J [see Eq. (29)]. A formal expression for the angle variable ϕ is given by

$$\phi = \frac{\partial W}{\partial J}. \quad (26)$$

The action variable J can be expressed as

$$J = \frac{1}{2\pi} \oint \phi P_r dr = \frac{1}{\pi} \int_{r_-}^{r_+} \{2[H_0 - V_0(r, P_\theta)]\}^{1/2} dr, \quad (27)$$

where the turning points r_\pm solve the algebraic equation

$$H_0 = V_0(r_\pm, P_\theta), \quad (28)$$

and $r_+ > r_-$ is assumed. Because the action variable J increases monotonically with increasing H_0 , Eq. (27) can be inverted to yield a Hamiltonian of the form

$$H_0 = H_0(J, P_\theta). \quad (29)$$

The betatron oscillation frequency can then be expressed as

$$\omega_\beta(J, P_\theta) = \frac{\partial H_0}{\partial J}, \quad (30)$$

which, in general, must be evaluated numerically. Before presenting numerical results, we discuss two special cases.

For particle motion inside the mean beam envelope with $r_+ < \bar{r}_b$, it is readily shown from Eq. (27) that the action variable can be expressed as

$$J = \frac{SH_0}{2\sigma} + \frac{P_\theta}{2}, \quad (31)$$

where use has been made of Eqs. (21) and (22). It follows from Eqs. (30) and (31) that the betatron oscillation frequency is given by

$$\omega_\beta = \frac{\partial H_0}{\partial J} = \frac{2\sigma}{S}, \quad (32)$$

which is independent of the amplitude, as expected for particle motion in the beam interior. Note that the factor of 2 in Eq. (32) arises from the fact that in the present description of the betatron oscillations, the radial coordinate $r = (x^2 + y^2)^{1/2}$ is used as a generalized coordinate, instead of a Cartesian coordinate, say x .

As the outer oscillation amplitude r_+ increases well beyond the mean beam envelope (\bar{r}_b), the oscillation frequency increases because the influence of space charge on the betatron oscillations become less pronounced. In the limit where $r_+ \gg \bar{r}_b$, the betatron frequency is given by

$$\omega_\beta = \frac{2\sigma_v}{S}, \quad (33)$$

where $\sigma_v = \epsilon_T \int_{s-s}^{s+s} ds/r_b^2(s)|_{K=0}$ is the vacuum phase advance.

Figure 4 shows a plot of the betatron oscillation frequency ω_β versus normalized betatron oscillation amplitude $(r_+ - r_0)/r_0$ for the same choices of system parameters as in Figs. 2 and 3.

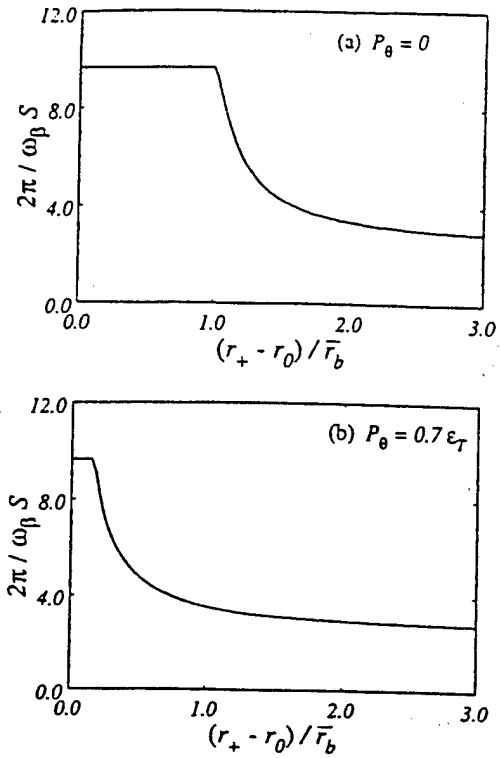


FIG. 4. Plots of the normalized betatron oscillation period $2\pi/\omega_\beta S$ [Eq. (30)] vs normalized betatron oscillation amplitude $(r_+ - r_0)/\bar{r}_b$ for the same choices of system parameters as in Figs. 2(a) and 2(b), respectively.

B. Nonlinear resonances

Under the influence of the perturbation H_1 , a variety of nonlinear resonances occur due to the coupling of the (slow) betatron oscillations and the (fast) oscillations in the focusing parameter $\kappa_z(s)$ and associated modulation in the beam envelope $r_b(s)$. The locations and widths of the nonlinear resonances are analyzed in this section.

Making use of the action-angle variables (ϕ, J) discussed in Sec. III A, we express the total Hamiltonian H formally as

$$H(\phi, J, P_\theta, s) = H_0(J, P_\theta) + H_1(\phi, J, s). \quad (34)$$

Expanding H_1 in a Fourier series representation in ϕ and s , we obtain

$$H_1 = \sum_{n=-\infty}^{\infty} \sum_{l=-\infty}^{\infty} a_{nl}(J) \exp[i(n\phi + 2l\pi s/S)], \quad (35)$$

where the Fourier coefficients $a_{nl}(J)$ are given by

$$a_{nl}(J) = \frac{1}{2\pi S} \int_0^S ds \int_0^{2\pi} d\phi H_1(J, \phi, s) \times \exp[-i(n\phi + 2l\pi s/S)]. \quad (36)$$

A nonlinear resonance occurs when the resonance condition

$$n \frac{d\phi}{ds} + \frac{2l\pi}{S} \equiv n\omega_\beta(J, P_\theta) + \frac{2l\pi}{S} = 0 \quad (37)$$

is satisfied. Of particular interest in the present analysis are the primary nonlinear resonances with $l = -1$ that satisfy the resonance condition

$$n\omega_\beta(J_n, P_\theta) = \frac{2\pi}{S}, \quad (38)$$

where J_n determines the location of the primary resonance of order n in the phase space (ϕ, J) , i.e., at $J = J_n$.

To estimate the width of the n th-order primary resonance, we retain a single resonance term in the Fourier series in Eq. (20) and express the Hamiltonian approximately as

$$H(\phi, J, P_\theta, s) \cong H_0(J, P_\theta) + 2|a_{n,-1}(J)|\cos(n\phi - 2\pi s/S + \alpha_{n,-1}). \quad (39)$$

Here, $\alpha_{n,-1}(J)$ is the argument of the complex Fourier coefficient $a_{n,-1}$, and use has been made of $a_{n,-1} = |a_{n,-1}|\exp(i\alpha_{n,-1}) = a_{n,-1}^*$. Expanding $H_0(J)$ about $J = J_n$, the Hamiltonian in Eq. (39) can be approximated by

$$\begin{aligned} H(\phi, J, P_\theta, s) &\cong H_0(J_n, P_\theta) + \omega_\beta(J_n, P_\theta)(J - J_n) \\ &+ \frac{1}{2} \frac{\partial}{\partial J} \omega_\beta(J, P_\theta)|_{J=J_n} (J - J_n)^2 \\ &+ 2|a_{n,-1}(J_n)|\cos(n\phi - 2\pi s/S + \alpha_{n,-1}). \end{aligned} \quad (40)$$

Performing a canonical transformation with $\phi - 2\pi s/nS + \alpha_{n,-1}/n \rightarrow \phi$ and $H \rightarrow H - 2\pi J/nS$, the Hamiltonian in Eq. (40) becomes

$$\begin{aligned} H(\phi, J, P_\theta, s) &= \frac{1}{2} \left(\frac{\partial \omega_\beta}{\partial J} \right)_{J=J_n} (\delta J)^2 \\ &+ 2|a_{n,-1}(J_n)|\cos(n\phi) + \text{const.}, \end{aligned} \quad (41)$$

where $\delta J = J - J_n$, and use has been made of the resonance condition in Eq. (38). It follows from Eq. (41) that the full width of the n th-order primary resonance is given by

$$\Delta J_n = \left[\frac{32|a_{n,-1}(J_n)|}{(\partial \omega_\beta / \partial J)_{J=J_n}} \right]^{1/2} \quad (42)$$

in the action variable, or equivalently by

$$\Delta r_n = \left(\frac{\partial r}{\partial J} \right)_{P_\theta, J=J_n} \Delta J_n \quad (43)$$

in the radial coordinate.

The procedure for evaluating the resonance width ΔJ_n in Eq. (42) is the following. First, to determine $(\partial \omega_\beta / \partial J)_{J=J_n}$ and associated quantities such as J_n , Eq. (38) is solved numerically in terms of outer turning point $r_n = r(J_n, \phi = 0) \geq r_0$, using Newton's method. This gives the values of r_n , J_n , $H_0(r_n, P_\theta)$, $(\partial \omega_\beta / \partial r)_{r=r_n}$, etc. Using the chain rule for differentiation, this procedure also allows the numerical evaluation of $(\partial \omega_\beta / \partial J)_{J=J_n}$. Second, to determine the Fourier coefficient $a_{n,-1}(J_n)$, the Hamiltonian perturbation $H_1(J_n, \phi, s)$ is computed numerically on a two-dimensional mesh in the variables ϕ and s , where ϕ ranges from 0 to 2π and s ranges from 0 to S . A two-dimensional discrete Fourier transform is then used to evaluate the Fourier coefficient $a_{n,-1}(J_n)$, instead of the continuous representation in Eq.

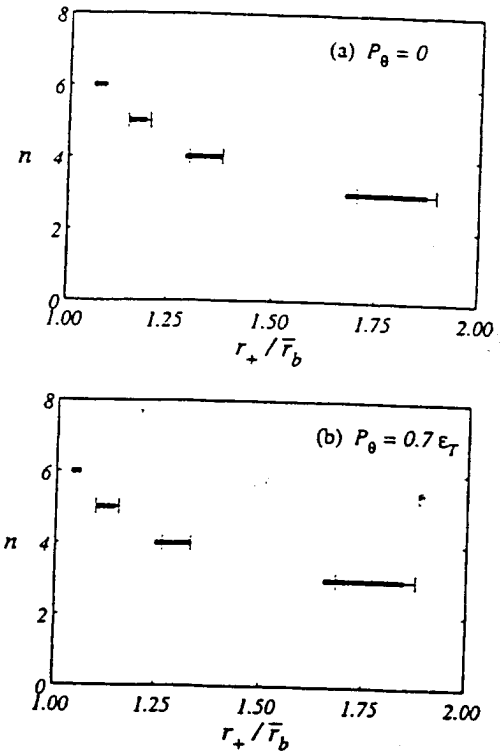


FIG. 5. Plots of the locations and full widths of the primary resonances of order $n=3-6$ obtained for the choices of system parameters corresponding to: (a) $\eta=0.2$, $\sigma_v=80^\circ$ ($S^2\hat{\kappa}_z=8.712$), $\sigma=26.2^\circ$ ($SK/\epsilon_T=3.8$), $\omega_b=0$, and $P_\theta=0$; and (b) $\eta=0.2$, $\sigma_v=80^\circ$ ($S^2\hat{\kappa}_z=8.712$), $\sigma=26.2^\circ$ ($SK/\epsilon_T=3.8$), $\omega_b=0$, and $P_\theta/\epsilon_T=0.7$. The solid lines correspond to the analytical estimates given in Eq. (42), whereas the dotted lines are obtained by integrating Eq. (17) numerically.

(36). Finally, the resonance width ΔJ_n (or corresponding resonance width Δr_n in radial coordinate r) is obtained by substituting the values of $a_{n,-1}(J_n)$ and $(\partial \omega_\beta / \partial J)_{J=J_n}$ into Eq. (42).

Figure 5 shows plots of the locations and full widths of the primary resonances of order $n=3-6$ obtained for the choices of system parameters corresponding to: (a) $\eta=0.2$, $\sigma_v=80^\circ$ ($S^2\hat{\kappa}_z=8.712$), $\sigma=26.2^\circ$ ($SK/\epsilon_T=3.8$), $\omega_b=0$, and $P_\theta=0$; and (b) $\eta=0.2$, $\sigma_v=80^\circ$ ($S^2\hat{\kappa}_z=8.712$), $\sigma=26.2^\circ$ ($SK/\epsilon_T=3.8$), $\omega_b=0$, and $P_\theta/\epsilon_T=0.7$. In Fig. 5, the solid lines correspond to the analytical estimates given in Eq. (43), whereas the dotted lines are obtained by integrating Eq. (17) numerically. For the lower-order primary nonlinear resonances with $n=3, 4$, and 5 , the analytical estimates are in good agreement with the numerical results. For the sixth-order primary nonlinear resonance, however, we cannot obtain an analytical estimate of its width because numerical noise becomes sizable in computing the Fourier amplitude $a_{6,-1}$.

The nonlinear resonances for the cases presented in Figs. 5(a) and 5(b) are further illustrated with the Poincaré surface-of-section plots²¹ shown in Figs. 6(a) and 6(b), respectively. Here, the Poincaré surface-of-section plots are generated by plotting the successive intersections of 15 test-particle trajectories, obtained from numerical integration of Eq. (17), with the phase space (r, P) at the lattice points

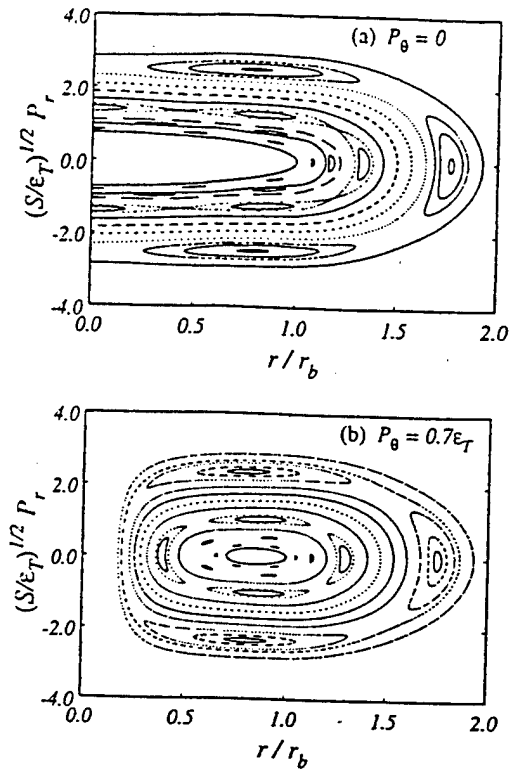


FIG. 6. Poincaré surface-of-section plots in the phase space (r, P_r) for 15 test particle trajectories moving through the periodic step-function lattice from $s/S = 0$ to 1000 under the influence of the space-charge forces in a KV beam equilibrium. Here, the choices of systems parameters in (a) and (b) are the same as in Figs. 5(a) and 5(b), respectively.

$s = 0, S, 2S, \dots, 1000S$. Evidently, the locations and widths of the primary nonlinear resonances shown in Fig. 6 are in agreement with those shown in Fig. 5.

IV. PHASE SPACE STRUCTURE

In this section, use is made of the Poincaré surface-of-section method to examine the phase-space structure described by the Hamiltonian H in Eq. (18). Of particular interest are the nonlinear resonances and chaotic particle motion of test particles outside the boundary of the phase space occupied by the interior beam particles making up the rigid-rotor Vlasov equilibrium distribution f_0 (Refs. 23 and 24) in Eq. (A1). The phase-space boundary of the rigid-rotor Vlasov equilibrium is a closed surface in the three-dimensional phase space (r, P_r, P_θ) at any given axial distance s . A projection of such a boundary onto the phase space (r, P_θ) can be determined from

$$[\mathcal{H}_\perp + \omega_b P_\theta - \frac{1}{2}(1 - \omega_b^2)\epsilon_T]_{P_R=0} = 0, \quad (44)$$

where P_R , P_θ , and \mathcal{H}_\perp are defined in Eqs. (A4), (A5), and (A7), respectively. Substituting Eqs. (A2)–(A5) and (A7) into Eq. (44) yields

$$\left[\frac{P_\theta r_b(s)}{\epsilon_T r} + \omega_b \frac{r}{r_b(s)} \right]^2 = (1 - \omega_b^2) \left[1 - \frac{r^2}{r_b^2(s)} \right]. \quad (45)$$

Figure 7 shows plots of the normalized canonical angular momentum P_θ/ϵ_T versus normalized radius r/r_b described by Eq. (45) for the following choices of system parameters:

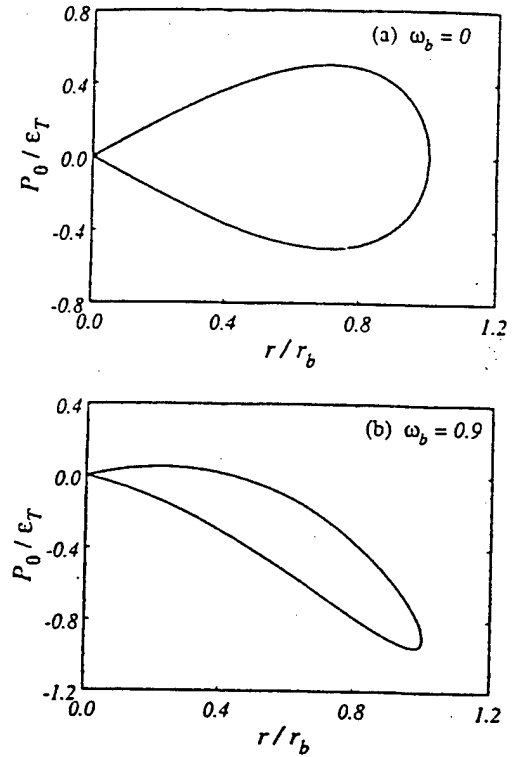


FIG. 7. Plots of the normalized canonical angular momentum P_θ/ϵ_T vs normalized radius r/r_b calculated from Eq. (45) for the choices of system parameters: (a) $\omega_b = 0$ and (b) $\omega_b = 0.9$.

(a) $\omega_b = 0$ and (b) $\omega_b = 0.9$. All of the interior beam particles in the equilibrium distribution are enclosed by such a loop shown in Fig. 7.

The phase-space structure for test particle motion is illustrated by the Poincaré surface-of-section plots shown in Figs. 8–10 for a wide range of system parameters. The Poincaré surface-of-section plots in Figs. 8–10 are generated by plotting the successive intersections of test-particle trajectories, obtained from numerical integration of Eq. (17), with the phase space (r, P_r) at the lattice points $s = 0.5S, 1.5S, 2.5S$, etc.

Figure 8 shows Poincaré surface-of-section plots in the phase space (r, P_r) for 15 test particle trajectories moving through the periodic step-function lattice from $s/S = 0.5$ to 1000.5 under the influence of the space-charge forces in a KV beam equilibrium. In Fig. 8, the choices of system parameters correspond to: (a) $\sigma_v = 80^\circ$, $\eta = 0.2$, $\sigma = 11.0^\circ$ ($SK/\epsilon_T = 10$), $\omega_b = 0$, and $P_\theta/\epsilon_T = 0$; and (b) $\sigma_v = 80^\circ$, $\eta = 0.2$, $\sigma = 11.0^\circ$ ($SK/\epsilon_T = 10$), $\omega_b = 0$, and $P_\theta/\epsilon_T = 0.45$. For both cases shown in Fig. 8, one test particle is initialized at the phase-space boundary of the KV equilibrium distribution, and the corresponding test-particle orbit is represented in Fig. 8(a) by the inner curved arc approaching $r/r_b = 1$, and in Fig. 8(b) by the innermost contour extending from $r/r_b = 0.54$ to 0.84 . The remaining test particles are initialized outside the beam, i.e., outside the phase-space boundary of the KV equilibrium distribution. Some of these particles undergo chaotic motion. By comparing Fig. 8(a) with Fig. 8(b), it is evident that the phase-space structure changes significantly as the canonical angular momentum P_θ is varied. In particular, it is interesting to observe that there are many

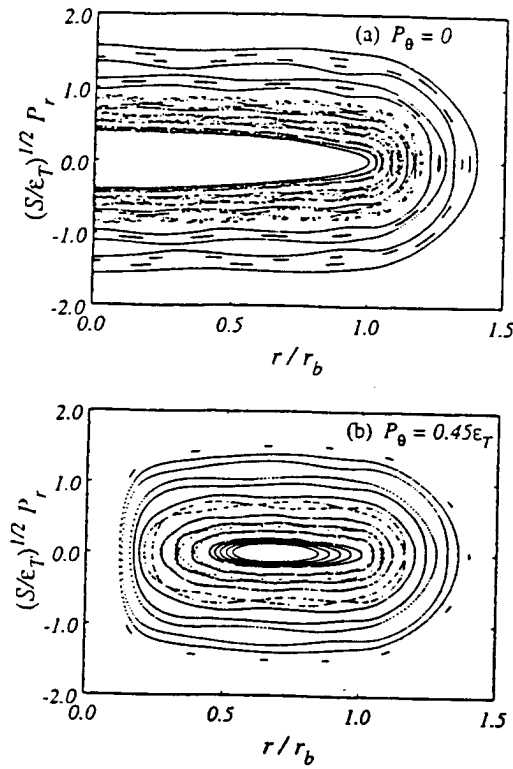


FIG. 8. Poincaré surface-of-section plots in the phase space (r, P_r) for 15 test particle trajectories moving through the periodic step-function lattice from $s/S = 0.5$ to 1000.5 under the influence of the space-charge forces in a KV beam equilibrium. Here, the choices of system parameters correspond to: (a) $\sigma_v = 80^\circ$, $\eta = 0.2$, $\sigma = 11.0^\circ$ ($SK/\epsilon_T = 10$), $\omega_b = 0$, and $P_\theta/\epsilon_T = 0$; and (b) $\sigma_v = 80^\circ$, $\eta = 0.2$, $\sigma = 11.0^\circ$ ($SK/\epsilon_T = 10$), $\omega_b = 0$, and $P_\theta/\epsilon_T = 0.45$.

nonlinear resonances and chaotic regions in the vicinity of the phase-space boundary of the KV equilibrium distribution for the case shown in Fig. 8(a) ($P_\theta = 0$), whereas the nonlinear resonances and chaotic regions are well separated, by a dense set of invariant curves, i.e., KAM surfaces,²¹ from the phase-space boundary of the KV equilibrium distribution for the case shown in Fig. 8(b) ($P_\theta/\epsilon_T = 0.45$). In general, as the canonical angular momentum P_θ increases in magnitude, the nonlinear resonances and chaotic regions move further away from the phase-space boundary of the KV equilibrium distribution. Consequently, for a KV equilibrium, particles with $P_\theta = 0$ are the most likely to escape from the beam interior to enter into chaotic regions in phase space, forming a halo.

The Poincaré surface-of-section plots in Fig. 9 illustrate how the phase-space structure varies as the beam intensity, measured by the normalized parameter SK/ϵ_T , is increased. The choices of system parameters in Fig. 9 correspond to $\sigma_v = 80^\circ$, $\eta = 0.2$, $\omega_b = 0$, and $P_\theta/\epsilon_T = 0$ at the following normalized beam intensities: (a) $SK/\epsilon_T = 0.5$ ($\sigma = 66.8^\circ$), (b) $SK/\epsilon_T = 1.0$ ($\sigma = 56.3^\circ$), (c) $SK/\epsilon_T = 3.0$ ($\sigma = 31.5^\circ$), and (d) $SK/\epsilon_T = 7.0$ ($\sigma = 15.4^\circ$). For the low-intensity case shown in Fig. 9(a), the phase space is almost entirely regular. For the moderate-intensity cases shown in Figs. 9(b) and 9(c), nonlinear resonances appear. The most pronounced among these resonances is the third-order primary nonlinear resonance. As the beam intensity is further increased, the widths of

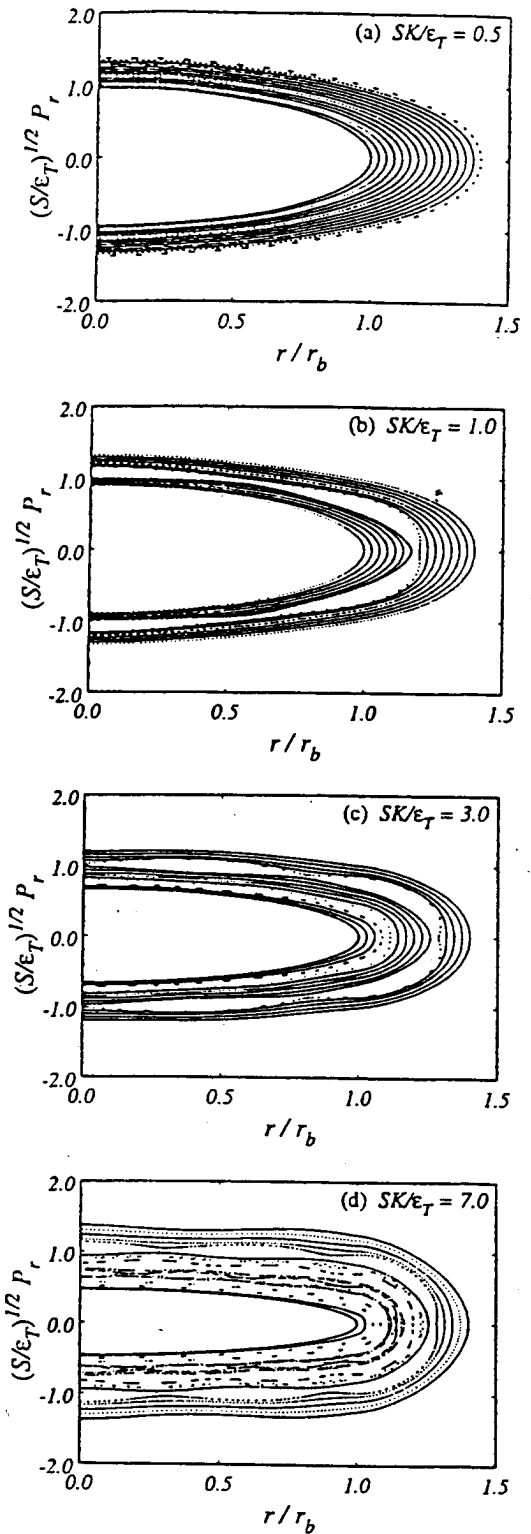


FIG. 9. Poincaré surface-of-section plots in the phase space (r, P_r) for 15 test particle trajectories moving through the periodic step-function lattice from $s/S = 0.5$ to 1000.5 under the influence of the space-charge forces in a KV beam equilibrium at several beam intensities. Here, the choices of systems parameters correspond to $\sigma_v = 80^\circ$, $\eta = 0.2$, $\omega_b = 0$, and $P_\theta/\epsilon_T = 0$ at the following normalized beam intensities: (a) $SK/\epsilon_T = 0.5$ ($\sigma = 66.8^\circ$), (b) $SK/\epsilon_T = 1.0$ ($\sigma = 56.3^\circ$), (c) $SK/\epsilon_T = 3.0$ ($\sigma = 31.5^\circ$), and (d) $SK/\epsilon_T = 7.0$ ($\sigma = 15.4^\circ$).

higher-order nonlinear resonances increase, which is evident from Fig. 9(d). In general, the nonlinear resonances and chaotic regions increase in size as the beam intensity is increased.

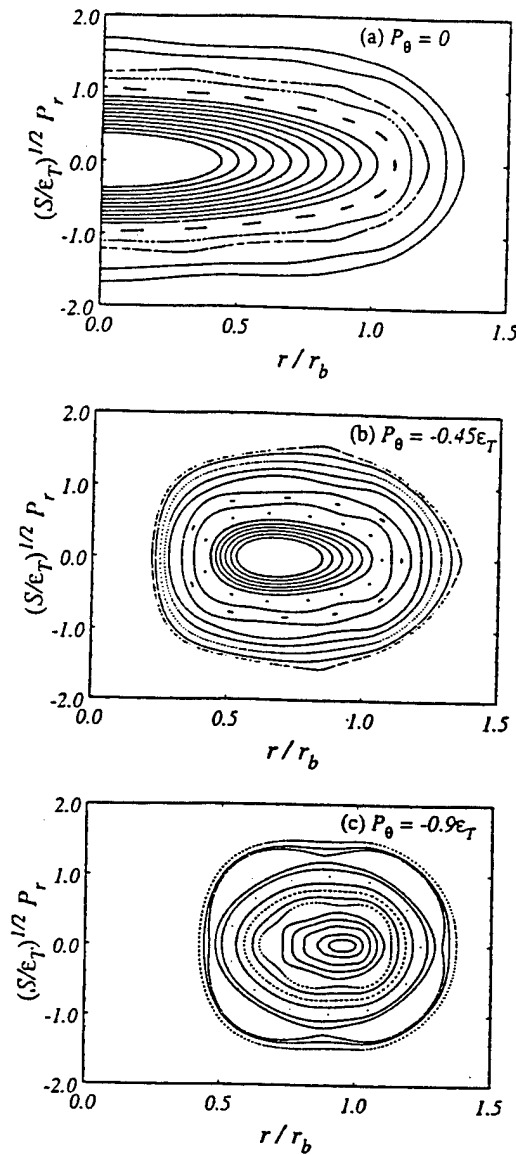


FIG. 10. Poincaré surface-of-section plots in the phase space (r, P_r) for 15 test particle trajectories moving through the periodic step-function lattice from $s/S = 0.5$ to 1000.5 under the influence of the space-charge forces in a rigid-rotor Vlasov equilibrium. Here, the choices of system parameters correspond to: $\sigma_v = 80^\circ$, $\eta = 0.2$, $\sigma = 11.0^\circ$ ($SK/\epsilon_T = 10$), $\omega_b = 0.9$, and (a) $P_\theta/\epsilon_T = 0$, (b) $P_\theta/\epsilon_T = -0.45$, and (c) $P_\theta/\epsilon_T = -0.9$.

The influence of beam rotation ($\omega_b \neq 0$) on the phase-space structure is illustrated by the Poincaré surface-of-section plots shown in Fig. 10. The choices of system parameters in Fig. 10 correspond to: $\sigma_v = 80^\circ$, $\eta = 0.2$, $\sigma = 11.0^\circ$ ($SK/\epsilon_T = 10$), $\omega_b = 0.9$, and (a) $P_\theta/\epsilon_T = 0$, (b) $P_\theta/\epsilon_T = -0.45$, and (c) $P_\theta/\epsilon_T = -0.9$. For all three cases shown in Fig. 10, the innermost orbit corresponds to a test particle that is initialized at the phase space boundary of the rigid-rotor Vlasov equilibrium. By comparing Fig. 10 with Fig. 8 for the KV distribution where the beam rotation is absent ($\omega_b = 0$), we find that the presence of beam rotation tends to reduce the degree of chaotic behavior in phase space. This is evident when we compare Fig. 10(c) with Fig. 8(a). For both cases shown in Fig. 10(c) and Fig. 8(a), the value of P_θ is chosen such that the boundary of the equilibrium distribution extends to $r = r_b$ [see Fig. 7 or Eq. (45)].

Finally, we discuss the implications of the rich nonlinear resonance structure and chaotic particle motion for beam halo formation. Based on a comprehensive study of the phase-space structure for test-particle motion for vacuum phase advance $\sigma_v = 80^\circ$, we have shown that the phase-space structure is almost entirely regular at low beam intensity (phase advance $\sigma \geq 70^\circ$, say), whereas at moderate beam intensity ($30^\circ \leq \sigma \leq 70^\circ$), nonlinear resonances appear, the most pronounced of which is the third-order primary nonlinear resonance. As the beam intensity is further increased ($\sigma \lesssim 30^\circ$), the widths of the higher-order nonlinear resonances increase, and the chaotic region of phase space increases in size. Furthermore, the many chaotic layers associated with the separatrices of the primary and secondary nonlinear resonances are still divided by the remaining invariant KAM surfaces, even at very high beam intensities. Therefore, in the context of the present test-particle analysis, chaotic layers do *not* form an extended chaotic region in phase space. In actual beam propagation experiments, however, it is expected that sufficient beam mismatch or perturbations about the periodically focused beam equilibrium can cause the particles to cross the invariant surfaces and form a halo.

V. CONCLUSIONS

Test particle motion has been analyzed analytically and numerically in the field configuration consisting of the equilibrium self-electric and self-magnetic fields of a thin, continuous, intense charged-particle beam and an applied periodic focusing solenoidal magnetic field. In the present analysis, the self fields were determined self-consistently, assuming the beam to have a rigid-rotor Vlasov equilibrium distribution. The canonical equations of motion for individual test particles were derived from a Hamiltonian. Using the Hamilton-Jacobi method, the betatron oscillations of test particles in the average self fields and applied field were analyzed, and the nonlinear resonances induced by periodic modulations in the self fields and applied field were determined. Analytical estimates of the locations and widths of the primary nonlinear resonances were found to be in good agreement with Poincaré surface-of-section plots obtained by integrating numerically the equations of motion.

Use was made of the Poincaré surface-of-section method to analyze the phase-space structure for test particle motion outside the outermost envelope of the beam over a wide range of system parameters. It was found that the phase-space structure changes significantly as the canonical angular momentum (P_θ), beam intensity (as measured by SK/ϵ_T or σ/σ_v), vacuum phase advance σ_v , or beam rotation (ω_b) is varied. For an intense beam with KV equilibrium distribution ($\omega_b = 0$), it was shown that the chaotic regions approach the phase-space boundary of the equilibrium distribution as the canonical angular momentum P_θ decreases in magnitude. Consequently, when there are perturbations about the equilibrium, particles with zero canonical angular momentum are the most likely to escape from the beam interior to enter into the chaotic regions, forming a halo. The phase-space structure was also analyzed for test-particle motion under the in-

fluence of the self fields of an intense beam with a rigid-rotor Vlasov equilibrium distribution ($\omega_b \neq 0$). It was found that the presence of beam rotation reduces the degree of chaotic behavior in phase space.

For $\sigma_v < 80^\circ$, the test-particle analysis showed that at very high beam intensities, the chaotic layers associated the separatrices of nonlinear resonances are still divided by the remaining invariant KAM surfaces and do not overlap completely to form an extended chaotic region. Although the chaotic layers do not form an extended chaotic region in the context of present test-particle analysis, any sizable beam mismatch or perturbations about the periodically-focused beam equilibrium may cause particles to cross the invariant surfaces, thereby resulting in a halo.

ACKNOWLEDGMENTS

This research was supported by Department of Energy under Grant No. DE-FG02-95ER-40919 and Contract No. DE-AC02-76-CH0-3073, and by Air Force Office of Scientific Research under Grant No. F49620-97-1-0325. The research by R.P. was also supported by CAPES, Brazil.

APPENDIX: RIGID-ROTOR VLASOV EQUILIBRIUM

The transverse phase-space distribution that self-consistently generates the density profile in Eq. (3) is given by the rigid-rotor Vlasov equilibrium distribution function^{23,24}

$$f_b^0(R, P_R, P_\Theta) = \frac{N_b}{2\pi^2 \epsilon_T} \delta \left[\mathcal{H}_\perp + \omega_b P_\Theta - \frac{1}{2} (1 - \omega_b^2) \epsilon_T \right]. \quad (A1)$$

In Eq. (A1), $\omega_b = \text{const.}$ ($-1 < \omega_b < 1$) is a parameter measuring beam rotation relative to the Larmor frame. The normalized canonical phase-space variables $(R, \Theta, P_R, P_\Theta)$ are related to the Larmor-frame phase-space variables $(\tilde{r}, \tilde{\theta}, \tilde{P}_r, \tilde{P}_\theta)$ by

$$R = \frac{\sqrt{\epsilon_T}}{r_b(s)} \tilde{r}, \quad (A2)$$

$$\Theta = \tilde{\theta}, \quad (A3)$$

$$P_R = \frac{1}{\sqrt{\epsilon_T}} \left[r_b(s) \frac{d\tilde{r}}{ds} - \tilde{r} \frac{d}{ds} r_b(s) \right], \quad (A4)$$

$$P_\Theta = \tilde{P}_\theta, \quad (A5)$$

through the generating function

$$F_2(\tilde{r}, \tilde{\theta}, P_R, P_\Theta, s) = \frac{\sqrt{\epsilon_T}}{r_b(s)} \tilde{r} P_R + \tilde{\theta} P_\Theta + \frac{\tilde{r}^2}{r_b(s)} \frac{d}{ds} r_b(s). \quad (A6)$$

The effective transverse Hamiltonian \mathcal{H}_\perp occurring in Eq. (A1) is defined for $R < \sqrt{\epsilon_T}$ (or equivalently for $\tilde{r} < r_b$) by

$$\begin{aligned} \mathcal{H}_\perp(R, P_R, P_\Theta) &= \frac{r_b^2(s)}{\epsilon_T} \left[H_\perp(R, P_R, P_\Theta, s) - \frac{K}{2} - K \ln \frac{r_w}{r_b(s)} \right] \\ &= \frac{1}{2} \left(P_R^2 + \frac{P_\Theta^2}{R^2} + R^2 \right), \end{aligned} \quad (A7)$$

where $H_\perp(R, \Theta, P_R, P_\Theta, s) = \tilde{H}_\perp(\tilde{r}, \tilde{\theta}, \tilde{P}_r, \tilde{P}_\theta, s) + \partial F_2 / \partial s$ is the Hamiltonian expressed in the canonical variables $(R, \Theta, P_R, P_\Theta)$.

For a particle moving in the beam interior ($R < \sqrt{\epsilon_T}$ or equivalently $\tilde{r} < r_b$), it follows from the Hamilton equations of motion, $dR/ds = \partial H_\perp / \partial P_R$, $d\Theta/ds = \partial H_\perp / \partial P_\Theta$, $dP_R/ds = -\partial H_\perp / \partial R$, and $dP_\Theta/ds = -\partial H_\perp / \partial \Theta = 0$, that the effective transverse energy \mathcal{H}_\perp is a constant of the motion, although the transverse Hamiltonian H_\perp , in general, is not a constant of the motion. Because H_\perp is independent of Θ , the canonical angular momentum P_Θ is also a constant of the motion, in agreement with Eqs. (16) and (A5). Therefore, the equilibrium distribution function f_b^0 satisfies exactly the steady-state nonlinear Vlasov equation

$$\frac{\partial f_b^0}{\partial s} + \frac{\partial H_\perp}{\partial P_R} \frac{\partial f_b^0}{\partial R} - \frac{\partial H_\perp}{\partial R} \frac{\partial f_b^0}{\partial P_R} = 0 \quad (A8)$$

with $\partial f_b^0 / \partial s = 0$. Making use of $\int dx' dy' \dots = [\epsilon_T / r_b^2(s) R] \int dP_R dP_\Theta \dots$, it is readily shown that $n_b(r, s) = \int dx' dy' f_b^0$ is indeed identical to the step-function density profile defined in Eq. (3).

¹Space Charge Dominated Beams and Applications of High Brightness Beams, edited by S. Y. Lee [AIP Conf. Proc. 377 (1996)], and references therein.

²I. Haber, D. Kehne, M. Reiser, and H. Rudd, Phys. Rev. A 44, 5194 (1991).

³J. S. O'Connell, T. P. Wangler, R. S. Mills, and K. R. Crandall, *Proceedings of the 1993 Particle Accelerator Conference* (IEEE, Piscataway, NJ, 1993), Vol. 5, p. 3657.

⁴C. Chen and R. C. Davidson, Phys. Rev. Lett. 72, 2195 (1994); Phys. Rev. E 49, 5679 (1994).

⁵Q. Qian, R. C. Davidson, and C. Chen, Phys. Plasmas 1, 3104 (1994).

⁶R. L. Gluckstern, Phys. Rev. Lett. 73, 1247 (1994).

⁷T. Chen, J. Irwin, and R. Siemann, Phys. Rev. E 49, 2323 (1994).

⁸L. M. Lagniel, Nucl. Instrum. Methods Phys. Res. A 345, 1576 (1995); *Proceedings of the Fifth European Particle Accelerator Conference, 1996* (unpublished), p. 163.

⁹Q. Qian, R. C. Davidson, and C. Chen, Phys. Plasmas 2, 2674 (1995).

¹⁰C. Chen and R. A. Jameson, Phys. Rev. E 52, 3074 (1995).

¹¹S. Y. Lee and A. Riabko, Phys. Rev. E 51, 1609 (1995); A. Riabko *et al.*, *ibid.* 51, 3529 (1995).

¹²I. Haber, D. A. Callahan, A. Friedman, D. P. Grote, D. Kehne, A. B. Langdon, M. Reiser, H. Rudd, H. Suk, D. X. Wang, and J. G. Wang, in Ref. 1, p. 105.

¹³F. L. Krawczyk, J. H. Billen, R. D. Ryne, H. Takeda, and L. M. Young, in *Proceedings of the 1995 Particle Accelerator Conference* (IEEE, Piscataway, NJ, 1995), p. 2306, and references therein.

¹⁴S. Yu, S. Eylon, E. Henestroza, and D. Grote, in Ref. 1, p. 134.

¹⁵C. Chen, Y. Fink, R. C. Davidson, and Q. Qian, *Proceedings of the 11th International Conference on High Power Particle Beams* (Institute of Plasma Physics, Academy of Sciences of the Czech Republic, 1996), p. 1018.

¹⁶Y. Fink, C. Chen, and W. P. Marable, Phys. Rev. E 55, 7557 (1997).

¹⁷M. Pabst, K. Bongardt, and A. P. Letchford, in Ref. 1, p. 343.

¹⁸R. W. Gamett, J. H. Billen, K. C. D. Chan, R. Genzlinger, E. R. Gray, S. Nath, R. Rusnak, D. L. Schrage, J. E. Stovall, H. Takeda, R. Wood, T. P. Wangler, and L. M. Young, in Ref. 1, p. 60.

¹⁹R. Pakter and C. Chen, *Proceedings of 1997 Particle Accelerator Conference* (IEEE, Piscataway, NJ, 1997), p. 1938.

- ²⁰H. Okamoto and M. Ikegami, Phys. Rev. E 55, 4694 (1997).
- ²¹A. J. Lichtenberg and M. A. Lieberman, *Regular and Chaotic Dynamics*, 2nd ed. (Springer, New York, 1992).
- ²²R. C. Davidson, *Physics of Nonneutral Plasmas* (Addison-Wesley, Reading, MA, 1990).
- ²³C. Chen, R. Pakter, and R. C. Davidson, Phys. Rev. Lett. 79, 225 (1997).
- ²⁴R. C. Davidson and C. Chen, Part. Accel. 59, 175 (1998).
- ²⁵I. M. Kapchinskij and V. V. Vladimirkij, in *Proceedings of the International Conference on High Energy Accelerators* [European Laboratory for Particle Physics (CERN), Geneva, 1959], p. 274.
- ²⁶M. Reiser, *Theory and Design of Charged-Particle Beams* (Wiley, New York, 1994).
- ²⁷H. Goldstein, *Classical Mechanics*, 2nd ed. (Addison-Wesley, Reading, MA, 1981).

Guiding Optical Light in Air Using an All-Dielectric Structure

Yoel Fink, Daniel J. Ripin, Shanhui Fan, Chiping Chen, John D. Joannopoulos, and Edwin L. Thomas

Abstract—The emergence of a dielectric omnidirectional multilayer structure [1]–[4] opens new opportunities for low loss broad-band guiding of light in air. We demonstrate the effectiveness of such an approach by fabricating a broad-band, low-loss hollow waveguide in the 10- μm region and measuring its transmission around a 90° bend. The generality of the solution enables the application of the method to many wavelengths of interest important in telecommunication applications as well as for guiding high-power lasers in medical and other fields of use.

Index Terms—Dielectric, high-power lasers, hollow waveguides, light conduits, low-loss broad-band transmission, medical lasers, multimode waveguide, omnidirectional reflectors, optical fibers, optical confinement, single-mode waveguide.

I. INTRODUCTION

GUIDING light in dielectric fibers has had a tremendous impact on many aspects of our life—we rely on fiber optics for communications as well as for illumination and a host of medical applications. The typical optical fiber has a high index core and a low index cladding such that the light is confined to the core by total internal reflection. Two inherent drawbacks exist in this approach: the first is absorption. Since the light is traveling through a dense medium for long distances, material absorption becomes significant even in low loss materials. To compensate for losses the fiber is doped with erbium which is used to amplify the signal. This in turn limits the bandwidth of the fiber to that of the narrow erbium excitation lines. The other weakness follows from the confinement mechanism—total internal reflection which confines light only of a limited angle. Conventional optical fibers cannot guide light around sharp turns, which is especially important in optical integrated circuits. Light guided in a hollow waveguide lined with an omnidirectional reflecting film propagates primarily through air and will therefore have substantially lower absorption losses. In addition, the confine-

ment mechanism does not have angular dependence allowing for guiding light around sharp bends with little or no leakage.

Most hollow waveguides fabricated to date [5]–[7], have internal metallic and dielectric layers. It has been shown [8] that the addition of dielectric layers to a metallic waveguide could lower the losses significantly. In contrast, our system is an all dielectric waveguide which confines all frequencies contained in its omnidirectional range. In principle this type of structure can have lower losses than the combined metal and dielectric structure since the waves do not interact with a lossy metallic layer. Although our proof of concept demonstration involves a large diameter multimode waveguide, one can fabricate a much smaller tube that could in principle be made to support a single mode.

II. PRINCIPLE OF OPERATION

A schematic of the hollow tube is presented in Fig. 1, as well as the index of refraction profile. In a realistic light guiding scenario involving many bends there exist no global symmetries and thus one cannot distinguish between independent TE and TM modes. Locally one can define a plane of incidence with respect to the normal to the film surface and the incident wave vector. Light entering into such a tube will invariably hit the walls many times and explore a wide range of angle of incidence of both polarizations with respect to any local plane of incidence. Since the air region is bounded by a structure that has a gap which encompasses all angles and polarizations the wave will be reflected back into the tube and will propagate along the hollow core as long as $k_z \neq 0$.

III. SAMPLE PREPARATION PROCEDURE

A Drummond 1.92 mm o.d. silica glass capillary tube was cleaned in concentrated sulfuric acid. The first tellurium layer was thermally evaporated using a LADD 30 000 evaporator fitted with a Sycon Instruments STM100 film thickness monitor. The capillary tube was axially rotated to ensure uniformity during coating. The first polymer layer was deposited by dip coating the capillary tube in a solution of 5.7 g polystyrene DOW 615APR in 90 g toluene. The next layer is tellurium deposited in the same method outlined above. The subsequent polymer layers are made of polyurethane diluted in mineral spirits. The device has a total of nine layers, five Te and four polymer and a total length of 10 cm. The layer thickness are approximately 0.8 μm for the tellurium layer (refractive index 4.6) and 1.6 μm for the polystyrene layer (refractive index 1.59). An optimal design will vary the layer thickness according to the zeros of the Bessel functions. Performance as

Manuscript received August 13, 1999. This work was supported in part by the Defense Advanced Research Agency through the U.S. Army Research Office under Grant DAAG55-97-1-0366 and by the Air Force Office of Scientific Research under Grants F49620-97-1-0325 and F49620-97-1-0385.

Y. Fink is with the Department of Materials Science and the Plasma Science and Fusion Center, Massachusetts Institute of Technology, Cambridge, MA 02139 USA (e-mail: yoel@mit.edu).

D. J. Ripin, S. Fan, and J. D. Joannopoulos are with the Department of Physics, Massachusetts Institute of Technology, Cambridge, MA 02139 USA (e-mail: shanhfan@mit.edu).

C. Chen is with the Plasma Science and Fusion Center, Massachusetts Institute of Technology, Cambridge, MA 02139 USA.

E. L. Thomas is with the Department of Materials Science, Massachusetts Institute of Technology, Cambridge, MA 02139 USA (e-mail: elt@mit.edu).

Publisher Item Identifier S 0733-8724(99)08813-1.

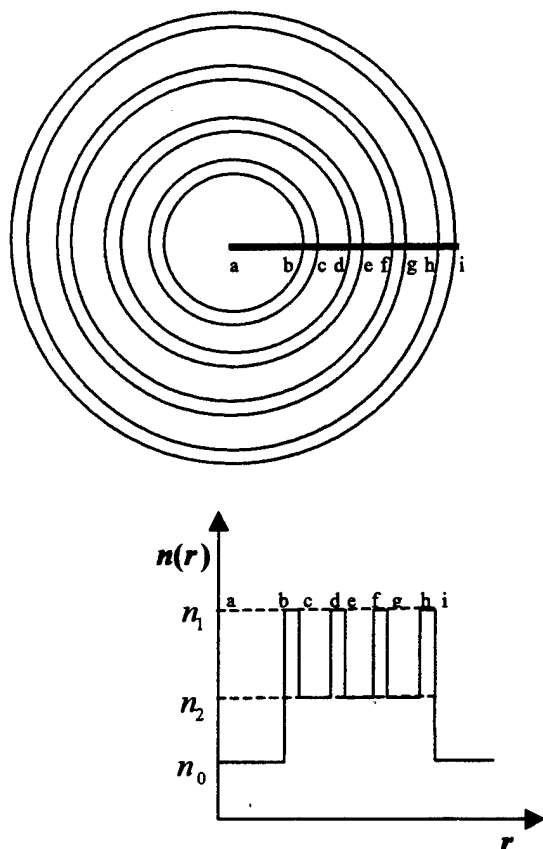


Fig. 1. Cross section of the hollow waveguide showing the hollow core and the dielectric films, also shown is the index of refraction profile in the radial direction.

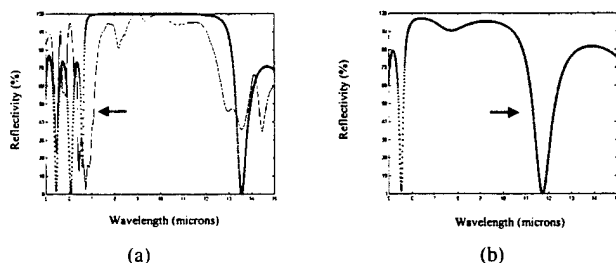


Fig. 2. (a) Measured (dashed) and calculated (dots) normal incidence reflectance for hollow waveguide in the radial direction. (b) Calculated grazing incidence reflectance for the TM mode.

well as the layer thickness were monitored by IR spectroscopy. The reflectivity of the deposited structure was measured in the radial direction using a Nicolet FTIR microscope and a variable size aperture, to ensure domination by radial reflection. The coated capillary tube was then inserted in a heat shrink tube which was filled with silicone rubber. Finally, the glass tube was dissolved using concentrated hydrofluoric acid (48%). The resulting hollow tube assembly is thus lined with the mirror coating and is both flexible and mechanically stable.

IV. RESULTS AND DISCUSSION

The reflectance measurements and simulations are shown for normal incidence in Fig. 2(a). The measured gap width is smaller than predicted, probably due to microdefects in the Te

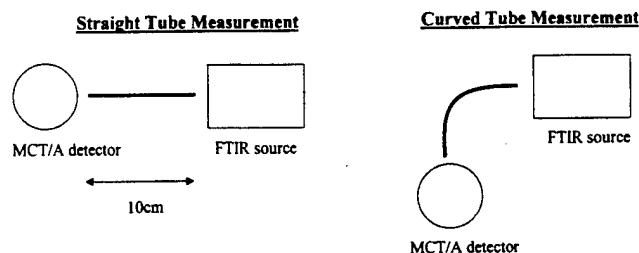


Fig. 3. Hollow tube transmission measurement setup on the spectrophotometer (FTIR).

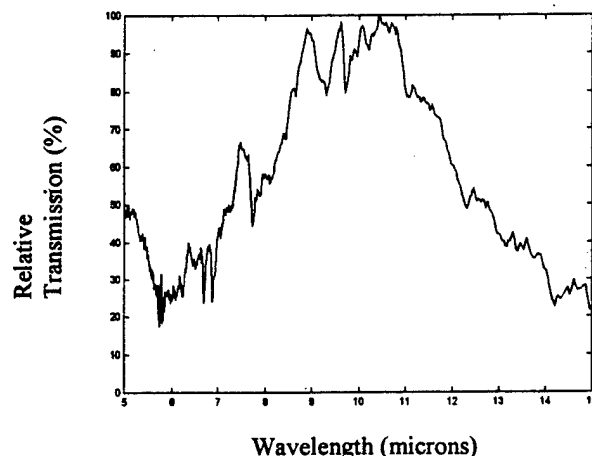


Fig. 4. Transmission through the hollow waveguide around a 90° bend as a function of wavelength.

layers. In addition there are absorption (8 μm) peaks due to the polyurethane. Fig. 2(b) is the calculation of the reflectance at grazing incidence for the TM mode. Since the omnidirectional frequency range is defined from above (high frequency edge) by the normal incidence gap edge (arrow) and from below by the grazing incidence gap edge (arrow) the extent of the gap is completely defined by these two data points. The extent of the omnidirectional range for the parameters used in this experiment is approximately 40% [1], [2].

The transmission through the tube was measured using a Nicolet Magna 860 FTIR bench with an MCT/A detector. The transmission was measured around a 90° bend at a radius of curvature of approximately 1 cm, which was compared, to the straight tube transmission to correct for entrance and exit effects. A schematic of the measurement layout is presented in Fig. 3.

The results shown in Fig. 4 indicate a high transmission around the 90° bend for a spectral band that corresponds to the omnidirectional gap. The relatively high noise level in the measurement is due to the lack of purge. This measurement provides a proof-of-concept indicating the low loss characteristics and guiding abilities of the all dielectric hollow waveguide.

ACKNOWLEDGMENT

The authors would like to thank T. McClure for valuable assistance in the optical setup. This work made use of the National Science Foundation Shared Experimental Analytical Facility.

REFERENCES

- [1] J. N. Winn, Y. Fink, S. Fan, and J. D. Joannopoulos. "Omnidirectional reflection from a one-dimensional photonic crystal." *Opt. Lett.*, vol. 23, no. 20, pp. 1573-1575, 1998.
 - [2] Y. Fink, J. N. Winn, S. Fan, J. Michel, C. Chen, J. D. Joannopoulos, and E. L. Thomas. "An omnidirectional dielectric reflector." *Science*, vol. 282, pp. 1679-1682, 1998.
 - [3] D. N. Chigrin, A. V. Lavrinenko, D. A. Yarotsky, and S. V. Gaponenko. "Observation of total omnidirectional reflection from a one-dimensional dielectric lattice." *Appl. Phys. A*, vol. 68, pp. 25-28, 1999.
 - [4] P. S. J. Russell, S. Tredwell, and P. J. Roberts. "Full photonic bandgaps and spontaneous emission control in 1D multilayer dielectric structures." *Opt. Commun.*, vol. 160, no. 1-3, pp. 66-71, 1999.
 - [5] M. Miyagi, A. Hongo, Y. Aizawa, and S. Kawakami. "Fabrication of germanium-coated nickel hollow waveguides for infrared transmission." *Appl. Phys. Lett.*, vol. 43, pp. 430-432, 1983.
 - [6] N. Croitoru, J. Dror, and I. Gannot. "Characterization of hollow fibers for the transmission of infrared radiation." *Appl. Opt.*, vol. 29, pp. 1805-1809, 1990.
 - [7] Y. Matsuura and J. Harrington. "Hollow glass waveguides with three-layer dielectric coating fabricated by chemical vapor deposition." *J. Opt. Soc. Amer.*, vol. 14, no. 6, 1997.
 - [8] M. Miyagi and S. Kawakami. "Design theory of dielectric coated circular metallic waveguides for infrared transmission." *J. Lightwave Technol.*, vol. LT-2, pp. 116-126, 1984.
 - [9] P. Yeh, A. Yariv, and E. Marom. "Theory of a Bragg fiber." *J. Opt. Soc. Amer.*, vol. 68, no. 9, 1978.
- Yoel Fink.** photograph and biography not available at the time of publication.
- Daniel J. Ripin.** photograph and biography not available at the time of publication.
- Shanhui Fan.** photograph and biography not available at the time of publication.
- Chiping Chen.** photograph and biography not available at the time of publication.
- John D. Joannopoulos.** photograph and biography not available at the time of publication.
- Edwin L. Thomas.** photograph and biography not available at the time of publication.

Stability properties of coherently gyrating relativistic electron beams

J. A. Davies^{a)} and C. Chen

Plasma Science and Fusion Center, Massachusetts Institute of Technology, Cambridge, Massachusetts 02139

(Received 14 November 1997; accepted 11 June 1998)

An investigation is made of the effects of nongyrotropic equilibrium distributions in the phase angle of p_{\perp} on the stability properties of a relativistic electron beam propagating along and gyrating about an applied uniform magnetic field. Perturbations are assumed to vary spatially only in the direction of the applied magnetic field, so that generated electromagnetic and longitudinal electric fields propagate parallel to the applied field. The two equilibrium distributions considered are the time-dependent distribution $f_0(p_{\perp}, p_z, \xi)$ with $\xi = \phi - \Omega_c t / \gamma$ and the axial-dependent distribution $f_0(p_{\perp}, p_z, \zeta)$ with $\zeta = \phi - m\Omega_c z / p_z$. A Vlasov-Maxwell analysis leads to integral equations relating the field Fourier components. These equations reduce to algebraic equations when no spread in γ is present in the time-dependent equilibrium distribution and when no spread in p_z is present in the axial-dependent distribution. Numerical computations for these special cases show that a rich variety of stability properties are obtained by changing the distributions in ξ and ζ . © 1998 American Institute of Physics. [S1070-664X(98)03309-6]

I. INTRODUCTION

During the past two decades, extensive studies have been made of the stability properties of a relativistic electron beam propagating along an applied uniform magnetic field $B_0 \hat{e}_z$.¹⁻¹² If the beam possesses a population inversion associated with the component of momentum perpendicular to the field (p_{\perp}), then this system may be subject to the whistler and cyclotron-resonance maser instabilities, which initiate the process of converting electron-beam kinetic energy into coherent electromagnetic radiation. The cyclotron-resonance maser instability provides the basis for existing and proposed electronic amplifiers and oscillators such as the gyrotron and the cyclotron-autoresonance maser.¹³⁻²⁴ With the inclusion of thermal background electrons in addition to the beam, this instability is of interest in such problems in space- and astrophysics²⁵⁻³⁰ as the generation of auroral kilometric and Jovian decametric radiation.

In this paper, we carry out a stability analysis of this system (exclusive of an ambient thermal background) using Vlasov-Maxwell theory. We make the assumption that the spatial variation of all quantities is in the z -direction only; however, the electron beam is not assumed to be gyrotropic in the phase angle ϕ of the component of the particle momentum normal to the z -axis. Most previous analyses of this system assume that the equilibrium distribution is of the form $f_0(p_{\perp}, p_z)$, i.e., that the beam is gyrotropic. Analyses of the nongyrotropic case are limited in number. Using the eikonal approximation, Fruchtman and Friedland have considered the case of a stationary amplifier with a nongyrotropic equilibrium distribution of the form $f_0(p_{\perp}, p_z, \xi) = p_{\perp}^{-1} \delta(p_{\perp} - p_{\perp 0}) \delta(p_z - p_{z0}) g(\xi)$, where $\xi = \phi - m\Omega_c z / p_z$ and Ω_c is the nonrelativistic cyclotron frequency. Both a

fluid model⁷ and a kinetic model⁸ were employed. Fruchtman⁹ has extended the kinetic model (without employing the eikonal approximation) to include a thermal spread in the transverse momentum. Kho *et al.*,¹⁰ using the same equilibrium distribution, have dropped the assumption of a stationary amplifier but assume that the left-hand polarized perturbed radiation field can be ignored. Chen *et al.*¹⁹ consider TE modes for the case of a helical relativistic electron beam in a cylindrical waveguide. In an application to space plasmas, Freund *et al.*²⁷ consider the case of a diffuse electron beam propagating in a cold magnetized ambient plasma. The beam is coherent in phase, and has a thermal spread in p_{\perp} but no spread in p_z .

Two equilibrium distributions are introduced in Sec. II. These are the time-dependent distribution $f_0(p_{\perp}, p_z, \xi)$ where $\xi = \phi - \Omega_c t / \gamma$ and the spatial-dependent distribution $f_0(p_{\perp}, p_z, \zeta)$ where $\zeta = \phi - m\Omega_c z / p_z$. By manipulating Fourier transforms of the Vlasov-Maxwell equations, we obtain sets of equations relating components of the perturbed right- and left-hand polarized electromagnetic and the electrostatic fields. For the time-dependent equilibrium, these relations are given in Eqs. (26)–(28). The relations for the spatial-dependent equilibrium distribution appear in Eqs. (41)–(43). In either case, these relations are integral equations, not algebraic equations. Equations (26)–(28) reduce to algebraic equations only if there is no spread in p (i.e., in γ) in the time-dependent equilibrium distribution. Moreover, Eqs. (41)–(43) reduce to algebraic equations only if there is no spread in p_z in the spatial-dependent equilibrium distribution.

The analysis of these integral equations is the subject of current research and is not dealt with further in this paper. Instead, in the remainder of the paper, we deal with cases in which the integral equations reduce to algebraic equations.

Stability properties for the case of the time-dependent equilibrium distribution with no spread in p are considered

^{a)}Permanent address: Department of Physics, Clark University, Worcester, Massachusetts 01610.

in Sec. III. Most generally, spreads in the pitch angle $\alpha = \tan^{-1}(p_{\perp}/p_z)$ and the phase angle ϕ may be present. In this case, the integral equations (26)–(28) reduce to just three algebraic relations presented in Eq. (58) of Sec. III A. The corresponding exact dispersion relation, relating complex frequencies and complex wave numbers, is the three by three determinant relation in Eq. (64). In Sec. III B, we consider the more restrictive case of no spread in the pitch angle α in the equilibrium distribution. (Then, both p_{\perp} and p_z have definite equilibrium values.) In this case, the dispersion relation in Eq. (64) reduces to the tenth-degree polynomial relation in Eq. (69). Numerical computations of growth-rate curves ($\text{Im } \hat{\omega}$ vs \hat{k} , real) and properties of eigenmodes of Eq. (58) are presented in Sec. III C for the case of definite equilibrium p_{\perp} and p_z and various equilibrium distributions in ϕ .

An analogous treatment is given in Sec. IV for the case of the axial-dependent equilibrium distribution with no spread in p_z . Spreads in p_{\perp} and ϕ are still permitted. For this case, it is shown in Sec. IV A that the integral equations (41)–(43) reduce to the three algebraic relations in Eq. (89). The exact dispersion relation for the system is given by the three by three determinant equation (95). Although no assumption of a steady state has been made in the derivation of Eq. (95), the result in Eq. (95) is the same as that obtained in the steady-state analysis of Ref. 9. In Sec. IV B, the additional condition that there be no equilibrium spread in p_{\perp} is imposed. Then (as in the time-dependent case) the dispersion relation reduces to the tenth-degree polynomial equation (100) relating the complex frequency and complex wave number. Numerical computations of growth-rate curves and properties of the eigenmodes of Eq. (89) for this case are presented in Sec. IV C.

A summary of our results and conclusions is presented in Sec. V.

II. FORMULATION OF THE PROBLEM

A beam consists of relativistic electrons, which propagate along and gyrate about a uniform magnetic field $\mathbf{B}_0 = B_0 \hat{e}_z$. Initially the beam is in an equilibrium state in which temporally and spatially varying electromagnetic fields are absent. The initial growth rates of these fields are obtained by regarding them as small perturbations on the equilibrium. The system is treated as one dimensional in the sense that the spatial variation of all variables is in the z -direction only. Consequently, only electromagnetic waves propagating parallel or antiparallel to the uniform field \mathbf{B}_0 are included in this analysis. Furthermore, equilibrium self-fields are assumed to be negligibly small, so that results discussed below are limited to the case of a small ratio of the plasma frequency to the cyclotron frequency.⁶

A. Equilibrium distributions

A single-particle momentum \mathbf{p} can be described by the components p_{\perp} , p_z , and ϕ , where ϕ is the phase angle (as shown in Fig. 1). This paper deals with two systems in which the phase angle ϕ is not necessarily random in the equilibrium distribution. One simple constant of the single-particle motion involving ϕ is $\xi = \phi - (\Omega_c/\gamma)t$, where Ω_c

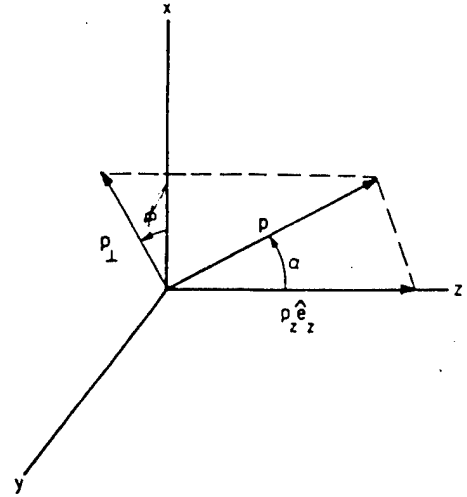


FIG. 1. The phase angle ϕ and the pitch angle α of the single particle momentum \mathbf{p} .

$= eB_0/mc$ is the nonrelativistic electron cyclotron frequency, $-e$ and m are the electron charge and rest mass, respectively, c is the speed of light *in vacuo*, t is the time, and $\gamma = (1 + p^2/m^2c^2)^{1/2} = (1 + p_{\perp}^2/m^2c^2 + p_z^2/m^2c^2)^{1/2}$ is the relativistic mass factor of the electron. An equilibrium distribution of the form

$$f_0(\mathbf{p}, t) = f_0(p_{\perp}, p_z, \xi), \quad (1)$$

where

$$\xi = \phi - \frac{\Omega_c}{\gamma}t, \quad (2)$$

corresponds to an equilibrium electron beam that is homogeneous in the configuration space at any given time. Since the equilibrium distribution (1) is nonstationary in the momentum space, we refer to it as the time-dependent equilibrium distribution.

Another simple constant of the single-particle motion involving ϕ is

$$\zeta = \phi - \frac{\Omega_c}{\gamma} \frac{z}{v_z} = \phi - m \frac{\Omega_c}{p_z} z, \quad (3)$$

where \mathbf{v} is the electron velocity. Use of ζ gives rise to an alternative equilibrium distribution

$$f_0(z, \mathbf{p}) = f_0(p_{\perp}, p_z, \zeta). \quad (4)$$

In this case, the equilibrium distribution is constant in time at any given z . It is analogous to a typical laboratory situation where the beam is introduced into the interaction region at some initial $z=0$ with a given distribution in ϕ . Then, if interactions with the electromagnetic field are excluded, the electrons move along the field lines with constant v_z and gyrate around them with the constant relativistic cyclotron frequency Ω_c/γ . Consequently, the phase at any value of z is the phase at $z=0$ plus $\Omega_c z/\gamma v_z$. We refer to this distribution as the axial-dependent equilibrium distribution.

The time- and axial-dependent distributions are illustrated with examples in Fig. 2. It is shown in the Appendix

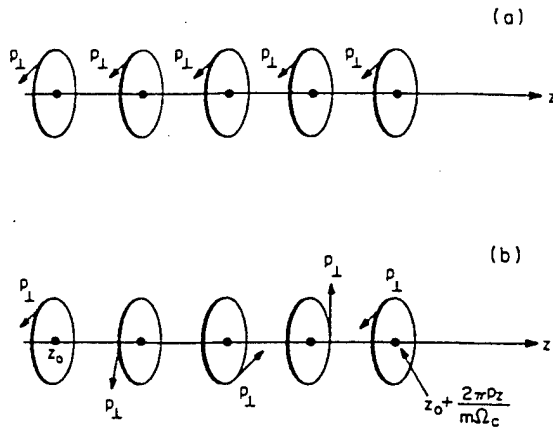


FIG. 2. Schematic diagrams of (a) the time-dependent phase distribution at a single instant of time for the case where $\xi=0$ for all particles, and (b) of the axial dependent distribution for all time for the case where $\xi=0$ for all particles.

that the two distributions in Eqs. (1) and (4) are physically different in the sense that neither can be transformed into the other by a Lorentz transformation.

In the remainder of this section, we derive linearized equations relating components of the perturbed electromagnetic fields for each of the distributions in Eqs. (1) and (4).

B. Perturbation analysis for the time-dependent equilibrium distribution

The equilibrium distribution is of the form in Eq. (1), i.e., $f_0(\mathbf{p}, t) = f_0(p_\perp, p_z, \xi) = f_0(p_\perp, p_z, \phi - \Omega_c t / \gamma)$. The distribution is assumed to be periodic in ξ and (for fixed t) in ϕ with period 2π . Consequently, the normalization of $f_0(p_\perp, p_z, \phi - \Omega_c t / \gamma)$ over momentum space is time-independent and is defined by

$$\int_{-\infty}^{\infty} dp_z \int_0^{\infty} dp_\perp \int_0^{2\pi} d\phi p_\perp f_0(p_\perp, p_z, \phi - \frac{\Omega_c}{\gamma} t) = 1. \quad (5)$$

As time progresses, the distribution evolves under perturbations into

$$f(z, \mathbf{p}, t) = f_0(\mathbf{p}, t) + f_1(z, \mathbf{p}, t), \quad (6)$$

where $f_1(z, \mathbf{p}, t)$ is considered to be a small perturbation. To first order in the perturbation, the time evolution of this quantity is governed by the linearized Vlasov equation,

$$\begin{aligned} \frac{df_1}{dt} \bigg|_0 &= \frac{\partial}{\partial t} f_1(z, \mathbf{p}, t) + v_z \frac{\partial}{\partial z} f_1(z, \mathbf{p}, t) \\ &\quad - \frac{e}{c} \mathbf{v} \times \mathbf{B}_0 \cdot \nabla_{\mathbf{p}} f_1(z, \mathbf{p}, t) \\ &= e \left(\mathbf{E}_1 + \frac{\mathbf{v} \times \mathbf{B}_1}{c} \right) \cdot \nabla_{\mathbf{p}} f_0(p_x, p_y, p_z, t), \end{aligned} \quad (7)$$

where the total time derivative is along a characteristic of the unperturbed motion [i.e., $z(t+\tau) = z + v_z \tau$, $p_z(t+\tau) = p_z$, $p_\perp(t+\tau) = p_\perp$, $\phi(t+\tau) = \phi + \Omega_c \tau / \gamma$, and the variable of integration τ is in the range from $-\infty$ to 0]. The fields $\mathbf{E}_1(z, t)$

and $\mathbf{B}_1(z, t)$ are regarded as small perturbations governed by Maxwell's equations, which in the present treatment reduce to

$$\frac{\partial^2}{\partial z^2} E_{1\pm}(z, t) - \frac{1}{c^2} \frac{\partial^2}{\partial t^2} E_{1\pm}(z, t) = \frac{4\pi}{c^2} \frac{\partial}{\partial t} J_{1\pm}(z, t), \quad (8)$$

$$\frac{\partial}{\partial z} E_{1\pm}(z, t) = \pm \frac{i}{c} \frac{\partial}{\partial t} B_{1\pm}(z, t), \quad (9)$$

$$\frac{\partial E_{1z}}{\partial z}(z, t) = 4\pi \rho_1(z, t), \quad (10)$$

$$B_{1z}(z, t) = 0. \quad (11)$$

In the above equations:

$$E_{1\pm}(z, t) = E_{1x}(z, t) \pm i E_{1y}(z, t), \quad (12)$$

$$B_{1\pm}(z, t) = B_{1x}(z, t) \pm i B_{1y}(z, t), \quad (13)$$

$$J_{1\pm}(z, t) = -en_0 \int d^3p f_1(z, \mathbf{p}, t) \frac{p_\pm}{\gamma m}, \quad (14)$$

$$\rho_1(z, t) = -en_0 \int d^3p f_1(z, \mathbf{p}, t), \quad (15)$$

$$p_\pm = \gamma m v_\pm = p_\perp \exp(\pm i\phi), \quad (16)$$

where n_0 is the mean electron number density. The fields (E_{1-}, B_{1-}) and (E_{1+}, B_{1+}) represent right- and left-hand circularly polarized transverse electromagnetic waves, respectively, whereas the field $(E_{1z}, B_{1z}=0)$ describes longitudinal (electrostatic) waves.

Because most of the integration of Eq. (7) along characteristics is standard, not all of the details will be given here. We remark that before integrating, it is convenient to express the x - and y -components of the vectors that appear in Eq. (7) in terms of v_\pm , $E_{1\pm}$, and $B_{1\pm}$. Moreover, $\partial f_0(p_x, p_y, p_z, t) / \partial p_x$, $\partial f_0(p_x, p_y, p_z, t) / \partial p_y$, and $\partial f_0(p_x, p_y, p_z, t) / \partial p_z$ must be expressed in terms of $\partial f_0(p_\perp, p_z, \xi) / \partial p_\perp$, $\partial f_0(p_\perp, p_z, \xi) / \partial p_z$, $\partial f_0(p_\perp, p_z, \xi) / \partial \xi$, because the latter partial derivatives are constant on a characteristic. Once these constant derivatives are removed from the integral sign, the subsequent calculation of the Fourier transform of $f_1(z, \mathbf{p}, t)$ is facilitated by rewriting them in terms of $\partial f_0(p_\perp, p_z, \phi, t) / \partial p_\perp$, $\partial f_0(p_\perp, p_z, \phi, t) / \partial p_z$, $\partial f_0(p_\perp, p_z, \phi, t) / \partial \phi$, and $\partial f_0(p_\perp, p_z, \phi, t) / \partial t$. The expression obtained for $f_1(z, \mathbf{p}, t)$ is

$$\begin{aligned}
f_1(z, p_\perp, p_z, \phi, t) = & U(p_\perp, p_z, \phi, t) \int_{-\infty}^0 d\tau \exp\left(i \frac{\Omega_c}{\gamma} \tau\right) E_{1-}(z + v_z \tau, t + \tau) \\
& + \frac{e}{2} \exp(i\phi) \frac{p_\perp \Omega_c}{\gamma^3 m^2 c^2} \frac{\partial}{\partial \phi} f_0(p_\perp, p_z, \phi, t) \int_{-\infty}^0 d\tau \exp\left(i \frac{\Omega_c}{\gamma} \tau\right) E_{1-}(z + v_z \tau, t + \tau) \\
& + V(p_\perp, p_z, \phi, t) \int_{-\infty}^0 d\tau \exp\left(i \frac{\Omega_c}{\gamma} \tau\right) B_{1-}(z + v_z \tau, t + \tau) \\
& + U^*(p_\perp, p_z, \phi, t) \int_{-\infty}^0 d\tau \exp\left(-i \frac{\Omega_c}{\gamma} \tau\right) E_{1+}(z + v_z \tau, t + \tau) \\
& + \frac{e}{2} \exp(-i\phi) \frac{p_\perp \Omega_c}{\gamma^3 m^2 c^2} \frac{\partial}{\partial \phi} f_0(p_\perp, p_z, \phi, t) \int_{-\infty}^0 d\tau \exp\left(-i \frac{\Omega_c}{\gamma} \tau\right) E_{1+}(z + v_z \tau, t + \tau) \\
& + V^*(p_\perp, p_z, \phi, t) \int_{-\infty}^0 d\tau \exp\left(-i \frac{\Omega_c}{\gamma} \tau\right) B_{1+}(z + v_z \tau, t + \tau) + e \frac{\partial}{\partial p_z} f_0(p_\perp, p_z, \phi, t) \\
& \times \int_{-\infty}^0 d\tau E_{1z}(z + v_z \tau, t + \tau) + \frac{e p_z \Omega_c}{\gamma^3 m^2 c^2} \frac{\partial}{\partial \phi} f_0(p_\perp, p_z, \phi, t) \int_{-\infty}^0 d\tau \tau E_{1z}(z + v_z \tau, t + \tau). \quad (17)
\end{aligned}$$

In the above equation,

$$\begin{aligned}
U(p_\perp, p_z, \phi, t) = & \frac{e}{2} \exp(i\phi) \left(\frac{\partial}{\partial p_\perp} + \frac{i}{p_\perp} \frac{\partial}{\partial \phi} \right) f_0(p_\perp, p_z, \phi, t), \\
V(p_\perp, p_z, \phi, t) = & \frac{e}{2} \frac{\exp(i\phi)}{\gamma m c} \left(-i p_z \frac{\partial}{\partial p_\perp} + i p_\perp \frac{\partial}{\partial p_z} + \frac{p_z}{p_\perp} \frac{\partial}{\partial \phi} \right) f_0(p_\perp, p_z, \phi, t).
\end{aligned}$$

In order to relate components of the perturbed electromagnetic fields, it is necessary to obtain Fourier (or Laplace) transforms of $f_1(z, \mathbf{p}, t)$ [Eq. (17)] and of Maxwell's equations (8)–(11). The simple assumption that all variables vary as $\exp[i(kz - \omega t)]$ leads to inconsistent results. In general, one cannot assume an infinite series of terms of the form $\exp\{i[kz - (\omega - n\Omega_c/\gamma)t]\}$ (where n is an integer), because γ is not defined if $f_0(p_\perp, p_z, \xi)$ contains an energy spread. In the present analysis, we define the spatial and temporal Fourier transforms by

$$F(k, \omega) = \frac{1}{2\pi} \int_{-\infty}^{\infty} dz \int_{-\infty}^{\infty} dt F(z, t) \exp[i(\omega t - kz)], \quad (18)$$

$$F(z, t) = \frac{1}{2\pi} \int_{-\infty}^{\infty} dk \int_{-\infty}^{\infty} d\omega F(k, \omega) \exp[i(kz - \omega t)].$$

The calculation of the Fourier transform of $f_1(z, \mathbf{p}, t)$, denoted by $f_1(k, \mathbf{p}, \omega)$, requires use of the convolution theorem

$$(F_1 F_2)(k, \omega) = \frac{1}{2\pi} \int_{-\infty}^{\infty} dk' \int_{-\infty}^{\infty} d\omega' F_1(k', \omega') F_2(k - k', \omega - \omega'). \quad (19)$$

Then, using Eqs. (17)–(19), together with the Fourier transform of the Maxwell equation (9), and assuming that orders of multiple integrals can be interchanged, we obtain (after a lengthy calculation) the following expression for the Fourier transform:

$$\begin{aligned}
f_1(k, p, \omega) = & \frac{1}{2} \frac{e}{\sqrt{2\pi}} \exp(i\phi) \int_{-\infty}^{+\infty} d\omega' \left\{ \left[\omega - \omega' - kv_z - \frac{\Omega_c}{\gamma} \right]^{-1} \left[\frac{\omega - \omega' - kv_z}{\omega - \omega'} \left(i \frac{\partial}{\partial p_\perp} - \frac{1}{p_\perp} \frac{\partial}{\partial \phi} \right) + i \frac{p_\perp}{\gamma m c} \frac{ck}{\omega - \omega'} \frac{\partial}{\partial p_z} \right] \right. \\
& \times f_0(p_\perp, p_z, \phi, \omega') + \left[\omega - \omega' - kv_z - \frac{\Omega_c}{\gamma} \right]^{-2} \frac{p_\perp \Omega_c}{\gamma^3 m^2 c^2} \frac{\partial}{\partial \phi} f_0(p_\perp, p_z, \phi, \omega') \left. \right\} E_{1-}(k, \omega - \omega') \\
& + \frac{1}{2} \frac{e}{\sqrt{2\pi}} \exp(-i\phi) \int_{-\infty}^{+\infty} d\omega' \left\{ \left[\omega - \omega' - kv_z + \frac{\Omega_c}{\gamma} \right]^{-1} \left[\frac{\omega - \omega' - kv_z}{\omega - \omega'} \left(i \frac{\partial}{\partial p_\perp} + \frac{1}{p_\perp} \frac{\partial}{\partial \phi} \right) \right. \right. \\
& + i \frac{p_\perp}{\gamma m c} \frac{ck}{\omega - \omega'} \frac{\partial}{\partial p_z} \left. \right] f_0(p_\perp, p_z, \phi, \omega') + \left[\omega - \omega' - kv_z + \frac{\Omega_c}{\gamma} \right]^{-2} \frac{p_\perp \Omega_c}{\gamma^3 m^2 c^2} \frac{\partial}{\partial \phi} f_0(p_\perp, p_z, \phi, \omega') \left. \right\} \\
& \times E_{1+}(k, \omega - \omega') + \frac{e}{\sqrt{2\pi}} \int_{-\infty}^{+\infty} d\omega' \left\{ [\omega - \omega' - kv_z]^{-1} i \frac{\partial}{\partial p_z} f_0(p_\perp, p_z, \phi, \omega') \right. \\
& + [\omega - \omega' - kv_z]^{-2} \frac{p_z \Omega_c}{\gamma^3 m^2 c^2} \frac{\partial}{\partial \phi} f_0(p_\perp, p_z, \phi, \omega') \left. \right\} E_{1z}(k, \omega - \omega'). \quad (20)
\end{aligned}$$

The Fourier transforms of the Maxwell equations (8) and (10) are

$$\begin{aligned}
(\omega^2 - c^2 k^2) E_{1\pm}(k, \omega) \\
= 4\pi i e n_0 \int_0^\infty dp_\perp \int_{-\infty}^\infty dp_z \int_0^{2\pi} d\phi \frac{p_\perp^2}{\gamma m} \\
\times \exp(\pm i\phi) f_1(k, p_\perp, p_z, \phi, \omega), \quad (21)
\end{aligned}$$

$$\begin{aligned}
k E_{1z}(k, \omega) \\
= 4\pi i e n_0 \int_0^\infty dp_\perp \int_{-\infty}^\infty dp_z \int_0^{2\pi} d\phi p_\perp f_1(k, p_\perp, p_z, \phi, \omega). \quad (22)
\end{aligned}$$

By referring to Eq. (20), it is seen that Eqs. (21) and (22) are a set of integral equations (with variable of integration ω') relating the Fourier transforms of the fields $E_{1\pm}$ and E_{1z} .

Partial derivatives of $f_0(p_\perp, p_z, \phi, \omega')$ appear in the expression for $f_1(k, p, \omega)$ in Eq. (20). These derivatives are removed from the integrands in Eqs. (21) and (22) by integrating by parts with respect to p_\perp , p_z , and ϕ , employing the periodicity of $f_0(p_\perp, p_z, \phi, \omega')$ in ϕ . The procedure is straightforward but requires much algebra.

The periodicity of $f_0(p_\perp, p_z, \xi)$ in ξ (or ϕ) has not yet been fully employed in this analysis. Expansion of $f_0(p_\perp, p_z, \xi)$ in a Fourier series gives

$$f_0(p_\perp, p_z, \xi) = \frac{1}{\sqrt{2\pi}} \sum_{n=-\infty}^{+\infty} g_n(p_\perp, p_z) \exp(in\xi), \quad (23)$$

where

$$g_n(p_\perp, p_z) = \frac{1}{\sqrt{2\pi}} \int_0^{2\pi} d\xi f_0(p_\perp, p_z, \xi) \exp(-in\xi). \quad (24)$$

Because $f_0(p_\perp, p_z, \xi)$ is real, $g_n^*(p_\perp, p_z) = g_{-n}(p_\perp, p_z)$. From Eq. (23), we see that the temporal Fourier transform of $f_0(p_\perp, p_z, \xi) = f_0(p_\perp, p_z, \phi, t)$ is given by

$$f_0(p_\perp, p_z, \phi, \omega) = \sum_{n=-\infty}^{+\infty} g_n(p_\perp, p_z) \exp(in\phi) \delta\left(\omega - n \frac{\Omega_c}{\gamma}\right). \quad (25)$$

With the aid of Eq. (25), the integrations over ω' can be carried out in Eqs. (21) and (22). Moreover, with the aid of the relation $\int_0^{2\pi} d\phi \exp(in\phi) = 2\pi \delta_{n0}$, the integrals over ϕ can also be completed. In fact, only the $n=0, 1$, and -1 terms of the infinite series in Eq. (25) contribute to the right-hand sides of Eqs. (21) and (22). In the nonrelativistic limit of $\gamma=1$, the integral equations in (21) and (22) reduce to algebraic equations relating the Fourier transforms of the fields $E_{1\pm}$ and E_{1z} because of the Dirac delta function in Eq. (25). However, in the general case, $\gamma = (p^2/m^2 c^2 + 1)^{1/2} = [(p_\perp^2 + p_z^2)/m^2 c^2 + 1]^{1/2}$. Consequently, Eqs. (21) and (22) remain integral equations in the two variables p_\perp and p_z , relating such unknown functions as $E_{1-}(k, \omega + 2\Omega_c/\gamma(p_\perp, p_z))$, $E_{1z}(k, \omega + \Omega_c/\gamma(p_\perp, p_z))$, and $E_{1+}(k, \omega)$.

Equations (21) and (22) can be reduced to a set of integral equations in the single variable p by replacing the variables p_\perp and p_z with the new variables p and α , where $\alpha = \tan^{-1}(p_\perp/p_z)$ is the pitch angle shown in Fig. 1. Setting $dp_\perp dp_z = p dp d\alpha$ in the equations obtained from Eqs. (21) and (22), we obtain the following set of simultaneous integral equations relating the Fourier transforms of the perturbed fields $E_{1\pm}$ and E_{1z} :

$$\begin{aligned}
D_{--}(k, \omega, \Omega_c) E_{1-}(k, \omega) \\
= \int_0^\infty dp p^2 \chi_{-+}(k, \omega, \Omega_c, p) E_{1+}\left(k, \omega - \frac{2\Omega_c}{\gamma(p)}\right) \\
+ \int_0^\infty dp p^2 \chi_{-z}(k, \omega, \Omega_c, p) E_{1z}\left(k, \omega - \frac{\Omega_c}{\gamma(p)}\right), \quad (26)
\end{aligned}$$

$$\begin{aligned}
D_{++}(k, \omega, \Omega_c) E_{1+}(k, \omega) \\
= \int_0^\infty dp p^2 \chi_{+-}(k, \omega, \Omega_c, p) E_{1-} \left(k, \omega + \frac{2\Omega_c}{\gamma(p)} \right) \\
+ \int_0^\infty dp p^2 \chi_{+z}(k, \omega, \Omega_c, p) E_{1z} \left(k, \omega + \frac{\Omega_c}{\gamma(p)} \right), \quad (27)
\end{aligned}$$

$$\begin{aligned}
D_{zz}(k, \omega) E_{1z}(k, \omega) \\
= \int_0^\infty dp p^2 \chi_{z+}(k, \omega, \Omega_c, p) E_{1+} \left(k, \omega - \frac{\Omega_c}{\gamma(p)} \right) \\
+ \int_0^\infty dp p^2 \chi_{z-}(k, \omega, \Omega_c, p) E_{1-} \left(k, \omega + \frac{\Omega_c}{\gamma(p)} \right). \quad (28)
\end{aligned}$$

In the above integral equations:

$$\begin{aligned}
D_{--}(k, \omega, \Omega_c) \\
= \omega^2 - c^2 k^2 - \frac{\sqrt{2}\pi}{2} \Omega_p^2 \int_0^\infty dp \int_0^\pi d\alpha p g_0(p, \alpha) \\
\times \left[\frac{2p \sin \alpha}{\gamma} \left(\omega - \frac{k p \cos \alpha}{\gamma m} \right) \left(\omega - \frac{k p \cos \alpha}{\gamma m} - \frac{\Omega_c}{\gamma} \right)^{-1} \right. \\
\left. - \frac{p^3 \sin^3 \alpha}{\gamma^3 m^2 c^2} \left(\omega^2 - c^2 k^2 \right) \left(\omega - \frac{k p \cos \alpha}{\gamma m} - \frac{\Omega_c}{\gamma} \right)^{-2} \right], \quad (29)
\end{aligned}$$

$$D_{++}(k, \omega, \Omega_c) = D_{--}(k, \omega, -\Omega_c), \quad (30)$$

$$\begin{aligned}
D_{zz}(k, \omega) = 1 - \sqrt{2}\pi \Omega_p^2 \int_0^\infty dp \int_0^\pi d\alpha p^2 g_0(p, \alpha) \\
\times \frac{\sin \alpha}{\gamma} \left(1 - \frac{p^2 \cos^2 \alpha}{\gamma^2 m^2 c^2} \right) \left(\omega - \frac{k p \cos \alpha}{\gamma m} \right)^{-2}, \quad (31)
\end{aligned}$$

$$\begin{aligned}
\chi_{+-}(k, \omega, \Omega_c, p) = -\frac{\sqrt{2}\pi}{2} \Omega_p^2 \omega \int_0^\pi d\alpha p^2 g_2(p, \alpha) \\
\times \frac{\sin^3 \alpha}{\gamma^3 m^2 c^2} \left(\omega - \frac{2\Omega_c}{\gamma} \right)^{-1} \\
\times \left(\omega^2 - 2\omega \frac{\Omega_c}{\gamma} - c^2 k^2 \right) \\
\times \left(\omega - \frac{k p \cos \alpha}{\gamma m} - \frac{\Omega_c}{\gamma} \right)^{-2}, \quad (32)
\end{aligned}$$

$$\chi_{+-}(k, \omega, \Omega_c, p) = \chi_{-+}^*(k^*, \omega^*, -\Omega_c, p), \quad (33)$$

$$\begin{aligned}
\chi_{-z}(k, \omega, \Omega_c, p) = -\sqrt{2}\pi \omega \Omega_p^2 \int_0^\pi d\alpha p g_1(p, \alpha) \\
\times \frac{\sin^2 \alpha}{\gamma^2 m c} \left(\frac{\omega p \cos \alpha}{\gamma m c} - c k \right) \\
\times \left(\omega - \frac{k p \cos \alpha}{\gamma m} - \frac{\Omega_c}{\gamma} \right)^{-2}, \quad (34)
\end{aligned}$$

$$\chi_{+z}(k, \omega, \Omega_c, p) = \chi_{-z}^*(k^*, \omega^*, -\Omega_c, p), \quad (35)$$

$$\begin{aligned}
\chi_{z-}(k, \omega, \Omega_c, p) \\
= -\frac{\sqrt{2}\pi}{2} \Omega_p^2 \left(\omega + \frac{\Omega_c}{\gamma} \right)^{-1} \int_0^\pi d\alpha p g_{-1}(p, \alpha) \\
\times \frac{\sin^2 \alpha}{\gamma^2 m c} \left[\frac{p \cos \alpha}{\gamma m c} \left(\omega + \frac{\Omega_c}{\gamma} \right) - c k \right] \left(\omega - \frac{k p \cos \alpha}{\gamma m} \right)^{-2} \\
= \frac{1}{2} \left(\omega + \frac{\Omega_c}{\gamma} \right)^{-2} \chi_{-z}^* \left(k^*, \omega^* + \frac{\Omega_c}{\gamma}, \Omega_c, p \right), \quad (36)
\end{aligned}$$

$$\chi_{z+}(k, \omega, \Omega_c, p) = \chi_{z-}^*(k^*, \omega^*, -\Omega_c, p). \quad (37)$$

Here $\Omega_p = (4\pi n_0 e^2 / m)^{1/2}$ is the nonrelativistic plasma frequency.

Notice that the structure of Eqs. (26)–(28) is a coupling of $E_{1-}(k, \omega')$, $E_{1z}(k, \omega' - [\Omega_c / \gamma(p)])$, and $E_{1+}(k, \omega' - [2\Omega_c / \gamma(p)])$ over the range of p for which the equilibrium distribution is nonvanishing.

C. Perturbation analysis for the axial-dependent equilibrium distribution

The analysis for the case of the equilibrium distribution in Eq. (4), i.e., $f_0(z, \mathbf{p}) = f_0(p_\perp, p_z, \zeta) = f_0(p_\perp, p_z, \phi - m\Omega_c z / p_z)$ is similar to the analysis of the previous section. The distribution is assumed periodic in ζ and (for fixed z) in ϕ with period 2π . Consequently, the normalization of $f_0(p_\perp, p_z, \phi - m\Omega_c z / p_z)$ over momentum space is independent of z . It is defined to be

$$\int_{-\infty}^\infty dp_z \int_0^\infty dp_\perp \int_0^{2\pi} d\phi p_\perp f_0 \left(p_\perp, p_z, \phi - m \frac{\Omega_c}{p_z} z \right) = 1. \quad (38)$$

The linearized Vlasov equation for the system is the same as Eq. (7) except that the factor $f_0(p_x, p_y, p_z, t)$ on the right-hand side is to be replaced with $f_0(z, p_x, p_y, p_z)$. Maxwell's equations (8)–(16) are applicable without modification. The derivation of integral equations relating the Fourier transforms of the perturbed fields involves a great deal of algebra but closely parallels that given in Sec. II B for the spatially homogeneous equilibrium distribution. Consequently, we omit the details of the derivation. We remark that in the present derivation z plays much the same role as t in the previous derivation and k much the same role as ω . Periodicity of $f_0(p_\perp, p_z, \zeta)$ in ζ gives rise to the Fourier series expansion

$$f_0(p_\perp, p_z, \zeta) = \frac{1}{\sqrt{2\pi}} \sum_{n=-\infty}^{+\infty} h_n(p_\perp, p_z) \exp(in\zeta), \quad (39)$$

where

$$h_n(p_\perp, p_z) = \frac{1}{\sqrt{2\pi}} \int_0^{2\pi} d\zeta f_0(p_\perp, p_z, \zeta) \exp(-in\zeta). \quad (40)$$

For the z -dependent equilibrium distribution $f_0(p_\perp, p_z, \phi - m\Omega_c z / p_z)$, the integral equations are

$$\begin{aligned}
D'_{-}(k, \omega, \Omega_c) E_{1-}(k, \omega) \\
= \int_{-\infty}^{\infty} dp_z \eta_{-+}(k, \omega, \Omega_c, p_z) E_{1+} \left(k + \frac{2m\Omega_c}{p_z}, \omega \right) \\
+ \int_{-\infty}^{\infty} dp_z \eta_{-z}(k, \omega, \Omega_c, p_z) E_{1z} \left(k + \frac{m\Omega_c}{p_z}, \omega \right), \quad (41)
\end{aligned}$$

$$\begin{aligned}
D'_{++}(k, \omega, \Omega_c) E_{1+}(k, \omega) \\
= \int_{-\infty}^{\infty} dp_z \eta_{+-}(k, \omega, \Omega_c, p_z) E_{1-} \left(k - \frac{2m\Omega_c}{p_z}, \omega \right) \\
+ \int_{-\infty}^{\infty} dp_z \eta_{+z}(k, \omega, \Omega_c, p_z) E_{1z} \left(k - \frac{m\Omega_c}{p_z}, \omega \right), \quad (42)
\end{aligned}$$

$$\begin{aligned}
D'_{zz}(k, \omega) E_{1z}(k, \omega) \\
= \int_{-\infty}^{\infty} dp_z \eta_{z-}(k, \omega, \Omega_c, p_z) E_{1-} \left(k - \frac{m\Omega_c}{p_z}, \omega \right) \\
+ \int_{-\infty}^{\infty} dp_z \eta_{z+}(k, \omega, \Omega_c, p_z) E_{1+} \left(k + \frac{m\Omega_c}{p_z}, \omega \right). \quad (43)
\end{aligned}$$

In the above integral equations:

$$\begin{aligned}
D'_{-}(k, \omega, \Omega_c) \\
= \omega^2 - c^2 k^2 - \frac{\sqrt{2}\pi}{2} \Omega_p^2 \int_{-\infty}^{\infty} dp_z \int_0^{\infty} dp_{\perp} h_0(p_{\perp}, p_z) \frac{p_{\perp}}{\gamma} \\
\times \left[2 \left(\omega - \frac{kp_z}{\gamma m} \right) \left(\omega - \frac{kp_z}{\gamma m} - \frac{\Omega_c}{\gamma} \right)^{-1} \right. \\
\left. - \frac{p_{\perp}^2}{\gamma^2 m^2 c^2} (\omega^2 - c^2 k^2) \left(\omega - \frac{kp_z}{\gamma m} - \frac{\Omega_c}{\gamma} \right)^{-2} \right], \quad (44)
\end{aligned}$$

$$D'_{++}(k, \omega, \Omega_c) = D'_{-}(k, \omega, -\Omega_c), \quad (45)$$

$$\begin{aligned}
D'_{zz}(k, \omega) = 1 - \sqrt{2}\pi \Omega_p^2 \int_{-\infty}^{\infty} dp_z \int_0^{\infty} dp_{\perp} p_{\perp} h_0(p_{\perp}, p_z) \\
\times \gamma^{-1} \left(1 - \frac{p_z^2}{\gamma^2 m^2 c^2} \right) \left(\omega - \frac{kp_z}{\gamma m} \right)^{-2}, \quad (46)
\end{aligned}$$

$$\begin{aligned}
\eta_{-+}(k, \omega, \Omega_c, p_z) \\
= \frac{\sqrt{2}\pi}{2} \Omega_p^2 \int_0^{\infty} dp_{\perp} h_2(p_{\perp}, p_z) \frac{p_{\perp}^3}{\gamma^3 m^2 c^2} \\
\times \left[-\omega^2 + c^2 k^2 \left(k + \frac{2m\Omega_c}{p_z} \right) \right] \left(\omega - \frac{kp_z}{\gamma m} - \frac{\Omega_c}{\gamma} \right)^{-2}, \quad (47)
\end{aligned}$$

$$\eta_{+-}(k, \omega, \Omega_c, p_z) = \eta_{-+}^*(k^*, \omega^*, -\Omega_c, p_z), \quad (48)$$

$$\begin{aligned}
\eta_{-z}(k, \omega, \Omega_c, p_z) = \sqrt{2}\pi \Omega_p^2 \omega \int_0^{\infty} dp_{\perp} h_1(p_{\perp}, p_z) \frac{p_{\perp}^2}{\gamma^3 m^2 c^2} \\
\times (-\omega p_z + k \gamma m c^2) \left(\omega - \frac{kp_z}{\gamma m} - \frac{\Omega_c}{\gamma} \right)^{-2}, \quad (49)
\end{aligned}$$

$$\eta_{+z}(k, \omega, \Omega_c, p_z) = \eta_{-z}^*(k^*, \omega^*, -\Omega_c, p_z), \quad (50)$$

$$\begin{aligned}
\eta_{z-}(k, \omega, \Omega_c, p_z) = \frac{\sqrt{2}\pi}{2} \frac{\Omega_p^2}{k} \int_0^{\infty} dp_{\perp} h_{-1}(p_{\perp}, p_z) \frac{p_{\perp}^2}{\gamma^2 m c^2} \\
\times \left[-\frac{kp_z}{\gamma m} + \frac{c^2 k}{\omega} \left(k - \frac{m\Omega_c}{p_z} \right) \right] \\
\times \left(\omega - \frac{kp_z}{\gamma m} \right)^{-2}, \quad (51)
\end{aligned}$$

$$\eta_{z+}(k, \omega, \Omega_c, p_z) = \eta_{z-}^*(k^*, \omega^*, -\Omega_c, p_z). \quad (52)$$

The structure of Eqs. (41)–(43) is the coupling of $E_{1-}(\hat{k}', \omega)$ to $E_{1z}(\hat{k}' + m\Omega_c/p_z, \omega)$ and $E_{1+}(\hat{k}' + 2m\Omega_c/p_z, \omega)$ over the range of p_z for which the equilibrium distribution is nonvanishing.

D. Some special cases

In general Eqs. (26)–(28) [Eqs. (41)–(43)] couple the right- and left-hand circularly polarized radiation fields $E_{1\pm}$ and the longitudinal, relativistic, plasma wave field E_{1z} . However, if $g_{\pm 1}(p_{\perp}, p_z) = g_{\pm 1}(p, \alpha) = 0$ [$h_{\pm 1}(p_{\perp}, p_z) = 0$], then Eq. (28) decouples from Eqs. (26) and (27) [Eq. (43) decouples from Eqs. (41) and (42)] to yield the dispersion relation for longitudinal plasma oscillations. The radiation fields remain coupled. From Eq. (24) [Eq. (40)], it is seen that this situation occurs whenever the Fourier series for $f_0(p_{\perp}, p_z, \phi - \Omega_c t / \gamma)$ [$f_0(p_{\perp}, p_z, \phi - m\Omega_c z / p_z)$] contains neither $\cos \phi$ nor $\sin \phi$ components.

If $g_{\pm 2}(p_{\perp}, p_z) = g_{\pm 2}(p, \alpha) = 0$ [$h_{\pm 2}(p_{\perp}, p_z) = 0$] then all three fields ($E_{1\pm}$ and E_{1z}) remain coupled, however, the radiation fields couple only through the electrostatic oscillations and not directly with each other. From Eq. (24) [Eq. (40)], it is seen that this situation occurs whenever the Fourier series for $f_0(p_{\perp}, p_z, \phi - (\Omega_c / \gamma) t)$ [$f_0(p_{\perp}, p_z, \phi - (m\Omega_c / p_z) z)$] contains neither $\cos 2\phi$ nor $\sin 2\phi$ components.

Finally, if $g_{\pm 1}(p_{\perp}, p_z) = g_{\pm 2}(p_{\perp}, p_z) = 0$ [$h_{\pm 1}(p_{\perp}, p_z) = h_{\pm 2}(p_{\perp}, p_z) = 0$], then Eqs. (26)–(28) [Eqs. (41)–(43)] decouple completely and reduce to the dispersion relations

$$D_{--}(k, \omega, \Omega_c) = 0, \quad (53)$$

$$D_{++}(k, \omega, \Omega_c) = 0, \quad (54)$$

$$D_{zz}(k, \omega) = 0. \quad (55)$$

These dispersion relations are identical to those for the case in which the distribution in ϕ is uniformly random. Referring to Eqs. (24) and (40), we see that $g_0(p_{\perp}, p_z)$

$= (1/\sqrt{2\pi}) \int_0^{2\pi} d\xi f_0(p_\perp, p_z, \xi)$ and $h_0(p_\perp, p_z) = (1/\sqrt{2\pi}) \times \int_0^{2\pi} d\eta f_0(p_\perp, p_z, \eta)$. For the case of a uniformly random distribution in ϕ [i.e., $f_0(p_\perp, p_z)$], both of these expressions reduce to $g_0(p_\perp, p_z) = h_0(p_\perp, p_z) = \sqrt{2\pi} f_0(p_\perp, p_z)$. For this case either Eqs. (26) and (27) or Eqs. (41) and (42) reduce to the dispersion relations for the cyclotron resonance maser with random phase obtained by Chu and Hirshfield.¹

The analysis of Eqs. (26)–(28) [(41)–(43)] as integral equations is the subject of present research and results of the analysis will be presented in a subsequent paper. However, many important special cases exist in which the equations reduce to algebraic equations from which dispersion relations can be derived. Some of these cases will be analyzed in the remainder of this paper.

III. DISPERSION CHARACTERISTICS FOR THE TIME-DEPENDENT EQUILIBRIUM DISTRIBUTION WITHOUT ENERGY SPREAD

In the previous section, it was noted that, for a uniformly random equilibrium distribution in ϕ , Eqs. (26)–(28) decouple and reduce to the well known dispersion relations in Eqs. (53)–(55). In this section it is shown that as long as there is no energy spread in the equilibrium distribution in Eq. (1), the integral equations (26)–(28) reduce to algebraic relations between the Fourier components of the fields even when the distributions are not uniform in ϕ . The dispersion characteristics are illustrated with numerical examples for the time-dependent equilibrium distribution with no spread in p_\perp or p_z .

A. Analysis

For a beam with a definite energy $\gamma(p_0)mc^2 \equiv \gamma_0 mc^2 = (p_0^2 c^2 + m^2 c^4)^{1/2}$ the most general distribution in Eq. (1) is of the form

$$f_0(p, \alpha, \xi) = \frac{1}{p^2} \delta(p - p_0) \hat{f}_0(p_0, \alpha, \xi), \quad (56)$$

where $\xi = \phi - \Omega_c t / \gamma$. From Eq. (24), the coefficients in the Fourier series expansion of this distribution are

$$g_n(p, \alpha) = \frac{1}{p^2} \delta(p - p_0) \hat{g}_n(p_0, \alpha), \quad (57)$$

$$\hat{g}_n(p_0, \alpha) = \frac{1}{\sqrt{2\pi}} \int_0^{2\pi} d\xi \hat{f}_0(p_0, \alpha, \xi) \exp(-in\xi).$$

Substitute Eq. (57) into Eqs. (29)–(37) and then substitute the results into the integral equations (26)–(28). After replacing ω with $\omega - 2\Omega_c / \gamma_0$ in Eq. (27) and with $\omega - \Omega_c / \gamma_0$ in Eq. (28), we obtain three homogeneous algebraic equations relating just three field components. Expressed in matrix notation, these equations are

$$\mathbf{DE} = 0, \quad (58)$$

where

$$\mathbf{D} = \begin{pmatrix} D_{--}(k, \omega, \Omega_c, p_0) & -\hat{\chi}_{-+}(k, \omega, \Omega_c, p_0) & -\hat{\chi}_{-z}(k, \omega, \Omega_c, p_0) \\ -\hat{\chi}_{+-}\left(k, \omega - \frac{2\Omega_c}{\gamma_0}, \Omega_c, p_0\right) & D_{++}\left(k, \omega - \frac{2\Omega_c}{\gamma_0}, \Omega_c, p_0\right) & -\hat{\chi}_{+z}\left(k, \omega - \frac{2\Omega_c}{\gamma_0}, \Omega_c, p_0\right) \\ -\hat{\chi}_{z-}\left(k, \omega - \frac{\Omega_c}{\gamma_0}, \Omega_c, p_0\right) & -\hat{\chi}_{z+}\left(k, \omega - \frac{\Omega_c}{\gamma_0}, \Omega_c, p_0\right) & D_{zz}\left(k, \omega - \frac{\Omega_c}{\gamma_0}, p_0\right) \end{pmatrix}, \quad (59)$$

and

$$\mathbf{E} = \begin{pmatrix} E_{1-}(k, \omega) \\ E_{1+}\left(k, \omega - \frac{2\Omega_c}{\gamma_0}\right) \\ E_{1z}\left(k, \omega - \frac{\Omega_c}{\gamma_0}\right) \end{pmatrix}. \quad (60)$$

The quantities $\hat{\chi}_{ij}$ appearing in the matrix in Eq. (59) are obtained from the corresponding quantities in Eqs. (32)–(37) simply by replacing each $g_n(p, \alpha)$ with $\hat{g}_n(p_0, \alpha)$ and setting $p = p_0$ and $\gamma = \gamma_0$. Moreover, from Eqs. (29)–(31), the diagonal matrix elements can be expressed as

$$\begin{aligned} D_{--}(k, \omega, \Omega_c, p_0) &= \omega^2 - c^2 k^2 - \frac{\sqrt{2\pi}}{2} \Omega_p^2 \int_0^\pi d\alpha \hat{g}_0(p_0, \alpha) \\ &\times \left[\frac{2\sin\alpha}{\gamma_0} \left(\omega - \frac{kp_0 \cos\alpha}{\gamma_0 m} \right) \left(\omega - \frac{kp_0 \cos\alpha}{\gamma_0 m} - \frac{\Omega_c}{\gamma_0} \right)^{-1} \right. \\ &\left. - \frac{p_0^2 \sin^3 \alpha}{\gamma_0^3 m^2 c^2} (\omega^2 - c^2 k^2) \left(\omega - \frac{kp_0 \cos\alpha}{\gamma_0 m} - \frac{\Omega_c}{\gamma_0} \right)^{-2} \right], \end{aligned} \quad (61)$$

$$D_{++}(k, \omega, \Omega_c, p_0) = \hat{D}_{--}(k, \omega, -\Omega_c, p_0), \quad (62)$$

$$D_{zz}(k, \omega, p_0)$$

$$= 1 - \sqrt{2\pi} \Omega_p^2 \int_0^\pi d\alpha \hat{g}_0(p_0, \alpha) \frac{\sin \alpha}{\gamma_0} \times \left(1 - \frac{p_0^2 \cos^2 \alpha}{\gamma_0^2 m^2 c^2} \right) \left(\omega - \frac{kp_0 \cos \alpha}{\gamma_0 m} \right)^{-2}. \quad (63)$$

Recall that $\Omega_p = (4\pi e^2 n_0 / m)^{1/2}$ is the nonrelativistic plasma frequency.

The dispersion relation for this system is

$$\det D(k, \omega) = 0. \quad (64)$$

From Eq. (60), it is seen that, for a given value of the wave number k , the frequency ω is that of the right-hand polarized wave E_{1-} . The corresponding frequencies of the left-hand polarized wave E_{1+} and of the electrostatic wave E_{1z} are $\omega - 2\Omega_c / \gamma_0$ and $\omega - \Omega_c / \gamma_0$, respectively. We point out that once the assumption of one-dimensional spatial dependence is made and equilibrium self-fields are neglected, the dispersion relation is exact for equilibrium distributions of definite energy.

Again notice why, in the general case, the field components are related by integral equations (26)–(28) instead of algebraic equations. If the distribution $f_0(p, \alpha, \phi - \Omega_c t / \gamma(p))$ is nonvanishing over a continuous range of energies $\gamma(p)mc^2$, then the mode $E_{1-}(k, \omega)$ will be coupled to a continuum of modes $E_{1+}(k, \omega - 2\Omega_c / \gamma(p))$ and $E_{1z}(k, \omega - \Omega_c / \gamma(p))$.

B. Case of definite p_\perp and p_z

As numerical examples, we consider equilibria of definite $p_\perp = p_0 \sin \alpha_0$ and $p_z = p_0 \cos \alpha_0$. Consequently, the factor $\hat{f}_0(p_0, \alpha, \xi)$ in Eq. (56) is

$$\hat{f}_0(p_0, \alpha, \xi) = \frac{\delta(\alpha - \alpha_0)}{\sin \alpha} \Phi(\xi), \quad (65)$$

where $\Phi(\xi)$ is a function of period 2π . From Eq. (5), the normalization condition on $\Phi(\xi)$ is

$$\int_0^{2\pi} d\phi \Phi\left(\phi - \frac{\Omega_c}{\gamma} t\right) = \int_0^{2\pi} d\xi \Phi(\xi) = 1. \quad (66)$$

Moreover, from Eq. (57),

$$\hat{g}_n(p_0, \alpha) = \frac{1}{\sqrt{2\pi}} \frac{\delta(\alpha - \alpha_0)}{\sin \alpha} s_n, \quad (67)$$

where

$$s_n = \int_0^{2\pi} d\xi \Phi(\xi) \exp(-in\xi). \quad (68)$$

From Eq. (66), $s_0 = 1$. Also notice that $s_{-n} = s_n^*$.

Substituting Eq. (67) into Eqs. (61)–(63) and into Eqs. (29)–(31) with $g_n(p, \alpha)$ replaced by $\hat{g}_n(p_0, \alpha)$, we can express the dispersion relation in Eq. (64) as the following tenth degree polynomial equation (in either $\hat{\omega}$ or \hat{k}) with real coefficients:

$$\begin{aligned} M_{--}(\hat{k}, \hat{\omega}) M_{++}(\hat{k}, \hat{\omega}) M_{zz}(\hat{k}, \hat{\omega}) = & \frac{1}{2} \left(\frac{\omega_p^2}{\omega_c^2} \right)^2 \beta_1^2 |s_1|^2 [(\beta_z \hat{\omega} - \hat{k})^2 M_{++}(\hat{k}, \hat{\omega}) + (\beta_z \hat{\omega} - 2\beta_z - \hat{k})^2 M_{--}(\hat{k}, \hat{\omega})] \\ & + \frac{1}{4} \left(\frac{\omega_p^2}{\omega_c^2} \right)^2 \beta_1^4 |s_2|^2 (\hat{\omega}^2 - 2\hat{\omega} - \hat{k}^2)^2 M_{zz}(\hat{k}, \hat{\omega}) \\ & - \frac{1}{4} \left(\frac{\omega_p^2}{\omega_c^2} \right)^3 \beta_1^4 (s_2 s_{-1}^2 + s_{-2} s_1^2) (\hat{\omega}^2 - 2\hat{\omega} - \hat{k}^2) (\beta_z \hat{\omega} - 2\beta_z - \hat{k}) (\beta_z \hat{\omega} - \hat{k}). \end{aligned} \quad (69)$$

In Eq. (69), $\omega_p^2 = \Omega_p^2 / \gamma_0$ is the relativistic plasma frequency squared, and $\omega_c = \Omega_c / \gamma_0$ is the relativistic cyclotron frequency. Dimensionless frequencies and wave numbers are $\hat{\omega} = \omega / \omega_c$ and $\hat{k} = ck / \omega_c$. Dimensionless velocities are given by $\beta_\perp = v_{\perp 0} / c$ and $\beta_z = v_{z0} / c$, where $v_{\perp 0} = p_0 \sin \alpha_0 / \gamma(p_0)m$ and $v_{z0} = p_0 \cos \alpha_0 / \gamma(p_0)m$. Finally,

$$M_{--}(\hat{k}, \hat{\omega}) = (\hat{\omega}^2 - \hat{k}^2) (\hat{\omega} - \hat{k} \beta_z - 1)^2 - \frac{\omega_p^2}{\omega_c^2} (\hat{\omega} - \hat{k} \beta_z) \times (\hat{\omega} - \hat{k} \beta_z - 1) + \frac{1}{2} \frac{\omega_p^2}{\omega_c^2} \beta_1^2 (\hat{\omega}^2 - \hat{k}^2), \quad (70)$$

$$\begin{aligned} M_{++}(\hat{k}, \hat{\omega}) = & ((\hat{\omega} - 2)^2 - \hat{k}^2) (\hat{\omega} - \hat{k} \beta_z - 1)^2 \\ & - \frac{\omega_p^2}{\omega_c^2} (\hat{\omega} - \hat{k} \beta_z - 2) (\hat{\omega} - \hat{k} \beta_z - 1) \\ & + \frac{1}{2} \frac{\omega_p^2}{\omega_c^2} \beta_1^2 ((\hat{\omega} - 2)^2 - \hat{k}^2), \end{aligned} \quad (71)$$

$$M_{zz}(\hat{k}, \hat{\omega}) = (\hat{\omega} - \hat{k} \beta_z - 1)^2 - \frac{\omega_p^2}{\omega_c^2} (1 - \beta_z^2). \quad (72)$$

The dispersion relation in Eq. (69), which is valid for both complex $\hat{\omega}$ and complex \hat{k} , is invariant under the transformation

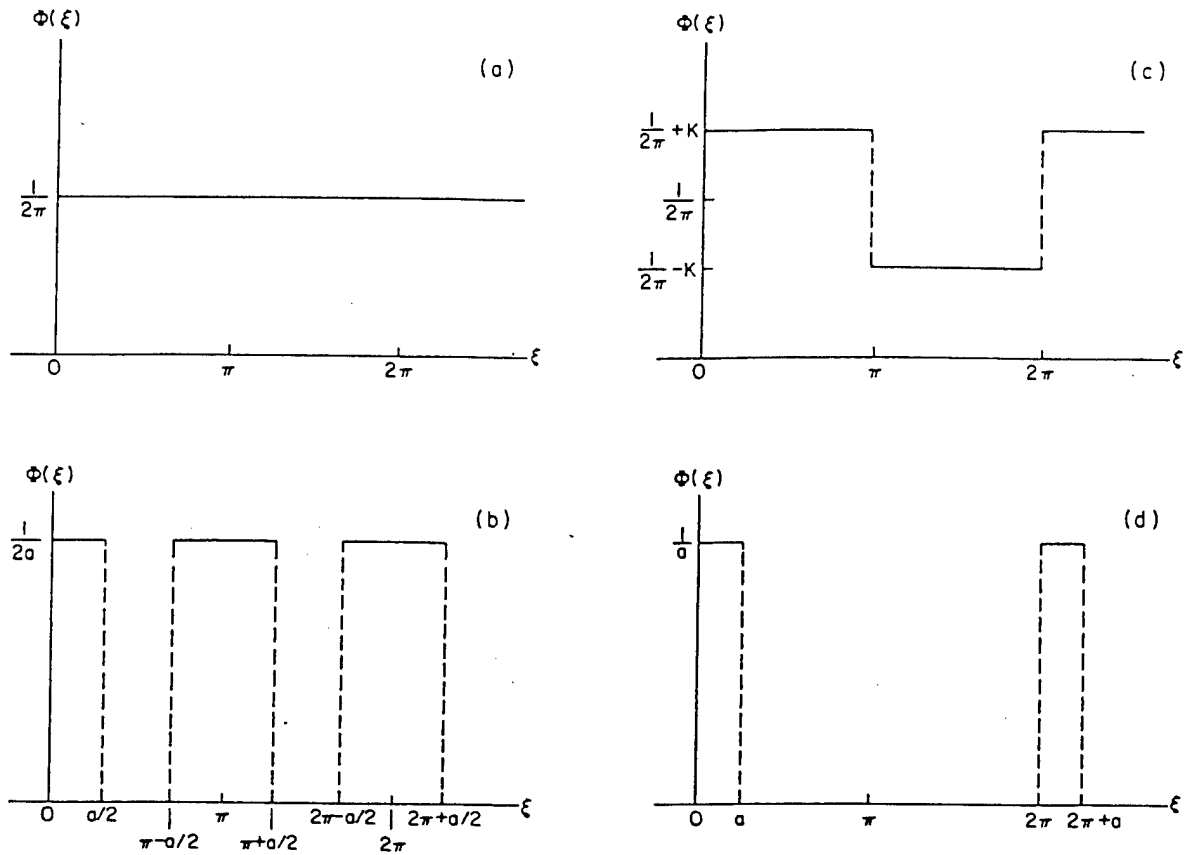


FIG. 3. Distributions in phase $\Phi(\xi)$ used in numerical examples. Plot (a) is a uniformly random (gyrotropic) distribution. Also shown are plots of nongyrotropic distributions for which (b) $s_1=0$ and $s_2=\sin a/a$, (c) $s_1=-4iK$ and $s_2=0$, and (d) $s_1=(2/a)\exp(-ia/2)\sin(a/2)$ and $s_2=(1/a)\exp(-ia)\sin a$.

$$\hat{k} \rightarrow -\hat{k}^*, \quad \hat{\omega} \rightarrow -\hat{\omega}^* + 2. \quad (73)$$

For the case of the distribution in Eq. (65), the behavior of the eigenmode \mathbf{E} in Eq. (58) under this transformation is easily determined by applying the transformation to the elements of \mathbf{D} and \mathbf{E} in Eq. (58). If either $s_1 \neq 0$ or $s_2 \neq 0$, then

$$\frac{E_{1+}(\hat{k}, \hat{\omega}-2)}{E_{1-}(\hat{k}, \hat{\omega})} \rightarrow \frac{E_{1+}(-\hat{k}^*, -\hat{\omega}^*)}{E_{1-}(-\hat{k}^*, -\hat{\omega}^*+2)} = \frac{E_{1-}^*(\hat{k}, \hat{\omega})}{E_{1+}^*(\hat{k}, \hat{\omega}-2)}, \quad (74)$$

and, if $s_1 \neq 0$,

$$\frac{E_{1+}(\hat{k}, \hat{\omega}-2)}{E_{1z}(\hat{k}, \hat{\omega}-1)} \rightarrow \frac{E_{1+}(-\hat{k}^*, -\hat{\omega}^*)}{E_{1z}(-\hat{k}^*, -\hat{\omega}^*+1)} = \frac{E_{1-}^*(\hat{k}, \hat{\omega})}{E_{1z}^*(\hat{k}, \hat{\omega}-1)},$$

$$\frac{E_{1-}(\hat{k}, \hat{\omega})}{E_{1z}(\hat{k}, \hat{\omega}-1)} \rightarrow \frac{E_{1-}(-\hat{k}^*, -\hat{\omega}^*+2)}{E_{1z}(-\hat{k}^*, -\hat{\omega}^*+1)} = \frac{E_{1+}^*(\hat{k}, \hat{\omega}-2)}{E_{1z}^*(\hat{k}, \hat{\omega}-1)}. \quad (75)$$

Equation (69) gives the ten branches of the dispersion relation $\hat{\omega}(\hat{k})$. The behavior of $\hat{\omega}/\hat{k}$ for large $|\hat{k}|$ is easily determined for each of these branches. As $|\hat{k}| \rightarrow \infty$, $\hat{\omega}(\hat{k})/\hat{k} \rightarrow +1$ for two branches, $\hat{\omega}(\hat{k})/\hat{k} \rightarrow -1$ for two branches, and $\hat{\omega}(\hat{k})/\hat{k} \rightarrow \beta_z$ for six branches.

Simple expressions are easily obtained for the large $|\hat{k}|$ behaviors of $\hat{\omega}(\hat{k})$ for all ten branches if either s_1 or s_2 vanishes in Eq. (68). If $s_1=0$ and $s_2 \neq 0$, then [from Eqs. (57) and (67)] $g_1(p, \alpha)=0$ and $g_2(p, \alpha) \neq 0$. It follows from

the discussion in Sec. II D that the electromagnetic components are coupled and the electrostatic component is uncoupled. [Such a situation holds for (but is not exclusive to) the distribution $\Phi(\xi)$ in Fig. 3(b), provided that the parameter $a \neq \pi$. For this distribution, $s_1=0$ and $s_2=\sin a/a$.] Two of the branches pertain to the uncoupled electrostatic waves and obey the exact dispersion relations

$$\hat{\omega} = \hat{k}\beta_z + 1 \pm \frac{\omega_p}{\omega_c} (1 - \beta_z^2)^{1/2}. \quad (76)$$

For sufficiently large $|\hat{k}|$, the remaining eight branches obey the approximate dispersion relations

$$\hat{\omega} = \hat{k}\beta_z + 1 \pm \frac{i}{\sqrt{2}} \frac{\omega_p}{\omega_c} \beta_\perp (1 + |s_2|)^{1/2}, \quad (77)$$

$$\hat{\omega} = \hat{k}\beta_z + 1 \pm \frac{i}{\sqrt{2}} \frac{\omega_p}{\omega_c} \beta_\perp (1 - |s_2|)^{1/2}, \quad (78)$$

$$\hat{\omega} = \pm \left(\hat{k}^2 + \frac{\omega_p^2}{\omega_c^2} \right)^{1/2}, \quad (79)$$

$$\hat{\omega} = 2 \pm \left(\hat{k}^2 + \frac{\omega_p^2}{\omega_c^2} \right)^{1/2}. \quad (80)$$

For real \hat{k} , Eqs. (77) and (78) give two branches with positive $\text{Im } \hat{\omega}$ provided that $|s_2| < 1$. In this case, growth-rate curves ($\text{Im } \hat{\omega}$ vs real \hat{k}) will show two unstable branches at large \hat{k} .

If $s_1 \neq 0$ and $s_2 = 0$, then [from Eqs. (57) and (67)] $g_2(p, \alpha) = 0$ and $g_1(p, \alpha) \neq 0$. It follows from the discussion in Sec. II D that the transverse electromagnetic waves are coupled through the longitudinal electrostatic wave. [A non-exclusive example of a distribution $\Phi(\xi)$ having this property (if $K \neq 0$) is presented in Fig. 3(c). Using Eq. (68), we find that $s_1 = -4iK$ and $s_2 = 0$ for this example.] In this case, the large $|\hat{k}|$ approximations for four of the ten branches of the dispersion relation are the same as those given in Eqs. (79) and (80) for the distribution previous case. Approximations for the remaining six branches are

$$\hat{\omega} = \hat{k}\beta_z + 1 \pm \frac{i}{\sqrt{2}} \frac{\omega_p}{\omega_c} \beta_\perp, \quad (81)$$

$$\hat{\omega} = \hat{k}\beta_z + 1 \pm \frac{1}{\sqrt{2}} \frac{\omega_p}{\omega_c} \kappa_+, \quad (82)$$

$$\hat{\omega} = \hat{k}\beta_z + 1 \pm \frac{i}{\sqrt{2}} \frac{\omega_p}{\omega_c} \kappa_-, \quad (83)$$

where

$$\kappa_\pm = \left\{ \mp \left(\frac{\beta_\perp^2}{2} - (1 - \beta_z^2) \right) + \left[\left(\frac{\beta_\perp^2}{2} - (1 - \beta_z^2) \right)^2 + 4\beta_\perp^2(1 - \beta_z^2) \left(\frac{1}{2} - |s_1|^2 \right) \right]^{1/2} \right\}^{1/2}. \quad (84)$$

[The maximum possible value of K in Fig. 3(c) is $1/2\pi$, and the corresponding maximum value of $|s_1|$ is $2/\pi = 0.6366\dots$. It is evident from Eq. (84) that the κ_\pm are real and positive for all $|s_1| < 1/\sqrt{2} = 0.7071\dots$. Consequently, Eqs. (81) and (83) provide for two unstable modes at large values of real \hat{k} for the distribution in Fig 4(c).]

A nonexclusive example of a distribution for which neither s_1 nor s_2 vanishes (unless the parameter $a = \pi$ or 2π) is presented in Fig. 3(d). From Eq. (68), it follows that in this example $s_1 = (2/a)\exp(-ia/2)\sin(a/2)$ and $s_2 = (1/a) \times \exp(-ia)\sin a$. If both s_1 and s_2 are nonvanishing, determining the large $|\hat{k}|$ behavior of the dispersion relation in Eq. (69) is more difficult than in the previous cases. Four of the large- $|\hat{k}|$ branches are given by Eqs. (79) and (80). The behaviors of the remaining six branches (including all that may show growth at large, real \hat{k}) are determined by solving a cubic equation in $(\hat{\omega} - \hat{k}\beta_z - 1)^2$. Further details will not be given in this paper.

Unless $s_1 = s_2 = 0$, some of the eigenmodes \mathbf{E} in Eq. (58) will involve two or more of the components $E_{1-}(\hat{k}, \hat{\omega})$, $E_{1+}(\hat{k}, \hat{\omega} - 2)$, and $E_{1z}(\hat{k}, \hat{\omega} - 1)$. A quantity that will be employed to measure the relative importance of $E_{1-}(\hat{k}, \hat{\omega})$ and $E_{1+}(\hat{k}, \hat{\omega} - 2)$ is the Poynting flux ratio defined by

$$\left| \frac{S_+(\hat{k}, \hat{\omega} - 2)}{S_-(\hat{k}, \hat{\omega})} \right| = \left| \frac{\hat{\omega}}{\hat{\omega} - 2} \right| \left| \frac{E_{1+}(\hat{k}, \hat{\omega} - 2)}{E_{1-}(\hat{k}, \hat{\omega})} \right|^2. \quad (85)$$

This quantity is the ratio of the time-averaged Poynting vectors that the field associated with each component would produce in the absence of the other component. A time-dependent interference term due to the different frequencies of the components is not included.

C. Numerical examples

In the following numerical examples, \hat{k} is restricted to be real. Then, $\text{Im } \hat{\omega} > 0$ indicates an unstable mode. If \hat{k} is restricted to be real, then the transformation in Eq. (73) is equivalent to inverting a plot of $\text{Re } \hat{\omega}$ vs \hat{k} (real) through the point $(\hat{k}, \text{Re } \hat{\omega}) = (0, 1)$ and reflecting a plot of $\text{Im } \hat{\omega}$ vs \hat{k} (real) through the $\text{Im } \hat{\omega}$ -axis. It follows from the invariance of the dispersion relation in Eq. (69) under this transformation and from Eqs. (74) and (75) that there is no loss of generality if numerical examples are limited to the case of nonnegative real \hat{k} .

Parameter values in all of the numerical examples below in Figs. 4–7 are $\hat{\omega}_p^2/\hat{\omega}_c^2 = 0.05$, $\gamma_0 = 2$, and $\alpha_0 = 0.4$. In order to ensure that values selected for s_1 and s_2 are realistic [i.e., correspond to $\Phi(\xi) \geq 0$ in Eq. (65)], we assume that $\Phi(\xi)$ has one of the functional forms shown in Figs. 3(a)–3(d).

Example 1: If the distribution $\Phi(\xi)$ is uniform [see Fig. 3(a)], then $s_1 = s_2 = 0$. [Such a distribution is also attained with $a = \pi$ in Fig. 3(b), $K = 0$ in Fig. 3(c), or $a = 2\pi$ in Fig. 3(d).] In this case, the dispersion relation in Eq. (69) decouples into the three independent relations $M_{--}(\hat{k}, \hat{\omega}) = 0$, $M_{++}(\hat{k}, \hat{\omega}) = 0$, and $M_{zz}(\hat{k}, \hat{\omega}) = 0$. These are, respectively, the dispersion relations for uncoupled right- and left-handed circularly polarized electromagnetic waves and for the electrostatic wave. For a given \hat{k} , the frequencies of these waves are $\hat{\omega}$, $\hat{\omega} - 2$, and $\hat{\omega} - 1$, respectively. Growth-rate curves ($\text{Im } \hat{\omega}$ vs \hat{k}) for this limiting case are presented in Fig. 4(a) over the interval $0 \leq \hat{k} \leq 10$. Corresponding plots of $\text{Re } \hat{\omega}$ vs \hat{k} over the interval $0 \leq \hat{k} \leq 1.4$ are presented in Fig. 4(b). Letters on these plots designate corresponding points on the two diagrams. The points *B* and *C* in Fig. 4(a) coincide. The growth-rate curve segments *CDG* and *HI* are obtained from $M_{--}(\hat{k}, \hat{\omega}) = 0$, and a corresponding eigenmode \mathbf{E} in Eq. (58) has only $E_{1-}(\hat{k}, \hat{\omega})$ as a nonvanishing component. The growth-rate curve segments *AB* and *FEJ* are obtained from $M_{++}(\hat{k}, \hat{\omega}) = 0$. A corresponding eigenmode has only one nonvanishing component, namely $E_{1+}(\hat{k}, \hat{\omega} - 2)$.

The plot of $\text{Re } \hat{\omega}$ vs \hat{k} in Fig. 4(b) is needed for the proper interpretation of the growth-rate curves in Fig. 4(a). If $\hat{k} > 0$ and $\text{Re } \hat{\omega} > 0$, then $E_{1-}(\hat{k}, \hat{\omega})$ and $E_{1+}(\hat{k}, \hat{\omega})$ are, respectively, components associated with right-hand polarized (RHP) and left-hand polarized (LHP) waves that travel in the forward (positive- z) direction. If $\hat{k} > 0$ (as before) but $\text{Re } \hat{\omega} < 0$, then the handedness of these waves is unchanged, however, they now travel in the backward (negative- z) direction. Similarly, the electrostatic wave associated with $E_{1z}(\hat{k}, \hat{\omega})$ is

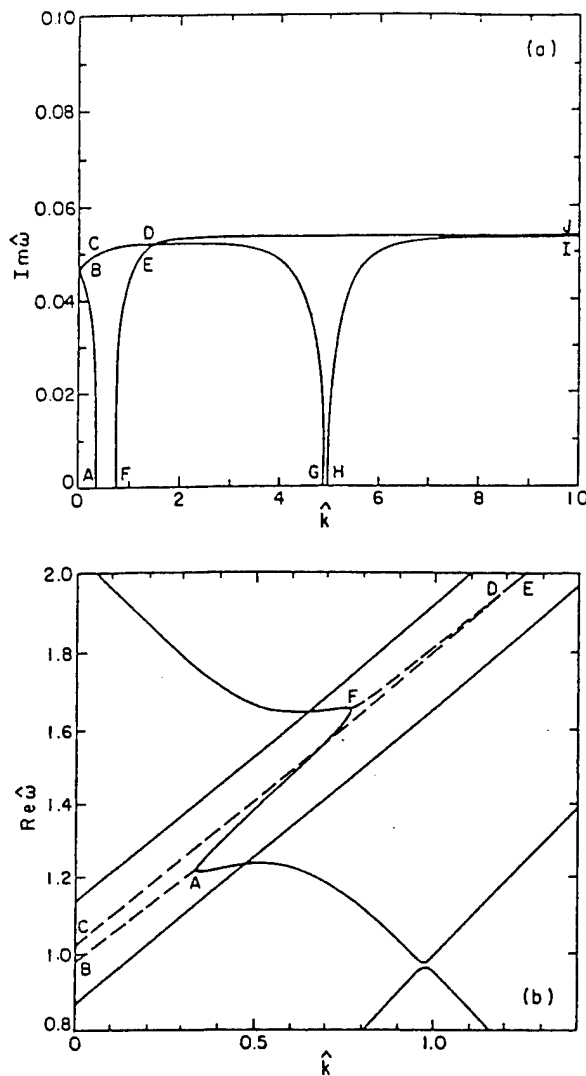


FIG. 4. Plots of complex $\hat{\omega}$ vs \hat{k} (real) for the system parameters $\omega_p^2/\omega_p^2 = 0.05$, $\gamma_0 = 2$, and $\alpha_0 = 0.4$. The time-dependent equilibrium distribution in phase is characterized by $s_1 = s_2 = 0$. Plots are (a) $\text{Im } \hat{\omega}$ vs \hat{k} for $0 \leq \hat{k} \leq 10$ and (b) $\text{Re } \hat{\omega}$ vs \hat{k} for $0 \leq \hat{k} \leq 1.4$.

backward traveling if $\hat{k} > 0$ and $\text{Re } \hat{\omega} < 0$. As an illustration of the use of Fig. 4(b) in interpreting Fig. 4(a), consider the segmented growth-rate curve $A(BC)DG$, which gives the growth rate of the cyclotron maser instability. Segment AB pertains to $E_{1+}(\hat{k}, \hat{\omega} - 2)$. From Fig. 4(b), it is seen that $\text{Re } \hat{\omega} - 2 < 0$ everywhere on AB . Consequently, the growth-rate curve AB in Fig. 4(a) pertains to growing, backward-traveling, LHP electromagnetic waves. Similarly, segment CDG in Fig. 4(a) pertains to $E_{1-}(\hat{k}, \hat{\omega})$. Reference to Fig. 4(b) shows that $\text{Re } \hat{\omega} > 0$ everywhere on CDG , so that growth-rate curve segment CDG in Fig. 4(a) pertains to growing, forward-traveling, RHP electromagnetic waves. Similar analysis shows that the growth-rate curve HI for the whistler instability pertains to forward-traveling, RHP electromagnetic waves. Also, the growth-rate curve segment FE pertains to backward-traveling LHP waves, and the segment EJ pertains to forward-traveling LHP waves. Because all of the roots of $M_{zz}(\hat{k}, \hat{\omega})$ are real, no corresponding growth-rate curves appear in Fig. 4(a).

Electromagnetic and beam waves are said to be in resonance for the cyclotron maser instability when $\hat{\omega} = \hat{k}$ and $\hat{\omega} = \hat{k}\beta_z + 1$. These resonance values of $\hat{\omega}$ and \hat{k} are given by $\hat{\omega}_r = \hat{k}_r = 1/(1 - \beta_z)$. In this example, $\hat{k}_r = 4.94$. Figure 4(a) conforms with the well-known fact that no growth of RHP radiation occurs at $\hat{k} = \hat{k}_r$ in an uncoupled system.

Finally, it is emphasized that no special relation exists between the LHP and RHP waves considered above when $s_1 = s_2 = 0$. However, the plots in Fig. 4 will be approached by any system using our parameters in the limit in which both s_1 and s_2 approach zero.

Example 2: An explicit example of a nonuniform distribution in phase is obtained by selecting $a = \pi/4$ in Fig. 3(b). Then the unperturbed electron beam consists of two streams with respective distributions centered about $\xi = 0$ and $\xi = \pi$. Each distribution is a water bag of width $\pi/4$. The corresponding parameters defined in Eq. (68) are $s_1 = 0$ and $s_2 = 2\sqrt{2}/\pi$. Because $s_1 = 0$, the eigenmodes E in Eq. (58) are of two types. The first type of eigenmode has only $E_{1z}(\hat{k}, \hat{\omega})$ as a nonvanishing component. The corresponding dispersion relation is $M_{zz}(\hat{k}, \hat{\omega}) = 0$, which does not allow for growth. [See Eq. (76).] The second type of eigenmode has two nonvanishing components, namely $E_{1-}(\hat{k}, \hat{\omega})$ and $E_{1+}(\hat{k}, \hat{\omega} - 2)$. Some of these eigenmodes are unstable.

Growth-rate curves for this system for $0 \leq \hat{k} \leq 15$ and corresponding plots of $\text{Re } \hat{\omega}$ vs \hat{k} (for $0 \leq \hat{k} \leq 1.5$) are presented in Figs. 5(a) and 5(b). As a measure of the relative importance of the RHP and LHP electromagnetic waves associated with unstable modes, plots of the Poynting flux ratio in Eq. (85) as a function of \hat{k} (for unstable modes only) are presented in Fig. 5(c). Letters show corresponding points in Figs. 5(a)–5(c). By comparing Figs. 5(a) and 5(b), we see that the growth-rate curve segments BA , CD , and FE pertain to modes consisting of a forward-traveling RHP electromagnetic wave (because $\text{Re } \hat{\omega} > 0$) and a backward-traveling LHP electromagnetic wave (because $\text{Re } \hat{\omega} - 2 < 0$). All other segments of the growth-rate curves pertain to modes consisting of forward traveling RHP and LHP electromagnetic waves.

In the case of a uniform distribution in ξ (example 1), no growth of RHP electromagnetic waves occurs at the resonance wave number $\hat{k} = \hat{k}_r = 4.94$. [See Fig. 4(a).] The growth-rate curve CDH in Fig. 5(a) shows a mode at $\hat{k} = \hat{k}_r = 4.94$ which grows significantly faster than any mode in Fig. 4(a). From Fig. 5(a), we see that the RHP Poynting flux associated with the mode is almost 20 times the LHP Poynting flux. Consequently, growth of RHP radiation is now possible at $\hat{k} = \hat{k}_r$, although it must be accompanied by a smaller growing component of LHP radiation. We remark that among computations so far carried out those for systems with two-stream distributions in ξ (with a phase difference of π) show the most rapid growth rates at $\hat{k} = \hat{k}_r$.

Referring to Fig. 5(a), we see that there are two unstable branches at large \hat{k} in conformity with Eqs. (77) and (78). From Fig. 5(c), it is seen that, for either branch at large \hat{k} , the RHP Poynting flux is approximately double that of the LHP

Poynting flux. Finally, note from Fig. 5(c) that for unstable eigenmodes at small \hat{k} the ratio of the backward traveling LHP Poynting flux to the forward traveling RHP Poynting flux depends very strongly on the branch of the dispersion relation and varies rapidly with \hat{k} for a given branch.

Example 3: As a second example of a nonuniform phase distribution, select the form of $\Phi(\xi)$ in Fig. 3(c) and choose the parameter value $K=1/2\pi$. [Equivalently, we could let $a=\pi$ in Fig. 3(d).] Then the equilibrium particle phases are uniformly distributed between $\xi=0$ and $\xi=\pi$, and no particles have phases in the range $\pi<\xi<2\pi$. Fourier components in Eq. (68) are $s_1=-2i/\pi$ and $s_2=0$. Because $s_2=0$, the field components $E_{1-}(\hat{k},\hat{\omega})$ and $E_{1+}(\hat{k},\hat{\omega}-2)$ are indirectly coupled through the electrostatic component $E_{1z}(\hat{k},\hat{\omega}-1)$. Consequently, the eigenmodes **E** in Eq. (58) will (in general) have three nonvanishing field components. Growth-rate curves for this example are presented in Fig. 6(a) for $0\leq\hat{k}\leq 10$, and corresponding plots of $\text{Re } \hat{\omega}$ vs \hat{k} (for the interval $0\leq\hat{k}\leq 2$) are given in Fig. 6(b). Plots of the Poynting flux ratio in Eq. (85) are shown in Fig. 6(c). Finally, as a measure of the relative importance of the electrostatic component of the unstable eigenmodes, we present a plot of $2^{-1/2}|E_{1-}(\hat{k},\hat{\omega})/E_{1z}(\hat{k},\hat{\omega}-1)|$ vs \hat{k} in Fig. 6(d). (The factor of $2^{-1/2}$ appears in the field ratio because $2^{-1/2}E_{1\pm}$ is the proper normalization of coefficients of the complex unit vectors for LHP and RHP waves when comparison is to be made with Cartesian field components.) Letters show corresponding points in Figs. 6(a)–6(d).

Reference to Figs. 6(a) and 6(b) shows that the wave associated with the component $E_{1+}(\hat{k},\hat{\omega}-2)$ is left-hand polarized and backwards traveling for eigenmodes on the growth-rate curve segments *GH*, *ABC*, and *DEF*. The electrostatic wave associated with $E_{1z}(\hat{k},\hat{\omega}-1)$ is forward traveling for all unstable modes except for those modes on the growth-rate curve *ABC* for which \hat{k} is very close to zero. All other components of unstable eigenmodes represent forward-traveling waves.

Referring to Fig. 6(a), we see that two unstable branches of the dispersion relation are present at large values of \hat{k} in conformity with Eqs. (81) and (83). From Figs. 6(c) and 6(d), it is seen that the RHP Poynting flux exceeds that of the LHP electromagnetic wave by a factor of approximately 3 for both branches at large \hat{k} . The electrostatic contribution to eigenmodes on the upper branch is relatively very small. On the other hand, the electrostatic field amplitude in eigenmodes on the lower branch is of the same order of magnitude as the LHP electromagnetic field amplitude.

Two branches, *MNO* and *GHI*, show moderate growth rates at the resonance $\hat{k}=\hat{k}_r=4.94$. Reference to Figs. 6(c) and 6(d) shows that the RHP Poynting flux is significantly larger than the LHP Poynting flux for the eigenmodes associated with either of these branches at $\hat{k}=\hat{k}_r$. Moreover, $|E_{1-}(\hat{k},\hat{\omega})/E_{1z}(\hat{k},\hat{\omega}-1)|>10$ for either branch at $\hat{k}=\hat{k}_r$. Again, this behavior is in contrast with the case of a uniform distribution in ξ where no growth of RHP electromagnetic radiation takes place at the resonance value of \hat{k} . However,

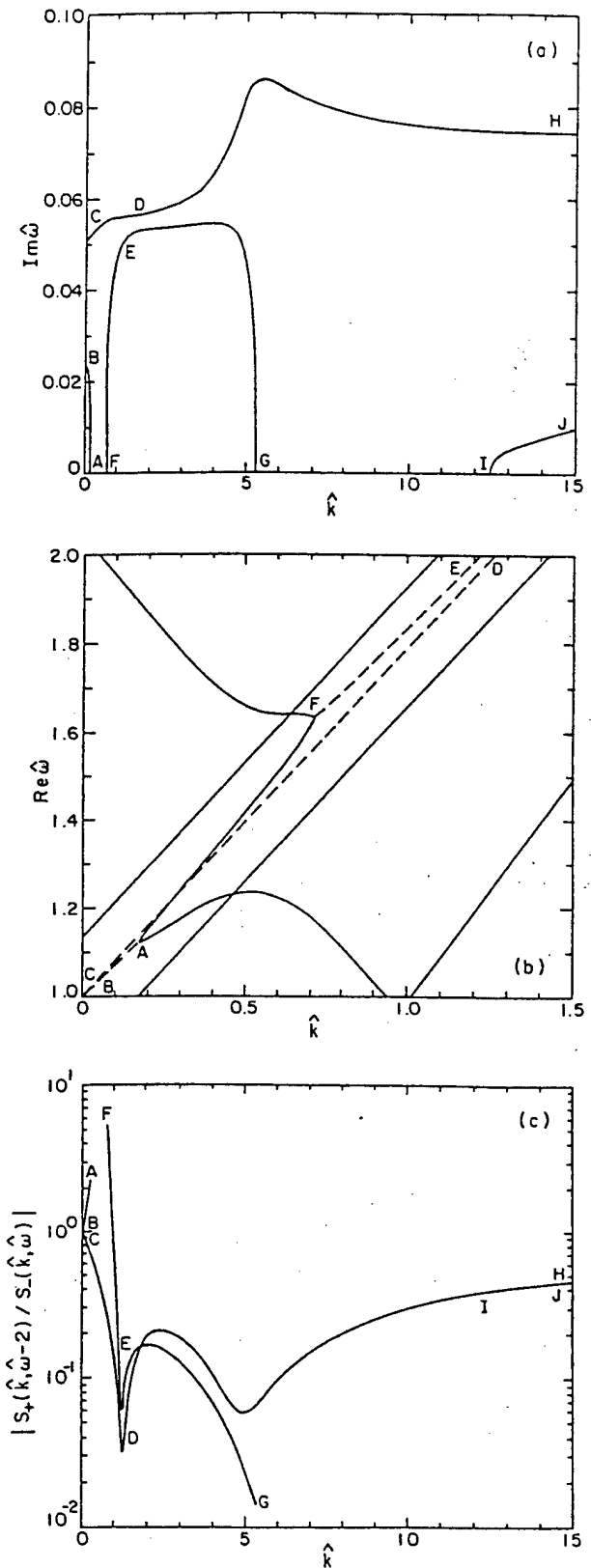


FIG. 5. Dispersion relations and properties of corresponding eigenvectors for system parameters $\omega_c^2/\omega_p^2=0.05$, $\gamma_0=2$, and $\alpha_0=0.4$. The time-dependent equilibrium distribution in phase is characterized by $s_1=0$ and $s_2=2\sqrt{2}/\pi$. Plots are (a) $\text{Im } \hat{\omega}$ vs \hat{k} for $0\leq\hat{k}\leq 15$ and (b) $\text{Re } \hat{\omega}$ vs \hat{k} for $0\leq\hat{k}\leq 1.5$. Also shown for unstable eigenmodes is (c) the Poynting flux ratio in Eq. (85) vs \hat{k} .

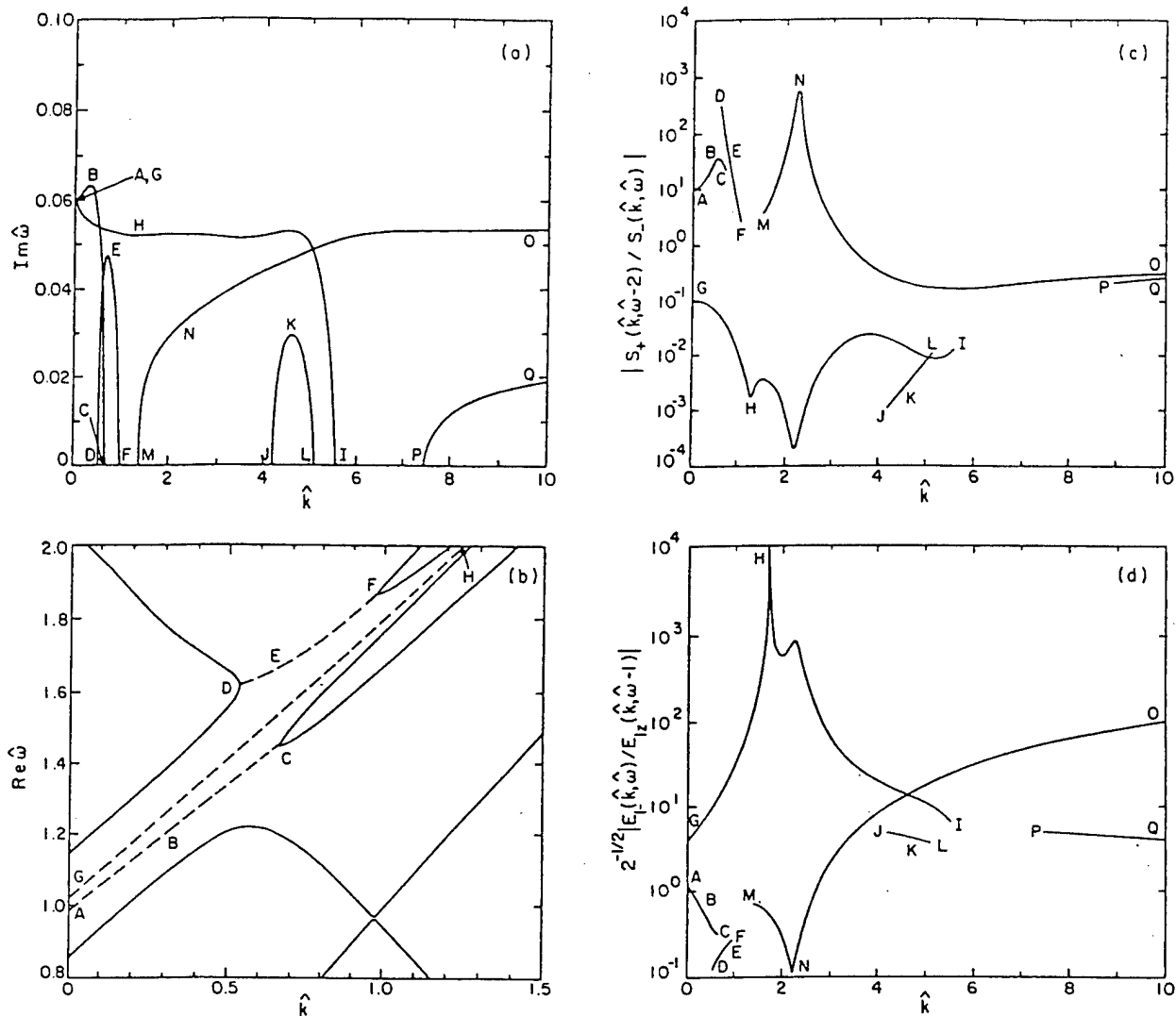


FIG. 6. Dispersion relations and properties of corresponding eigenvectors for system parameters $\omega_c^2/\omega_p^2=0.05$, $\gamma_0=2$, and $\alpha_0=0.4$. The time-dependent equilibrium distribution in phase is characterized by $s_1=-2i/\pi$ and $s_2=0$. Plots are (a) $\text{Im } \hat{\omega}$ vs \hat{k} for $0 \leq \hat{k} \leq 10$ and (b) $\text{Re } \hat{\omega}$ vs \hat{k} for $0 \leq \hat{k} \leq 1.5$. Also shown for unstable eigenmodes are (c) the Poynting flux ratio in Eq. (85) vs \hat{k} and (d) $2^{-1/2}|E_{1x}(\hat{k}, \hat{\omega})/E_{1x}(\hat{k}, \hat{\omega}-1)|$ vs \hat{k} .

the growth rates at $\hat{k}=\hat{k}_r$ in Fig. 6(a) are not large, being slightly less than the maximum growth rates that appear in Fig. 4(a) for the case of a uniform distribution.

Although the growth-rate peak ABC is very narrow, eigenmodes at points near its maximum are the fastest growing modes of this system. Moreover, reference to Fig. 6(c) shows that these modes contain a relatively strong backward-traveling, LHP component.

Example 4: As our final numerical example, we treat the limit of $a=0$ for the distribution in Fig. 3(d). In the limit, the distribution becomes $\Phi(\xi)=\sum_{-\infty}^{\infty}\delta(\xi-2n\pi)$ with $s_1=s_2=1$. In this case, $\phi=\omega_c t$ for all particles in the equilibrium beam. Growth-rate curves for the interval $0 \leq \hat{k} \leq 8$ and plots of $\text{Re } \hat{\omega}$ vs \hat{k} for the interval $0 \leq \hat{k} \leq 1.5$ appear in Figs. 7(a) and 7(b), respectively. For unstable eigenmodes, plots of the Poynting flux ratio in Eq. (85) vs \hat{k} and $2^{-1/2}|E_{1x}(\hat{k}, \hat{\omega})/E_{1x}(\hat{k}, \hat{\omega}-1)|$ vs \hat{k} are presented in Figs. 7(c) and 7(d), respectively. Letters on these graphs show corresponding points. Eigenmodes belonging to growth-rate curve segments

ABC and DE have backward-traveling LHP components and forward-traveling RHP and electrostatic components. A tiny growth-rate peak appears at G in Fig. 7(a). Reference to Fig. 7(b) shows that its LHP and electrostatic components are backward traveling. Eigenmodes on all other segments contain only forward-traveling components.

A striking feature of the growth-rate curves in Fig. 7(a) is that no growth occurs for values of \hat{k} greater than approximately 6.2. That is, no branches of the dispersion relation show growth in the limit of large \hat{k} . [Suppression of instability in the whistler by the electrostatic wave is discussed in Ref. 10.] Also, notice the interval of no growth FH ($1.4 \leq \hat{k} \leq 2$).

Another striking feature is the great height of the growth peak ABC . From Fig. 7(c), we see that the Poynting flux of the backward-traveling LHP electromagnetic wave exceeds that of the forward-traveling RHP electromagnetic wave over most of the interval of this growth peak. The amplitude of the forward-traveling electrostatic wave is seen [from Figs.

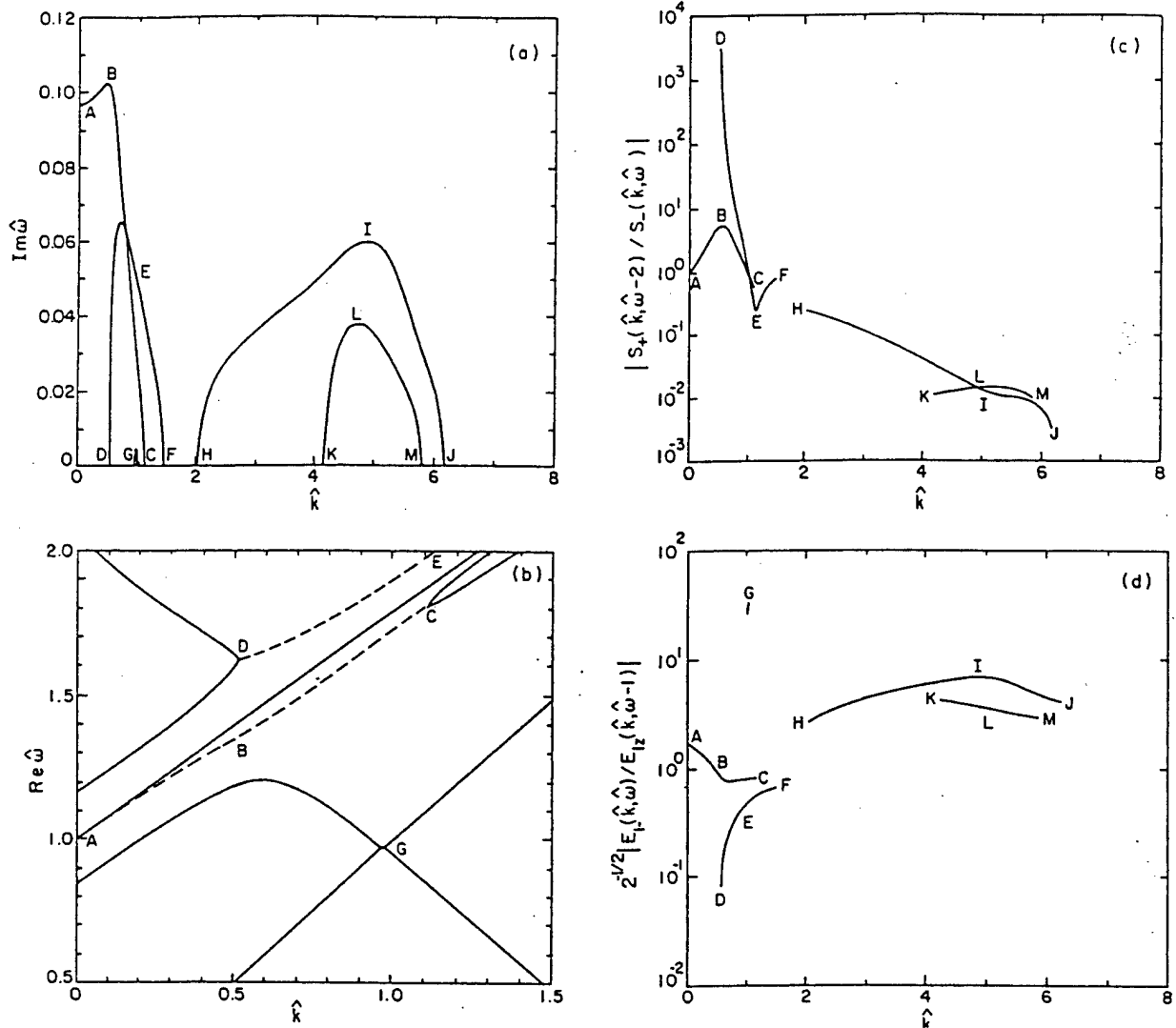


FIG. 7. Dispersion relations and properties of corresponding eigenvectors for system parameters $\omega_c^2/\omega_p^2=0.05$, $\gamma_0=2$, and $\alpha_0=0.4$. The time-dependent equilibrium distribution in phase is characterized by $s_1=s_2=1$. Plots are (a) $\text{Im } \hat{\omega}$ vs \hat{k} for $0 \leq \hat{k} \leq 8$ and (b) $\text{Re } \hat{\omega}$ vs \hat{k} for $0 \leq \hat{k} \leq 1.5$. Also shown for unstable eigenmodes are (c) the Poynting flux ratio in Eq. (85) vs \hat{k} and (d) $2^{-1/2} |E_+(\hat{k}, \hat{\omega}) / E_{12}(\hat{k}, \hat{\omega} - 1)|$ vs \hat{k} .

7(c) and 7(d)] to be of the same order of magnitude as the amplitudes of the electromagnetic waves.

Again, we see growth of RHP electromagnetic waves at the resonance wave number $\hat{k}=\hat{k}_r=4.94$. In fact, the maximum of the growth-rate curve HJJ in Fig. 7(a) is situated very close to the resonance wave number, and the growth rate at this maximum exceeds any growth rate for the gyrotronic case in Fig. 4(a). From Figs. 7(c) and 7(d), it is seen that the largest component for eigenmodes near this maximum is that corresponding to forward-traveling RHP electromagnetic radiation.

To summarize, it is evident that a richness of structure in the growth-rate curves can be produced by introducing non-uniform distributions $\Phi(\xi)$. Using proper choices of $\Phi(\xi)$, temporal growth rates near $\hat{k}=\hat{k}_r$ can be significantly increased and growth rates at large \hat{k} can be on the one hand enhanced or on the other hand completely suppressed. Two-stream equilibrium distributions such as that in example 2 seem to be most effective in enhancing growth rates at the

resonance $\hat{k}=\hat{k}_r$. Gaps of no growth can be introduced at moderate values of \hat{k} . At small values of \hat{k} where eigenmodes may contain backward-traveling components, growth rates and the properties of eigenmodes can be greatly changed by changing $\Phi(\xi)$. [This latter fact suggests, but does not prove, that absolute instability properties may depend strongly on $\Phi(\xi)$. However, no pinch-point analyses of these systems have been carried out.³¹⁻³³]

IV. DISPERSION CHARACTERISTICS FOR THE AXIAL-DEPENDENT EQUILIBRIUM DISTRIBUTION WITHOUT AXIAL MOMENTUM SPREAD

A. Analysis

Finally, we consider the axial-dependent equilibrium distribution $f_0(p_\perp, p_z, \xi) = f_0(p_\perp, p_z, \phi - m\Omega_c z/p_z)$ for which the perturbed field components are related by the integral equations (41)–(43). Even if the equilibrium distribution is not uniformly random in ϕ , Eqs. (41)–(43) will re-

duce to algebraic equations if there is no spread in p_z in the equilibrium distribution. (A spread in energy is permitted if it is due only to a spread in p_\perp .) The most general equilibrium distribution having this property is

$$f_0(p_\perp, p_z, \zeta) = \delta(p_z - p_{z0}) \hat{f}_0(p_\perp, p_{z0}, \zeta). \quad (86)$$

It follows from Eq. (40) that

$$h_n(p_\perp, p_z) = \delta(p_z - p_{z0}) \hat{h}_n(p_\perp, p_{z0}), \quad (87)$$

where

$$\hat{h}_n(p_\perp, p_{z0}) = \frac{1}{\sqrt{2\pi}} \int_0^{2\pi} d\zeta \hat{f}_0(p_\perp, p_{z0}, \zeta) \exp(-in\zeta). \quad (88)$$

Three homogeneous equations relating just three field components are found using a procedure similar to that used in obtaining Eq. (58). In matrix form the equations are

$$\mathbf{D}' \mathbf{E}' = 0, \quad (89)$$

where

$$\mathbf{D}' = \begin{pmatrix} \hat{D}'_{--}(k, \omega, \Omega_c, p_{z0}) & -\hat{\eta}_{-+}(k, \omega, \Omega_c, p_{z0}) & -\hat{\eta}_{-z}(k, \omega, \Omega_c, p_{z0}) \\ -\hat{\eta}_{+-}(k + 2m\Omega_c/p_{z0}, \omega, \Omega_c, p_{z0}) & \hat{D}'_{++}(k + 2m\Omega_c/p_{z0}, \omega, \Omega_c, p_{z0}) & -\hat{\eta}_{+z}(k + 2m\Omega_c/p_{z0}, \omega, \Omega_c, p_{z0}) \\ -\hat{\eta}_{z-}(k + m\Omega_c/p_{z0}, \omega, \Omega_c, p_{z0}) & -\hat{\eta}_{z+}(k + m\Omega_c/p_{z0}, \omega, \Omega_c, p_{z0}) & \hat{D}'_{zz}(k + m\Omega_c/p_{z0}, \omega, p_{z0}) \end{pmatrix}, \quad (90)$$

and

$$\mathbf{E}' = \begin{pmatrix} E_{1-}(k, \omega) \\ E_{1+}(k + 2m\Omega_c/p_{z0}, \omega) \\ E_{1z}(k + m\Omega_c/p_{z0}, \omega) \end{pmatrix}. \quad (91)$$

The quantities $\hat{\eta}_{ij}$ in Eq. (90) are obtained from the corresponding quantities in Eqs. (47)–(52) by replacing $h_n(p_\perp, p_z)$ with $\hat{h}_n(p_\perp, p_{z0})$, p_z with p_{z0} , and γ with $\gamma(p_\perp, p_{z0})$. The remaining quantities in Eq. (90) can be obtained from Eqs. (44)–(46). They are

$$\begin{aligned} \hat{D}'_{--}(k, \omega, \Omega_c, p_{z0}) &= \omega^2 - c^2 k^2 - \frac{\sqrt{2\pi}}{2} \Omega_p^2 \int_0^\infty dp_\perp \hat{h}_0(p_\perp, p_{z0}) \frac{p_\perp}{\gamma(p_\perp, p_{z0})} \\ &\times \left[2 \left(\omega - \frac{kp_{z0}}{\gamma(p_\perp, p_{z0})m} \right) \left(\omega - \frac{kp_{z0}}{\gamma(p_\perp, p_{z0})m} - \frac{\Omega_c}{\gamma(p_\perp, p_{z0})} \right)^{-1} - \frac{p_\perp^2}{\gamma^2(p_\perp, p_{z0})m^2 c^2} (\omega^2 - c^2 k^2) \right. \\ &\left. \times \left(\omega - \frac{kp_{z0}}{\gamma(p_\perp, p_{z0})m} - \frac{\Omega_c}{\gamma(p_\perp, p_{z0})} \right)^{-2} \right], \quad (92) \end{aligned}$$

$$\hat{D}'_{++}(k, \omega, \Omega_c, p_{z0}) = \hat{D}'_{--}(k, \omega, -\Omega_c, p_{z0}), \quad (93)$$

$$\begin{aligned} \hat{D}'_{zz}(k, \omega, p_{z0}) &= 1 - \sqrt{2\pi} \Omega_p^2 \int_0^\infty dp_\perp p_\perp \hat{h}_0(p_\perp, p_{z0}) \gamma^{-1}(p_\perp, p_{z0}) \\ &\times \left(1 - \frac{p_{z0}^2}{\gamma^2(p_\perp, p_{z0})m^2 c^2} \right) \left(\omega - \frac{kp_{z0}}{\gamma(p_\perp, p_{z0})m} \right)^{-2}. \quad (94) \end{aligned}$$

Once the assumption is made that equilibrium self-fields can be neglected, the exact dispersion relation for the case of definite $p_z = p_{z0}$ is

$$\det \mathbf{D}'(k, \omega) = 0. \quad (95)$$

For a given frequency ω , the wave number of the right-hand polarized wave E_{1-} is k . The wave numbers of the fields E_{1+} and E_{1z} are $k + 2m\Omega_c/p_{z0}$ and $k + m\Omega_c/p_{z0}$, respectively. Although no assumption of a steady state has been made in the derivation of Eqs. (89)–(95), these results are the same as those obtained in Eqs. (60)–(62) of the steady-state analysis of Ref. 9.

Finally, we emphasize that the eigenmode \mathbf{E} in Eq. (60) is of a different nature than the eigenmode \mathbf{E}' in Eq. (92). The eigenmode \mathbf{E} is a composite of three components which refer to waves of the same propagation vector but of different frequencies. These frequencies differ by fixed real values. On the other hand, the eigenmode \mathbf{E}' is a composite of three modes which refer to waves of the same frequency but of different propagation vectors. These propagation vectors differ by fixed real values. In either case, if \hat{k} is restricted to real values, then temporal growth or decay rates are given by $\text{Im } \hat{\omega}$ for all components. If $\hat{\omega}$ is restricted to real values, then spatial growth or decay rates are given by $\text{Im } \hat{k}$ for all components.

B. Case of definite p_\perp and p_z

As in Sec. III, we present numerical examples for cases in which both $p_z = p_{z0}$ and $p_\perp = p_{\perp 0}$ have definite values in the equilibrium distribution. Consequently, the factor $\hat{f}_0(p_\perp, p_{z0}, \zeta)$ in Eq. (86) is selected to be of the form

$$\hat{f}_0(p_\perp, p_{z0}, \zeta) = \frac{\delta(p_\perp - p_{\perp 0})}{p_\perp} \Psi(\zeta), \quad (96)$$

where $\Psi(\zeta)$ is a periodic function of ζ (or ϕ) of period 2π . From Eq. (5), the normalization condition on $\Psi(\zeta)$ is

$$\int_0^{2\pi} d\phi \Psi\left(\phi - m \frac{\Omega_c}{p_z} z\right) = \int_0^{2\pi} d\zeta \Psi(\zeta) = 1. \quad (97)$$

It follows from Eq. (88) that

$$\hat{h}_n(p_\perp, p_{z0}) = \frac{1}{\sqrt{2\pi}} \frac{\delta(p_\perp - p_{\perp 0})}{p_\perp} w_n, \quad (98)$$

where

$$w_n = \int_0^{2\pi} d\zeta \Psi(\zeta) \exp(-in\zeta). \quad (99)$$

Notice that $w_0 = 1$ and that $w_{-n} = w_n^*$.

With the aid of Eqs. (92)–(94) and Eqs. (46)–(52), we obtain the dispersion relation in Eq. (95) for the case of definite p_\perp and p_z . The dispersion relation is

$$\begin{aligned} M_{--}(\hat{k}, \hat{\omega}) M'_{++}(\hat{k}, \hat{\omega}) M_{zz}(\hat{k}, \hat{\omega}) &= \frac{1}{2} \left(\frac{\omega_p^2}{\omega_c^2} \right)^2 \beta_\perp^2 |w_1|^2 \left\{ (\beta_z \hat{\omega} - \hat{k})^2 M'_{++}(\hat{k}, \hat{\omega}) + \left[\beta_z \hat{\omega} - \left(\hat{k} + \frac{2}{\beta_z} \right) \right]^2 M_{--}(\hat{k}, \hat{\omega}) \right\} \\ &+ \frac{1}{4} \left(\frac{\omega_p^2}{\omega_c^2} \right)^2 \beta_\perp^4 |w_2|^2 \left[\hat{\omega}^2 - \hat{k} \left(\hat{k} + \frac{2}{\beta_z} \right) \right]^2 M_{zz}(\hat{k}, \hat{\omega}) \\ &- \frac{1}{4} \left(\frac{\omega_p^2}{\omega_c^2} \right)^3 \beta_\perp^4 (w_2 w_{-1}^2 + w_{-2} w_1^2) \left[\hat{\omega}^2 - \hat{k} \left(\hat{k} + \frac{2}{\beta_z} \right) \right] \left[\beta_z \hat{\omega} - \left(\hat{k} + \frac{2}{\beta_z} \right) \right] (\beta_z \hat{\omega} - \hat{k}). \end{aligned} \quad (100)$$

Dimensionless frequencies, wave numbers, and velocity components are defined as in Sec. III B, and

$$\begin{aligned} M'_{++}(\hat{k}, \hat{\omega}) &= \left[\hat{\omega}^2 - \left(\hat{k} + \frac{2}{\beta_z} \right)^2 \right] (\hat{\omega} - \hat{k} \beta_z - 1)^2 \\ &- \frac{\omega_p^2}{\omega_c^2} (\hat{\omega} - \hat{k} \beta_z - 2) (\hat{\omega} - \hat{k} \beta_z - 1) \\ &+ \frac{1}{2} \frac{\omega_p^2}{\omega_c^2} \beta_\perp^2 \left[\hat{\omega}^2 - \left(\hat{k} + \frac{2}{\beta_z} \right)^2 \right]. \end{aligned} \quad (101)$$

The quantities $M_{--}(\hat{k}, \hat{\omega})$ and $M_{zz}(\hat{k}, \hat{\omega})$ are defined in Eqs. (70) and (72), respectively.

Like Eq. (69), Eq. (100) is valid for complex $\hat{\omega}$ and complex \hat{k} . It is invariant under the transformation

$$\hat{k} \rightarrow -\hat{k}^* - \frac{2}{\beta_z}, \quad \hat{\omega} \rightarrow -\hat{\omega}^*. \quad (102)$$

In analogy with Eq. (74), it follows from the matrix equation (90) that, if either $w_1 \neq 0$ or $w_2 \neq 0$, then under the transformation in Eq. (102)

$$\begin{aligned} \frac{E_{1+}(\hat{k} + 2/\beta_z, \hat{\omega})}{E_{1-}(\hat{k}, \hat{\omega})} &\rightarrow \frac{E_{1+}(-\hat{k}^*, -\hat{\omega}^*)}{E_{1-}(-\hat{k}^* - 2/\beta_z, -\hat{\omega}^*)} \\ &= \frac{E_{1-}^*(\hat{k}, \hat{\omega})}{E_{1+}^*(\hat{k} + 2/\beta_z, \hat{\omega})}. \end{aligned} \quad (103)$$

Moreover, in analogy with Eq. (75), if $w_1 \neq 0$, then under the transformation in Eq. (102)

$$\begin{aligned} \frac{E_{1+}(\hat{k} + 2/\beta_z, \hat{\omega})}{E_{1z}(\hat{k} + 1/\beta_z, \hat{\omega})} &\rightarrow \frac{E_{1+}(-\hat{k}^*, -\hat{\omega}^*)}{E_{1z}(-\hat{k}^* - 1/\beta_z, -\hat{\omega}^*)} \\ &= \frac{E_{1-}^*(\hat{k}, \hat{\omega})}{E_{1z}^*(\hat{k} + 1/\beta_z, \hat{\omega})}, \\ \frac{E_{1-}(\hat{k}, \hat{\omega})}{E_{1z}(\hat{k} + 1/\beta_z, \hat{\omega})} &\rightarrow \frac{E_{1-}(-\hat{k}^* - 2/\beta_z, -\hat{\omega}^*)}{E_{1z}(-\hat{k}^* - 1/\beta_z, -\hat{\omega}^*)} \\ &= \frac{E_{1+}^*(\hat{k} + 2/\beta_z, \hat{\omega})}{E_{1z}^*(\hat{k} + 1/\beta_z, \hat{\omega})}. \end{aligned} \quad (104)$$

The ratio of the time averaged Poynting vectors associated with the individual $E_{1+}(\hat{k} + 2/\beta_z, \hat{\omega})$ and $E_{1-}(\hat{k}, \hat{\omega})$ fields is

$$\left| \frac{S_+(\hat{k} + 2/\beta_z, \hat{\omega})}{S_-(\hat{k}, \hat{\omega})} \right| = \left| \frac{\hat{k} + 2/\beta_z}{\hat{k}} \right| \left| \frac{E_{1+}(\hat{k} + 2/\beta_z, \hat{\omega})}{E_{1-}(\hat{k}, \hat{\omega})} \right|^2. \quad (105)$$

Like the dispersion relation in Eq. (69) of Sec. III B, Eq. (100) is a tenth-degree polynomial equation in either \hat{k} or $\hat{\omega}$. The large $|\hat{k}|$ behavior of $\hat{\omega}(\hat{k})/\hat{k}$ given by Eq. (100) is the same as that given by Eq. (69), including two branches with $\hat{\omega}(\hat{k})/\hat{k} \approx 1$, two branches with $\hat{\omega}(\hat{k})/\hat{k} \approx -1$, and six branches with $\hat{\omega}(\hat{k})/\hat{k} \approx \hat{k} \beta_z$.

If either w_1 or w_2 vanishes, approximations for $\hat{\omega}(\hat{k})$ valid for large values of \hat{k} are readily determined and are found to be very similar to those found in the previous section for the case of the time-dependent equilibrium. If $w_1 = 0$ and $w_2 \neq 0$, then the transverse electromagnetic components are coupled to each other and the electrostatic component is uncoupled. The large $|\hat{k}|$ behaviors of the ten

branches of the dispersion relation in Eq. (100) are similar to those given in Eqs. (76)–(80) for the corresponding case ($s_1 = 0, s_2 \neq 0$) of the dispersion relation in Eq. (69). Four of the branches now obey Eqs. (76) and (79). Four branches obey Eqs. (77) and (78) with s_2 replaced by w_2 , that is

$$\hat{\omega} \approx \hat{k}\beta_z + 1 \pm \frac{i}{\sqrt{2}} \frac{\omega_p}{\omega_c} \beta_{\perp} (1 + |w_2|)^{1/2}, \quad (106)$$

$$\hat{\omega} \approx \hat{k}\beta_z + 1 \pm \frac{i}{\sqrt{2}} \frac{\omega_p}{\omega_c} \beta_{\perp} (1 - |w_2|)^{1/2}. \quad (107)$$

Finally, Eq. (82) is no longer valid and is replaced by

$$\hat{\omega} = \pm \left[(\hat{k} + 2\beta_z)^2 + \frac{\omega_p^2}{\omega_c^2} \right]^{1/2}, \quad (108)$$

for the two remaining branches. Growth-rate curves for $|w_2| < 1$ will show two unstable branches of the dispersion relation in Eq. (100) for large values of real \hat{k} .

If $w_1 \neq 0$ and $w_2 = 0$, then the transverse electromagnetic components of an eigenmode are coupled through the longitudinal electrostatic component. The large $|\hat{k}|$ behavior of the dispersion relation in Eq. (100) is similar to that of the dispersion relation in Eq. (69) for the analogous case of $s_1 \neq 0$ and $s_2 = 0$. Four of the branches obey Eqs. (79) and (81). Four additional branches obey Eqs. (82) and (83) with the quantity s_1 in Eq. (84) replaced with w_1 , that is

$$\hat{\omega} \approx \hat{k}\beta_z + 1 \pm \frac{1}{\sqrt{2}} \frac{\omega_p}{\omega_c} \kappa'_+, \quad (109)$$

$$\hat{\omega} \approx \hat{k}\beta_z + 1 \pm \frac{i}{\sqrt{2}} \frac{\omega_p}{\omega_c} \kappa'_-, \quad (110)$$

where

$$\kappa'_{\pm} = \left\{ \mp \left(\frac{\beta_{\perp}^2}{2} - (1 - \beta_z^2) \right) + \left[\left(\frac{\beta_{\perp}^2}{2} - (1 - \beta_z^2) \right)^2 + 4\beta_{\perp}^2(1 - \beta_z^2) \left(\frac{1}{2} - |w_1|^2 \right) \right]^{1/2} \right\}^{1/2}. \quad (111)$$

The remaining two branches obey Eq. (106). At large real \hat{k} , growth-rate curves will show two unstable branches of the dispersion relation in Eq. (100) if $|w_1| < 1/\sqrt{2}$.

Finally, if neither w_1 nor w_2 vanish, then the large $|\hat{k}|$ behaviors of four of the branches of the dispersion relation in Eq. (100) are given by Eqs. (79) and (106). The behaviors of the remaining six branches are obtained by solving a cubic equation in $(\hat{\omega} - \hat{k}\beta_z - 1)^2$. We do not include an analysis of the equation in this paper.

C. Numerical examples

Before the numerical examples are presented, one final point of clarification must be made. Throughout this paper, we have followed the usual terminology and referred to $E_{1-}(\hat{k}, \hat{\omega})$ and $E_{1+}(\hat{k}, \hat{\omega})$ as components representing RHP- and LHP-electromagnetic waves, respectively. However, this

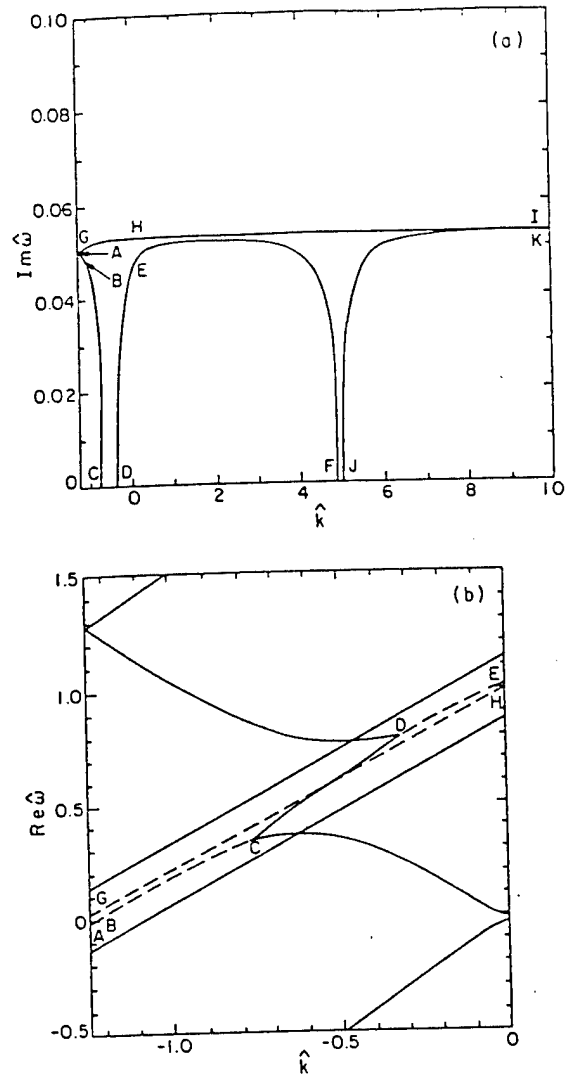


FIG. 8. Plots of complex $\hat{\omega}$ vs \hat{k} (real) for the system parameters $\omega_c^2/\omega_p^2 = 0.05$, $\gamma_0 = 2$, and $\alpha_0 = 0.4$. The spatial-dependent equilibrium distribution in phase is characterized by $w_1 = w_2 = 0$. Plots are (a) $\text{Im} \hat{\omega}$ vs \hat{k} for $-1.254 \leq \hat{k} \leq 10$ and (b) $\text{Re} \hat{\omega}$ vs \hat{k} for $-1.254 \leq \hat{k} \leq 0$.

nomenclature is proper only if $\text{Re} \hat{k} > 0$. If $\text{Re} \hat{k} < 0$, then the roles played by these components are reversed and $E_{1-}(\hat{k}, \hat{\omega})$ and $E_{1+}(\hat{k}, \hat{\omega})$ represent LHP and RHP electromagnetic waves, respectively. If (in addition) $\text{Re} \hat{\omega} > 0$, then both waves are backward traveling. Moreover, if $\text{Re} \hat{\omega} < 0$, then both waves are forward traveling.

As in Sec. III, the following numerical computations are limited to the case of real \hat{k} . Then, from Eq. (102), Eq. (100) is invariant under the transformation $\hat{\omega} \rightarrow -\hat{\omega}^*$ and $\hat{k} \rightarrow -\hat{k} - 2/\beta_z$. This transformation is equivalent to inverting a plot of $\text{Re} \hat{\omega}$ vs \hat{k} (real) through the point $(\hat{k}, \text{Re} \hat{\omega}) = (-1/\beta_z, 0)$ and reflecting a plot of $\text{Im}(\hat{\omega})$ vs \hat{k} (real) through the vertical line $\hat{k} = -1/\beta_z$. Because of Eqs. (103) and (104), no new information is obtained from the transformed eigenvectors. Consequently, the region $\hat{k} < -1/\beta_z$ is omitted from the following plots.

Parameter values used below are the same as those used in previous numerical examples (i.e., $\hat{\omega}_p^2/\hat{\omega}_c^2 = 0.05$, $\gamma_0 = 2$,

and $\alpha_0=0.4$). Functional forms considered for $\Psi(\zeta)$ are chosen as $\Psi(\zeta)=\Phi(\zeta)$, where $\Phi(\zeta)$ is defined in Figs. 3(a)–3(d). Moreover each of the examples below is the analog (for the axial-dependent distribution) of the example of the same number in Sec. III C (for the time-dependent distribution).

Example 1: For $w_1=w_2=0$, which can be obtained from the uniform $\Psi(\zeta)$ corresponding to Fig. 3(a), the dispersion relation in Eq. (100) reduces to the three independent dispersion relations $M_{--}(\hat{k}, \hat{\omega})=0$, $M'_{++}(\hat{k}, \hat{\omega})=0$, and $M_{zz}(\hat{k}, \hat{\omega})=0$ for uncoupled right- and left-circularly polarized transverse waves and the longitudinal electrostatic wave, respectively. For a given frequency, the respective wave numbers for these waves are \hat{k} , $\hat{k}+2/\beta_z$, and $\hat{k}+1/\beta_z$. Growth-rate curves are shown in Fig. 8(a) for $-1/\beta_z = -1.254 \leq \hat{k} \leq 10$. Plots of $\text{Re } \hat{\omega}$ vs \hat{k} for $-1/\beta_z \leq \hat{k} \leq 0$ are presented in Fig. 8(b). Letters show corresponding points in Figs. 8(a) and 8(b).

In Fig. 8(a), the growth-rate curve segments GH and HI are obtained from roots of $M'_{++}(\hat{k}, \hat{\omega})$, so that the corresponding eigenmodes have a single nonvanishing component $E_{1+}(\hat{k}+2/\beta_z, \hat{\omega})$. Referring to Fig. 8(b), we see that $\text{Re } \hat{\omega} > 0$ and $\hat{k}+2/\beta_z > 0$ on both segments. Consequently, both segments represent unstable electromagnetic waves that are LHP and forward traveling. All other growth-rate curve segments in Fig. 8(a) are obtained from roots of $M_{--}(\hat{k}, \hat{\omega})=0$, so that the corresponding eigenmodes have a single nonvanishing component $E_{1-}(\hat{k}, \hat{\omega})$. For all points of the short growth-rate curve segment AB , reference to Fig. 8(b) shows that $\hat{k} < 0$ and $\text{Re } \hat{\omega} < 0$. Consequently, growth-rate curve segment AB pertains to unstable, forward-traveling LHP electromagnetic waves. Similarly, $\hat{k} < 0$ and $\text{Re } \hat{\omega} > 0$ for eigenmodes on growth-rate curve segments BC and DE , so that these segments represent unstable backward-traveling, LHP electromagnetic waves. The remaining growth-rate curve segments (EF and JK) pertain to unstable forward-traveling, RHP electromagnetic waves. As expected, there is no growth of the RHP electromagnetic wave at the resonance wave number $k_r = 1/(1-\beta_z) = 4.94$. The eigenmodes obtained from roots of $M'_{++}(\hat{k}, \hat{\omega})$ are of course completely decoupled from the eigenmodes obtained from roots of $M_{--}(\hat{k}, \hat{\omega})=0$. Nevertheless, Fig. 8(a) represents the limit approached by any system with our parameters as both w_1 and w_2 approach zero.

This example is analogous to example 1 shown in Figs. 4(a) and 4(b) in Sec. III C. Comparing Figs. 4(a) and 8(a), we see that they differ in two respects. First, the growth-rate curve in Fig. 8(a) obtained from $M'_{++}(\hat{k}, \hat{\omega})=0$ has the same form as the growth-rate curve in Fig. 4(a) obtained from $M_{++}(\hat{k}, \hat{\omega})=0$ but is displaced to the left by $2/\beta_z = 2.508$. Second, no information is lost in Figs. 4(a) and 4(b) by ignoring the negative \hat{k} -axis. However, only $\hat{k} < -1/\beta_z$ can be ignored in Figs. 8(a) and 8(b) without losing information.

Example 2: For $w_1=0$ and $w_2=2\sqrt{2}/\pi$, which can be obtained if $\Psi(\zeta)$ corresponds to Fig. 3(b) with $a=\pi/4$, the equilibrium beam consists of two streams, each with a water-

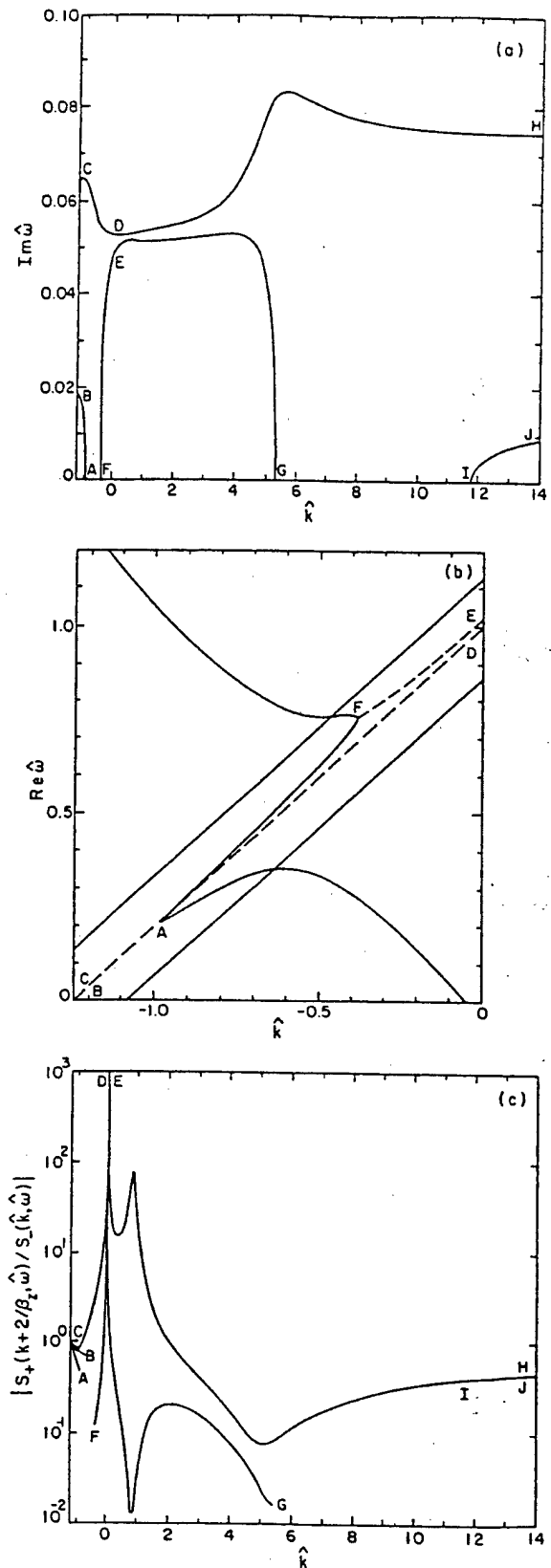


FIG. 9. Dispersion relations and properties of corresponding eigenvectors for system parameters $\omega_c^2/\omega_p^2=0.05$, $\gamma_0=2$, and $\alpha_0=0.4$. The spatial-dependent equilibrium distribution in phase is characterized by $w_1=0$ and $w_2=2\sqrt{2}/\pi$. Plots are (a) $\text{Im } \hat{\omega}$ vs \hat{k} for $-1.254 \leq \hat{k} \leq 14$ and (b) $\text{Re } \hat{\omega}$ vs \hat{k} for $-1.254 \leq \hat{k} \leq 0$. Also shown for unstable eigenmodes is (c) the Poynting flux ratio in Eq. (105) vs \hat{k} .

bag distribution in ϕ of width $\pi/4$. One distribution is centered at $\phi = m\Omega_c z/p_{z0}$ and the other at $\phi = m\Omega_c z/p_{z0} + \pi$. As z varies, each center rotates about the direction of the applied field lines with a characteristic wavelength of $2\pi p_{z0}/m\Omega_c = 2\pi v_{z0}/\omega_c$.

Growth-rate curves (for $-1.25 \leq \hat{k} \leq 16$) and corresponding plots of $\text{Re } \hat{\omega}$ vs \hat{k} (for $-1.25 \leq \hat{k} \leq 0$) are presented in Figs. 9(a) and 9(b). Plots of the Poynting ratio in Eq. (105) vs \hat{k} (for $-1.25 \leq \hat{k} \leq 16$) appear in Fig. 9(c). Letters show corresponding points on these plots. The letters have also been chosen to correlate with letters on the corresponding plots for example 2 of Sec. III C in Figs. 5(a)–5(c), which is analogous to the present example. Superficially the plots in Figs. 9(a)–9(c) are very similar to the corresponding plots in Figs. 5(a)–5(c). However, it is emphasized that the eigenmodes are very different in the two cases. The eigenmodes for Fig. 5 consist of the nonvanishing components $E_{1-}(\hat{k}, \hat{\omega})$ and $E_{1+}(\hat{k}, \hat{\omega} - 2)$, whereas the eigenmodes for Fig. 9 consist of the nonvanishing components $E_{1-}(\hat{k}, \hat{\omega})$ and $E_{1+}(\hat{k} + 2/\beta_z, \hat{\omega})$.

By comparing Figs. 9(a) and 9(b), it is easily seen that the eigenmodes belonging to the growth-rate curve segments BA , CD , and FE consist of LHP, forward-traveling electromagnetic waves [from $E_{1+}(\hat{k} + 2/\beta_z, \hat{\omega})$] and LHP, backward-traveling electromagnetic waves [from $E_{1-}(\hat{k}, \hat{\omega})$]. (The corresponding modes in Fig. 5 consist of RHP, forward-traveling and LHP, backward-traveling electromagnetic waves.) From Fig. 9(c), we see that the backward Poynting flux is relatively strong for most eigenmodes on CA and that it varies rapidly with \hat{k} for eigenmodes on CD and FE . The infinity in the Poynting flux ratio at the cutoff at $\hat{k} = 0$ is due to the factor $|(\hat{k} + 2/\beta_z)/\hat{k}|$ in Eq. (105). All of the remaining growth-rate curve segments in Fig. 9(a) pertain to eigenmodes consisting of a forward-traveling RHP and a forward-traveling LHP component. Notice that the branch CDH of the dispersion relation shows a growth rate at the resonance $\hat{k}_r = 4.94$ which is significantly greater than any growth rate for the uncoupled system in Fig. 8(a). Reference to Fig. 9(c) shows that the Poynting flux of RHP electromagnetic radiation is dominant in the corresponding eigenmode. (This behavior is similar to that found at $\hat{k} = \hat{k}_r$ for example 2 in Sec. III C.) Figures 5(a) and 9(a) are very similar at large values of \hat{k} in conformity with previous analytic results pertaining to the large \hat{k} behaviors of Eq. (69) when $s_1 = 0$ and Eq. (100) when $w_1 = 0$.

Example 3: The analog of example 3 of Sec. III [whose stability properties are summarized in Figs. 6(a)–6(d)] is obtained by setting $w_1 = -2i/\pi$ and $w_2 = 0$ in Eq. (98). Growth-rate curves for $-1.25 \leq \hat{k} \leq 10$ are presented in Fig. 10(a). Details of the growth-rate curves in the negative \hat{k} interval ($-1.25 \leq \hat{k} \leq 0$) are shown in Fig. 10(b). Corresponding plots of $\text{Re } \hat{\omega}$ vs \hat{k} (for $-1.25 \leq \hat{k} \leq 0$) are presented in Fig. 11(a). Plots of the Poynting ratio in Eq. (105) vs \hat{k} appear in Fig. 11(b). The component $E_{1z}(\hat{k} + 1/\beta_z, \hat{\omega})$ will not necessarily vanish for unstable eigenmodes of this system. Consequently, plots of $E_{1-}(\hat{k}, \hat{\omega})/E_{1z}(\hat{k} + 1/\beta_z, \hat{\omega})$

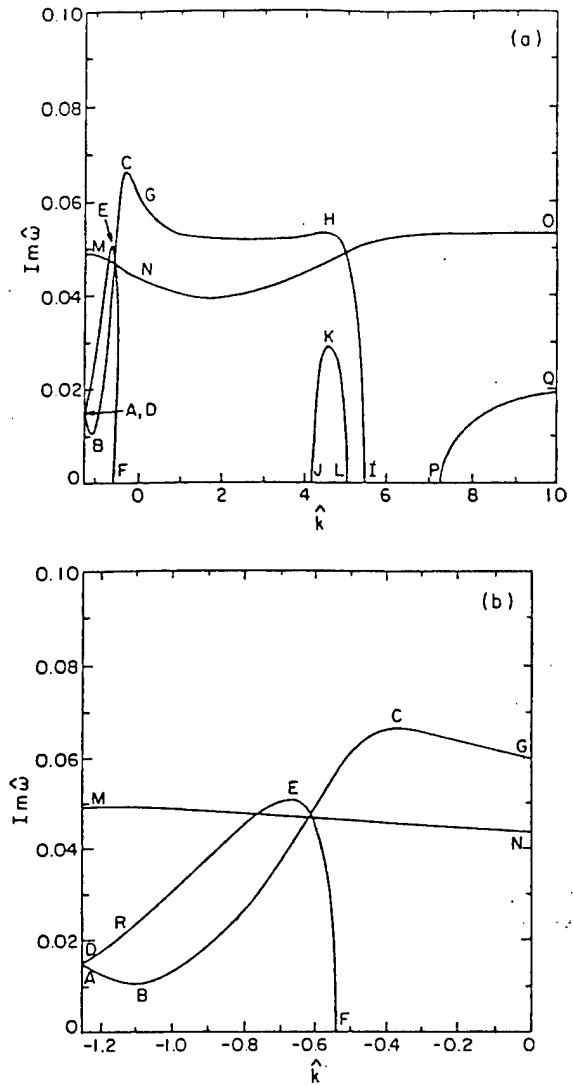


FIG. 10. Growth-rate curves ($\text{Im } \hat{\omega}$ vs \hat{k} , real) for system parameters $\omega_p^2/\omega_c^2 = 0.05$, $\gamma_0 = 2$, and $\alpha_0 = 0.4$. The spatial-dependent equilibrium distribution in phase is characterized by $w_1 = -2i/\pi$ and $w_2 = 0$. Plots are (a) $\text{Im } \hat{\omega}$ vs \hat{k} for $-1.25 \leq \hat{k} \leq 10$ and (b) a detail of the previous plot for $-1.25 \leq \hat{k} \leq 0$.

vs \hat{k} for unstable modes are presented in Fig. 11(c). Letters show corresponding points in Figs. 10 and 11.

A detailed comparison of Figs. 10 and 11(a) gives the following description of the unstable eigenmodes. The components of an eigenmode pertaining to the short growth-rate curve segment DR are two forward-traveling LHP electromagnetic waves [from $E_{1-}(\hat{k}, \hat{\omega})$ and $E_{1+}(\hat{k} + 2/\beta_z, \hat{\omega})$] and a backward-traveling electrostatic wave [from $E_{1z}(\hat{k} + 1/\beta_z, \hat{\omega})$]. The components pertaining to the growth-rate curve segments REF , $ABCG$, and MN are a backward-traveling LHP electromagnetic wave [from $E_{1-}(\hat{k}, \hat{\omega})$], a forward-traveling LHP electromagnetic wave [from $E_{1+}(\hat{k} + 2/\beta_z, \hat{\omega})$], and a forward traveling electrostatic wave [from $E_{1z}(\hat{k} + 1/\beta_z, \hat{\omega})$]. All other growth-rate curve segments have eigenmodes consisting of forward traveling LHP and RHP electromagnetic waves and a forward traveling electrostatic wave.

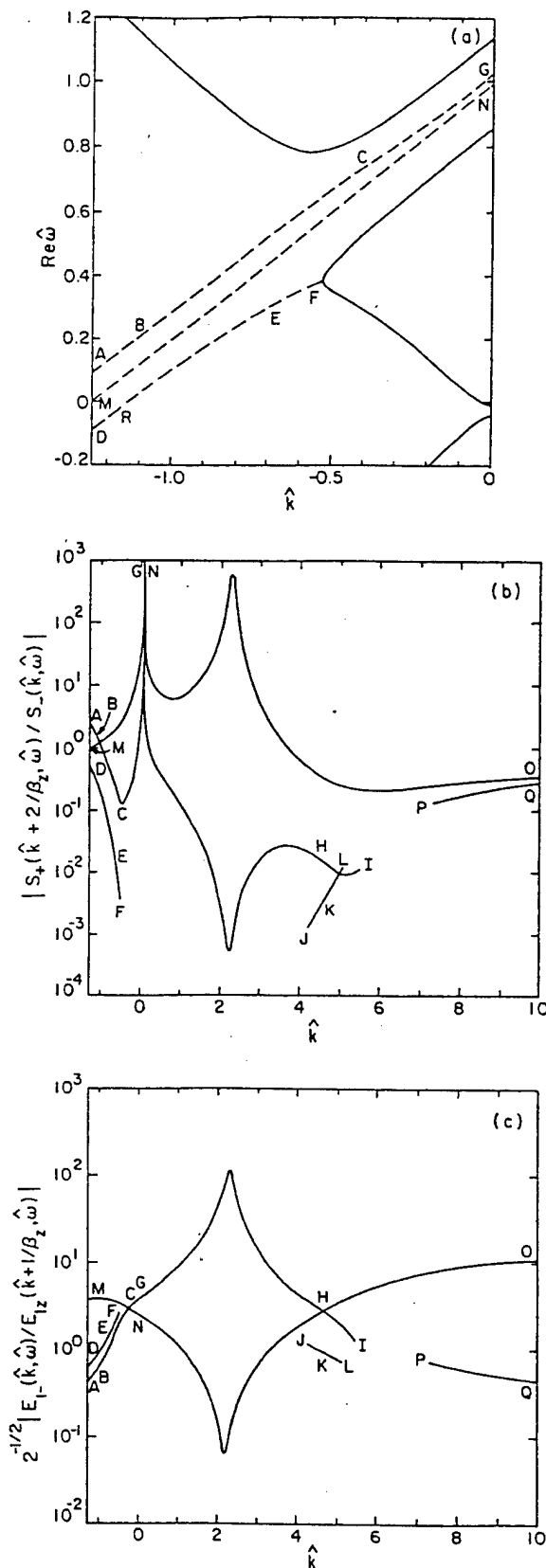


FIG. 11. Additional properties of the system whose growth-rate curves are plotted in Fig. 10. Plot (a) of $\text{Re } \hat{\omega}$ vs \hat{k} for $-1.254 \leq \hat{k} \leq 0$. Shown for unstable eigenmodes are (b) the Poynting flux ratio in Eq. (105) vs \hat{k} and (c) $2^{-1/2} |E_{1-}(\hat{k}, \hat{\omega}) / E_{1z}(\hat{k} + 1/\beta_z, \hat{\omega})|$ vs \hat{k} .

The most rapidly growing eigenmode of this system is that at point C in Figs. 10(a) and 10(b). The components of this eigenmode are a backward-traveling LHP wave, a forward-traveling LHP wave, and a forward-traveling electrostatic wave. Reference to Figs. 11(b) and 11(c) shows that the backward-traveling component [which arises from $E_{1-}(\hat{k}, \hat{\omega})$] is the largest component both in amplitude and energy transfer. A similar situation was found for small $|\hat{k}|$ in Fig. 6(a) for the axial-dependent case except that the forward-traveling electromagnetic component was found to be RHP.

Two branches of the growth-rate curves in Figs. 10(a) and 10(b) (MNO and ABCGHI) show moderate growth rates at the resonance wave number $\hat{k}_r = 4.94$. For both of these branches, Figs. 11(b) and 11(c) show that the eigenmode at $\hat{k}_r = 4.94$ has a relatively large RHP electromagnetic component. Again we see that this behavior differs from that of the uncoupled system in Fig. 8(a), which shows no growth of RHP electromagnetic waves at the resonance wave number. The growth rates at \hat{k}_r are approximately the same in Fig. 6(a) for the time-dependent equilibrium and Fig. 10(a) for the axial-dependent equilibrium; however, the electrostatic components of the corresponding eigenvectors are of greater relative amplitude in the axial-dependent case than in the time-dependent case. [Compare Fig. 11(c) with Fig. 6(d).]

Finally, at large values of \hat{k} , Figs. 10(a) and 6(a) approximate each other closely. This fact conforms with our previous results giving the large- $|\hat{k}|$ behaviors of Eq. (69) for $s_2 = 0$ and Eq. (100) for $w_2 = 0$. However, the corresponding eigenmodes [E in Eq. (60) and E' in Eq. (91)] are different even in the limit of large \hat{k} . By comparing Fig. 6(d) with Fig. 11(c), it is seen that (at large \hat{k}) the electrostatic component is relatively much stronger in the case of the axial-dependent equilibrium distribution.

Example 4: To obtain the analog of example 4 of Sec. III C (whose stability properties are summarized in Fig. 7), choose $w_1 = w_2 = 1$. These values are obtained by choosing $\Psi(\zeta) = \sum_{n=-\infty}^{\infty} \delta(\zeta - 2n\pi)$, so that in effect the phase of any particle is given by $\phi = m\Omega_z z/p_z$. Growth-rate curves (for $-1.254 \leq \hat{k} \leq 8$) and corresponding plots of $\text{Re } \hat{\omega}$ vs \hat{k} (for $-1.254 \leq \hat{k} \leq 0$) are presented in Figs. 12(a) and 12(b), respectively. For unstable branches of the dispersion relation in Eq. (100), plots of the Poynting flux ratio in Eq. (105) vs \hat{k} and $E_{1-}(\hat{k}, \hat{\omega}) / E_{1z}(\hat{k} + 1/\beta_z, \hat{\omega})$ vs \hat{k} are presented in Figs. 12(c) and 12(d), respectively. Letters show corresponding points in these plots. The letters correspond only loosely to those in Fig. 7.

Comparing Figs. 12(a) and 12(b), we see that the components of an eigenmode on growth-rate curve segment DN are a backward-traveling LHP electromagnetic wave [$E_{1+}(\hat{k} + 2/\beta_z, \hat{\omega})$], a forward-traveling LHP electromagnetic wave [$E_{1-}(\hat{k}, \hat{\omega})$], and a backward-traveling electrostatic wave [$E_{1z}(\hat{k} + 1/\beta_z, \hat{\omega})$]. Eigenmodes on growth-rate curve segments ACB and NEF consist of a backward-traveling LHP electromagnetic wave [$E_{1-}(\hat{k}, \hat{\omega})$], a forward-

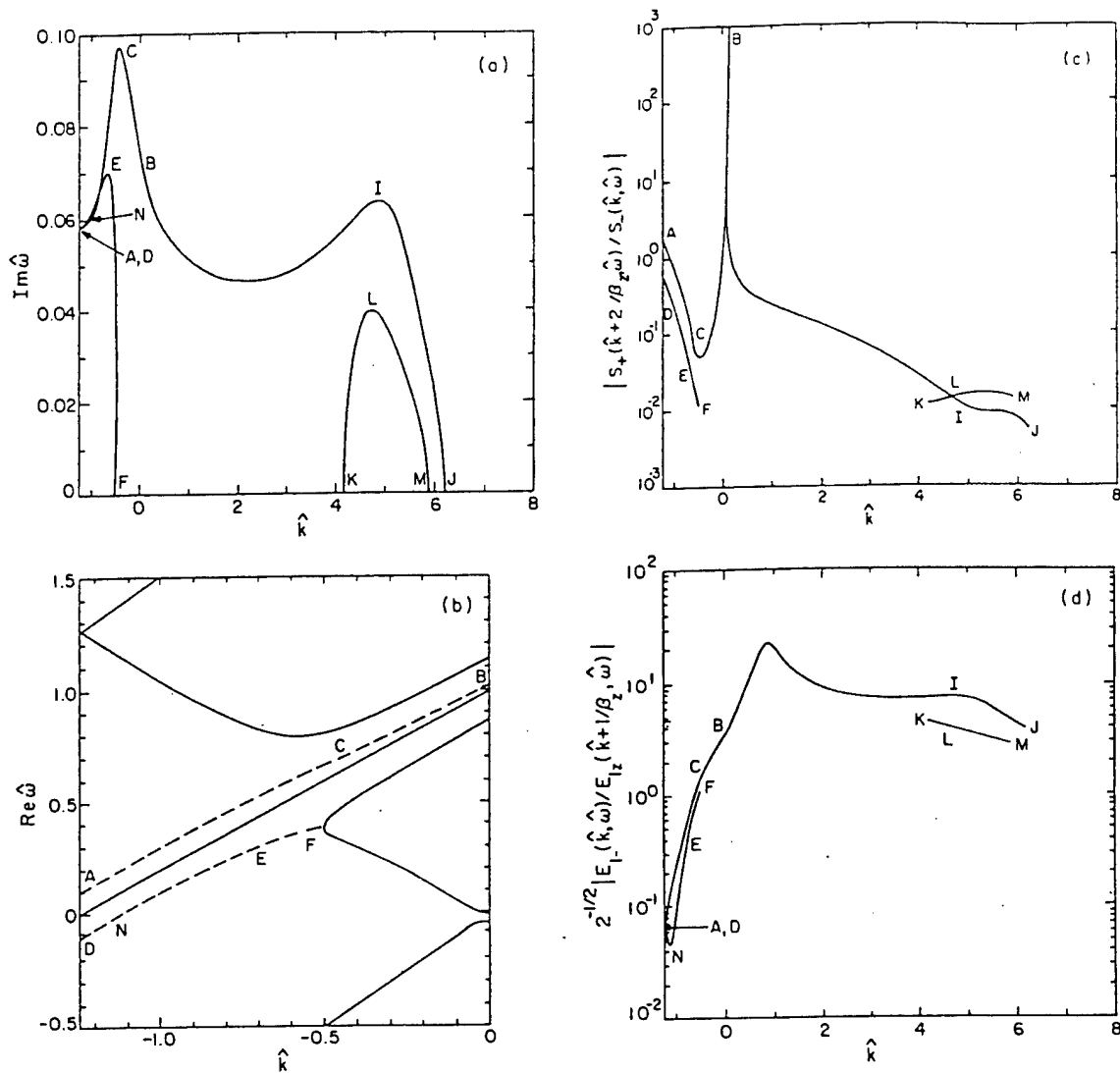


FIG. 12. Dispersion relations and properties of corresponding eigenvectors for system parameters $\omega_z^2/\omega_p^2=0.05$, $\gamma_0=2$, and $\alpha_0=0.4$. The axial-dependent equilibrium distribution in phase is characterized by $w_1=w_2=1$. Plots are (a) $\text{Im } \hat{\omega}$ vs \hat{k} for $-1.25 \leq \hat{k} \leq 8$ and (b) $\text{Re } \hat{\omega}$ vs \hat{k} for $-1.25 \leq \hat{k} \leq 0$. Also shown for unstable eigenmodes are (c) the Poynting flux ratio in Eq. (105) vs \hat{k} and (d) $2^{-1/2} |E_{1-}(\hat{k}, \hat{\omega}) / E_{1z}(\hat{k} + 1/\beta_z, \hat{\omega})|$ vs \hat{k} .

traveling LHP electromagnetic wave $[E_{1+}(\hat{k} + 2/\beta_z, \hat{\omega})]$, and a forward-traveling electrostatic wave $[E_{1z}(\hat{k} + 1/\beta_z, \hat{\omega})]$. Eigenmodes on all other growth-rate curve segments consist of forward traveling RHP and LHP electromagnetic waves and a forward-traveling electrostatic wave.

Some properties of the growth-rate curves in Fig. 12(a) are similar to those in Fig. 7(a). Like Fig. 7(a), Fig. 12(a) shows no growth at large values of \hat{k} . Both sets of curves show very large growth rates at small values of $|\hat{k}|$, where backward waves occur [i.e., near point B in Fig. 7(a) and point C in Fig. 12(a)]. The eigenmode at point C in Fig. 12(a) consists of a backward-traveling LHP electromagnetic wave [from $E_{1-}(\hat{k}, \hat{\omega})$], and forward-traveling LHP electromagnetic and electrostatic modes. Reference to Figs. 12(c) and 12(d) shows that the backward-traveling component exceeds the other two components in amplitude. In Sec. III C, a similar situation was found to exist at point B in Fig. 7(a), except that the forward-traveling electromagnetic component is RHP. Like Fig. 7(a), Fig. 12(a) shows a fairly large growth

rate at the resonance wave number on the branch **ACBIJ**. Moreover, Figs. 12(c) and 12(d) show that the corresponding eigenmode has a relatively strong RHP electromagnetic component.

Finally, notice that no gap appears in the growth-rate curves in Fig. 12(a) to correspond to the gap between points F and H in Fig. 7(a).

D. Remarks concerning numerical examples

The analysis of the above numerical examples for the axial-dependent equilibrium leads to the same general conclusions as those given in Sec. III C for the time-dependent equilibrium. A rich structure of different growth-rate curves and unstable eigenmodes can be induced by varying the form of $\Psi(\zeta)$, i.e., the values of w_1 and w_2 . A suitable choice of $\Psi(\zeta)$ can significantly increase growth rates of RHP electromagnetic waves at the resonance wave number $\hat{k}=1/(1-\beta_z)$ and can significantly increase or reduce growth rates at large values of \hat{k} . At small values of \hat{k} , where backward-

traveling components are present, growth rates and the structures of eigenmodes depend strongly on the form of $\Psi(\zeta)$. This fact suggests that properties of absolute instabilities may depend strongly on $\Psi(\zeta)$. However, a study of this conjecture has not been carried out.

For the same parameters $(\Omega_c, \gamma_0, \alpha_0)$, growth rate curves for corresponding $(s_1=w_1, s_2=w_2)$ time-dependent and axial-dependent systems usually show some resemblance. Nevertheless, the eigenmode structures are very different in the two cases. In the time-dependent case, unstable eigenmodes for coupled systems consist of two or three components of the same wave numbers and different frequencies, whereas in the axial-dependent case the components have the same frequencies and different wave numbers. Moreover, for small values of \hat{k} , the handedness and directions of motion of components may differ between the two cases.

V. CONCLUSIONS

We have studied stability properties of a relativistic electron beam propagating along an applied magnetic field $B_0 \hat{e}_z$, using the Maxwell-Vlasov equations under the constraint that spatially dependent quantities are functions of z only. Of particular interest are those cases in which the equilibrium distribution is not uniformly random in the electron gyrophase angle ϕ . Two equilibrium distributions have been considered. These are the time-dependent distribution $f_0(p_\perp, p_z, \xi)$, where $\xi = \phi - \Omega_c t / \gamma$, and the spatial-dependent distribution $f_0(p_\perp, p_z, \zeta)$, where $\zeta = \phi - m\Omega_c z / p_z$. Since neither of these distributions can be converted into the other by a Lorentz transformation, the distributions represent two physically different systems. It is found that in general the Fourier components of the perturbed electric and magnetic fields are related by the integral equations (26)–(28) for the case of the time-dependent equilibrium distribution, and by the integral equations (41)–(43) for the case of the spatial-dependent equilibrium distribution. In our numerical analysis, however, we consider special cases in which the integral equations reduce to algebraic equations even though the equilibrium distribution is not uniformly random in phase.

If there is no spread in electron energies (or equivalently p) in the time-dependent equilibrium distribution, then the integral equations (26)–(28) reduce to just three algebraic equations [Eq. (58)] relating the Fourier components $E_{1-}(k, \omega)$, $E_{1+}(k, \omega - 2\omega_c)$, and $E_{1z}(k, \omega - \omega_c)$ of the perturbed fields. Consequently, an eigenmode of the system consists of a RHP electromagnetic wave, a LHP electromagnetic wave, and an electrostatic wave. These components have the same wave number, and the same spatial and temporal growth or decay rates, but have different frequencies. [The electrostatic component is decoupled if the Fourier coefficient $\hat{g}_1(p_0, \alpha)$ in Eq. (57) vanishes, and all three components decouple if $\hat{g}_2(p_0, \alpha)$ also vanishes.]

If there is no spread in the axial component of momentum (p_z) in the spatial-dependent equilibrium distribution, then the integral equations (41)–(43) reduce to just three algebraic equations [Eq. (89)] relating the perturbed field Fourier components $E_{1-}(k, \omega)$, $E_{1+}(k + 2m\Omega_c / p_{z0}, \omega)$, and

$E_{1z}(k + m\Omega_c / p_{z0}, \omega)$. Therefore the components of an eigenmode are a RHP electromagnetic wave, a LHP electromagnetic wave, and an electrostatic wave. These components have the same frequency, and the same spatial and temporal growth or decay rates, but have different wave numbers. [In analogy with the time-dependent case, the electrostatic component is decoupled if the Fourier coefficient $\hat{h}_1(p_\perp, p_{z0})$ in Eq. (88) vanishes, and all of the components decouple if $\hat{h}_2(p_\perp, p_{z0})$ also vanishes.]

Numerical computations of stability properties have been carried out for both the time- and spatial-dependent equilibrium distributions for the case where no spread is present in both p and the pitch angle α (or equivalently in both p_\perp and p_z). In this case the frequencies and wave numbers can be normalized to the relativistic cyclotron frequency ω_c by defining $\hat{\omega} = \omega / \omega_c$ and $\hat{k} = ck / \omega_c$. The computations are restricted to real values of \hat{k} , so that $\text{Im } \hat{\omega} > 0$ indicates temporal growth. It is found that (for fixed applied magnetic field, energy, and pitch angle) a rich variety of growth-rate curves and eigenmodes can be obtained by changing the dependence of the equilibrium distribution on the phase angle. Appropriate choices of the phase-angle dependence can significantly increase growth rates near the resonance wave number $\hat{k}_r = 1/(1 - \beta_z)$. Growth rates at large values of \hat{k} can on the one hand be enhanced and on the other hand be suppressed altogether. Moreover, finite intervals (in \hat{k}) of no growth can be produced. Finally, growth rate curves and the form of eigenvectors at small values of $|\hat{k}|$, where backward traveling components are present, are particularly sensitive to the ϕ -dependence of the equilibrium distribution.

Based on the results obtained in this paper, we conclude that coherently gyrating electron beams can interact with electromagnetic and electrostatic waves in a rich manner, even in one-dimensional configurations. Such interactions are important if they occur in an extended space or time. Therefore it is critical to take into account these interactions in the design of coherent radiation devices based on coherently gyrating electron beams.

As an important area in our current research, we are analyzing the integral equations to determine the structures of eigenmodes in the general case. We also point out that the results of this work are readily extended by Lorentz transformations to frames of reference in which the distributions in phase vary both spatially and temporally. (See the Appendix.) Consequently, another area of current research is the extension of our analysis to spatiotemporal distributions.^{21–24}

ACKNOWLEDGMENT

This research was supported in part by the Air Force Office of Scientific Research, Grant Nos. F49620-94-1-0374 and F49620-97-1-0325.

APPENDIX: RELATIONS BETWEEN EQUILIBRIUM DISTRIBUTIONS

In this paper, we consider equilibrium distributions whose form in the laboratory reference frame is either $f_0(\mathbf{p}, t) = f_0(p_\perp, p_z, \xi)$ or $f_0(\mathbf{z}, p) = f_0(p_\perp, p_z, \zeta)$. Also, in

this appendix, we define f_0 to be n_0 times the equilibrium distribution used throughout the rest of this paper. Below it is shown that, under a Lorentz transformation to a new reference frame moving in the z -direction relative to the laboratory frame with velocity $\beta_u = u/c$, either of these forms is transformed into combinations of the two original forms.

It is well known that a distribution $f_0(z, \mathbf{p}, t)$ is invariant under a Lorentz transformation. Consequently, under the Lorentz transformations described above the distribution becomes

$$f_0(z', \mathbf{p}', t') = f_0(z, \mathbf{p}, t), \quad (\text{A1})$$

where

$$\begin{aligned} z &= \gamma_u(z' + \beta_u c t'), \\ c t &= \gamma_u(c t' + \beta_u z'), \\ p_z &= \gamma_u(p'_z + \beta_u \gamma' m c), \\ \gamma m c &= \gamma_u(\gamma' m c + \beta_u p'_z). \end{aligned} \quad (\text{A2})$$

Moreover, $p_\perp = p'_\perp$, $\phi = \phi'$, and $\gamma_u = (1 - \beta_u^2)^{-1/2}$.

Expressing $\xi = \Omega_c t / \gamma$ in terms of transformed (primed) quantities, we find that

$$\begin{aligned} \xi &= (1 + \beta_u \beta'_z)^{-1} \xi' + \beta'_z \beta_u (1 + \beta_u \beta'_z)^{-1} \zeta' \\ &= \gamma_u^2 (1 - \beta_u \beta'_z) \xi' + \gamma_u^2 \beta_u (\beta'_z - \beta_u) \zeta', \end{aligned} \quad (\text{A3})$$

where $\beta_z = v_z/c$, and

$$\xi' = \phi - \frac{\Omega_c}{\gamma'} t', \quad (\text{A4})$$

$$\zeta' = \phi - \frac{\Omega_c}{\gamma'} \frac{z'}{v'_z} = \phi - \frac{m \Omega_c}{p'_z} z'. \quad (\text{A5})$$

Consequently, if the laboratory frame distribution is of the form $f_0(\mathbf{p}, t) = f_0(p_\perp, p_z, \xi)$, then the moving frame distribution will be of the form $f'_0(z', \mathbf{p}', t') = f_0(p_\perp, p'_z, c_1 \xi' + c_2 \zeta')$, where $c_1 = (1 + \beta_u \beta'_z)^{-1}$ and $c_2 = \beta'_z \beta_u (1 + \beta_u \beta'_z)^{-1}$. Notice that $c_1 + c_2 = 1$ and that $c_1 > 0$, so that a Lorentz transformation cannot change the form of a distribution from $f_0(p_\perp, p_z, \xi)$ into $f'_0(p_\perp, p'_z, \xi')$ for any value of \mathbf{p}' . Finally, notice that Eq. (55) must be applied with care to the singular case of $\beta_u = \beta_z$ (i.e., $\beta'_z = 0$), because $\zeta' \rightarrow \infty$ as $\beta'_z \rightarrow 0$. In this singular case, $\xi = \xi' - \beta_z \Omega_c z' / \gamma' c$ where $\gamma' = (p_\perp^2 / m^2 c^2 + 1)^{1/2}$.

Expressing $\zeta = \phi - m \Omega_c z / \gamma p_z = \phi - \Omega_c z / \gamma v_z$ in terms of primed quantities, we obtain

$$\begin{aligned} \zeta &= \frac{\beta_u}{(\beta_u + \beta'_z)} \xi' + \frac{\beta'_z}{(\beta_u + \beta'_z)} \zeta' \\ &= \frac{\gamma_u^2 \beta_u}{\beta_z} (1 - \beta_z \beta_u) \xi' + \frac{\gamma_u^2}{\beta_z} (\beta'_z - \beta_u) \zeta'. \end{aligned} \quad (\text{A6})$$

Under a Lorentz transformation, a distribution of the form $f_0(z, \mathbf{p}) = f_0(p_\perp, p_z, \xi)$ attains the form $f'_0(z', \mathbf{p}', t') = f'_0(p_\perp, p'_z, c_1 \xi' + c_2 \zeta')$, where now $c_1 = \beta_u / (\beta_u + \beta'_z)$ and $c_2 = \beta'_z / (\beta_u + \beta'_z)$. Again, notice that $c_1 + c_2 = 1$. In the singular case of $\beta_u \rightarrow \beta_z$ (i.e., $\beta'_z \rightarrow 0$), Eq. (A6) reduces to $\zeta = \xi' - (\Omega_c / \gamma') (z' / v_z)$. Consequently, a Lorentz transformation cannot change the form of a distribution from $f_0(p_\perp, p_z, \xi)$ into $f'_0(p_\perp, p'_z, \xi')$ for any value of \mathbf{p}' .

Finally, we remark that if the laboratory frame is taken to be the primed frame, then distributions of definite ξ in Eq. (A3) or definite ζ in Eq. (A6) are referred to as spatiotemporal distributions in the literature.²¹⁻²⁴

¹K. R. Chu and J. L. Hirschfield, Phys. Fluids 21, 461 (1978).

²R. C. Davidson and P. H. Yoon, Phys. Rev. A 39, 2534 (1989).

³P. H. Yoon and R. C. Davidson, Phys. Rev. A 35, 2619 (1987).

⁴P. H. Yoon and R. C. Davidson, Phys. Rev. A 35, 2718 (1987).

⁵P. H. Yoon and R. C. Davidson, J. Plasma Phys. 43, 269 (1990).

⁶H. S. Uhm and R. C. Davidson, Phys. Fluids 29, 2713 (1986).

⁷A. Fruchtman and L. Friedland, J. Appl. Phys. 53, 4011 (1982).

⁸A. Fruchtman and L. Friedland, IEEE J. Quantum Electron. 19, 327 (1983).

⁹A. Fruchtman, Phys. Fluids B 4, 4101 (1992).

¹⁰T. H. Kho, A. T. Lin, and L. Chen, Phys. Fluids 31, 3120 (1988).

¹¹C. Chen, J. A. Davies, G. Zhang, and J. Wurtele, Phys. Rev. Lett. 69, 73 (1992).

¹²P. Yoon and T. Chang, J. Plasma Phys. 42, 193 (1989).

¹³V. L. Bratman, N. S. Ginsberg, G. S. Nusinovich, M. I. Petelin, and P. S. Strelkov, Int. J. Electron. 61, 541 (1981).

¹⁴T. H. Kho and A. T. Lin, Phys. Fluids B 2, 822 (1990).

¹⁵K. R. Chen, J. M. Dawson, A. T. Lin, and T. Katsouleas, Phys. Fluids B 3, 1270 (1991).

¹⁶B. G. Danly, J. A. Davies, K. D. Pendergast, R. J. Tempkin, and J. S. Wurtele, Proc. SPIE, Microwave and Particle Beam Sources and Directed Energy Concepts 1061, 243 (1989).

¹⁷C. Chen and J. S. Wurtele, Phys. Rev. Lett. 65, 3389 (1990).

¹⁸C. Chen and J. S. Wurtele, Phys. Fluids B 3, 2133 (1991).

¹⁹C. Chen, B. G. Danly, G. Shevets, and J. S. Wurtele, IEEE Trans. Plasma Sci. 20, 149 (1992).

²⁰H. P. Freund and C. Chen, Int. J. Electron. 72, 1005 (1992).

²¹A. K. Ganguly and J. L. Hirschfield, Phys. Rev. Lett. 70, 291 (1993); Phys. Rev. E 47, 4364 (1993).

²²J. L. Hirschfield, Phys. Rev. A 44, 6845 (1991).

²³J. L. Hirschfield, Phys. Rev. A 46, 5161 (1992).

²⁴C. S. Kou, D. B. McDermott, N. C. Luhmann, and K. R. Chu, IEEE Trans. Plasma Sci. 18, 343 (1990).

²⁵C. S. Wu, Space Sci. Rev. 41, 215 (1985).

²⁶H. P. Freund, C. S. Wu, and J. D. Gaffey, Jr., Phys. Fluids 27, 1396 (1984).

²⁷H. P. Freund, J. Q. Dong, C. S. Wu, and L. C. Lee, Phys. Fluids 30, 3106 (1987).

²⁸P. H. Yoon and D. Krauss-Varban, Phys. Fluids B 2, 1918 (1990).

²⁹P. H. Yoon and C. S. Wu, Phys. Rev. A 44, 6819 (1991).

³⁰L. F. Ziebell and P. H. Yoon, Phys. Plasmas 2, 1285 (1995).

³¹A. Bers, Handbook of Plasma Physics, Vol. 1, Basic Plasma Physics I, edited by A. A. Galeev and R. N. Sudan (North-Holland, Amsterdam, 1983), Chap. 3.2.

³²Y. Y. Lau, K. R. Chu, L. R. Barnett, and V. I. Granatstein, Int. J. Infrared Millim. Waves 2, 373 (1981).

³³J. A. Davies, Phys. Fluids B 1, 663 (1989).

A Dielectric Omnidirectional Reflector

Yoel Fink, Joshua N. Winn, Shanhui Fan, Chiping Chen,
Jurgen Michel, John D. Joannopoulos, Edwin L. Thomas*

A design criterion that permits truly omnidirectional reflectivity for all polarizations of incident light over a wide selectable range of frequencies was used in fabricating an all-dielectric omnidirectional reflector consisting of multilayer films. The reflector was simply constructed as a stack of nine alternating micrometer-thick layers of polystyrene and tellurium and demonstrates omnidirectional reflection over the wavelength range from 10 to 15 micrometers. Because the omnidirectionality criterion is general, it can be used to design omnidirectional reflectors in many frequency ranges of interest. Potential uses depend on the geometry of the system. For example, coating of an enclosure will result in an optical cavity. A hollow tube will produce a low-loss, broadband waveguide, whereas a planar film could be used as an efficient radiative heat barrier or collector in thermoelectric devices.

Mirrors, probably the most prevalent of optical devices, are used for imaging and solar energy collection and in laser cavities. One can distinguish between two types of

mirrors, the age-old metallic and the more recent dielectric. Metallic mirrors reflect light over a broad range of frequencies incident from arbitrary angles (that is, omnidirectional reflectance). However, at infrared and optical frequencies, a few percent of the incident power is typically lost because of absorption. Multilayer dielectric mirrors are used primarily to reflect a narrow range of frequencies incident from a particular angle or particular angular range. Unlike their metallic counterparts, dielectric reflectors can be extremely low loss. The ability to reflect light of arbitrary angle of incidence for all-dielectric structures has been associated with the existence of a

Y. Fink, Department of Material Science and Engineering and Plasma Science and Fusion Center, Massachusetts Institute of Technology, Cambridge, MA 02139, USA. J. N. Winn, S. Fan, J. D. Joannopoulos, Department of Physics, Massachusetts Institute of Technology, Cambridge, MA 02139, USA. C. Chen, Plasma Science and Fusion Center, Massachusetts Institute of Technology, Cambridge, MA 02139, USA. J. Michel and E. L. Thomas, Department of Material Science and Engineering, Massachusetts Institute of Technology, Cambridge, MA 02139, USA.

*To whom correspondence should be addressed.

complete photonic band gap (1-3), which can exist only in a system with a dielectric function that is periodic along three orthogonal directions. In fact, a recent theoretical analysis predicted that a sufficient condition for the achievement of omnidirectional reflection in a periodic system with an interface is the existence of an overlapping

band gap regime in phase space above the light cone of the ambient media (4). Now we extend the theoretical analysis and provide experimental realization of a multilayer omnidirectional reflector operable in infrared frequencies. The structure is made of thin layers of materials with different dielectric constants (polystyrene and tellu-

rium) and combines characteristic features of both the metallic and dielectric mirrors. It offers metallic-like omnidirectional reflectivity together with frequency selectivity and low-loss behavior typical of multilayer dielectrics.

We consider a system that is made of an array of alternating dielectric layers coupled to a homogeneous medium, characterized by n_0 (such as air with $n_0 = 1$), at the interface. Electromagnetic waves are incident upon the multilayer film from the homogeneous medium. Although such a system has been analyzed extensively in the literature (5-7), the possibility of omnidirectional reflectivity was not recognized until recently. The generic system is described by the index of refraction profile in Fig. 1, where h_1 and h_2 are the layer thickness and n_1 and n_2 are the indices of refraction of the respective layers. The incident wave has a wave vector $\mathbf{k} = k_x \hat{e}_x + k_y \hat{e}_y$, and a frequency of $\omega = c|\mathbf{k}|/n_0$, where c is the speed of light in vacuum and \hat{e}_x and \hat{e}_y are unit vectors in the x and y directions, respectively. The wave vector together with the normal to the periodic structure defines a mirror plane of symmetry that allows us to distinguish between two independent electromagnetic modes: transverse electric (TE) modes and transverse magnetic (TM) modes. For the TE mode, the electric field is perpendicular to the plane, as is the magnetic field for the TM mode. The distribution of the electric field of the TE mode (or the magnetic field in the TM mode) in a particular layer within the stratified structure can be written as a sum of two plane waves traveling in opposite directions. The amplitudes of the two plane waves in a particular layer α of one cell are related to the amplitudes in the same layer of an adjacent cell by a unitary 2×2 translation matrix $U^{(\alpha)}$ (7).

General features of the transport properties of the finite structure can be understood when the properties of the infinite structure are elucidated. In a structure with an infinite number of layers, translational symmetry along the direction perpendicular to the layers leads to Bloch wave solutions of the form

$$E_K(x, y) = E_K(x) e^{iKx} e^{iky} \quad (1)$$

where $E_K(x, y)$ is a field component, $E_K(x)$ is periodic, with a period of length a , and K is the Bloch wave number given by

$$K = \frac{i}{a} \ln \left(\frac{1}{2} \text{Tr}(U^{(\alpha)}) \right) \pm \left\{ \frac{1}{4} [\text{Tr}(U^{(\alpha)})]^2 - 1 \right\}^{1/2} \quad (2)$$

Solutions of the infinite system can be propagating or evanescent, corresponding

Fig. 1. Schematic of the multilayer system showing the layer parameters (n_α and h_α are the index of refraction and thickness of layer α , respectively), the incident wave vector \mathbf{k} , and the electromagnetic mode convention. E and B are the electric and magnetic fields, respectively.

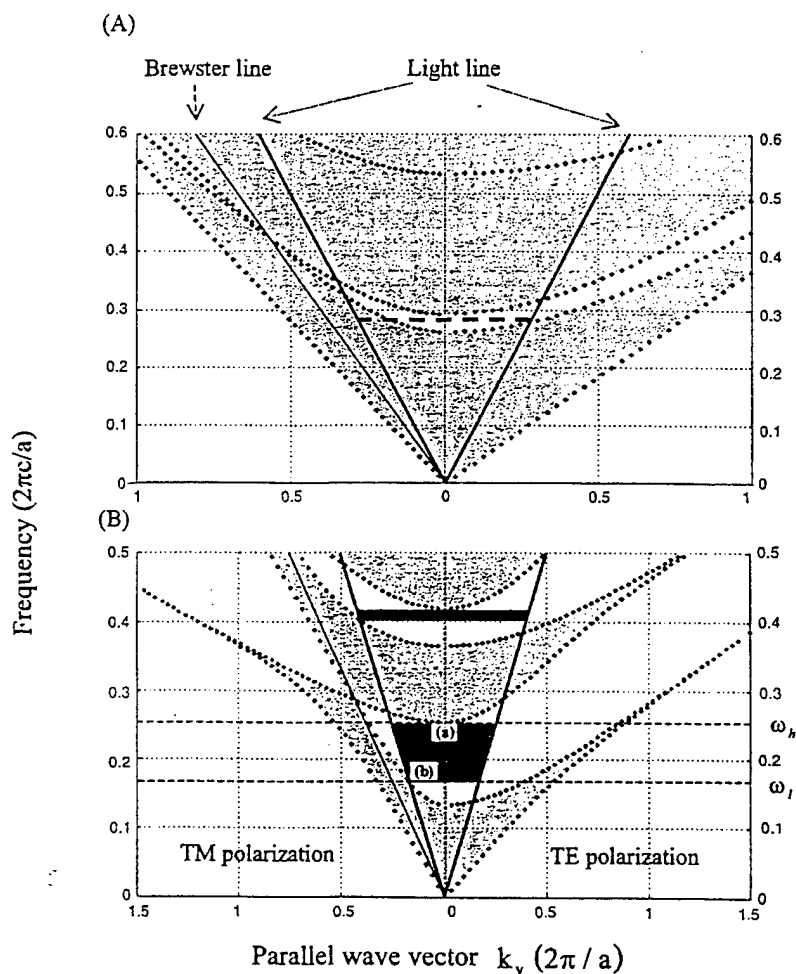
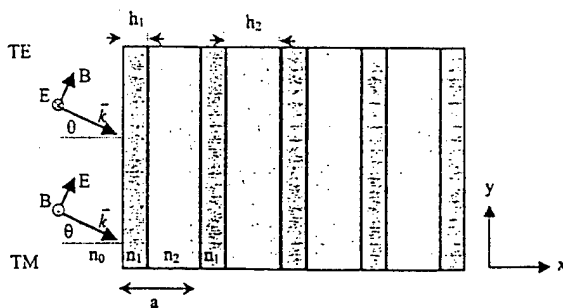


Fig. 2. (A) Projected band structure of a multilayer film with the light line and Brewster line, exhibiting a reflectivity range of limited angular acceptance with $n_0 = 1$, $n_1 = 2.2$ and $n_2 = 1.7$ and a thickness ratio of $h_2/h_1 = 2.2/1.7$. (B) Projected band structure of a multilayer film together with the light line and Brewster line, showing an omnidirectional reflectance range at the first and second harmonic. Propagating states, light gray; evanescent states, white; and omnidirectional reflectance range, dark gray. The film parameters are $n_1 = 4.6$ and $n_2 = 1.6$ with a thickness ratio of $h_2/h_1 = 1.6/0.8$. These parameters are similar to the actual polystyrene-tellurium film parameters measured in the experiment.

to real or imaginary Bloch wave numbers, respectively. The solution of Eq. 2 defines the band structure for the infinite system, $\omega(K, k_y)$. It is convenient to display the solutions of the infinite structure by projecting the $\omega(K, k_y)$ function onto the $\omega-k_x$ plane. Examples of such projected structures are shown in Fig. 2. A and B. The light gray areas highlight phase space where K is strictly real, that is, regions of propagating states, whereas the white areas represent regions containing evanescent states. The shape of the projected band structures for the multilayer film can be understood intuitively. At $k_y = 0$, the band gap for waves traveling normal to the layers is recovered. For $k_y > 0$, the bands curve upward in frequency. As $k_y \rightarrow \infty$, the modes become largely confined to the slabs with the high index of refraction and do not couple between layers (and are therefore independent of k_x).

For a finite structure, the translational symmetry in the directions parallel to the layers is preserved; hence, k_y remains a conserved quantity. In the direction perpendicular to the layers, the translational symmetry no longer exists. Nevertheless, the K number, as defined in Eq. 2, is still relevant, because it is determined purely by the dielectric and structural property of a single bilayer. In regions where K is imaginary, the electromagnetic field is strongly attenuated. As the number of layers is increased, the transmission coefficient decreases exponentially, whereas the reflectivity approaches unity.

Because we are primarily interested in waves originating from the homogeneous medium external to the periodic structure, we will focus only on the portion of phase space lying above the light line. Waves originating from the homogeneous medium satisfy the condition $\omega \geq ck_y/n_0$, where n_0 is the refractive index of the homogeneous medium, and therefore they must reside above the light line. States of the homogeneous medium with $k_y = 0$ are normal incident, and those lying on the $\omega = ck_y/n_0$ line with $k_x = 0$ are incident at an angle of 90° .

The states in Fig. 2A that are lying in the restricted phase space defined by the light line and that have a (ω, k_y) corresponding to the propagating solutions (gray areas) of the crystal can propagate in both the homogeneous medium and the structure. These waves will partially or entirely transmit through the film. Those states with (ω, k_y) in the evanescent regions (white areas) can propagate in the homogeneous medium but will decay in the crystal—waves corresponding to this portion of phase space will be reflected off the structure.

The multilayer system leading to Fig. 2A represents a structure with a limited reflectivity cone because for any frequency one can always find a k_x vector for which a wave at that frequency can propagate in the crystal and hence transmit through the film. For example, a wave with $\omega = 0.285 \times 2\pi c/a$ (dashed horizontal line in Fig. 2A) will be reflected for a range of k_x values ranging from 0 (normal incidence) to $0.285 \times 2\pi/a$ (90° incidence) in the TE mode, whereas in the TM mode it begins to transmit at a value of $k_x = 0.187 \times 2\pi/a$ ($\sim 41^\circ$ incidence). The necessary and sufficient criterion (δ) for omnidirectional reflectivity at a given frequency is that no transmitting state of the structure exists inside the light cone; this criterion is satisfied by frequency ranges marked in dark gray in Fig. 2B. In fact, the system leading to Fig. 2B exhibits two omnidirectional reflectivity ranges.

The omnidirectional range is defined from above by the normal incidence band edge $\omega_h(k_x = \pi/a, k_y = 0)$ (point a in Fig. 2B) and from below by the intersection of the top of the TM allowed band edge with the light line $\omega_l(k_x = \pi/a, k_y = \omega/c)$ (point b in Fig. 2B).

The exact expression for the band edges is

$$\frac{1 + \Lambda}{2} \cos(k_x^{(1)} h_1 + k_x^{(2)} h_2) + \frac{1 - \Lambda}{2} \cos(k_x^{(1)} h_1 - k_x^{(2)} h_2) + 1 = 0, \quad (3)$$

where $k_x^{(\alpha)} = \sqrt{(\omega n_\alpha/c)^2 - k_y^2}$ ($\alpha = 1, 2$) and

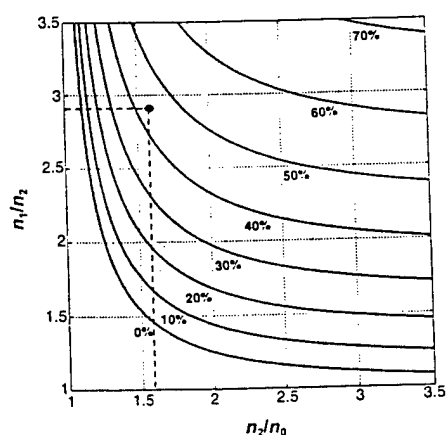


Fig. 3. (left). The range to midrange ratio $(\omega_h - \omega_l)/1/2(\omega_h + \omega_l)$, for the fundamental frequency range of omnidirectional reflection, plotted as contours. Here, the layers were set to quarter wave thickness and $n_1 > n_2$. The ratio for our materials is about 45% ($n_1/n_2 = 2.875$ and $n_2/n_0 = 1.6$). It is located at the intersection of the dashed lines (black dot). (dashed line) reflectance (in percent) as a function of wavelength for TM and TE modes at normal, 45° , and 80° angles of incidence, showing an omnidirectional reflectivity band.

$$\Lambda \equiv \begin{cases} \frac{1}{2} \left(\frac{k_x^{(2)}}{k_x^{(1)}} + \frac{k_x^{(1)}}{k_x^{(2)}} \right) \text{ TE} \\ \frac{1}{2} \left(\frac{n_1^2 k_x^{(2)}}{n_2^2 k_x^{(1)}} + \frac{n_2^2 k_x^{(1)}}{n_1^2 k_x^{(2)}} \right) \text{ TM} \end{cases} \quad (4)$$

A dimensionless parameter used to quantify the extent of the omnidirectional range is the range to midrange ratio defined as $(\omega_h - \omega_l)/1/2(\omega_h + \omega_l)$. Figure 3 is a plot of this ratio as a function of n_2/n_1 and n_1/n_0 , where ω_h and ω_l are determined by solutions of Eq. 3 with quarter wave layer thickness. The contours in this figure represent various equioomnidirectional ranges for different material index parameters and could be useful for design purposes.

It may also be useful to have an approximate analytical expression for the extent of the gap. This can be obtained by setting $\cos(k_x^{(1)} h_1 - k_x^{(2)} h_2) \approx 1$ in Eq. 3. We find that for a given incident angle θ_0 , the approximate width in frequency is

$$\Delta\omega(\theta_0) = \frac{2c}{h_1 \sqrt{n_1^2 - n_0^2 \sin^2 \theta_0} + h_2 \sqrt{n_2^2 - n_0^2 \sin^2 \theta_0}} \times \left[\cos^{-1} \left(-\frac{\Lambda - 1}{\Lambda + 1} \right) - \cos^{-1} \left(\frac{\Lambda - 1}{\Lambda + 1} \right) \right] \quad (5)$$

At normal incidence, there is no distinction between TM and TE modes. At increasingly oblique angles, the gap of the TE mode increases, whereas the gap of the TM mode decreases. In addition, the center of the gap shifts to higher frequencies. Therefore, the

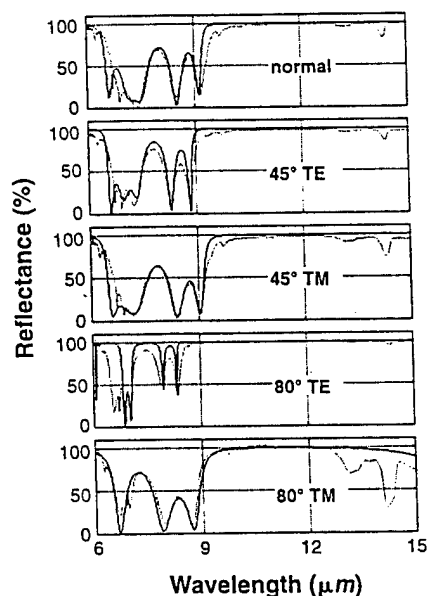


Fig. 4 (right). Calculated (solid line) and measured (dashed line) reflectance (in percent) as a function of wavelength for TM and TE modes at normal, 45° , and 80° angles of incidence, showing an omnidirectional reflectivity band.

criterion for the existence of omnidirectional reflectivity can be restated as the occurrence of a frequency overlap between the gap at normal incidence and the gap of the TM mode at 90°. Analytical expressions for the range to midrange ratio can be obtained by setting

$$\omega_h = \frac{2c}{h_2 n_2 + h_1 n_1} \cos^{-1} \left(- \left| \frac{n_1 - n_2}{n_1 + n_2} \right| \right) \quad (6a)$$

$$\omega_l = \frac{2c}{h_2 \sqrt{n_2^2 - n_0^2} + h_1 \sqrt{n_1^2 - n_0^2}} \times \cos^{-1} \left(\left| \frac{n_1^2 \sqrt{n_2^2 - n_0^2} - n_2^2 \sqrt{n_1^2 - n_0^2}}{n_1^2 \sqrt{n_2^2 - n_0^2} + n_2^2 \sqrt{n_1^2 - n_0^2}} \right| \right) \quad (6b)$$

Moreover, the maximum range width is attained for thickness values that are not equal to the quarter wave stack although the increase in band width gained by deviating from the quarter wave stack is typically only a few percent (4).

In general, the TM mode defines the lower frequency edge of the omnidirectional range. An example can be seen in Fig. 2B for a particular choice of the indices of refraction. This can be proven by showing that

$$\left. \frac{\partial \omega}{\partial k_y} \right|_{TM} \geq \left. \frac{\partial \omega}{\partial k_y} \right|_{TE} \quad (7)$$

in the region that resides inside the light line. The physical reason for Eq. 7 lies in the vectorial nature of the electric field. In the upper portion of the first band, the electric field concentrates its energy in the high dielectric regions. Away from normal incidence, the electric field in the TM mode has a component in the direction of periodicity, and this component forces a larger portion of the electric field into the low dielectric regions. The group velocity of the TM mode is therefore enhanced. In contrast, the electric field of the TE mode is always perpendicular to the direction of periodicity and can concentrate its energy primarily in the high dielectric region.

A polystyrene-tellurium (PS-Te) material system was chosen to demonstrate omnidirectional reflectivity. Tellurium has a high index of refraction and low loss characteristics in the frequency range of interest. In addition, its relatively low latent heat of condensation together with the high glass transi-

tion temperature of the PS minimizes diffusion of Te into the polymer layer. The choice of PS, which has a series of absorption peaks in the measurement range (9), demonstrates the competition between reflectivity and absorption that occurs when an absorption peak is located in the evanescent state region. The Te (0.8 μm) and PS (1.65 μm) films were deposited (10) sequentially to create a nine-layer film (11).

The optical response of this particular multilayer film was designed to have a high reflectivity region in the 10- to 15- μm range for any angle of incidence (in the experiment, we measure from 0° to 80°). The optical response at oblique angles of incidence was measured with a Fourier Transform Infrared Spectrometer (Nicolet 860) fitted with a polarizer (ZnS; SpectraTech) and an angular reflectivity stage (VeeMax; SpectraTech). At normal incidence, the reflectivity was measured with a Nicolet Infrared Microscope. A freshly evaporated aluminum mirror was used as a background for the reflectance measurements.

Good agreement between the calculated (12) and measured reflectance spectra at normal, 45°, and 80° incidence for the TM and TE modes is shown in Fig. 4. The regimes of high reflectivity at the different angles of incidence overlap, thus forming a reflective range of frequencies for light of any angle of incidence. The frequency location of the omnidirectional range is determined by the layer thickness and can be tuned to meet specifications. The range is calculated from Eq. 6 to be 5.6 μm , and the center wavelength is 12.4 μm , corresponding to a 45% range to midrange ratio shown in dashed lines in Fig. 3 for the experimental index of refraction parameters. These values are in agreement with the measured data. The calculations are for lossless media and therefore do not predict the PS absorption band at ~13 and 14 μm . The PS absorption peak is seen to increase at larger angles of incidence for the TM mode and to decrease for the TE mode. The physical basis for these phenomena lies in the relation between the penetration depth and the amount of absorption. The penetration depth is $\xi \propto \text{Im}(1/K)$, where K is the Bloch wave number. It can be shown that ξ is a monotonically increasing function of the incident angle for the TM mode of an omnidirectional reflector and is relatively constant for the TE mode. Thus, the TM mode penetrates deeper into the structure at increasing angles of incidence (Table 1) and is more readily absorbed. The magnitude of the imaginary part of the Bloch wave number for a mode lying in the gap is related to its distance from the band edges. This distance increases in the TE mode because of the widening of the gap at increasing angles of incidence and decreases in the TM mode because of the shrinking of the gap.

The PS-Te structure does not have a complete photonic band gap. Its omnidirectional reflectivity is due instead to the restricted phase space available to the propagating states of the system. The materials and processes were chosen for their low cost and applicability to large area coverage. The possibility of achieving omnidirectional reflectivity itself is not associated with any particular choice of materials and can be applied to many wavelengths of interest. Our structure offers metallic-like omnidirectional reflectivity for a wide range of frequencies and at the same time is of low loss. In addition, it allows the flexibility of frequency selection.

References and Notes

1. E. Yablonovitch, *Phys. Rev. Lett.* **58**, 2059 (1987).
2. S. John, *ibid.*, p. 2486.
3. J. D. Joannopoulos, R. Meade, J. N. Winn, *Photonic Crystals: Molding the Flow of Light* (Princeton Univ. Press, Princeton, NJ, 1995).
4. J. N. Winn et al., *Opt. Lett.*, **23**, 1573 (1998).
5. F. Abeles, *Ann. Phys.* **5**, 706 (1950).
6. M. Born and E. Wolf, *Principles of Optics* (Pergamon, ed. 6, 1980), p. 67.
7. P. Yeh et al., *J. Opt. Soc. Am.* **67**, 423 (1977).
8. A necessary condition for omnidirectional reflectivity is that light from outside the film cannot be allowed to access the Brewster angle $\theta_B = \tan^{-1}(n_1/n_2)$ of the multilayer structure because at this angle the TM mode will be transmitted through. This condition is met when the Brewster line lies outside of the light line or in terms of the refractive indices of the layers $\sin^{-1}(n_0/n_2) < \theta_B$. A sufficient condition is the existence of a particular frequency at which no propagating mode within the crystal exists between $k_y = 0$ and $k_y = n_0 \omega/c$. Figure 2A is an example of a structure that does not have an omnidirectional reflectivity range even though its Brewster crossing is inaccessible to light coming from the homogeneous medium (the Brewster crossing lies outside the light cone). This is due to the large group velocity of modes in the lower band edge of the TM mode that allow every frequency to couple to a propagating state in the crystal. This should be contrasted with Fig. 2B, which exhibits an omnidirectional reflectivity range (highlighted in dark gray); the high indices of refraction actually allow for the opening of an additional omnidirectional reflectivity range in the higher harmonic as well.
9. C. J. Pouchert, *The Aldrich Library of FT-IR Spectra*, vol. II (Aldrich Chemical, Milwaukee, WI, 1985), p. 12048.
10. A 0.8 \pm 0.09- μm -thick layer of tellurium (99.99+%; Strem Chemicals) was vacuum evaporated at 10^{-6} torr and 7A (Ladd Industries 30000) onto a NaCl 25-mm salt substrate (polished NaCl window; Wilmad Glass). The layer thickness and deposition rate were monitored in situ with a crystal thickness monitor (Sycon STM100). A 10% solution of polystyrene (Goodyear PS standard, 110,000 g/mol) in toluene was spin cast at 1000 rpm onto the tellurium-coated substrate and allowed to dry for a few hours; the polymer layer thickness is $1.65 \pm 0.09 \mu\text{m}$.
11. The nine-layer film sequence was Te/PS/Te/PS/Te/PS/Te/PS/Te.
12. The calculations were done with the transfer matrix method described in (5) with the film parameters.
13. We thank J. F. Hester and A. Urbas for their valuable assistance and M. G. Bawendi and G. B. Kenney for stimulating discussions and inspiration. Supported in part by Defense Advanced Research Agency through U.S. Army Research Office under grant DAAG55-97-1-0366 and by the Air Force Office of Scientific Research under grants F49620-97-1-0325 and F49620-97-1-0385.

Table 1. Penetration depth (ξ) at different angles of incidence for the TE and TM modes.

Angle of incidence (degrees)	ξ_{TM} (μm)	ξ_{TE} (μm)
0	2.51	2.51
45	3.05	2.43
80	4.60	2.39

6 August 1998; accepted 6 October 1998